題目(和文)	ナノ空間中に拘束されたホモポリマーとブロック鎖の結晶化
Title(English)	Crystallization of Homopolymers and Block Chains Confined in Nanodomains
著者(和文)	中川慎太郎
Author(English)	Shintaro Nakagawa
出典(和文)	学位:博士(工学), 学位授与機関:東京工業大学, 報告番号:甲第10121号, 授与年月日:2016年3月26日, 学位の種別:課程博士, 審査員:野島 修一,石曽根 隆,大塚 英幸,中嶋 健,戸木田 雅利
Citation(English)	Degree:Doctor (Engineering), Conferring organization: Tokyo Institute of Technology, Report number:甲第10121号, Conferred date:2016/3/26, Degree Type:Course doctor, Examiner:,,,,
学位種別(和文)	博士論文
Type(English)	Doctoral Thesis

DOCTORAL THESIS

Crystallization of Homopolymers and Block Chains Confined in Nanodomains

Shintaro NAKAGAWA

February 2016

Nojima Laboratory,
Department of Organic and Polymeric Materials,
Graduate School of Science and Engineering,

TOKYO INSTITUTE OF TECHNOLOGY

Contents

Abbreviations

Polymers

P4VP Poly(4-vinylpyridine)

PB Polybutadiene

PCL Poly(ε-caprolactone)

PE Polyethyelene

PEO Poly(ethylene oxide)

PLLA Poly(L-lactic acid)

PP polypropylene

PS Polystyrene

PVCH Polyvinylcyclohexane

PVL Poly(δ-valerolactone)

Reagents

CL ε-Caprolactone

DMAP *N*,*N*-Dimethyl-4-aminopyridine

DMF Dimethylformamide

DPE 1,1-Diphenylethylene

EDC 1-(3-Dimethylaminopropyl)-3-ethylcarbodiimide hydrochloride

PMDETA *N*,*N*,*N'*,*N'*,*N''*-Pentamethyldiethylenetriamine

TBAF Tetrabutylammonium fluoride

TBSCl *tert*-Butyldimethylsilyl chloride

TEA Triethylamine

THF Tetrahydrofuran

TsOH *p*-Toluenesulfonic acid

Others

CuAAC Copper(I)-catalyzed azide-alkyne cycloaddition

DSC Differential scanning calorimetry

^{1}H-NMR ^{1}H Nuclear magnetic resonance spectroscopy

IR Infrared spectroscopy

ONB *o*-Nitrobenzyl (group)

SAXS Small-angle X-ray scattering

TBS *tert*-Butyldimethylsilyl (group)

WAXD Wide-angle X-ray diffraction

Chapter 1

General Introduction

1.1 Crystallization of Spatially Restricted Polymers

Polymeric materials today are indispensable in everyday life. Their properties are tunable through many factors such as the primary structure, molecular weight, and thermal history. More flexible tuning is achieved in multicomponent systems such as polymer solutions and blends. In particular, confining polymer chains in nanometer-scale spaces (nanodomains) surrounded by a matrix component is attracting much attention because

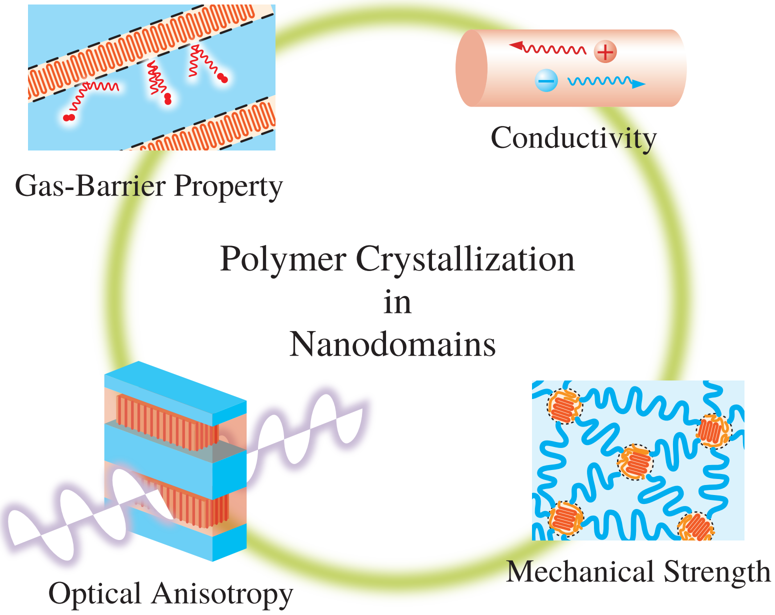

Figure 1.1. Schematic illustration of the physical properties of multicomponent polymeric materials that can be influenced by crystallization within nanodomains.

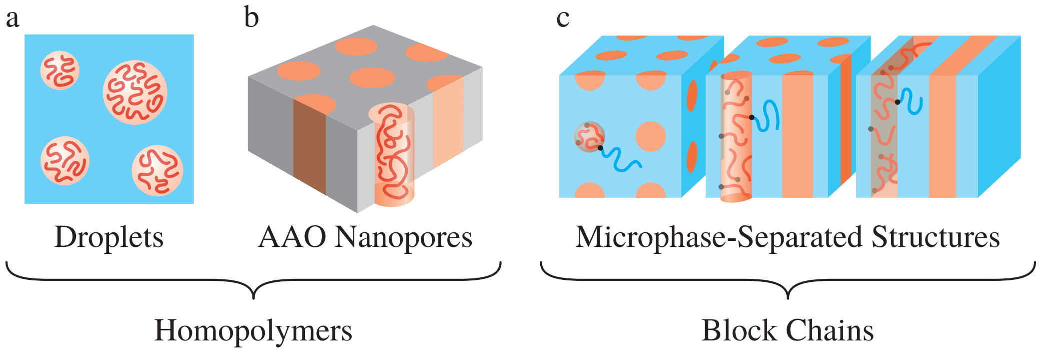

Figure 1.2. Schematic illustration describing the various experimental methods to study the crystallization behavior of polymer chains confined in nanodomains. Crystallizable polymer chains are drawn with orange curves.

of the anomalous behaviors induced by increased spatial restriction and/or interfacial interaction. On the other hand, a number of polymers having a sufficiently regular primary structure can crystallize. As is the case of low molecular weight substances, various physical properties of polymers, such as specific volume, mechanical strength, and optical properties, drastically change on crystallization. **Figure 1.1** illustrates the applications of polymeric materials in which polymer crystallization in nanodomains will play an important role. For example, crystallized polymers are known to possess low gas permeability than amorphous polymers because the polymer chains are regularly and densely packed in crystal lattices[1,2]. Another example is the ionic conductivity, which is the most important property for the use as polymer electrolytes[3,4]. The crystallinity should be kept low to achieve high ionic conductivity because the crystallization leads to a reduction of the chain mobility. It is thus of importance, both scientifically and technologically, to understand and control the crystallization behavior of polymer chains confined in nanodomains.

Various model systems have been conceived and used for this purpose, several of which are schematically described in **Figure 1.2**. The methods using droplets[5–16] (**Figure 1.2**a) or anodic aluminum oxide (AAO) nanopores[16–33] (**Figure 1.2**b) are widely used, compared to the other techniques such as nanolayered films[34–41], controlled pore glasses[42], or coaxial nanofibers[43]. These methods treat crystallizable homopolymers within nanodomains. Also extensively used to understand crystallization in nanodomains are block copolymers (**Figure 1.2**c), a class of polymers consisting of two or more chemically different chains covalently linked at their ends. Block copolymers can self-assemble to form well-ordered nanodomains called microphase-separated structures. Therefore, if one constituent block in a diblock copolymer is crystallizable in nature, it is possible to observe the crystallization within the microphase-separated structure. However, as is discussed later, block chains confined in microphase-separated structures should be distinguished from homopolymers confined in nanodomains since their ends are fixed onto nanodomain interfaces by block junctions. Therefore, in the following two sections, crystallization of homopolymers and block chains confined in nanodomains is discussed separately.

1.2 Crystallization of Homopolymers Confined in Nanodomains

In this section, general features of homopolymer crystallization within nanodomains are presented using illustrative examples selected from the literature.

1.2.1 Droplets

The simplest and hence historic method to investigate the properties of materials within nanometer-scale spaces is to disperse fine droplets of the material in an appropriate matrix (**Figure 1.2**a). This method was first invented to study the crystal nucleation of metals[44], and later applied to organic substances[45] and polymers such as polyethyelene (PE)[5,7–9,15], isotactic polypropylene (PP)[6–8,13], and poly(ethylene oxide) (PEO)[7,10–12,14].

For example, Massa and Dalnoki-Veress[11] investigated the crystallization of an ensemble of PEO droplets prepared by dewetting of a thin PEO film deposited on a polystyrene (PS) substrate. Each droplet occupied 200 - 500 μm^2 on the substrate. Nucleation events in each droplet could be observed by polarized optical microscopy, since the droplets were so small that the crystallization completed almost instantaneously once a nucleation event occurred inside. They found that supercooling needed to crystallize the droplets was significantly larger than that for bulk homopolymers. Moreover, the probability of nucleation was equal among the droplets with a similar size, that is, there were no droplets which inherently nucleate faster than others. These observations strongly indicate that the nucleation in this case is *homogeneous* in nature, unlike *heterogeneous* nucleation dominant in bulk homopolymers. While heterogeneous nucleation is caused by some inhomogeneities present in the system and hence usually occurs at a fixed position, homogeneous nucleation relies only on a spontaneous rearrangement of amorphous materials into crystal-like orders and therefore takes place at random both spatially and temporally. Another particularity of homogeneous nucleation is its high free energy barrier which makes the supercooling necessary to nucleate PEO homopolymers in droplets much larger than in bulk state. The study also showed that the probability of homogeneous nucleation (per unit volume of droplets) decreased with decreasing the volume of droplets, suggesting that the spatial restriction affects the dynamics of homogeneous nucleation. These conclusions are generally common in other reports on crystallization of homopolymers inside droplets despite the diversity of polymers and preparation methods used.

The interface can also affect the crystallization in droplets, because the interfacial area per unit volume is considerably larger than that in bulk state. Carvalho and Dalnoki-Veress[14] studied the crystallization of droplets of PEO homopolymers prepared on a rough surface of a crystallized isotactic PS film and showed that the nucleation always occurred at the edge of the droplet, in contrast with the droplet on the smooth surface which nucleated at its center (bulk). This finding suggests that the effects of interfaces cannot be ignored in some cases of confined crystallization.

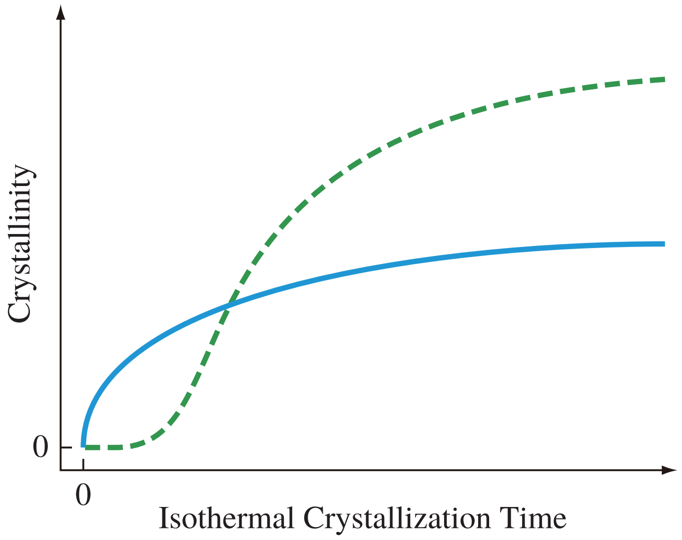

Figure 1.3. Schematic illustration showing the time evolution of crystallinity generally observed for polymer chains confined in isolated nanodomains (solid curve) and in bulk state (dashed curve).

1.2.2 Anodic Aluminum Oxide (AAO) Templates

Anodic aluminum oxide (AAO) templates are inorganic membranes with a hexagonal array of cylindrical nanopores having uniform and tunable diameter[46], into which crystalline homopolymers can infiltrate via capillary force (**Figure 1.2**b). Studies on the crystallization of various homopolymers confined in nanopores on AAO templates have been reported, including poly(vinylidene fluoride)[17,18,24], PE[19,20,26], syndiotactic PS[21–23,27], isotactic PP[25], PEO[26,28–30], poly(ε-caprolactone) (PCL)[31], and poly(L-lactic acid) (PLLA)[33].

For example, Shin and coworkers[19] observed the crystallization of PE homopolymers within AAO nanopores as a function of the pore diameter ranging from 15 to 110 nm. They found that the crystallinity of PE homopolymers confined in nanopores during isothermal crystallization started to increase without an induction time, as is schematically shown in **Figure 1.3** (solid curve). This is in clear contrast to the crystallization of bulk homopolymers, where the crystallinity increases after a finite induction time (dashed curve in **Figure 1.3**). In addition, the temperature at which the PE homopolymers

Figure 1.4. Schematic illustration showing the crystal orientation of PE homopolymers confined in AAO nanopores[19].

could crystallize was significantly lower in nanopores than in bulk state. These results are consistent with those obtained by droplet methods (Section 1.2.1) and suggest that homopolymers confined in AAO nanopores also crystallize via homogeneous nucleation mechanism. The melting temperature and crystallinity of PE homopolymers within the nanopores were significantly lower than that in bulk state, and decreased with decreasing nanopore diameter. Since the melting temperature is in general related to the crystal thickness, the low melting temperature of homopolymers within nanopores indicates that the spatial restriction prohibited the formation of thicker crystals. Similar results were generally obtained in other reports[20,28], though the heterogeneous nucleation is dominant in much larger nanopores[25].

An advantage of the AAO nanopore method over the droplet method (Section 1.2.1) is that it allows for the investigation of crystal orientation with respect to the nanopore axis. The work of Shin and coworkers described above[19] also reported the crystal orientation of PE homopolymers within AAO nanopores. In the range of nanopore diameter investigated, the *b* axis of PE crystals (the fastest growth axis) was oriented parallel to the long axis of the nanopore (**Figure 1.4**), suggesting that PE crystals growing along the nanopore axis were kinetically favored. This hypothesis was supported by the fact that the degree of orientation was higher in smaller nanopores. Many reports[17,18,21,23] are consistent with this result, though some reports show a random[18] or perpendicular[23,30,33] orientation of the *b* axis against the nanopore axis, the latter of which could be attributed to interfacial

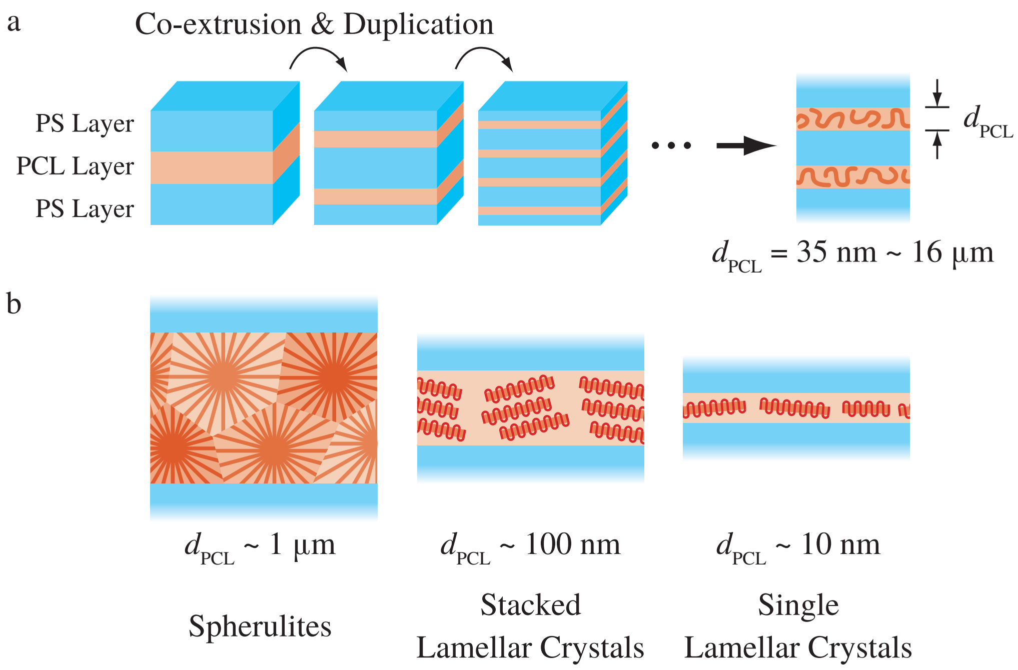

Figure 1.5. Schematic illustration of the preparation method (a) and resulting morphology in the crystallized state (b) of nanolayered films consisting of alternating layers of PCL and PS homopolymers, reported by Ponting and coworkers[39].

effects.

1.2.3 Other Methods

Although not widely used, there are still other unique methods to confine crystallizable homopolymers in nanodomains.

The group of Baer[34–41] developed a repeated co-extrusion technique to prepare nanolayered films consisting of alternating layers of two different homopolymers. This technique allows for confining homopolymers within lamellar nanodomains (nanolamellae), instead of spherical (or sphere-like) ones in the droplet method and cylindrical ones in the AAO template method. For example, Ponting and coworkers[39] studied the crystallization of PCL homopolymers confined in nanolamellae sandwiched between PS layers. The method of preparation is schematically depicted in **Figure 1.5**a. A film consisting of one PCL layer and two PS layers was repeatedly stretched and duplicated to

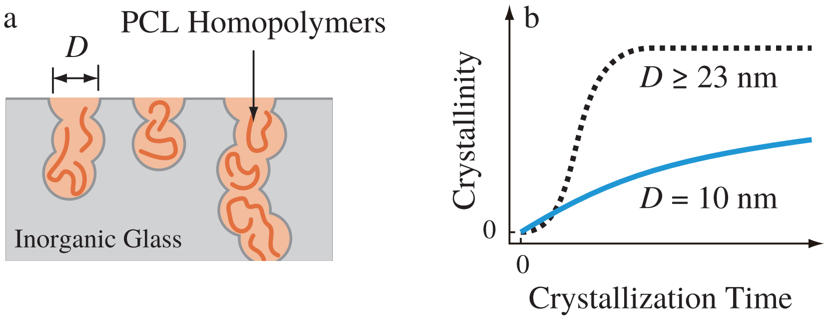

Figure 1.6. Schematic illustration showing the PCL homopolymers confined in nanopores of a controlled pore glass (a) and time evolution of crystallinity of PCL homopolymers confined in nanopores with $D = 10$ nm and $D \geq 23$ nm (b).

yield a nanolayered film in which PCL homopolymers and PS homopolymers were alternately stacked with the PCL layer thickness d_{PCL} ranging from 35 nm to 16 µm. Atomic force microscopy revealed that the morphology of PCL crystals depended on d_{PCL}, as is illustrated in **Figure 1.5**b. Spherulites or truncated spherulites were observed with d_{PCL} on the order of micrometer, whereas reducing d_{PCL} down to hundreds of nanometers led to a formation of stacks of crystal lamellae, which ultimately became double or single lamellar crystals for d_{PCL} of tens of nanometers. In the latter two morphologies, the *c* axis (chain direction) of PCL crystals oriented perpendicular to the nanolamella interface, resulting in an improved oxygen permeability by two orders of magnitude compared to the samples with larger d_{PCL}. In contrast to the crystallization of homopolymers in droplets and AAO nanopores, the crystallization kinetics of PCL homopolymers in nanolayered films during isothermal crystallization was qualitatively similar to that in the bulk state, which was characterized by a sigmoidal time evolution of the crystallinity with a finite induction time (dashed curve in **Figure 1.3**). This fact may indicate that the effects of spatial restriction imposed by nanolamellae are smaller than that by cylindrical nanopores of AAO templates and spherical (or sphere-like) nanodomains of droplet experiments.

Sanandaji and coworkers[42] used controlled pore glasses, which are an organic glass having cylinder-like nanopores on its surface, to study confined crystallization of PCL homopolymers as a function of the pore diameter *D* (**Figure 1.6**a). They found that

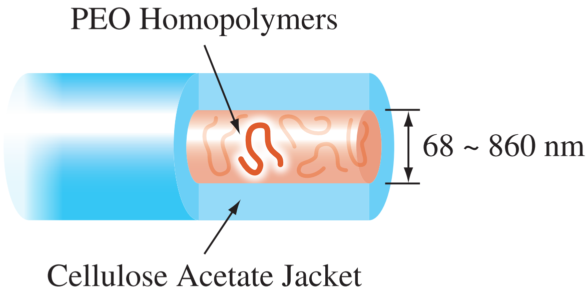

Figure 1.7. Schematic illustration of the structure of the fiber prepared by Luo and coworkers[43].

the crystallinity of PCL homopolymers confined in nanopores with $D = 10$ nm started to increase from time zero without any induction time, as is schematically described in **Figure 1.6**b. The crystallization rate and melting temperature were much lower than that of bulk homopolymers. On the other hand, PCL homopolymers confined in nanopores with $D \geq 23$ nm showed the crystallization behavior similar to that of bulk homopolymers (**Figure 1.6**b). These results are in accordance with the typical features of confined crystallization, except that the PCL homopolymers confined in 10 nm nanopores could crystallize at relatively high temperature (39 °C), which is inconsistent with the homogeneous nucleation-controlled crystallization mechanism. It is possible that the nanopore wall acts as a nucleation site.

Luo and coworkers[43] prepared a thin fiber of PEO homopolymers jacketed with cellulose acetate, which is schematically depicted in **Figure 1.7**, using a coaxial electrospinning technique. The PEO homopolymers crystallized in the nanocylinder surrounded by the cellulose acetate jacket. The melting temperature, crystallinity, and crystallite size of PEO homopolymers confined in nanocylinders with diameter less than 120 nm decreased sharply from those of bulk PEO homopolymers, whereas the difference between confined PEO homopolymers and bulk PEO homopolymers became insignificant with increasing the nanocylinder diameter. The result is qualitatively consistent with the knowledge on confined crystallization obtained by other methods.

1.2.4 General Conclusions

Various methods to study the crystallization of homopolymers confined in nanodomains were reviewed and some representative results were discussed. The general and widely accepted conclusions can be summarized as follows:

(1) The crystallization of homopolymers confined in nanodomains needs an anomalously large supercooling than bulk homopolymers. This is attributed to the homogeneous nucleation mechanism.

(2) The melting temperature and crystallinity of homopolymers confined in nanodomains are lower than those of bulk homopolymers, because the space available for crystal growth is extremely limited.

(3) The crystallization rate, melting temperature, and crystallinity decrease with decreasing the size of nanodomains.

(4) Homopolymers confined in anisotropic nanodomains such as AAO nanopores and nanolamellae in nanolayered films show a preferential crystal orientation with respect to the characteristic axis of nanodomains.

(5) The interfacial interaction between confined homopolymers and nanodomain walls also affects the crystallization.

1.3 Crystallization of Block Copolymers

Block copolymers consist of two or more chemically different polymer chains covalently linked at the chain ends, and are well known for its ability to self-assemble into the nanometer-scale morphology called the microphase-separated structure. The microphase-separated structure provides an ideal geometry to confine crystalline polymer chains and hence has been widely used to investigate the crystallization of polymer chains in

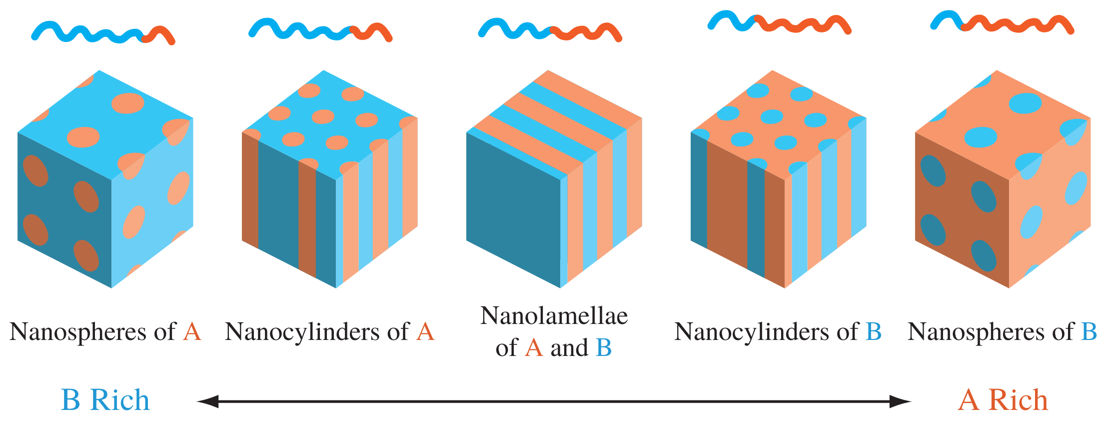

Figure 1.8. Schematic illustration of the microphase-separated structures commonly observed in segregated diblock copolymers.

nanodomains. This section discusses major features of the crystallization of block copolymers after a brief introduction to the microphase separation and microphase-separated structure of block copolymers.

1.3.1 Microphase Separation

The microphase separation of block copolymers occurs due to a conflict between an enthalpic repulsion and entropic attraction. Let us suppose a diblock copolymer, for example, consisting of two chemically different blocks A and B immiscible to each other. Each block tends to aggregate into as large a domain as possible due to an enthalpic repulsion with each other. However, block chains should be elongated to uniformly fill the domain, which is entropically unfavorable. A larger elongation is necessary in larger domains. Thus, the balance between these interactions ultimately leads to an equilibrium domain structure, typically tens of nanometers in size.

The size and shape of microphase-separated structures depend on the total molecular weight, volume fraction ϕ of each block, and the segregation strength χN between blocks, where χ is the Flory-Huggins interaction parameter and N the total number of statistical segments. **Figure 1.8** shows schematic illustrations of the microphase-separated structures typically observed for diblock copolymers. The shape of nanodomains changes from nanolamellae to nanocylinders and eventually to nanospheres, as the composition of the block copolymer becomes asymmetric. The minor component always forms the nanodomain surrounded by the matrix of the major component. Other microphase-separated structures such as gyroid structures and perforated lamellae have also been observed[47], though the regions they occupy on the ϕ-χN phase diagram are usually relatively small. The microphase separation of block copolymers with more complicated architecture, such as ABA triblock copolymers and ABC triblock terpolymers, has also been studied[47–49]. For example, an ABA symmetric triblock copolymer is known to exhibit the phase behavior similar to that of an AB diblock copolymer with half the molecular weight of the original triblock copolymer[48,49].

1.3.2 Possible Routes of Structure Formation on Crystallization

When one or more blocks in a block copolymer are crystalline, the development of the higher-order structure is controlled by an interplay between crystallization and microphase separation, making it complicated even in the simplest diblock copolymers. The diblock copolymers having one crystalline (C) and one amorphous (A) block (C-A diblock copolymers) are the best model system for confined crystallization and hence most extensively studied. The structure formation in the diblock copolymers consisting of two crystalline polymers (C-C diblock copolymers)[50,51] is more complex than that in C-A diblock copolymers and is not discussed here.

When a C-A diblock copolymer melt is cooled below the melting temperature T_m of C blocks, there are mainly two possible routes of structure formation[52,53], as is schematically illustrated in **Figure 1.9**. The selection between two routes depends on the glass transition temperature T_g of the A blocks and segregation strength χN between C and A blocks. If T_g of A blocks is much lower than T_m of C blocks (i.e., A blocks are rubbery when C blocks crystallize) and χN between two blocks is relatively small, the microphase-separated structure formed in the initial melt is completely destroyed and reorganized into a new morphology consisting of alternating crystalline lamellae

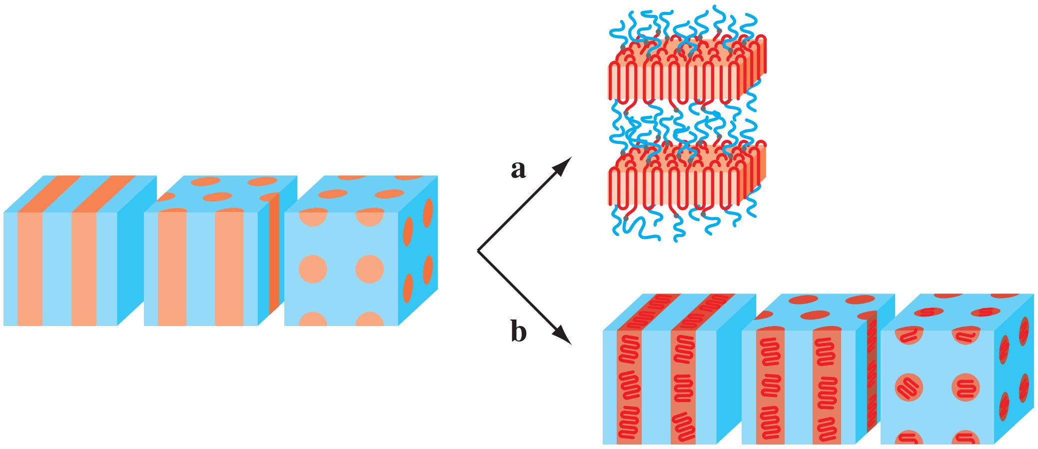

Figure 1.9. Schematic illustration of possible structure formation processes commonly observed for C-A block copolymers, namely the break-out crystallization (a) and confined crystallization (b).

and amorphous layers (**Figure 1.9**a). This type of crystallization is called the *break-out crystallization*. For example, Nojima and coworkers[54–56] studied the crystallization of PCL-*block*-polybutadiene (PCL-*b*-PB), where T_{m} of PCL blocks is much higher than T_{g} of PB blocks. They found that the crystallization of PCL blocks completely destroyed the microphase-separated structure formed in the melt, leading to the formation of a lamellar morphology consisting of alternating PCL lamellar crystals and amorphous layers containing PB blocks and amorphous portions of PCL blocks. Similar results were also obtained for a variety of systems[57–60].

On the other hand, if T_{g} of A blocks is higher than T_{m} of C blocks (i.e., A blocks are vitrified when C blocks crystallize) or χN is relatively large, the crystallization of C blocks takes place without destroying the initial microphase-separated structure (**Figure 1.9**b). This is called the *confined crystallization*.

1.3.3 Confined Crystallization

The vitrification of A blocks has been frequently exploited to study the confined crystallization of C blocks. In this case, C blocks are expected to crystallize without perturbing the microphase-separated structure formed in the melt, because they are sur-

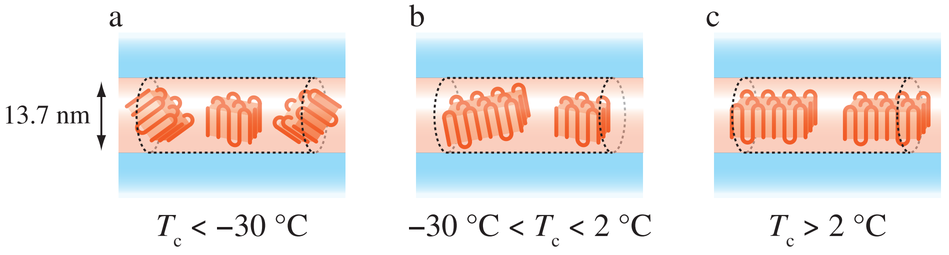

Figure 1.10. Schematic illustration of the orientation of PEO block chains within nanocylinders crystallized at $T_c < -30$ °C (a), -30°C $< T_c < 2$ °C (b), and $T_c > 2$ °C (c).

rounded by hard walls of vitrified A blocks. Hence this kind of confinement is termed *hard confinement*. A large number of reports[61–85] and reviews[50,51,86–89] have been published on the crystallization of block chains under hard confinement. For example, Loo and coworkers[68] investigated the crystallization behavior of PE-*block*-polyvinylcyclohexane (PE-*b*-PVCH), in which the PVCH matrix was vitrified at the point of crystallization of PE blocks. During cooling at a constant rate, the temperature at which PE blocks started to crystallize was 58 °C in nanospheres and 63 °C in nanocylinders, which was much lower than 87 °C observed in bulk PE homopolymers. Moreover, the crystallinity of PE blocks confined in nanospheres and nanocylinders during isothermal crystallization steeply increased from time zero without an induction time (solid curve in **Figure 1.3**). These observations suggest that the crystallization of block chains in such confined geometries is governed by homogeneous nucleation. However, they also found that the crystallization of PE blocks in bicontinuous nanodomains (gyroid) and nanolamellae proceeded by the heterogeneous nucleation and growth mechanism, indicating that the crystallization mechanism strongly depends on the shape of nanodomains.

Crystals of block chains in anisotropic nanodomains such as nanocylinders[70,82] and nanolamellae[76,77,90] can orient with respect to the characteristic axis of the nanodomain. Huang and coworkers[70], for example, studied the crystal orientation of PEO block chains confined in nanocylinders embedded in a PS matrix, using PEO-*b*-PS diblock copolymer/PS homopolymer blends. The crystal orientation depended on the crystallization

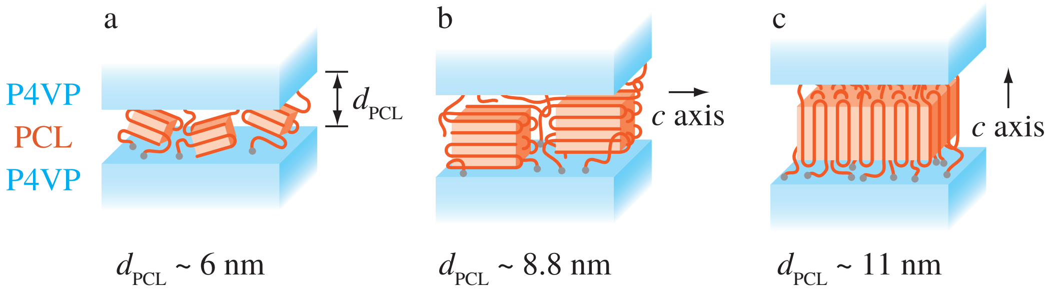

Figure 1.11. Schematic illustration of the crystal orientation of PCL blocks confined in nanolamellae formed in PCL-*b*-P4VP.

temperature T_c, as is schematically shown in **Figure 1.10**. PEO crystals had no preferential orientation when crystallized below −30 °C (a), whereas at higher T_c the *c* axis of PEO crystals began to orient perpendicular to the nanocylinder axis but with tilting (b). The orientation improved as increasing T_c and eventually reached the perpendicular orientation at $T_c > 2$ °C (c). The improvement of the crystal orientation with increasing T_c implies that the crystal growth along the nanocylinder axis was kinetically more favored than that along the off-axis direction. It is also known that the crystal orientation is controlled by nanocylinder diameter[82]. The crystal orientation within nanolamellae can be more complicated than that in nanocylinders. Sun and coworkers[76,77] investigated the crystal orientation of PCL block chains confined in nanolamellae formed by the microphase separation of PCL-*block*-poly(4-vinylpyridine) (PCL-*b*-P4VP) diblock copolymers as a function of PCL nanolamella thickness d_{PCL}, the results of which are schematically depicted in **Figure 1.11**. In nanolamellae with $d_{PCL} \sim 6$ nm, PCL crystals did not show preferential orientation (a), whereas in nanolamellae with $d_{PCL} \sim 8.8$ nm the *c* axis of PCL crystals (chain direction) oriented parallel to nanolamella interfaces (b). Interestingly, upon further increasing d_{PCL} to ~ 11 nm, the orientation of the *c* axis of PCL crystals with respect to the nanolamella interface changed from parallel to perpendicular (c). It is speculated that the *c* axis of PCL crystals at $d_{PCL} \sim 8.8$ nm should take the parallel orientation in order to maximize their thickness and hence stability, while $d_{PCL} \sim 11$ nm was large enough for perpendicularly oriented PCL crystals to attain

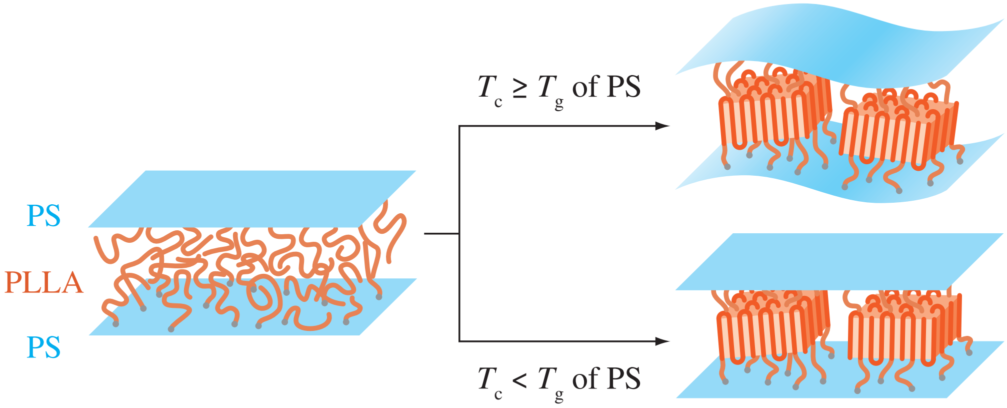

Figure 1.12. Schematic illustration showing the morphology of PLLA-*b*-PS after the crystallization at $T_\mathrm{c} \geq T_\mathrm{g}$ of PS (upper route) and $T_\mathrm{c} < T_\mathrm{g}$ of PS (lower route).

the optimal crystal thickness.

Confined crystallization can also be observed in some C-A diblock copolymers whose amorphous block is rubbery when C blocks crystallize, either by a strong segregation between two blocks[67,86,91–97] or by crosslinking of the amorphous matrix[98,99]. This kind of confinement is called *soft confinement*, since the rubbery matrix of A blocks surrounding C blocks is soft and hence can afford a slight deformation to accommodate large and stable crystals. For example, Ho and coworkers[95] investigated the crystallization of a lamella-forming PLLA-*b*-PS diblock copolymer. The morphology after the crystallization of PLLA blocks depended on the crystallization temperature T_c, as is schematically shown in **Figure 1.12**. When T_c was set below the glass transition temperature T_g of PS blocks, the crystallization of PLLA blocks did not perturb the nanolamellae formed in the melt state (**Figure 1.12**, lower route), whereas the crystallization of PLLA blocks above T_g of PS blocks led to the undulation of the nanolamellae (**Figure 1.12**, upper route). It was also suggested that the nucleation mechanism changed from homogeneous to heterogeneous upon increasing T_c. The deformation of nanodomains is also observed in sphere-forming PEO-*b*-PB/PB homopolymer blends[94]. The T_c-dependent morphological development is also reported by several authors[91,92,100–103].

1.3.4 General Conclusions

The current section explored the crystallization of block copolymers having one crystalline block. Following conclusions are commonly derived from these studies:

1. The crystallization of C-A diblock copolymers can be classified into *confined crystallization* and *break-out crystallization*.

2. In break-out crystallization, the microphase-separated structure is completely destroyed by the crystallization and reorganized into a lamellar morphology consisting of lamellar crystals and amorphous layers. Break-out crystallization occurs when the amorphous block is rubbery at the point of crystallization and the segregation strength between two blocks is sufficiently low.

3. In confined crystallization, the crystalline blocks crystallize without destroying the microphase-separated structure. Confined crystallization occurs when amorphous blocks are vitrified when crystalline blocks crystallize and/or the block copolymer is strongly segregated.

4. The crystallinity and melting temperature of block chains confined in nanodomains are significantly lower than those of bulk homopolymers, because the space available for the crystal growth is severely restricted.

5. Homogeneous nucleation is often observed in nanospheres, small nanocylinders, and small nanolamellae, while conventional heterogeneous nucleation and growth mechanism is seen in large nanocylinders, large nanolamellae, and gyroid structures.

6. The preferential orientation of crystals is observed in nanocylinders and nanolamellae and tends to be improved in larger nanodomains and at higher crystallization temperature. This is considered to be a consequence of the kinetic selection by nanodomains.

7. Confined crystallization within nanodomains surrounded by a rubbery amorphous matrix (crystallization under *soft confinement*) leads to a deformation of the nanodomains.

1.4 Chain Confinement

In the preceding two sections, the effects of spatial restriction, or *space confinement*, on the crystallization of homopolymers and block chains have been emphasized. It should be noted, however, that block chains confined in nanodomains differ substantially from homopolymers confined in the same nanodomains, that is, the block chains are tethered at (at least) one end onto nanodomain interfaces. This kind of restriction is hereafter termed as *chain confinement*. In order to fully understand the confined crystallization of block copolymers, the effects of chain confinement should also be known, which can only be achieved by comparing the crystallization of block chains and homopolymers under the same condition. This challenging problem remained unsolved until a novel method using photocleavable C-A diblock copolymers is available. The strategy for sample preparation is schematically depicted in **Figure 1.13**. A C-A diblock copolymer bearing a photocleavable *o*-nitrobenzyl group (ONB)[106–110] between two blocks first undergoes microphase separation which makes C block chains confined in nanodomains (**Figure 1.13**a). Subsequent photocleavage of ONB turns C block chains into C homopolymers (b). The nanodomain structure formed by the diblock copolymer is no longer in equilibrium, since the system is now a binary blend consisting of C and A homopolymers. Nevertheless, if the temperature is kept well below T_g of A block chains, it is expected that the nanodomain is preserved even in the absence of block junctions. Therefore, it is possible to compare the crystallization behavior of C block chains (a) and C homopolymers (b) both confined in an identical nanodomain.

Nojima and coworkers[104] synthesized poly(δ-valerolactone)-*block*-PS (PVL-*b*-PS) diblock copolymers with ONB inserted at the block junction and compared the crystal-

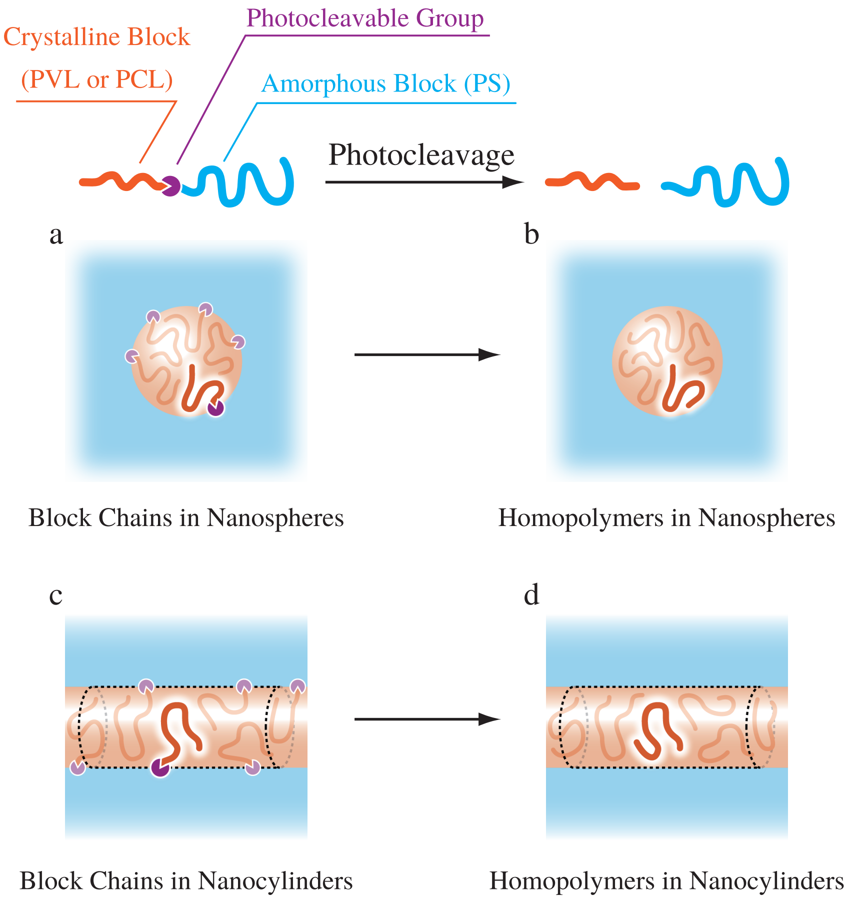

Figure 1.13. Schematic illustration showing the sample preparation strategy in refs [104, 105]. A C-A diblock copolymer having a photocleavable group between two blocks first forms a spherical microphase-separated structure (a). C block chains are then converted to C homopolymers by photocleavage of the block junction (b). The same method can be applied to different nanodomains such as nanocylinders (c and d).

lization behavior of PVL block chains and PVL homopolymers confined in spherical nanodomains with the diameter of 17.6 nm (**Figure 1.13**a and b) and cylindrical nanodomains with the diameter of 15.7 nm (c and d). In both nanodomains, the crystallization of PVL chains could take place only at a deep supercooling (90 °C or more below the T_{m}) and followed first-order kinetics, indicating that the crystallization was governed by homogeneous nucleation. The crystallinity and melting temperature of PVL blocks were lower than that of PVL homopolymers. The time evolution of the crystallinity of PVL block chains and PVL homopolymers is schematically illustrated in **Figure 1.14**. The major finding of the study was that the crystallinity of PVL block chains (solid curve in

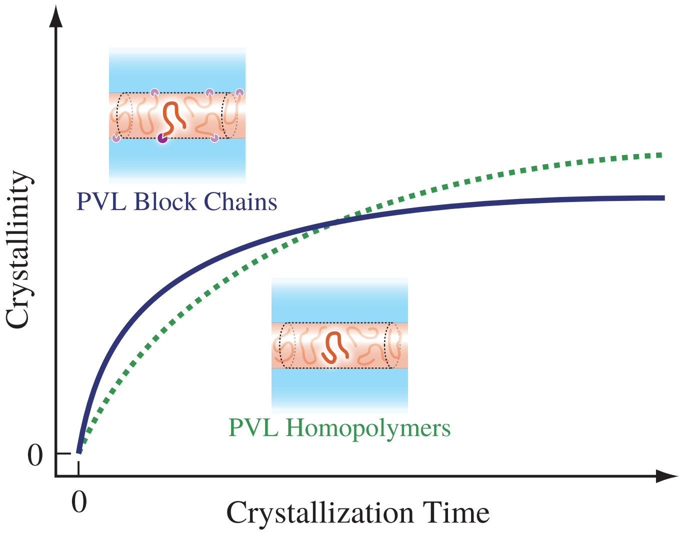

Figure 1.14. Schematic illustration showing the time evolution of crystallinity of PVL block chains (solid curve) and PVL homopolymers (dotted curve) confined in nanocylinders, drawn based on the data presented in ref [104].

Figure 1.14) was larger than that of PVL homopolymers (dotted curve) at the initial stage of isothermal crystallization. This rather striking result suggests that chain confinement may facilitate the crystal nucleation. However, the crystallinity of PVL block chains was later overtaken by that of PVL homopolymers, which led to the higher final crystallinity in PVL homopolymers than in PVL block chains. Combined with the fact that the melting temperature of PVL homopolymers was also higher than that of PVL block chains, the result suggests that chain confinement restricted the motion of PVL chains and hence reduced the accessible crystal thickness and size.

The influence of chain confinement on the crystal orientation within nanocylinders was also investigated[105]. PCL block chains (**Figure 1.13**c) and PCL homopolymers (d) were confined in an identical nanocylinder with the diameter D of 13.0 nm. It was found that the b axis of PCL crystals, which is the fastest growth axis, oriented parallel to the long axis of nanocylinder for both PCL block chains and homopolymers. However, the degree of crystal orientation for PCL block chains was lower than that for PCL homopolymers, indicating that the chain confinement impeded the favorable crystal growth along *b* direction.

It should be noted that photocleavable block copolymers are also gaining interests for applications such as the preparation of nanoporous materials[111–115] and dynamic manipulation of micelles and vesicles in solution for drug delivery systems[116–118].

In summary, the effects of chain confinement on crystallization within isolated nanodomains such as nanospheres and nanocylinders have been investigated using photocleavable C-A diblock copolymers. It was revealed that chain confinement reduced the crystal thickness and crystallinity, but accelerated the homogeneous nucleation. The crystal orientation was also frustrated by chain confinement.

1.5 Purpose and Outline of This Thesis

The works by Nojima and coworkers[104,105] focused on the concept of chain confinement, though its roles in confined crystallization of block chains are not thoroughly understood. Moreover, considering that the crystallization of homopolymers and block chains is significantly affected by space confinement, an interplay between chain confinement and space confinement should also be important. In this thesis, the author investigates the crystallization of homopolymers and block chains confined in nanodomains with various shapes and sizes (**Figure 1.15**). The aim of this thesis is to clarify the entire picture of the effects of chain confinement and space confinement on polymer crystallization and reveal the mechanism by which these confinement affect the crystallization. The author uses poly(ε-caprolactone) (PCL) as a model crystalline polymer throughout the entire thesis. The terms *PCL homopolymers* and *PCL block chains* are strictly distinguished, and the word *PCL chains* is used as a generic term including PCL homopolymers and PCL block chains.

This doctoral thesis comprises seven chapters and three appendices. Chapter 1, the present chapter, addresses the general background and purpose of this study. In Chapter 2, the author investigates the crystallization behavior of PCL homopolymers and PCL

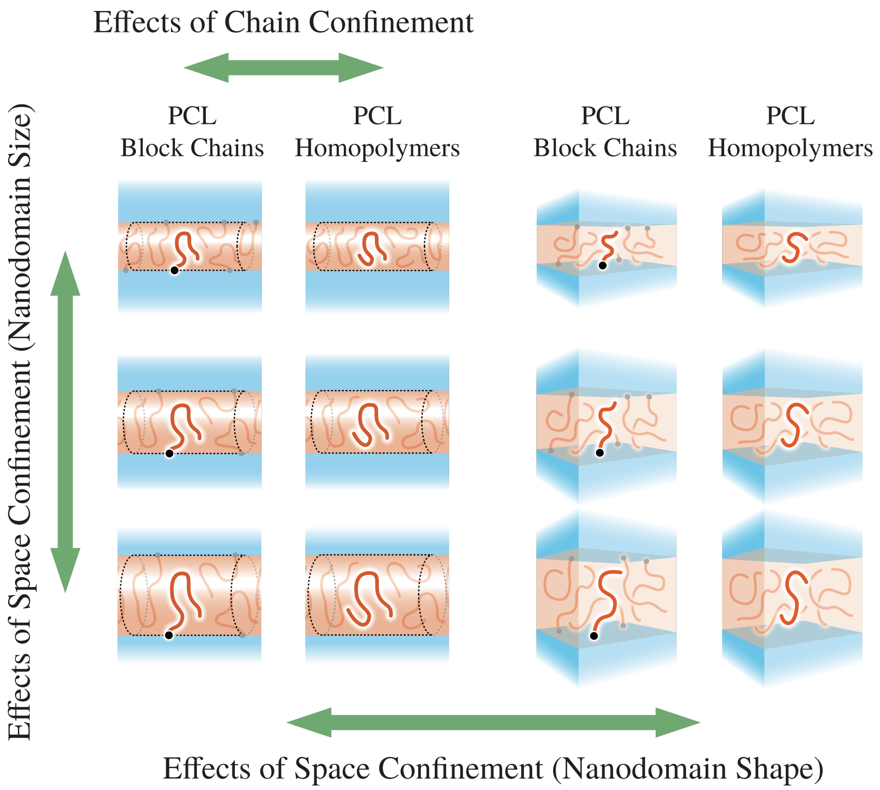

Figure 1.15. Schematic illustration showing the concept of this study. The crystallization of PCL homopolymers and PCL block chains confined in nanocylinders (left) or nanolamellae (right) with various sizes is compared.

block chains confined in nanocylinders with various sizes in order to reveal the effects of chain confinement on crystal nucleation and the relationship between chain confinement and space confinement. Chapter 3 treats the crystal orientation of PCL homopolymers and PCL block chains in nanocylinders with various diameters to elucidate the effects of chain confinement and space confinement on crystal growth within nanocylinders. In Chapter 4, the author examines the crystallization behavior of blends consisting of PCL homopolymers and PCL block chains confined in nanocylinders to understand the coupled effects of chain confinement and space confinement on the kinetics of crystal nucleation. Chapter 5 deals with the crystallization of PCL homopolymers and PCL block chains confined in nanolamellae. It is expected that the effects of chain confinement on both nucleation and growth are revealed, which is not possible under severe space confinement imposed by nanocylinders. In Chapter 6, the crystallization behavior of PCL chains tethered at *both ends*, *one end* and *no end* confined in an identical nanolamella is investigated to explore the effects of chain tethering at either or both of two chain-ends on the growth of PCL crystals. In Chapter 7, the major findings of preceding chapters are re-organized and comprehensively discussed on the viewpoint of the effects of space confinement and chain confinement on nucleation, growth, and thickening of polymer crystals. Methods and results for synthesis of the samples used in Chapters 2-5 and 6 are gathered in Appendices A and B, respectively. The method for the quantitative evaluation of the photocleavage yield for photocleavable block copolymer samples can be found in Appendix C.

References

1. Hiltner, A.; Liu, R. Y. F.; Hu, Y. S.; Baer, E. *Journal of Polymer Science Part B: Polymer Physics* **2005**, *43*, 1047–1063.
2. Duncan, T. V. *Journal of Colloid and Interface Science* **2011**, *363*, 1–24.
3. Croce, F.; Appetecchi, G. B.; Persi, L.; Scrosati, B. *Nature* **1998**, *394*, 456–458.
4. Wright, P. V. *MRS Bulletin* **2011**, *27*, 597–602.
5. Cormia, R. L.; Price, F. P.; Turnbull, D. *The Journal of Chemical Physics* **1962**, *37*, 1333.
6. Burns, J. R.; Turnbull, D. *Journal of Applied Physics* **1966**, *37*, 4021.
7. Koutsky, J. A.; Walton, A. G.; Baer, E. *Journal of Applied Physics* **1967**, *38*, 1832–1839.
8. Arnal, M. L.; Matos, M. E.; Morales, R. A.; Santana, O. O.; Müller, A. J. *Macromolecular Chemistry and Physics* **1998**, *199*, 2275–2288.
9. Massa, M. V.; Lee, M. S. M.; Dalnoki-Veress, K. *Journal of Polymer Science Part B: Polymer Physics* **2005**, *43*, 3438–3443.
10. Taden, A.; Landfester, K. *Macromolecules* **2003**, *36*, 4037–4041.
11. Massa, M. V.; Dalnoki-Veress, K. *Physical Review Letters* **2004**, *92*, 1–4.
12. Massa, M. V.; Carvalho, J. L.; Dalnoki-Veress, K. *Physical Review Letters* **2006**, *97*, 1–4.
13. Kailas, L.; Vasilev, C.; Audinot, J.-N.; Migeon, H.-N.; Hobbs, J. K. *Macromolecules* **2007**, *40*, 7223–7230.
14. Carvalho, J. L.; Dalnoki-Veress, K. *Physical Review Letters* **2010**, *105*, 237801–1.
15. Carvalho, J. L.; Dalnoki-Veress, K. *The European Physical Journal E* **2011**, *34*, 1–6.

16. Michell, R. M.; Blaszczyk-Lezak, I.; Mijangos, C.; Müller, A. J. *Polymer* **2013**, *54*, 4059–4077.

17. Steinhart, M.; Senz, S.; Wehrspohn, R. B.; Go, U.; Wendorff, J. H. *Macromolecules* **2003**, *36*, 3646–3651.

18. Steinhart, M.; Goering, P.; Dernaika, H.; Prabhukaran, M.; Goesele, U.; Hempel, E.; Thurn-Albrecht, T. *Physical Review Letters* **2006**, *97*, 027801.

19. Shin, K.; Woo, E.; Jeong, Y. G.; Kim, C.; Huh, J.; Kim, K.-W. *Macromolecules* **2007**, *40*, 6617–6623.

20. Woo, E.; Huh, J.; Jeong, Y. G.; Shin, K. *Physical Review Letters* **2007**, *98*, 136103.

21. Wu, H.; Wang, W.; Yang, H.; Su, Z. *Macromolecules* **2007**, *40*, 4244–4249.

22. Wu, H.; Wang, W.; Huang, Y.; Wang, C.; Su, Z. *Macromolecules* **2008**, *41*, 7755–7758.

23. Wu, H.; Wang, W.; Huang, Y.; Su, Z. *Macromolecular Rapid Communications* **2009**, *30*, 194–198.

24. Martín, J.; Mijangos, C.; Sanz, A.; Ezquerra, T. A.; Nogales, A. *Macromolecules* **2009**, *42*, 5395–5401.

25. Duran, H.; Steinhart, M.; Butt, H.-J.; Floudas, G. *Nano letters* **2011**, *11*, 1671–1675.

26. Michell, R. M.; Lorenzo, A. T.; Müller, A. J.; Lin, M.-C.; Chen, H.-L.; Blaszczyk-Lezak, I.; Martín, J.; Mijangos, C. *Macromolecules* **2012**, *45*, 1517–1528.

27. Li, M.; Wu, H.; Huang, Y.; Su, Z. *Macromolecules* **2012**, *45*, 5196–5200.

28. Maiz, J.; Martin, J.; Mijangos, C. *Langmuir* **2012**, *28*, 12296–303.

29. Martin, J.; Nogales, A.; Mijangos, C. *Macromolecules* **2013**, *46*, 7415–7422.

30. Guan, Y.; Liu, G.; Gao, P.; Li, L.; Ding, G.; Wang, D. *ACS Macro Letters* **2013**, *2*, 181–184.

31. Suzuki, Y.; Duran, H.; Akram, W.; Steinhart, M.; Floudas, G.; Butt, H.-J. *Soft Matter* **2013**, *9*, 9189.

32. Michell, R. M.; Blaszczyk-Lezak, I.; Mijangos, C.; Müller, A. J. *Journal of Polymer Science Part B: Polymer Physics* **2014**, *52*, 1179–1194.

33. Guan, Y.; Liu, G.; Ding, G.; Yang, T.; Müller, A. J.; Wang, D. *Macromolecules* **2015**, *48*, 2526–2533.

34. Wang, H.; Keum, J. K.; Hiltner, A.; Baer, E.; Freeman, B.; Rozanski, A.; Galeski, A. *Science* **2009**, *323*, 757–760.

35. Wang, H.; Keum, J. K.; Hiltner, A.; Baer, E. *Macromolecules* **2010**, *43*, 3359–3364.

36. Wang, H.; Keum, J. K.; Hiltner, A.; Baer, E. *Macromolecular Rapid Communications* **2010**, *31*, 356–61.

37. Lai, C.; Ayyer, R.; Hiltner, A.; Baer, E. *Polymer* **2010**, *51*, 1820–1829.

38. Flores, A.; Arribas, C.; Fauth, F.; Khariwala, D.; Hiltner, A.; Baer, E.; Baltá-Calleja, F. J.; Ania, F. *Polymer* **2010**, *51*, 4530–4539.

39. Ponting, M.; Lin, Y.; Keum, J. K.; Hiltner, A.; Baer, E. *Macromolecules* **2010**, *43*, 8619–8627.

40. Carr, J. M.; Langhe, D. S.; Ponting, M. T.; Hiltner, A.; Baer, E. *Journal of Materials Research* **2012**, *27*, 1326–1350.

41. Zhang, G.; Lee, P. C.; Jenkins, S.; Dooley, J.; Baer, E. *Polymer* **2014**, *55*, 663–672.

42. Sanandaji, N.; Ovaskainen, L.; Klein Gunnewiek, M.; Vancso, G.; Hedenqvist, M.; Yu, S.; Eriksson, L.; Roth, S.; Gedde, U. *Polymer* **2013**, *54*, 1497–1503.

43. Luo, H.; Huang, Y.; Wang, D.; Shi, J. *Journal of Polymer Science Part B: Polymer Physics* **2013**, *51*, 376–383.

44. Vonnegut, B. *Journal of Colloid Science* **1948**, *3*, 563–569.

45. Turnbull, D.; Cormia, R. L. *The Journal of Chemical Physics* **1961**, *34*, 820–831.

46. Masuda, H.; Fukuda, K. *Science* **1995**, *268*, 1466–8.

47. Castelletto, V.; Hamley, I. W. *Current Opinion in Solid State and Materials Science* **2004**, *8*, 426–438.

48. Matsen, M. W.; Thompson, R. B. *The Journal of Chemical Physics* **1999**, *111*, 7139–7146.

49. Matsen, M. W. *Macromolecules* **2012**, *45*, 2161–2165.

50. Castillo, R. V.; Müller, A. J. *Progress in Polymer Science* **2009**, *34*, 516–560.

51. Nakagawa, S.; Marubayashi, H.; Nojima, S. *European Polymer Journal* **2015**, *70*, 262–275.

52. Loo, Y.-L.; Register, R. A.; Ryan, A. J. *Macromolecules* **2002**, *35*, 2365–2374.

53. Nandan, B.; Hsu, J.-Y.; Chen, H.-L. *Journal of Macromolecular Science, Part C: Polymer Reviews* **2006**, *46*, 143–172.

54. Nojima, S.; Kato, K.; Yamamoto, S.; Ashida, T. *Macromolecules* **1992**, *25*, 2237–2242.

55. Nojima, S.; Nakano, H.; Ashida, T. *Polymer* **1993**, *34*, 4168–4170.

56. Nojima, S.; Nakano, H.; Takahashi, Y.; Ashida, T. *Polymer* **1994**, *35*, 3479–3486.

57. Ryan, A. J.; Hamley, I. W.; Bras, W.; Bates, F. S. *Macromolecules* **1995**, *28*, 3860–3868.

58. Hsu, J.-Y.; Hsieh, I.-F.; Nandan, B.; Chiu, F.-C.; Chen, J.-H.; Jeng, U.-S.; Chen, H.-L. *Macromolecules* **2007**, *40*, 5014–5022.

59. Ho, C.-H.; Jang, G.-W.; Lee, Y.-D. *Polymer* **2010**, *51*, 1639–1647.

60. Papadakis, C. M.; Darko, C.; Di, Z.; Troll, K.; Metwalli, E.; Timmann, A.; Reiter, G.; Förster, S. *The European Physical Journal. E* **2011**, *34*, 1–8.

61. Hamley, I. W.; Fairclough, J. P. A.; Ryan, A. J.; Bates, F. S.; Towns-Andrews, E. *Polymer* **1996**, *37*, 4425–4429.

62. Hamley, I. W.; Fairclough, J. P. A.; Terrill, N. J.; Ryan, A. J.; Lipic, P. M.; Bates, F. S.; Towns-Andrews, E. *Macromolecules* **1996**, *29*, 8835–8843.

63. Nojima, S.; Fujimoto, M.; Kakihara, H.; Sasaki, S. *Polymer Journal* **1998**, *30*, 968–975.

64. Quiram, D. J.; Register, R. A.; Marchand, G. R.; Adamson, D. H. *Macromolecules* **1998**, *31*, 4891–8.

65. Weimann, P. A.; Hajduk, D. A.; Chu, C.; Chaffin, K. A.; Brodil, J. C.; Bates, F. S. *Journal of Polymer Science Part B: Polymer Physics* **1999**, *37*, 2053–2068.

66. Zhu, L.; Cheng, S. Z. D.; Calhoun, B. H.; Ge, Q.; Quirk, R. P.; Thomas, E. L.; Hsiao, B. S.; Yeh, F.; Lotz, B. *Journal of the American Chemical Society* **2000**, *122*, 5957–5967.

67. Loo, Y.-L.; Register, R. A.; Ryan, A. J. *Physical Review Letters* **2000**, *84*, 4120–4123.

68. Loo, Y.-L.; Register, R. A.; Ryan, A. J.; Dee, G. T. *Macromolecules* **2001**, *34*, 8968–8977.

69. Zhu, L.; Mimnaugh, B. R.; Ge, Q.; Quirk, R. P.; Cheng, S. Z. D.; Thomas, E. L.; Lotz, B.; Hsiao, B. S.; Yeh, F.; Liu, L. *Polymer* **2001**, *42*, 9121–9131.

70. Huang, P.; Zhu, L.; Cheng, S. Z. D.; Ge, Q.; Quirk, R. P.; Thomas, E. L.; Lotz, B.; Hsiao, B. S.; Liu, L.; Yeh, F. *Macromolecules* **2001**, *34*, 6649–6657.

71. Shiomi, T.; Tsukada, H.; Takeshita, H.; Takenaka, K.; Tezuka, Y. *Polymer* **2001**, *42*, 4997–5004.

72. Huang, P.; Zhu, L.; Guo, Y.; Ge, Q.; Jing, A. J.; Chen, W. Y.; Quirk, R. P.; Cheng, S. Z. D.; Thomas, E. L.; Lotz, B.; Hsiao, B. S.; Avila-Orta, C. A.; Sics, I. *Macromolecules* **2004**, *37*, 3689–3698.

73. Takeshita, H.; Ishii, N.; Araki, C.; Miya, M.; Takenaka, K.; Shiomi, T. *Journal of Polymer Science Part B: Polymer Physics* **2004**, *42*, 4199–4206.

74. Huang, P.; Guo, Y.; Quirk, R. P.; Ruan, J.; Lotz, B.; Thomas, E. L.; Hsiao, B. S.; Avila-Orta, C. A.; Sics, I.; Cheng, S. Z. D. *Polymer* **2006**, *47*, 5457–5466.

75. Lorenzo, A. T.; Arnal, M. L.; Müller, A. J.; Boschetti-de-Fierro, A.; Abetz, V. *European Polymer Journal* **2006**, *42*, 516–533.

76. Sun, Y.-S.; Chung, T.-M.; Li, Y.-J.; Ho, R.-M.; Ko, B.-T.; Jeng, U.-S.; Lotz, B. *Macromolecules* **2006**, *39*, 5782–5788.

77. Sun, Y.-S.; Chung, T.-M.; Li, Y.-J.; Ho, R.-M.; Ko, B.-T.; Jeng, U.-S. *Macromolecules* **2007**, *40*, 6778–6781.

78. Boschetti-de-Fierro, A.; Lorenzo, A. T.; Müller, A. J.; Schmalz, H.; Abetz, V. *Macromolecular Chemistry and Physics* **2008**, *209*, 476–487.

79. Cai, T.; Qian, Y.; Ma, Y.; Ren, Y.; Hu, W. *Macromolecules* **2009**, *42*, 3381–3385.

80. Myers, S. B.; Register, R. A. *Macromolecules* **2010**, *43*, 393–401.

81. Gitsas, A.; Floudas, G.; Butt, H. J.; Pakula, T.; Matyjaszewski, K. *Macromolecules* **2010**, *43*, 2453–2462.

82. Chung, T.-M.; Wang, T.-C.; Ho, R.-M.; Sun, Y.-S.; Ko, B.-T. *Macromolecules* **2010**, *43*, 6237–6240.

83. Lin, M.-C.; Wang, Y.-C.; Chen, H.-L.; Müller, A. J.; Su, C.-J.; Jeng, U.-S. *Journal of Physical Chemistry B* **2011**, *115*, 2494–2502.

84. Kim, Y. Y.; Ahn, B.; Sa, S.; Jeon, M.; Roth, S. V.; Kim, S. Y.; Ree, M. *Macrmolecules* **2013**, *46*, 8235–8244.

85. Chen, L.; Jiang, J.; Wei, L.; Wang, X.; Xue, G.; Zhou, D. *Macromolecules* **2015**, *48*, 1804–1812.

86. Lin, M.-C.; Nandan, B.; Chen, H.-L. *Soft Matter* **2012**, *8*, 7306–7322.

87. He, W.-N.; Xu, J.-T. *Progress in Polymer Science* **2012**, *37*, 1350–1400.

88. Takeshita, H.; Shiomi, T.; Takenaka, K.; Arai, F. *Polymer* **2013**, *54*, 4776–4789.

89. Huang, S.; Jiang, S. *RSC Advances* **2014**, *4*, 24566.

90. Zhu, L.; Cheng, S. Z. D.; Calhoun, B. H.; Ge, Q. *Polymer* **2001**, *42*, 5829–5839.

91. Quiram, D. J.; Register, R. A.; Marchand, G. *Macromolecules* **1997**, *30*, 4551–4558.

92. Quiram, D. J.; Register, R. A.; Marchand, G. R.; Ryan, A. J. *Macromolecules* **1997**, *30*, 8338–8343.

93. Nojima, S.; Toei, M.; Hara, S.; Tanimoto, S.; Sasaki, S. *Polymer* **2002**, *43*, 4087–4090.

94. Chen, H.-L.; Li, H.-C.; Huang, Y.-Y.; Chiu, F.-C. *Macromolecules* **2002**, *35*, 2417–2422.

95. Ho, R.-M.; Lin, F.-H.; Tsai, C.-C.; Lin, C.-C.; Ko, B.-T.; Hsiao, B. S.; Sics, I. *Macromolecules* **2004**, *37*, 5985–5994.

96. Nojima, S.; Inokawa, D.; Kawamura, T.; Nitta, K.-h. *Polymer Journal* **2008**, *40*, 986–991.

97. Malek, A.; Dingenouts, N.; Beskers, T. F.; Fehrenbacher, U.; Barner, L.; Wilhelm, M. *European Polymer Journal* **2013**, *49*, 2704–2720.

98. Nojima, S.; Hashizume, K.; Rohadi, A.; Sasaki, S. *Polymer* **1997**, *38*, 2711–2718.

99. Lee, W.; Chen, H.-L.; Lin, T.-L. *Journal of Polymer Science Part B: Polymer Physics* **2002**, *40*, 519–529.

100. Rohadi, A.; Tanimoto, S.; Sasaki, S.; Nojima, S. *Polymer journal* **2000**, *32*, 859–865.

101. Nojima, S.; Kakihira, H.; Tanimoto, S.; Nakatani, H.; Sasaki, S. *Polymer Journal* **2000**, *32*, 75–78.

102. Xu, J.-T.; Yuan, J.-J.; Cheng, S.-Y. *European Polymer Journal* **2003**, *39*, 2091–2098.

103. Xu, J.-T.; Ryan, A. J.; Mai, S. M.; Yuan, J. J.; Cheng, S. Y. *Journal of Macromolecular Science, Part B: Physics* **2005**, *43*, 685–694.

104. Nojima, S.; Ohguma, Y.; Namiki, S.; Ishizone, T.; Yamaguchi, K. *Macromolecules* **2008**, *41*, 1915–1918.

105. Nojima, S.; Ohguma, Y.; Kadena, K.-i.; Ishizone, T.; Iwasaki, Y.; Yamaguchi, K. *Macromolecules* **2010**, *43*, 3916–3923.

106. Barltrop, J. A.; Plant, P. J.; Schofield, P. *Chemical Communications* **1966**, 822–823.

107. Guillier, F.; Orain, D.; Bradley, M. *Chemical Reviews* **2000**, *100*, 2091–158.

108. Yamaguchi, K.; Kitabatake, T.; Izawa, M.; Fujiwara, T.; Nishimura, H.; Futami, T. *Chemistry Letters* **2000**, *29*, 228–229.

109. Pellicciolі, A. P.; Wirz, J. *Photochemical & Photobiological Sciences* **2002**, *1*, 441–458.

110. Zhao, H.; Sterner, E. S.; Coughlin, E. B.; Theato, P. *Macromolecules* **2012**, *45*, 1723–1736.

111. Kang, M.; Moon, B. *Macromolecules* **2009**, *42*, 455–458.

112. Zhao, H.; Gu, W.; Sterner, E.; Russell, T. P.; Coughlin, E. B.; Theato, P. *Macromolecules* **2011**, *44*, 6433–6440.

113. Schumers, J.-M.; Vlad, A.; Huynen, I.; Gohy, J.-F.; Fustin, C.-A. *Macromolecular Rapid Communications* **2012**, *33*, 199–205.

114. Zhao, H.; Gu, W.; Thielke, M. W.; Sterner, E.; Tsai, T.; Russell, T. P.; Coughlin, E. B.; Theato, P. *Macromolecules* **2013**, *46*, 5195–5201.

115. Zhao, H.; Gu, W.; Kakuchi, R.; Sun, Z.; Sterner, E.; Russell, T. P.; Coughlin, E. B.; Theato, P. *ACS Macro Letters* **2013**, *2*, 966–969.

116. Cao, M.; Wang, J.-Q.; Chen, P.-C.; Xu, J.-T.; Fan, Z.-Q. *Journal of Polymer Science Part A: Polymer Chemistry* **2010**, *48*, 3834–3840.

117. Cabane, E.; Malinova, V.; Meier, W. *Macromolecular Chemistry and Physics* **2010**, *211*, 1847–1856.

118. Han, D.; Tong, X.; Zhao, Y. *Macromolecules* **2011**, *44*, 437–439.

Chapter 2

Crystallization of Block Chains and Homopolymers Confined in Nanocylinders

2.1 Introduction

The effects of *space confinement* on polymer crystallization have been studied using homopolymers confined in tiny droplets[1–3] and cylindrical nanodomains (nanocylinders) of anodic aluminum oxide (AAO) templates[4–8], where it has been reported that the crystallizable temperature, melting temperature, and crystallinity are significantly lower than those in the bulk state. The crystallization kinetics also changes by space confinement, from the conventional heterogeneous nucleation and growth mechanism to the homogeneous nucleation mechanism. Block copolymers are also frequently used to study the crystallization of polymer chains confined in nanodomains[9–13], since crystalline block chains can easily be confined in nanodomains formed by microphase separation of crystalline-amorphous diblock copolymers. For example, Chung and coworkers[14] investigated the crystallization of PCL block chains confined in nanocylinders embedded in a glassy P4VP matrix and found that the crystallization mechanism depended drastically on the nanocylinder diameter D. Heterogeneous nucleation and growth were observed in nanocylinders with $D \geq 13.7$ nm, whereas the crystallization of PCL block chains in nanocylinders with $D = 9.9$ nm was controlled by homogeneous nucleation.

Crystallization of block chains within nanodomains is also affected by *chain confinement*, the restriction on the chain motion imposed by tethered chain-ends. Nojima and coworkers[15] for the first time directly evaluated the effects of chain confinement on crystallization by comparing the crystallization behavior of PVL block chains and homopolymers in an identical nanosphere and nanocylinder. The melting temperature and crystallinity of PVL block chains were lower than those of PVL homopolymers, suggesting that the chain confinement prohibited the formation of thicker and larger crystals. Interestingly, PVL block chains crystallized faster than PVL homopolymers in both nanospheres and nanocylinders, indicating that the chain confinement facilitated the crystal nucleation of PVL chains. However, the roles of chain confinement in crystallization is not yet fully understood. In the present study, the crystallization of PCL block chains and homopolymers confined in nanocylinders is investigated as a function of the nanocylinder diameter D in order to clarify the effects of chain confinement and its relationship with space confinement.

2.2 Experimental

2.2.1 Model Systems

Figure 2.1 schematically illustrates the sample preparation strategy. The samples used in this study are PCL-*b*-PS diblock copolymers having a photocleavable *o*-nitrobenzyl group (ONB) in the block junction. They microphase-separate to form nanocylinders containing PCL block chains whose one end is tethered onto the nanodomain interface (**Figure 2.1**a). ONB is then cleaved by UV irradiation to convert PCL block chains to untethered PCL homopolymers (b). The reaction scheme of photocleavage is shown at the top of **Figure 2.1**. Since the sample at this point is actually a multi-component system mainly consisting of PCL and PS homopolymers, the nanocylinder structure previously formed is no longer in equilibrium. However, if the temperature is kept sufficiently lower than the glass transition temperature T_g of PS chains, the non-equilibrium nanocylinder structure will be frozen by the vitrified PS matrix. The melting temperature T_m of PCL

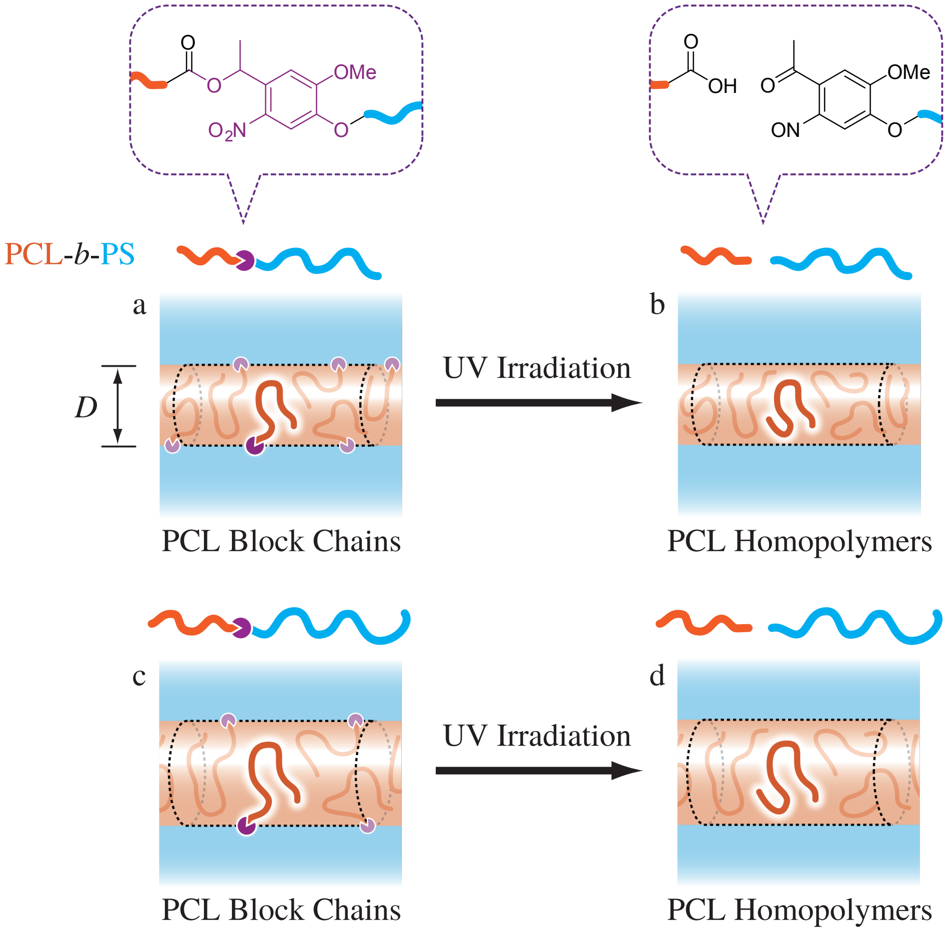

Figure 2.1. Schematic illustration showing the method for preparing the model systems. The microphase-separated PCL-*b*-PS diblock copolymer has PCL block chains confined in nanocylinders (a), which is converted to PCL homopolymers (b) by the photocleavage of ONB at block junctions via the reaction scheme shown at the top. Increasing the total molecular weight of the PCL-*b*-PS diblock copolymer allows for preparing PCL block chains and PCL homopolymers confined in a larger nanocylinder (c and d).

chains is at least ca. 30 °C lower than the glass transition temperature T_g of PS chains, therefore PCL chains can be melted and crystallized without destroying or deforming the nanocylinders even after the photocleavage of block junctions. Furthermore, in order to explore the impacts of different nanocylinder diameter *D* on the crystallization of PCL block chains and homopolymers, four PCL-*b*-PS diblock copolymers having a similar volume fraction of PCL blocks but different total molecular weights were used (**Figure 2.1**c and d).

Table 2.1. Characterization of the samples used in this study.

Code	M_n / g mol^{-1}			M_w/M_n[b]	ϕ_{PCL}[d]	D[e] / nm	f_h[f]
	PCL[a]	PS[b]	Total[c]				
PCL-*b*-PS1	7900	24100	32000	1.05	0.25	13.0	0
PCL/PS1	7900	24100	-	-	0.25	13.0	0.80
PCL-*b*-PS2	9400	27900	37300	1.03	0.25	14.9	0
PCL/PS2	9400	27900	-	-	0.25	14.9	0.87
PCL-*b*-PS3	12400	48900	61300	1.03	0.20	17.9	0
PCL/PS3	12400	48900	-	-	0.20	17.9	0.86
PCL-*b*-PS4	22600	70000	92600	1.08	0.24	27.0	0
PCL/PS4	22600	70000	-	-	0.24	27.0	0.82

[a] Determined by ^{1}H-NMR.

[b] Determined by GPC.

[c] Sum of M_ns of the PCL and PS blocks.

[d] Volume fraction of PCL chains calculated from M_ns and specific volumes of PCL and PS at 100 °C.

[e] Nanocylinder diameter calculated from the primary peak position in SAXS curves and volume fraction of PCL blocks.

[f] Mole fraction of PCL homopolymers in the system calculated from GPC chromatograms.

2.2.2 Samples and Sample Preparation

The method of synthesis and complete chemical structure of PCL-*b*-PS diblock copolymers are described in Appendix A. The molecular characterization of the synthesized PCL-*b*-PS diblock copolymers and that after UV irradiation are summarized in **Table 2.1**. PCL-*b*-PS1, PCL-*b*-PS2, PCL-*b*-PS3, and PCL-*b*-PS4 denote diblock copolymer samples in the increasing order of total molecular weight, while after UV irradiation they are denoted as PCL/PS1, PCL/PS2, PCL/PS3, and PCL/PS4, respectively. Unfortunately, the amount of neat PCL-*b*-PS4 was too small to investigate crystallization kinetics in detail, so the time evolution of crystallinity of PCL-*b*-PS4 and PCL/PS4 is not presented. All the diblock copolymers have the volume fraction of PCL block chains ϕ_{PCL} of 0.20 - 0.25 and hence are expected to form cylindrical microphase-separated structures, where nanocylinders of PCL chains are embedded in a PS matrix.

All experiments were performed on the sample films prepared by solution casting. Toluene solution of a PCL-*b*-PS diblock copolymer (ca. 20 g/L) was drop-cast on an ethylene-tetrafluoroethylene copolymer sheet, dried at 60 °C overnight, and annealed *in vacuo* at 120 °C for 3 h. Films thus obtained were circular in shape typically having the thickness of 50 μm and diameter of 5 mm. The UV light used to cleave ONB was generated by high pressure mercury lamp (USH-500SC, USHIO Inc., Japan) and filtered with aqueous solution of $CuSO_4$ to remove low wavelength light. UV irradiation was performed on amorphous PCL-*b*-PS films at room temperature with the intensity of 1.0 $\mathrm{W\,cm^{-2}}$ for more than 1 h.

2.2.3 Gel Permeation Chromatography (GPC)

Gel permeation chromatography (GPC) was employed to characterize the synthesized samples and monitor the progress of the photocleavage reaction. The GPC system used THF as an eluent and was equipped with two analytical columns (Shodex K-803L, Showa Denko, Japan), a dual-wavelength UV absorbance detector (Waters 2487, Waters, USA), and an RI detector (Waters 2410, Waters, USA). The elution time was calibrated by PS standards.

2.2.4 Small-angle X-ray Scattering (SAXS)

Microphase-separated structures formed in PCL-*b*-PS samples were examined using small-angle X-ray scattering (SAXS) with synchrotron radiation. The small-angle X-ray equipment for solution (SAXES) was used, which was installed at BL-10C of Photon Factory in High Energy Accelerator Research Organization, Tsukuba, Japan. The wavelength of X-ray λ was 0.1488 nm, and the sample-to-detector distance was ca. 2 m. Scattering curves were collected by a one-dimensional position-sensitive proportional counter (Rigaku, Japan) having 512 channels with a typical exposure time of 5 min. Scattered X-ray was appropriately attenuated by placing an aluminum sheet in front of the detector

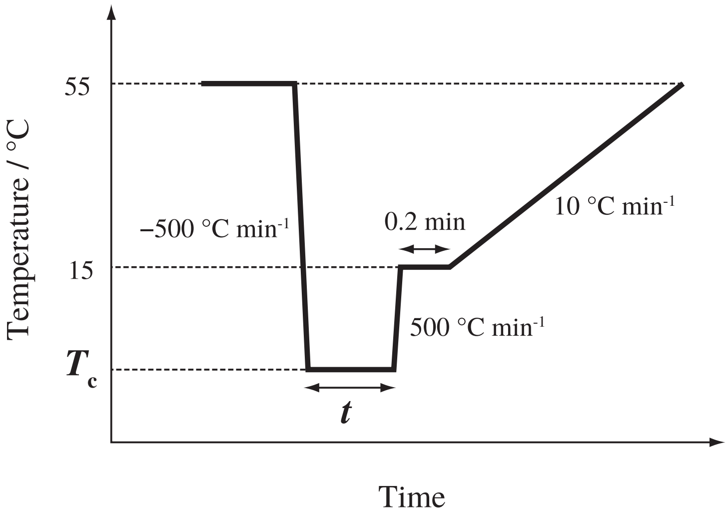

Figure 2.2. Temperature program for DSC measurements. The sample is first heated to 55 °C to erase previous thermal histories and then quenched to prescribed crystallization temperature T_c at -500 °C min^{-1}. After being held at T_c for crystallization time t, the sample is reheated to 15 °C at 500 °C min^{-1}, held for 0.2 min, and finally heated back to 55 °C at 10 °C min^{-1} to collect the endothermic heat flow caused by the melting of PCL crystals. The program is repeated with various t and T_c.

in order to prevent the counting loss. Raw data were corrected for background scattering and absorption and plotted against the magnitude of scattering vector s ($= 2\sin\theta/\lambda$), which was calibrated by 6th order scattering peak from a chicken tendon collagen having a long period of 65.3 nm.

2.2.5 Differential Scanning Calorimetry (DSC)

The melting temperature T_m and crystallinity X_c after the isothermal crystallization of PCL chains in the samples were measured by differential scanning calorimetry (DSC) with a DSC system equipped with a liquid nitrogen cooling device (Diamond DSC, Perkin Elmer, USA). Sample films (ca. 5 - 10 mg in weight) were sealed in an aluminum pan for measurements. **Figure 2.2** illustrates the temperature program applied. The sample was first heated to 55 °C to melt previously formed PCL crystals and then quenched to a crystallization temperature T_c at -500 °C min^{-1} followed by isothermal annealing for a

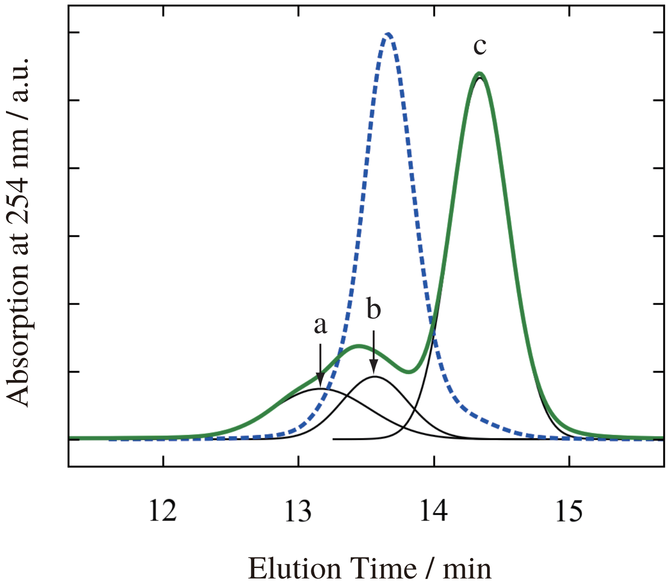

Figure 2.3. GPC chromatograms of PCL-*b*-PS2 before (dashed blue curve) and after (solid green curve) UV irradiation for 80 min with the intensity of 1.0 W cm^{-2}. The decomposed peaks corresponding to dimerized PS homopolymers (a), unreacted PCL-*b*-PS (b), and PS homopolymers (c) are drawn with solid black curves.

prescribed crystallization time t. Finally the sample was heated to 15 °C at 500 °C min^{-1}, held there for 0.2 min to stabilize the heat flow, and heated to 55 °C at 10 °C min^{-1} to collect endothermic signals arising from the melting of PCL crystals. T_m was taken as the peak temperature of the endothermic peak. X_c was calculated from the area of the endothermic peak ΔH_m by $X_\mathrm{c} = \Delta H_\mathrm{m}/(w_\mathrm{PCL}\Delta H_\mathrm{m}^{\circ})$, where $\Delta H_\mathrm{m}^{\circ}$ is the heat of fusion of PCL perfect crystal (135 J g^{-1} from ref[16]) and w_PCL the weight fraction of PCL chains in the sample.

2.3 Results and Discussion

2.3.1 Photocleavage Behavior

Figure 2.3 shows the GPC chromatograms of PCL-*b*-PS2 before and after UV irradiation obtained by the UV absorption detector at the wavelength of 254 nm. The chromatogram before UV irradiation (dashed curve) has a single sharp peak, whereas that after sufficient UV irradiation (solid curve) contains multiple peaks (denoted a, b, and c in **Figure 2.3**). Judging from the molecular weight, peaks a, b, and c can be assigned to dimerized PS homopolymers, unreacted PCL-*b*-PS, and PS homopolymers, respectively. The dimerization of PS homopolymers can be caused by nitroso groups generated by the photocleavage of ONB[17]. It should be noted that PCL homopolymers released from PCL-*b*-PS on photocleavage are not detected in **Figure 2.3** because they have no absorption at the wavelength used in the GPC measurement.

As a quantitative measure for the progress of the photocleavage reaction, the mole fraction of PCL homopolymers out of all PCL chains in the system (i.e., PCL block chains and PCL homopolymers) was defined as f_h. The GPC chromatogram after UV irradiation was first decomposed into three peaks (a, b, and c) by fitting with three Gaussian functions, then f_h was calculated from the area ratio of three peaks according to the method described in Section C.2 of Appendix C. **Table 2.1** shows the values of f_h for PCL/PS samples, which are higher than 80% in all the samples, though they do not reach 100% on further UV irradiation. The major reason for the incomplete photocleavage may be an impurity in ONB linkers and/or insufficient introduction of ONB linkers at the time of synthesis, which would produce inherently photo-inert diblock copolymer molecules. But the possibility of some side reaction involving active nitroso groups cannot be eliminated.

GPC measurements were also performed on the samples during UV irradiation as a function of the irradiation time to determine the time and intensity of UV irradiation necessary to attain maximum f_h. Typical results of these measurements appear in Section 4.3.1 of Chapter 4.

2.3.2 Microphase-separated Structures

Figure 2.4 shows the SAXS curves of PCL-*b*-PS1 (a), PCL-*b*-PS2 (b), PCL-*b*-PS3 (c), and PCL-*b*-PS4 (d), where dashed curves and blue solid curves indicate the data obtained in the amorphous state and after the crystallization at −50 °C for 4 h, respectively. The

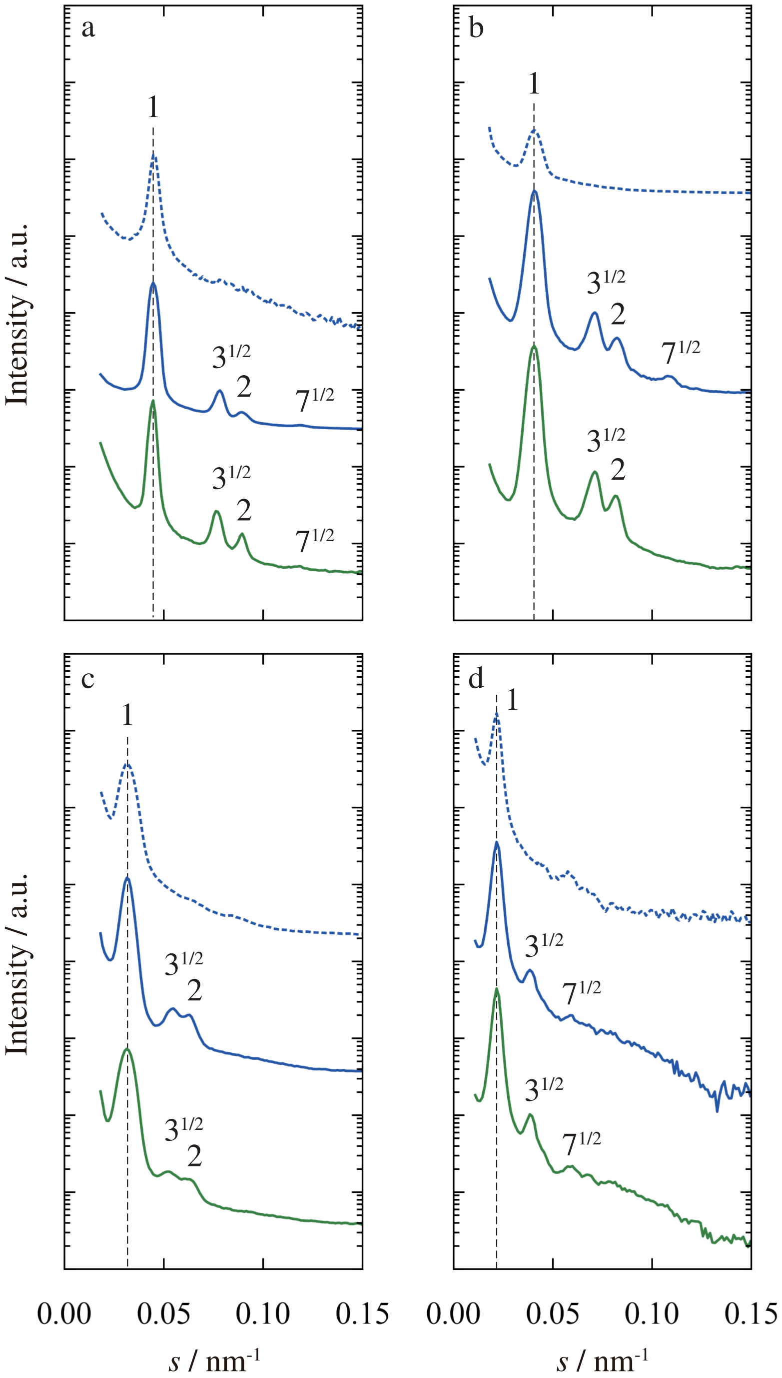

Figure 2.4. SAXS profiles of PCL-*b*-PS1 and PCL/PS1 (a), PCL-*b*-PS2 and PCL/PS2 (b), PCL-*b*-PS3 and PCL/PS3 (c), and PCL-*b*-PS4 and PCL/PS4 (d). Data for PCL-*b*-PS and PCL/PS samples with crystallized PCL chains are drawn with blue and green solid curves, respectively, whereas those for PCL-*b*-PS samples in the amorphous state are drawn with blue dotted curves. Vertical dashed lines indicate the positions of primary peaks.

data in the crystallized state exhibit a sharp primary peak and several higher order peaks located at the positions corresponding to a ratio of $1 : \sqrt{3} : 2 : (\sqrt{7})$, which indicate the formation of a hexagonally-packed cylindrical microphase-separated structure. Judging from the block composition, PCL chains are confined in nanocylinders surrounded by a PS matrix, but not vice versa. The data in the amorphous state (dashed curves) have a primary peak at exactly the same position as that in the crystallized state, strongly suggesting that the crystallization and melting of PCL chains do not affect the microphase-separated structure. However, higher order peaks observed in the crystallized state are diminished or vanished in the amorphous state. This can be explained by the weaker electron density contrast between amorphous PCL (337 e nm^{-3} at 100 °C[16]) and amorphous PS (332 e nm^{-3} at 100 °C[18]), compared to that between crystallized PCL (393 e nm^{-3} for a perfect crystal[16]) and amorphous PS. The SAXS curves of UV-irradiated (PCL/PS) samples in the crystallized state are also drawn in **Figure 2.4** by green solid curves. These SAXS curves completely retain the shape and primary peak position of those obtained before UV irradiation, suggesting that the photocleavage of block junctions does not perturb the nanocylinder structures. Therefore it can be said that PCL block chains and homopolymers confined in an identical nanocylinders were successfully prepared.

The diameter of nanocylinders D in each sample was determined from the primary peak position and volume fraction of PCL block chains ϕ_{PCL}. Since the spacing of primary peak L corresponds to the distance between two neighboring nanocylinder layers, D can be calculated by

$$D = 2\left(\frac{2\phi_{\mathrm{PCL}}}{3^{1/2}\pi}\right)^{1/2} L, \tag{2.1}$$

to be 13.0 nm for PCL-*b*-PS1 and PCL/PS1, 14.9 nm for PCL-*b*-PS2 and PCL/PS2, 17.9 nm for PCL-*b*-PS3 and PCL/PS3, and 27.0 nm for PCL-*b*-PS4 and PCL/PS4 (**Table 2.1**).

The validity of the nanocylinder diameter D thus determined can be examined via the dependence of D on the (number-averaged) degree of polymerization N. Ohta and

Kawasaki[19] derived the relationship between the equilibrium domain size D_e and radius of gyration R_g of a diblock copolymer in the strong segregation limit:

$$D_\mathrm{e} \propto C R_\mathrm{g}^{4/3} \tag{2.2}$$

where C is the correction coefficient that varies with the nanodomain shape and block composition. Here, D_e is defined as the diameter of nanocylinder D for cylindrical microphase-separated structures and thickness of PCL layers d_PCL for lamellar microphase-separated structures. Assuming that R_g is proportional to $N^{1/2}$ and defining "corrected" domain size $\tilde{D} = D_\mathrm{e}/C$, equation (2.2) is reduced to

$$\tilde{D} \propto N^{2/3} \tag{2.3}$$

and $\tilde{D}$ for nanocylinders and nanolamellae is written as

$$\tilde{D} = \frac{D}{2}\left(\frac{4\sqrt{2} f_\mathrm{PCL}(1-f_\mathrm{PCL})}{9(-1+\phi_\mathrm{PCL}-\ln\phi_\mathrm{PCL})}\right)^{-1/3} \quad \text{(for nanocylinders)}, \tag{2.4}$$

$$\tilde{D} = \frac{d_\mathrm{PCL}}{\phi_\mathrm{PCL}}\left(\frac{4\sqrt{2} f_\mathrm{PCL}(1-f_\mathrm{PCL})}{3\phi_\mathrm{PCL}^2(1-\phi_\mathrm{PCL})^2}\right)^{-1/3} \quad \text{(for nanolamellae)}, \tag{2.5}$$

where f_PCL is the fraction of the degree of polymerization of PCL chains against the total degree of polymerization N. Equation (2.3) implies that the double logarithmic plot of $\tilde{D}$ against N should be linear with the slope of $2/3$. **Figure 2.5** plots $\ln\tilde{D}$ against $\ln N$ for all PCL-*b*-PS and PS-*b*-PCL-*b*-PS block copolymer samples used in this study. PCL-*b*-PS5 is a cylinder-forming diblock copolymer used in Chapter 4, and PCL-*b*-PS6 and PCL-*b*-PS7 are lamella-forming diblock copolymers used in Chapter 5. SCS1 is a lamella-forming PS-*b*-PCL-*b*-PS triblock copolymer appearing in Chapter 6, whose N is set to half the actual value based on the knowledge that the phase behavior of symmetric triblock copolymer is similar to that of the diblock copolymer obtained by cutting it at the center of its middle block[20]. An excellent linear relationship with the slope of 2/3 is

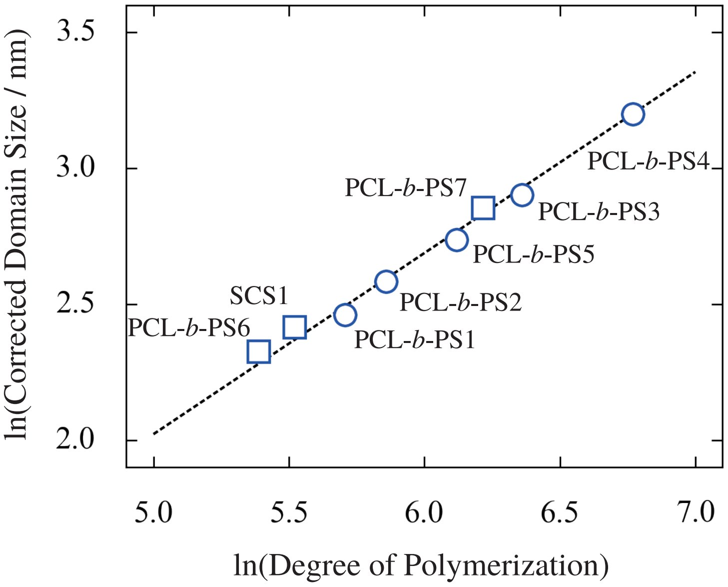

Figure 2.5. Double logarithmic plot of the corrected domain size $\tilde{D}$ against the (number-averaged) degree of polymerization N, for cylinder-forming PCL-*b*-PS1, PCL-*b*-PS2, PCL-*b*-PS3, PCL-*b*-PS4, and PCL-*b*-PS5 (circles), and lamella-forming PCL-*b*-PS6, PCL-*b*-PS7, and SCS1 (squares). N of SCS1 (PS-*b*-PCL-*b*-PS triblock copolymer) is taken as half the actual value. A dashed line denotes the result of linear fitting with the slope fixed to $2/3$.

observed in **Figure 2.5**, strongly suggesting the consistency of the nanodomain size in all the PCL-*b*-PS and PS-*b*-PCL-*b*-PS block copolymers used in this thesis.

2.3.3 Melting Behavior of PCL Chains

The melting temperature T_m and crystallinity X_c of bulk homopolymers are known to increase with increasing crystallization temperature T_c, because the thicker crystals with a smaller solid-liquid interfacial area are thermodynamically more stable than the thinner ones. However, the previous study on PVL-*b*-PS[15] found that T_m and X_c were constant independent of T_c, possibly because space confinement prohibited the thickening of PVL crystals. Similar phenomena were also observed in this study where T_m and X_c of PCL chains did not change with T_c in PCL-*b*-PS1 and PCL/PS1 ($T_c = -54 \pm 16$°C), PCL-*b*-PS2, PCL/PS2, PCL-*b*-PS3, and PCL/PS3 ($T_c = -45 \pm 5$°C), and PCL-*b*-PS4 and PCL/PS4 ($T_c = -30 \pm 10$°C). This invariability allowed for a direct comparison of T_m

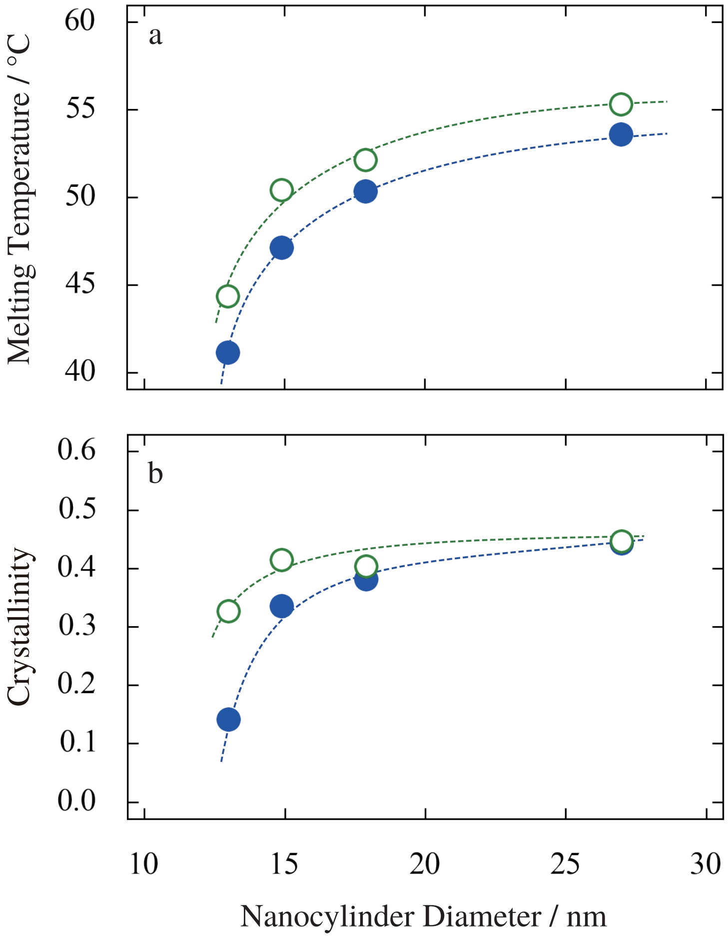

Figure 2.6. Melting temperature T_m (a) and crystallinity X_c (b) of PCL block chains (closed circles) and homopolymers (open circles) confined in nanocylinders, plotted against the nanocylinder diameter D. Dashed curves are just a guide for the eye.

and X_c between the samples at different T_cs. **Figure 2.6** shows the representative values of T_m (a) and X_c (b) of PCL chains in PCL-*b*-PS and PCL/PS samples plotted against the nanocylinder diameter D. T_m of both PCL block chains and PCL homopolymers drops sharply with decreasing D. Since T_m of bulk homopolymers generally reflects the thickness of lamellar crystals, the drop of T_m implies that the spatial restriction along the radial direction of the nanocylinder controls the crystal thickness. Also prominent in **Figure 2.6**a is that T_m of PCL homopolymers is always 2-4 °C higher than that of PCL block chains in the range of D investigated, indicating that chain confinement also reduces the crystal thickness.

Figure 2.6b shows that X_c also decreases sharply with reducing D, particularly at $D \leq 14.9$ nm. However, the difference in X_c between PCL block chains and PCL homopolymers is more significant in smaller nanocylinders ($D \leq 14.9$ nm), whereas it is negligibly small in larger nanocylinders ($D \geq 17.9$ nm). Considering that the effect of chain confinement on the crystal thickness does not significantly depend on D as shown in **Figure 2.6**a, the large reduction of X_c by chain confinement at smaller D may reflect the reduced lateral dimension of PCL crystals. This could be related to the crystal growth direction with respect to the nanocylinder axis, which is investigated in Chapter 3.

2.3.4 Crystallization Behavior of PCL Chains

Figure 2.7 shows the time development of X_c during isothermal crystallization of PCL-*b*-PS1 and PCL/PS1 (a), PCL-*b*-PS2 and PCL/PS2 (b), and PCL-*b*-PS3 and PCL/PS3 (c) at the crystallization temperature T_c indicated. It is clearly seen that the shape of the curves is completely different from those usually observed in bulk homopolymers: X_c increases sharply at the initial stage of crystallization without an induction time, followed by an asymptotic increase to a limiting value. Moreover, the supercooling needed to crystallize the PCL chains in these samples (> 80 °C) is significantly larger than that in bulk PCL homopolymers (typically 10 to 20 °C). These observations suggest that the crystallization kinetics of PCL chains in PCL-*b*-PS and PCL/PS samples are controlled by homogeneous nucleation, unlike the conventional heterogeneous nucleation and growth mechanism in bulk homopolymers.

It is clear from **Figure 2.7**a that the development of X_c with time is considerably different between PCL-*b*-PS1 and PCL/PS1, that is, X_c of PCL-*b*-PS1 increases slowly to reach a final X_c of ca. 0.15 after a long time (> 300 min), whereas that of PCL/PS1 increases quickly to reach a larger final X_c (~ 0.33) in less than 60 min. The difference between PCL block chains and PCL homopolymers is significantly diminished in PCL-*b*-PS2 and PCL/PS2 (b). Interestingly, X_c of PCL-*b*-PS3 is slightly higher than that of PCL/PS3 in the initial stage of crystallization (c), contrary to the relation be-

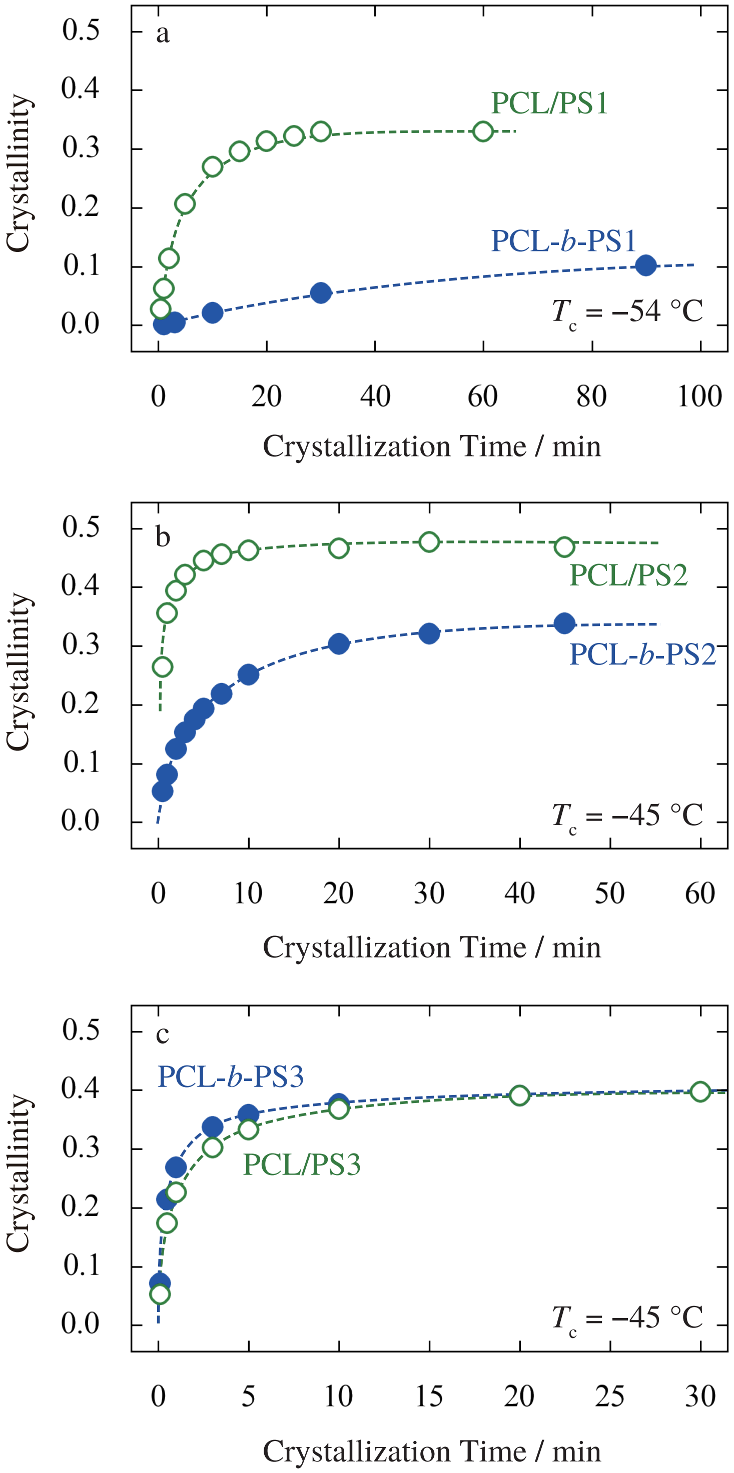

Figure 2.7. Time evolution of the crystallinity of PCL chains X_c during isothermal crystallization of PCL-*b*-PS1 and PCL/PS1 (a), PCL-*b*-PS2 and PCL/PS2 (b), and PCL-*b*-PS3 and PCL/PS3 (c). The crystallization temperature T_c is −54 °C for PCL-*b*-PS1 and PCL/PS1, and −45 °C for the other samples. Dashed curves are just a guide for the eye.

tween PCL block chains and PCL homopolymers in **Figure 2.7**a and b. A qualitatively similar behavior was reported in the previous study by Nojima and coworkers[21] on the crystallization of PVL block chains and PVL homopolymers confined in nanocylinders with $D = 15.7$ nm, which might be attributed to a possible acceleration of nucleation by chain confinement. The data in **Figure 2.7** indicate that the difference in X_c and the crystallization rate between PCL block chains and PCL homopolymers varies drastically with D.

Before discussing the D-dependence of the effects of chain confinement in detail, it is important to verify that the crystallization kinetics of PCL chains in PCL-*b*-PS and PCL/PS samples are controlled by homogeneous nucleation. In nucleation-controlled crystallization, it is assumed that the crystal growth in a nanodomain (or a part of one nanodomain in the case of nanocylinders) is instantaneous. In other words, the homogeneous nucleation process is the only rate-determining step of the crystallization. This assumption means that the crystallization rate at time t is proportional to the uncrystallized fraction, i.e.

$$\frac{\mathrm{d}\tilde{X}_\mathrm{c}(t)}{\mathrm{d}t} = k(1-\tilde{X}_\mathrm{c}(t)) \tag{2.6}$$

$$\Rightarrow \quad -\ln(1-\tilde{X}_\mathrm{c}(t)) = kt \tag{2.7}$$

where $\tilde{X}_\mathrm{c}(t)$ is the normalized crystallinity defined as $X_\mathrm{c}(t)/X_\mathrm{c}(\infty)$, and k the rate constant. On the other hand, the overall crystallization kinetics with various modes of nucleation and growth is often analysed by the Avrami equation[22,23]

$$-\ln(1-\tilde{X}_\mathrm{c}(t)) = Kt^n \tag{2.8}$$

$$\Rightarrow \quad \log(-\ln(1-\tilde{X}_\mathrm{c}(t))) = n\log t + \log K \tag{2.9}$$

where n is the parameter called the Avrami exponent, and K is another rate constant. Plotting $\log(-\ln(1-\tilde{X}_\mathrm{c}(t)))$ against $\log t$, which is known as the Avrami plot, should give

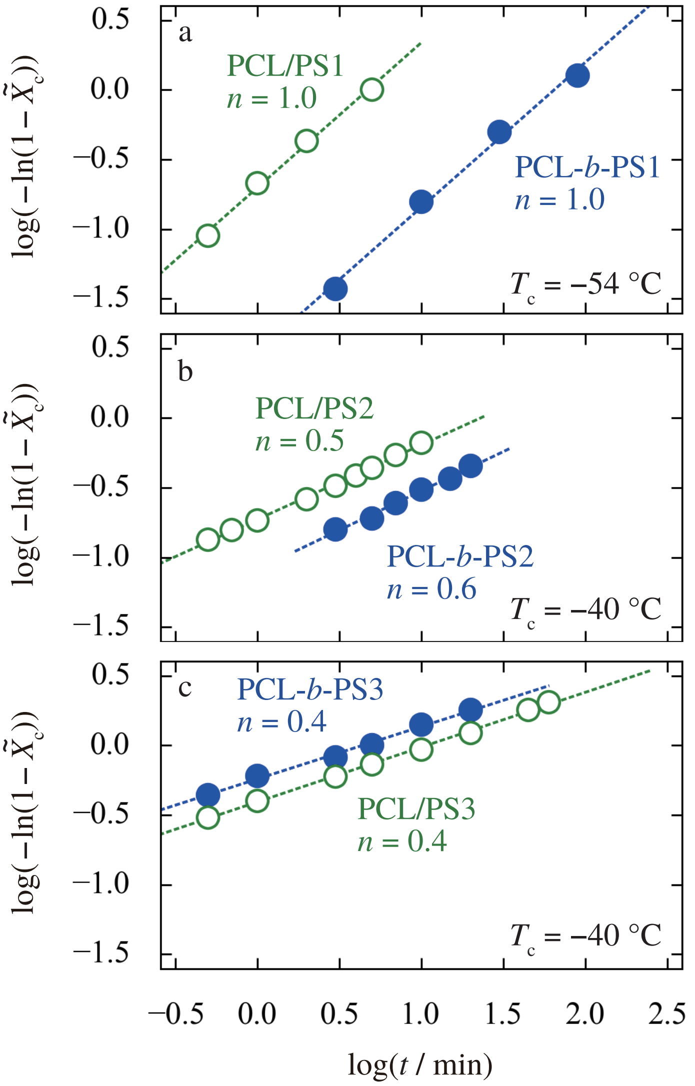

Figure 2.8. Avrami plot for the crystallization of PCL-*b*-PS1 and PCL/PS1 (a), PCL-*b*-PS2 and PCL/PS2 (b), and PCL-*b*-PS3 and PCL/PS3 (c) at the crystallization temperature T_c indicated. Dashed lines represent the results of linear fitting, whose slope is presented as the Avrami exponent n.

a straight line with the slope n and intercept $\log K$. The equation for first order kinetics (2.7) coincides with the Avrami equation (2.8) with the exponent n set to unity. Thus it is convenient to use the Avrami plot to analyse the crystallization kinetics. **Figure 2.8** shows the Avrami plots for PCL-*b*-PS (closed circles) and PCL/PS (open circles) samples at representative crystallization temperatures. All the data exhibit excellent linearity, from which the Avrami exponent n and rate constant K can be estimated. Values of n,

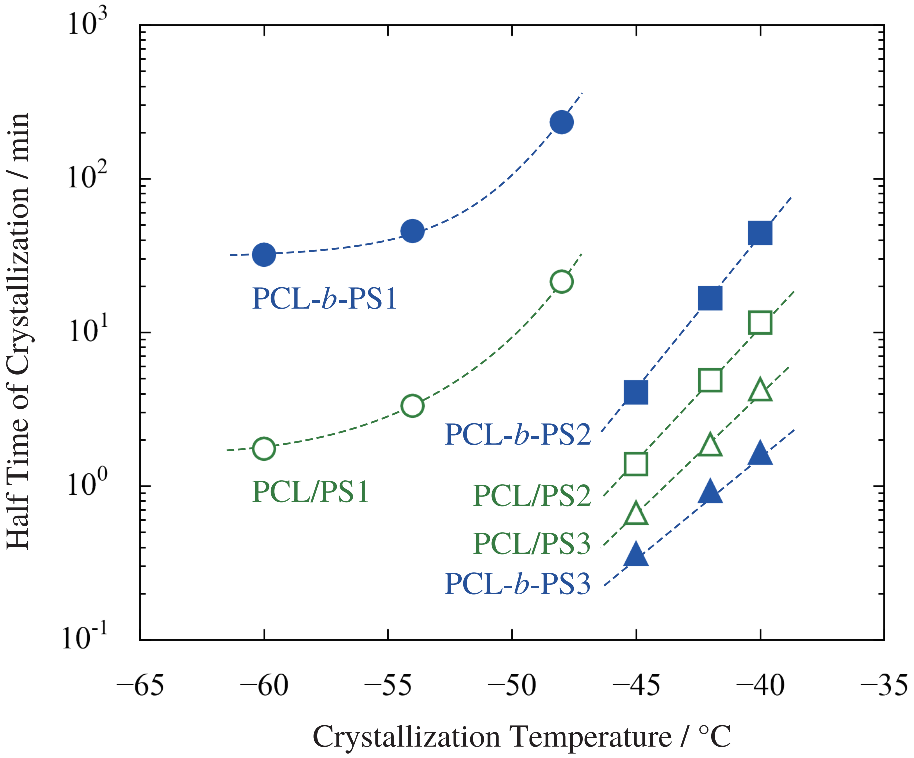

Figure 2.9. Crystallization half time $t_{1/2}$ plotted against crystallization temperature T_c for PCL-*b*-PS1 (closed circles), PCL/PS1 (open circles), PCL-*b*-PS2 (closed squares), PCL/PS2 (open squares), PCL-*b*-PS3 (closed triangles), and PCL/PS3 (open triangles).

also shown in **Figure 2.8**, are near unity for all the samples, suggesting that the first-order (or first-order-like) kinetics is dominant and hence nucleation is the only rate-determining step. Although the values of n for PCL-*b*-PS1 and PCL/PS1 (**Figure 2.8**a) are equal to 1.0, those in PCL-*b*-PS2 and PCL/PS2 (b) and PCL-*b*-PS3 and PCL/PS3 (c) are close to 1/2. Similar values of the Avrami exponent were also reported in several studies on confined crystallization of block chains[24–26], though no reasonable explanation for this anomaly has been provided.

For a quantitative analysis of the crystallization rate, the crystallization half time $t_{1/2}$, defined as the time required to achieve $\tilde{X}_c = 0.5$, was calculated by the relation $t_{1/2} = (\ln 2/K)^{1/n}$ using n and K obtained from linear fitting in **Figure 2.8**. **Figure 2.9** shows $t_{1/2}$ as a function of T_c for all PCL-*b*-PS and PCL/PS samples. The difference in $t_{1/2}$ between PCL block chains and homopolymers depends on D: PCL block chains

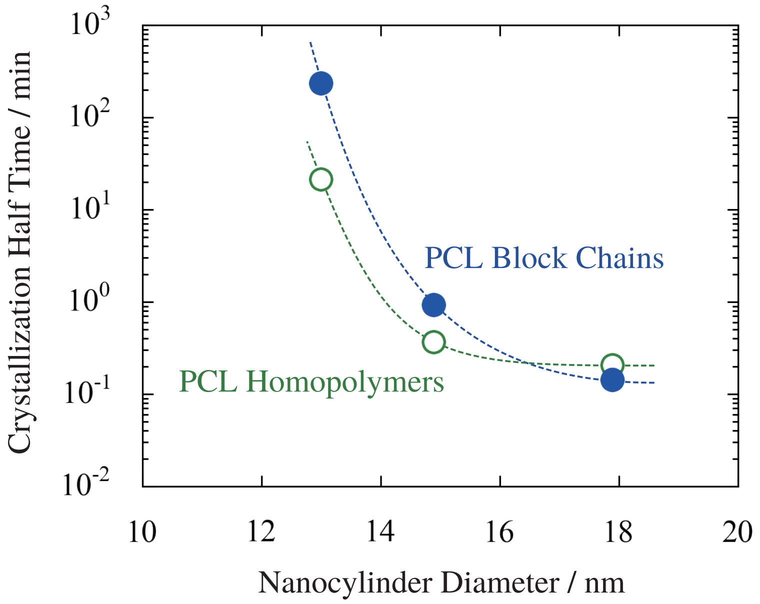

Figure 2.10. Crystallization half time $t_{1/2}$ at $T_c = -48$ °C plotted against the nanocylinder diameter D for PCL homopolymers (open circles) and PCL block chains (closed circles). The data at $D = 14.9$ and 17.9 nm were estimated by extrapolation.

crystallize much slower than PCL homopolymers in nanocylinders with $D = 13.0$ nm, while in nanocylinders with $D = 14.9$ nm the difference in $t_{1/2}$ between PCL block chains and PCL homopolymers is relatively small. The relation of the crystallization rate between PCL block chains and PCL homopolymers is reversed in nanocylinders with $D = 17.9$ nm. That is, PCL block chains crystallize faster than PCL homopolymers. These observations indicate that the effects of chain confinement change with the extent of space confinement.

It is interesting to plot $t_{1/2}$ for PCL homopolymers and PCL block chains at a certain T_c as a function of D in order to understand the complex effects of chain confinement and space confinement. However, the difference in the crystallization rate between PCL-*b*-PS1 (and PCL/PS1) and the other samples is so substantial that it is not possible to compare $t_{1/2}$ at the same T_c (**Figure 2.9**). Therefore, the data for PCL-*b*-PS2, PCL/PS2, PCL-*b*-PS3, and PCL/PS3 were extrapolated to $T_c = -48$ °C, the highest T_c applied for PCL-*b*-PS1 and PCL/PS1. The extrapolation was carried out assuming that $t_{1/2}$ obeys an Arrhenius-type T_c-dependence $\ln t_{1/2} = A + B/T_c$ where A and B are constants[24].

Figure 2.10 shows $t_{1/2}$ at $T_c = -48$ °C as a function of D for PCL homopolymers and PCL block chains. The reduction of $t_{1/2}$ for PCL homopolymers with increasing D is much severer at smaller D (13.0 nm $\leq D \leq$ 14.9 nm), whereas it is subtle at larger D (14.9 nm $\leq D \leq$ 17.9 nm). As was mentioned earlier, the difference in $t_{1/2}$ between PCL homopolymers and PCL block chains becomes smaller with increasing D from 13.0 nm to 14.9 nm, and the relation between two is completely reversed with further increasing D to 17.9 nm.

The complex interrelation of the crystallization rate between PCL homopolymers and PCL block chains may be explained by assuming that chain confinement has two opposing effects on crystal nucleation within nanocylinders, one that facilitates and another that hinders the formation of critical nuclei. The formation of homogeneous nuclei is considered to be driven by an incidental alignment of the chains into a crystal-like structure, which would become more difficult if the molecular motion is either too fast or too slow. It is reasonable to presume that a part of block chains near the block junction has low mobility due to chain confinement, which could act as a scaffold for nuclei formation. On the other hand, chain confinement might limit the diffusion of a whole chain, thereby reducing the chance of incidental nuclei formation. If there is a difference in the D-dependence between these two aspects of chain confinement, the interrelation of nucleation rate between PCL block chains and PCL homopolymers would vary or even be reversed, depending on D. This speculation will be rigorously examined later in Chapter 4.

2.4 Conclusions

The crystallization behavior of PCL homopolymers and PCL block chains confined in an identical nanocylinder was investigated as a function of nanocylinder diameter D. PCL block chains confined in nanocylinders were prepared by microphase separation of PCL-*b*-PS diblock copolymers, and subsequently converted to PCL homopolymers by the photocleavage of ONB at block junctions without perturbing the nanocylinder structure. The photocleavage reaction proceeded almost quantitatively for all the PCL-*b*-PS samples. The results of SAXS measurements indicated that all the PCL-*b*-PS samples formed a cylindrical microphase-separated structure, which was stable against the melting and crystallization of PCL chains as well as photocleavage of block junctions.

The conclusions about the melting and crystallization behavior of PCL homopolymers and PCL block chains are as follows:

1. Both space confinement and chain confinement reduced the melting temperature T_m and crystallinity X_c of PCL chains, suggesting that the thickness and probably lateral dimension of PCL crystals were restricted.

2. The crystallization of PCL chains in all the samples obeyed first-order kinetics, indicating that homogeneous nucleation was the rate-determining step of the crystallization.

3. Chain confinement significantly reduced the crystallization rate in smaller nanocylinders ($D = 13.0$ nm), while the extent of the reduction was smaller in larger nanocylinders ($D \leq 14.9$ nm). In nanocylinders with $D = 17.9$ nm, the acceleration of crystallization by chain confinement was observed. It was concluded that the effects of chain confinement on crystal nucleation in nanocylinders drastically depended on D.

References

1. Arnal, M. L.; Matos, M. E.; Morales, R. A.; Santana, O. O.; Müller, A. J. *Macromolecular Chemistry and Physics* **1998**, *199*, 2275–2288.
2. Massa, M. V.; Dalnoki-Veress, K. *Physical Review Letters* **2004**, *92*, 1–4.
3. Kailas, L.; Vasilev, C.; Audinot, J.-N.; Migeon, H.-N.; Hobbs, J. K. *Macromolecules* **2007**, *40*, 7223–7230.
4. Shin, K.; Woo, E.; Jeong, Y. G.; Kim, C.; Huh, J.; Kim, K.-W. *Macromolecules* **2007**, *40*, 6617–6623.
5. Duran, H.; Steinhart, M.; Butt, H.-J.; Floudas, G. *Nano letters* **2011**, *11*, 1671–1675.

6. Li, M.; Wu, H.; Huang, Y.; Su, Z. *Macromolecules* **2012**, *45*, 5196–5200.
7. Maiz, J.; Martin, J.; Mijangos, C. *Langmuir* **2012**, *28*, 12296–303.
8. Michell, R. M.; Blaszczyk-Lezak, I.; Mijangos, C.; Müller, A. J. *Journal of Polymer Science Part B: Polymer Physics* **2014**, *52*, 1179–1194.
9. Castillo, R. V.; Müller, A. J. *Progress in Polymer Science* **2009**, *34*, 516–560.
10. He, W.-N.; Xu, J.-T. *Progress in Polymer Science* **2012**, *37*, 1350–1400.
11. Lin, M.-C.; Nandan, B.; Chen, H.-L. *Soft Matter* **2012**, *8*, 7306–7322.
12. Takeshita, H.; Shiomi, T.; Takenaka, K.; Arai, F. *Polymer* **2013**, *54*, 4776–4789.
13. Nakagawa, T.; Nozaki, K.; Maeda, S.; Yamamoto, T. *Polymer* **2015**, *57*, 99–104.
14. Chung, T.-M.; Wang, T.-C.; Ho, R.-M.; Sun, Y.-S.; Ko, B.-T. *Macromolecules* **2010**, *43*, 6237–6240.
15. Nojima, S.; Ohguma, Y.; Namiki, S.; Ishizone, T.; Yamaguchi, K. *Macromolecules* **2008**, *41*, 1915–1918.
16. Crescenzi, V.; Manzini, G.; Calzolari, G.; Borri, C. *Polymer* **1972**, *8*, 449–463.
17. Guillier, F.; Orain, D.; Bradley, M. *Chemical Reviews* **2000**, *100*, 2091–158.
18. Richardson, M. J.; Savill, N. G. *Polymer* **1977**, *18*, 3–9.
19. Ohta, T.; Kawasaki, K. *Macromolecules* **1986**, *19*, 2621–2632.
20. Matsen, M. W.; Thompson, R. B. *The Journal of Chemical Physics* **1999**, *111*, 7139–7146.
21. Nojima, S.; Inokawa, D.; Kawamura, T.; Nitta, K.-h. *Polymer Journal* **2008**, *40*, 986–991.
22. Avrami, M. *The Journal of Chemical Physics* **1939**, *7*, 1103–1112.
23. Avrami, M. *The Journal of Chemical Physics* **1940**, *8*, 212–224.
24. Shiomi, T.; Tsukada, H.; Takeshita, H.; Takenaka, K.; Tezuka, Y. *Polymer* **2001**, *42*, 4997–5004.
25. Xu, J.-T.; Yuan, J.-J.; Cheng, S.-Y. *European Polymer Journal* **2003**, *39*, 2091–2098.
26. Xu, J.-T.; Ryan, A. J.; Mai, S. M.; Yuan, J. J.; Cheng, S. Y. *Journal of Macromolecular Science, Part B: Physics* **2005**, *43*, 685–694.

Chapter 3

Crystal Orientation of Homopolymers and Block Chains Confined in Nanocylinders

3.1 Introduction

Materials having macroscopically aligned structures are important since their properties along a particular direction are expected to be enhanced. In particular, the crystal orientation within nano-structured materials is interesting, because it can be controlled by various parameters such as the size and shape of nanodomains[1–4].

The most convenient way to investigate the crystal orientation of homopolymers confined in nanocylinders may be to use anodic aluminum oxide (AAO) templates[5–11], since they have well-defined cylindrical nanopores perfectly aligned perpendicular to the template surface. For example, Shin and coworkers[7] studied the crystal orientation of PE homopolymers confined in AAO nanopores with the diameter ranging from 15 to 110 nm, and found that the *b* axis of PE crystals (the fastest growth axis) oriented parallel to the long axis of the nanopore, suggesting that the PE crystals preferentially grew along the nanopore axis.

Crystalline-amorphous (C-A) diblock copolymers have also been extensively used to investigate the crystal orientation of block chains within anisotropic microphase-separated structures such as nanocylinders[12–16] or nanolamellae[17–25]. In this case, the nanodomains should be macroscopically aligned at first. Various experimental methods are available for this purpose including rotational shear flow[13–16,19,24], channel-die alignment[12,23,26], and rimming flow[22,27,28], among which the rotational shear flow method has been most popularly employed. For example, Chung and coworkers[14] investigated the crystal orientation of PCL block chains confined in nanocylinders formed in PCL-*b*-P4VP diblock copolymers. The nanocylinders were macroscopically aligned by applying a large-amplitude oscillating shear at a temperature well above the glass transition temperature of P4VP blocks. They found that the *c* axis (the main chain axis) of PCL crystals oriented perpendicular to the nanocylinder axis when the nanocylinder diameter D was greater than 9.9 nm, whereas no preferential orientation was observed in nanocylinders with $D = 9.9$ nm. This result demonstrates the impact of *space confinement* on the growth direction of crystals.

In Chapter 2, it was found that *chain confinement*, the restriction imposed by the chain ends immobilized on nanodomain interfaces, had significant influences on the crystallization dynamics. The previous work by Nojima and coworkers[15] investigated the crystal orientation of PCL homopolymers and PCL block chains both confined in an identical nanocylinder using a photocleavable PCL-*b*-PS diblock copolymer whose nanocylinders were macroscopically aligned by shear flow. They found that the *b* axis (fastest growing axis) oriented parallel to the nanocylinder axis in both PCL block chains and PCL homopolymers. The degree of crystal orientation for PCL homopolymers was better than that for PCL block chains, suggesting that chain confinement hindered the favorable crystal growth in which the *b* axis lie parallel to the long axis of nanocylinders. However, as was mentioned earlier, it is known that the crystal orientation within nanocylinders generally depends on the nanocylinder diameter D. Considering also that the effects of chain confinement on the crystal nucleation rate changed significantly by varying D (Chapter 2), it is meaningful to investigate the crystal orientation within nanocylinders in terms of both space confinement and chain confinement. In this study, the crystal orientation of PCL homopolymers and PCL block chains both confined in an identical nanocylinder with varying D is investigated in order to elucidate the effects of both space confinement and chain confinement on the crystal growth mode of PCL chains.

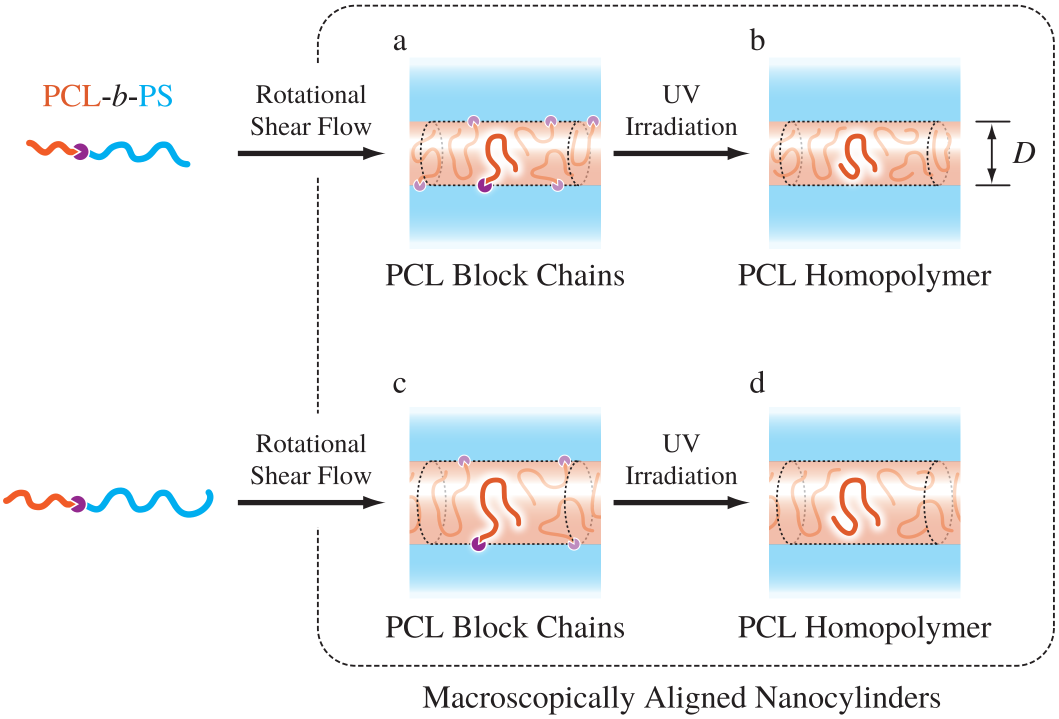

Figure 3.1. Schematic illustration of the sample preparation method in this study. A rotational shear flow is applied to a cylinder-forming PCL-*b*-PS diblock copolymer bearing a photocleavable ONB group in the block junction to macroscopically align the nanocylinders (a). Then PCL block chains are converted into PCL homopolymers by the photocleavage of ONB (b). Use of another PCL-*b*-PS diblock copolymer with a similar block composition but different molecular weight (c) allows for investigating the PCL crystal orientation as a function of the nanocylinder diameter *D*.

3.2 Experimental

3.2.1 Model Systems

Figure 3.1 shows the preparation procedure for the model systems used in this study. A PCL-*b*-PS diblock copolymer bearing an ONB at the block junction (left) is subjected to a rotational shear flow to macroscopically align the cylindrical microphase-separated structures (nanocylinders). PCL block chains confined in shear-aligned nanocylinders (a) are then converted into PCL homopolymers by photocleaving ONB at the block junction (b). Since the glass transition temperature T_g of PS chains is sufficiently higher than the melting temperature T_m of PCL chains, both the nanocylinder structure and its

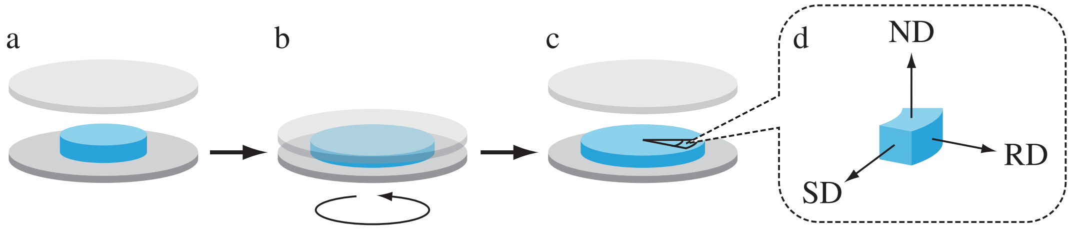

Figure 3.2. Schematic illustration showing the procedure of the shear alignment experiment. A sample disk placed between two parallel plates (a) is heated to 120 °C and pressed down to the thickness of 0.7 mm, then the rotational shear with the angular velocity of 3.14 rad s^{-1} was applied for 6 h (b). After cooling down to room temperature, a small piece is cut from the sample disk (c). The characteristic axes of the shear geometry are defined in panel d.

macroscopic alignment are expected to be preserved after the photocleavage. Moreover, it is possible to probe the crystal orientation of PCL chains as a function of nanocylinder diameter D by using PCL-*b*-PS diblock copolymers with different molecular weights but similar block compositions (c) as well as those after UV irradiation (d).

3.2.2 Samples and Sample Preparation

Samples used in this study, PCL-*b*-PS1, PCL/PS1, PCL-*b*-PS2, PCL/PS2, PCL-*b*-PS3, and PCL/PS3, are the same as those used in Chapter 2. The molecular characterization and the diameter of nanocylinders D can be found in **Table 2.1**.

Figure 3.2 schematically illustrates the procedure of the rotational shear flow experiment. A disk of a PCL-*b*-PS diblock copolymer shaped by pressing was placed between two parallel plates of a shearing stage (CSS-450, Linkam Scientific, UK) (**Figure 3.2**a) and heated to 120 °C. Then the gap between the plates was set to 0.7 mm, and the molten sample underwent rotational shear flow with the angular velocity of 3.14 rad s^{-1} (corresponding to the strain rate of 34 s^{-1} at the point where the distance from the center of the disk is 7.5 mm) for 6 h at 120 °C (b). After cooling to room temperature, small pieces with the lateral size of ca. 3×3 mm^2 were cut out from the sample disk (c) for measurements. Directions in the shear-aligned sample are defined in **Figure 3.2**d. SD denotes the shear direction, RD the radial direction of the sample disk, and ND the direction normal to both SD and RD.

Details of the apparatus used for UV irradiation is described in Section 2.2.2 of Chapter 2. Shear-aligned samples were irradiated with the intensity of 10 $\mathrm{W\,cm^{-2}}$ for 40 h to ensure uniform and complete photocleavage throughout the sample.

3.2.3 Two-dimensional Small-angle X-ray Scattering (2D-SAXS) and Wide-angle X-ray Diffraction (2D-WAXD)

The orientation of nanocylinders and PCL crystals within the nanocylinder was investigated by two-dimensional small-angle X-ray scattering (2D-SAXS) and wide-angle X-ray diffraction (2D-WAXD), respectively, both using Rigaku Nanoviewer SAXS system (Rigaku, Japan) with a rotating anode X-ray generator operating at 45 kV and 60 mA. The X-ray used was CuKα radiation with the wavelength λ of 0.1542 nm. 2D-SAXS and 2D-WAXD images were simultaneously collected using two imaging plates (IP) (BAS-SR 127, Fuji Film, Japan) having the effective area of 115×115 $\mathrm{mm^2}$. The IP for 2D-WAXD measurements, which had a hole at the center to pass the scattered X-rays in small-angle regions, was placed at the position where the distance from the sample was ca. 80 mm. The IP for 2D-SAXS measurements was placed behind an evacuated flight tube with the sample-to-detector distance of ca. 1 m. Each IP exposed to the scattered X-rays for 6-12 h was scanned by an IP reader (R-AXIS DS3C, Rigaku, Japan) with the resolution of 50×50 $\mathrm{\mu m^2}$. The obtained images were analysed using programs written by the author.

3.3 Results and Discussion

3.3.1 Orientation of Nanocylinders

Figure 3.3 shows the representative 2D-SAXS images of the shear-aligned PCL-*b*-PS2 and PCL/PS2. The images were taken with the incident X-ray beam parallel to

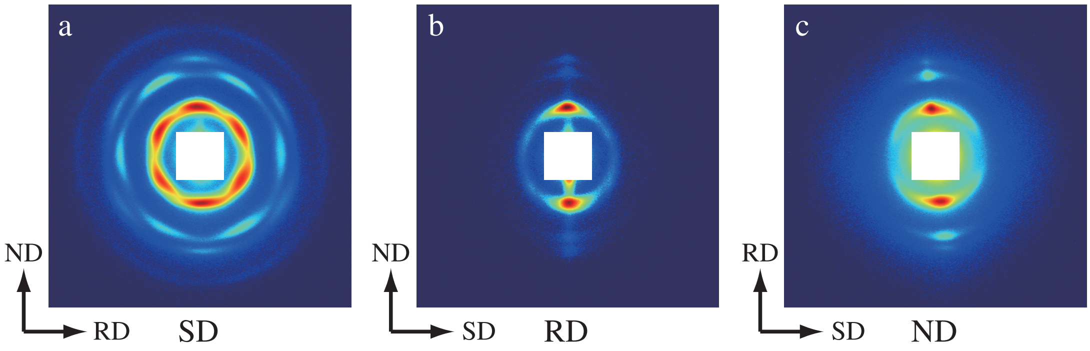
Before photocleavage (PCL-*b*-PS2)

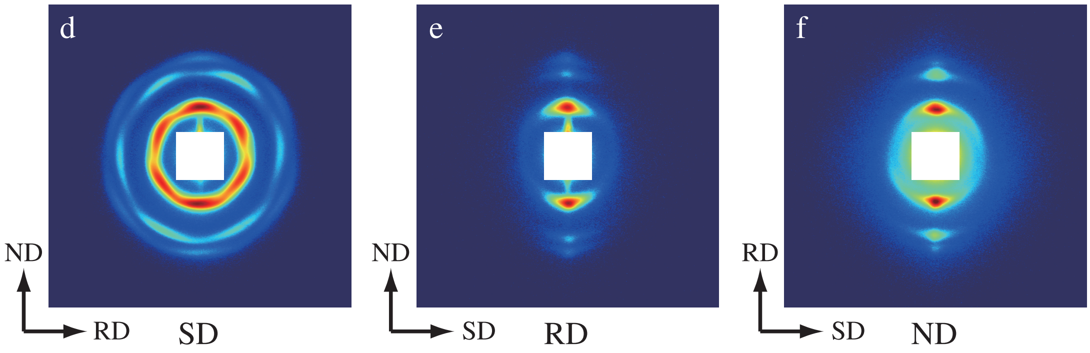
After photocleavage (PCL/PS2)

Figure 3.3. 2D-SAXS images obtained with the incident beam parallel to SD (a, d), RD (b, e), and ND (c, f) for shear-aligned PCL-*b*-PS2 (upper panels) and PCL/PS2 (lower panels) crystallized at −50 °C for 4 h. The color in the image changes from blue to green, yellow, and red, as the intensity increases in logarithmic scale.

SD (**Figure 3.3**a, d), RD (b, e), and ND (c, f). The image for PCL-*b*-PS2 viewed from SD (a) has a hexagonal symmetry, suggesting that hexagonally-packed nanocylinders are uniaxially oriented parallel to SD. This interpretation is strongly supported by the images viewed from RD (b) and ND (c), where spots on the meridian suggest the presence of periodically stacked structures along both RD and ND. A schematic illustration of the orientation of nanocylinders in PCL-*b*-PS2 is given in **Figure 3.4**. The 2D-SAXS images of PCL/PS2 (d, e, f) are almost identical to those of PCL-*b*-PS2, indicating that the uniaxial orientation of nanocylinders is completely preserved after photocleavage. In addition, 2D-SAXS images of PCL-*b*-PS1, PCL/PS1, PCL-*b*-PS3, and PCL/PS3 (not shown) were qualitatively similar to those of PCL-*b*-PS2 and PCL/PS2, suggesting that

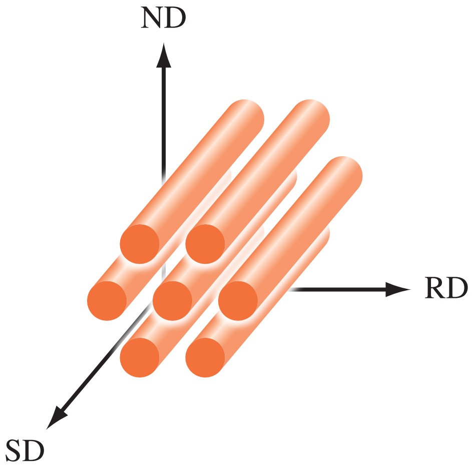

Figure 3.4. Schematic illustration showing the alignment of nanocylinders in shear-aligned PCL-*b*-PS and PCL/PS samples.

nanocylinders in these samples also had the uniaxial orientation described in **Figure 3.4**.

3.3.2 Crystal Orientation of PCL Chains

Figure 3.5 shows 2D-WAXD patterns of shear-aligned PCL-*b*-PS and PCL/PS samples viewed from ND, SD being parallel to the equator and RD the meridian. The samples were crystallized at −40 °C for sufficiently long time prior to the measurement, except for PCL-*b*-PS1 which was crystallized at −44 °C since the crystallization at −40 °C did not complete in a reasonable time. Two diffraction rings, the stronger one at a lower angle and the weaker one at a higher angle, are observed, which can be assigned to the (110) and (200) reflections of PCL crystals, respectively, using the literature data of the unit cell of PCL crystals. An orthorhombic crystal system with $a = 0.747$ nm, $b = 0.498$ nm, and $c = 1.705$ nm of PCL crystals[29] gives the (110) reflection at $2\theta = 21.41°$ and the (200) reflection at $2\theta = 23.76°$ with CuKα X-ray. Other reflections in the 2θ range covered by the 2D-WAXD measurements cannot be observed presumably because of low structure factor of these reflections and small total volume fraction of PCL crystals (~ 0.1) in the samples.

It is readily noticeable that the (110) reflection in PCL-*b*-PS1 (**Figure 3.5**a) and

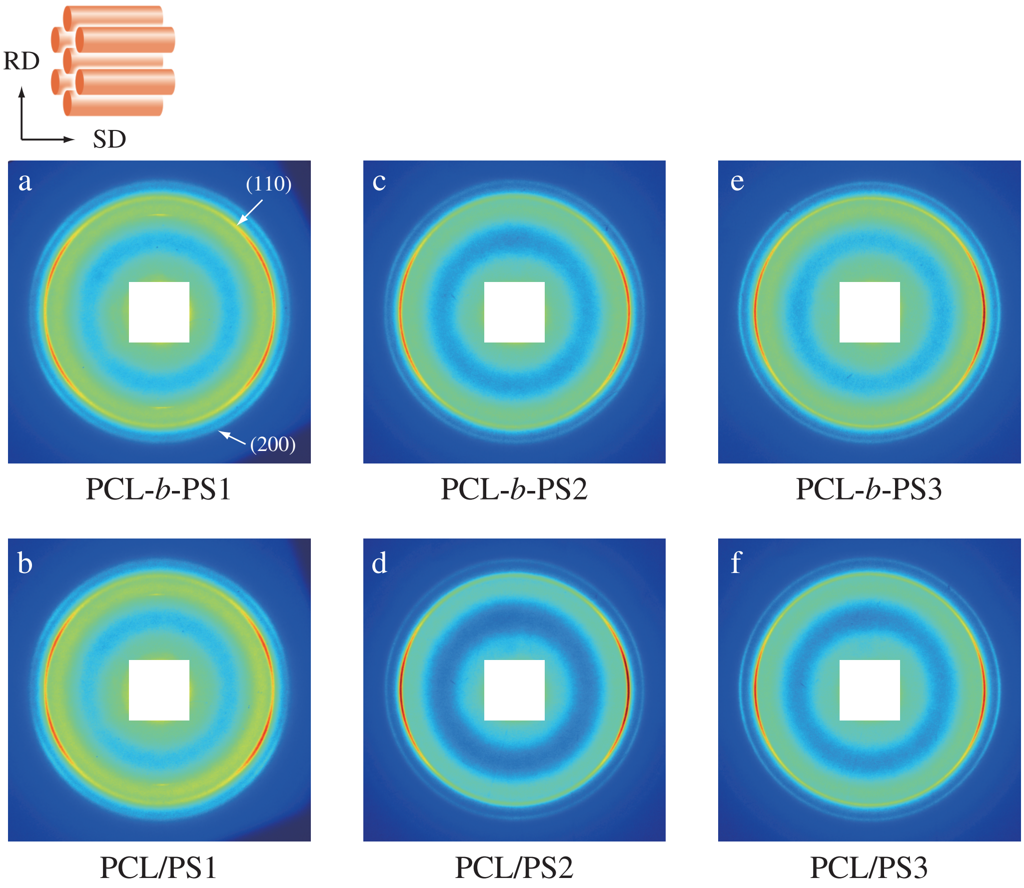

Figure 3.5. 2D-WAXD images of PCL-*b*-PS1 (a), PCL/PS1 (b), PCL-*b*-PS2 (c), PCL/PS2 (d), PCL-*b*-PS3 (e), and PCL/PS3 (f) sufficiently crystallized at −40 °C (or -44 °C for PCL-*b*-PS1). Incident X-ray beam was parallel to ND, and the equatorial and meridional directions of the images correspond to SD and RD, respectively. The (110) and (200) reflections are indicated by white arrows in panel a.

PCL/PS1 (b) forms an arc in each quadrant, which suggests that (110) plane normals have some preferential orientation around SD axis. On the other hand, the (110) reflection in PCL-*b*-PS2 (c), PCL/PS2 (d), PCL-*b*-PS3 (e), and PCL/PS3 (f) is concentrated around the equator, implying that the orientation of PCL crystals in these samples is different from that in PCL-*b*-PS1 and PCL/PS1. For a quantitative analysis on the orientation of PCL crystals, intensities of (110) and (200) reflections were evaluated as a function of azimuthal angle φ. The analysis method is illustrated in **Figure 3.6** taking PCL-*b*-PS2 crystallized at −40 °C (**Figure 3.5**c) as an example. Here φ is defined so that the right side of the equator in the 2D-WAXD image corresponds to $\varphi = 0$ from which φ counts

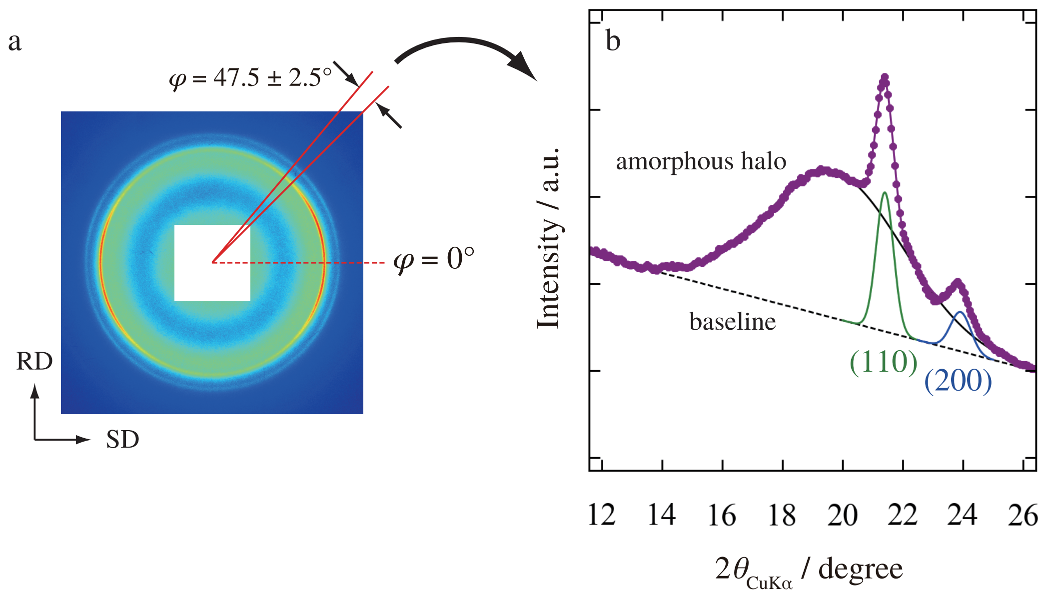

Figure 3.6. 2D-WAXD image (a) and sector-averaged 1D-WAXD curve (b) of PCL-*b*-PS2 crystallized at −40 °C, viewed from ND. The image in panel a is a reproduction of **Figure 3.5**c. The data points in panel b were obtained by azimuthal averaging of intensity in sector $\varphi = 42.5 \pm 2.5°$ (indicated by solid red lines in panel a), and solid curves represent the results of peak deconvolution.

up counterclockwise. A 5°-wide sector (**Figure 3.6**a) is circularly averaged to give a one-dimensional WAXD curve (b). Areas of the (110) and (200) peaks are then extracted by fitting the WAXD curve with three Gaussian functions, each corresponding to the amorphous halo, (110) reflection, and (200) reflection, respectively.

Figure 3.7 shows the integral intensity of the (110) (a) and (200) (b) reflections plotted against azimuthal angle φ. The azimuthal profiles of the (110) reflection drastically change from sample to sample: a set of two symmetrical peaks around $\varphi = 0°$ observed in PCL-*b*-PS1 and PCL/PS1 moves toward $\varphi = 0°$ in PCL-*b*-PS2 and PCL-*b*-PS2, and then merges into a single broad peak in PCL-*b*-PS3 and PCL/PS3. The φ-profiles of the (200) reflection also vary accordingly. Broad peaks centered around $\varphi = 90°$ and $-90°$ are present in PCL-*b*-PS1 and PCL/PS1, whereas they are smeared in PCL-*b*-PS2 and PCL/PS2. The profile for PCL-*b*-PS3 and PCL/PS3 is almost featureless. Qualitatively, these results indicate that the crystal orientation in PCL block chains and

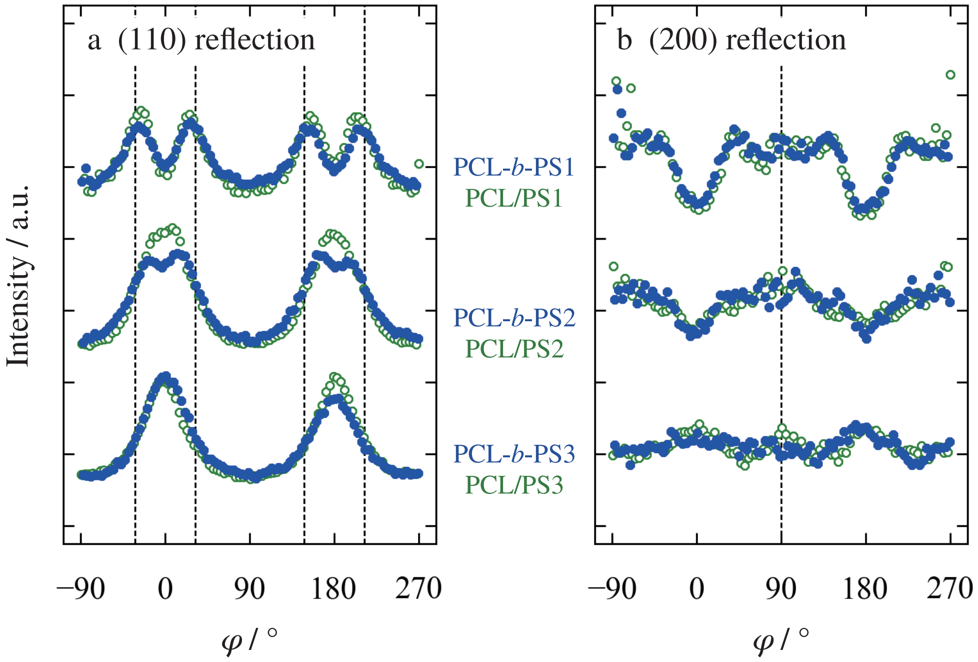

Figure 3.7. Azimuthal intensity profiles of the (110) (a) and (200) (b) reflections from the PCL crystals in each sample. The crystallization temperature was −40 °C for all the samples except for PCL-*b*-PS1 which was crystallized at −44 °C. Vertical dashed lines indicate the peak positions predicted by assuming that the *b* axis of PCL crystals orients parallel to the nanocylinder axis.

PCL homopolymers significantly depends on the nanocylinder diameter *D*. In the next section, the crystal orientation is analysed in detail on the basis of **Figure 3.7**.

3.3.3 Analysis of Crystal Orientation

The origin of the characteristic *φ*-profiles of PCL-*b*-PS1 and PCL/PS1 has already been explained in the previous study[30], but it is discussed here again for the sake of comparison with the other samples. **Figure 3.8**a illustrates the crystal orientation in PCL-*b*-PS1 and PCL/PS1 derived from the azimuthal profiles. If it is assumed that the *b* axis of PCL crystals orient parallel to the nanocylinder axis, (110) plane normals of PCL crystals tilt by 33.7° with respect to the nanocylinder axis (**Figure 3.8**a, top). Since the system has a rotational symmetry around the nanocylinder axis, (110) plane normals should be distributed uniformly around the nanocylinder axis (a, middle), which will give four arcs in the WAXD image (a, bottom). The actual peak position on the azimuthal

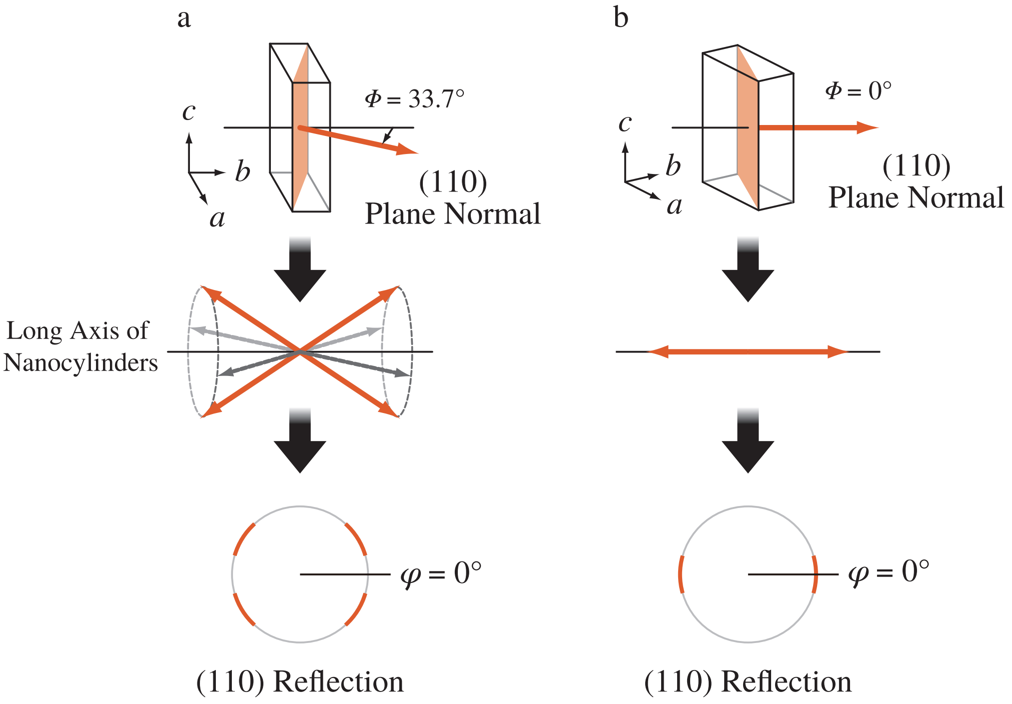

Figure 3.8. Schematic illustration of crystal orientation in PCL-*b*-PS1 and PCL/PS1 (a) and PCL-*b*-PS3 nad PCL/PS3 (b) proposed on the basis of **Figure 3.7**. The orientation of the *b* axis and (110) plane normals (top) is uniformly distributed around the nanocylinder axis (middle) to give the corresponding (110) reflection arcs (bottom).

profile is slightly different from the tilt angle of the plane normal Φ and is calculated by

$$\cos\varphi = \frac{\cos\Phi}{\cos\theta} \tag{3.1}$$

where 2θ is the scattering angle corresponding to the plane of interest. According to this relation, (110) plane normals tilting by 33.7° should yield four peaks at $\varphi = -32.1$, 32.1, 147.9, and 212.1°, the positions of which are marked with dashed lines in **Figure 3.7**a. The four peaks of PCL-*b*-PS1 and PCL/PS1 roughly match with the prediction. In addition, (200) plane normals should give two peaks at $\varphi = -90$ and 90° under the above assumption, which are actually observed in **Figure 3.7**b. These facts suggest that the crystal of PCL block chains and PCL homopolymers in nanocylinders with $D = 13.0$ nm grew one-dimensionally along the nanocylinder axis, extending its dimension along the *b* axis. Similar crystal orientation is reported for PCL block chains confined in nanocylinders formed in PCL-*b*-P4VP[14] and syndiotactic PS homopolymers confined in nanopores of AAO templates[9]. Considering that the *b* axis is the fastest growth axis in PCL crystals[31], it is speculated that spatial restriction in the radial direction of nanocylinders kinetically favors the crystal growth along the nanocylinder axis and excludes the growth along off-axis directions, thereby yielding the particular orientation of the crystals. It should also be noted that PCL/PS1 exhibits slightly sharper peaks in the azimuthal profile than PCL-*b*-PS1, suggesting that the favorable crystal growth is hindered by chain confinement. This would reduce the lateral dimension of PCL crystals and hence the crystallinity, as was observed in Chapter 2.

In contrast to PCL-*b*-PS1 and PCL/PS1, the intensity of the (110) reflection in PCL-*b*-PS3 and PCL/PS3 (**Figure 3.7**a) concentrates at $\varphi = 0$ and 90°. This can be explained by assuming that (110) plane normals of PCL crystals lie parallel to the nanocylinder axis, as is schematically illustrated in **Figure 3.8**b. Although (200) plane normals in this case will tilt against the nanocylinder axis by $\Phi = 56.3^\circ$ and exhibit four peaks at $\varphi = -52.7$, 52.7, 127.3, and 232.7°, the azimuthal profile of the (200) reflection (**Figure 3.7**b) shows no peak, presumably because the orientation of the crystals is poor. This particular crystal orientation suggests that in nanocylinders with $D = 17.9$ nm, PCL crystals can grow not only along the *b* axis but also along the *a* axis, that is, the crystal growth is two-dimensional. The looser spatial restriction in larger nanocylinders would allow the two-dimensional crystal growth in order to increase the lateral dimension of the crystal and hence the overall crystallinity X_c. The tilting of the crystallographic axis with respect to the nanocylinder axis was also reported by Huang and coworkers[19], who investigated the crystal orientation of PEO block chains confined in nanocylinders using a shear-aligned PEO-*b*-PS/PS blend. They found that the *c* axis (chain direction) tilted 90°against the nanocylinder axis at $T_c \geq 2$ °C, whereas the tilt angle gradually decreased on lowering T_c down to $T_c = -30$ °C. However, the 2D-WAXD images obtained in this study cannot be explained by the tilting of the *c* axis, because that would shift the (110) reflection toward the meridian. The difference between the azimuthal profiles of

PCL-*b*-PS3 and PCL/PS3 in **Figure 3.7** is negligible, suggesting that the effects of chain confinement on the crystal growth are insignificant in relatively large nanocylinders. The result is consistent with the fact that the crystallinity of PCL chains in PCL-*b*-PS3 and PCL/PS3 shows no significant difference (see **Figure 2.6** in Chapter 2).

Figure 3.7a shows that the azimuthal profile of the (110) reflection from PCL-*b*-PS2 contains four peaks, though their positions are clearly shifted toward $\varphi = 0$ and 180° compared to those of PCL-*b*-PS1 and PCL/PS1. The shift is even larger for PCL/PS2, where two peaks around $\varphi = 0^\circ$ (and 180°) get so close that they almost merge into one peak. There are two possible explanations for this behavior. One is that the PCL crystals grown in the two modes proposed in **Figure 3.8** coexist in one sample, which would give the superposition of the azimuthal profiles of PCL-*b*-PS1 and PCL-*b*-PS3. The other is that the crystal growth along the a axis gradually becomes possible with increasing D, which would render both the b axis and (110) plane normals tilted against the nanocylinder axis. It will be necessary to observe more independent reflections other than the (110) and (200) reflections to uniquely specify the crystal orientation modes in nanocylinders with $D = 14.9$ nm, which may be achieved with the aid of a synchrotron light source.

The proposed growth modes in smaller ($D = 13.0$ nm) and larger ($D = 17.9$ nm) nanocylinders are schematically described in **Figure 3.9**. In summary, PCL crystals in nanocylinders with $D = 13.0$ nm (a) grow one-dimensionally along the nanocylinder axis and the growth direction is parallel to the b axis. On the other hand, the growth of PCL crystals in nanocylinders with $D = 17.9$ nm (b) is two-dimensional with (110) plane normals parallel to the nanocylinder axis. The larger free space available in nanocylinders with $D = 17.9$ nm would increase the lateral size of the PCL crystals. In both cases, the effects of chain confinement are insignificant compared to those of space confinement. The growth mode of PCL crystals in nanocylinders with $D = 14.9$ nm is either a superposition of the two growth modes (a and b) or an intermediate between them.

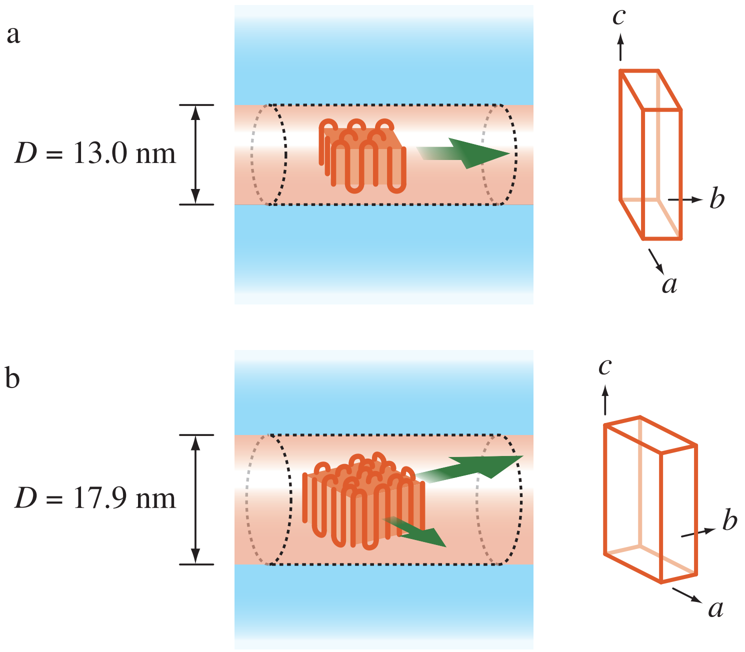

Figure 3.9. Schematic illustration of PCL crystals and their orientation in nanocylinders with $D = 13.0$ nm (a) and 17.9 nm (b).

3.4 Conclusions

The crystal orientation of PCL homopolymers and PCL block chains confined in nanocylinders with the diameter $D = 13.0$, 14.9, and 17.9 nm was examined. Nanocylinders formed in PCL-*b*-PS diblock copolymers were macroscopically aligned by a rotational shear flow, as confirmed by 2D-SAXS measurements.

Both space confinement and chain confinement affected the crystal orientation, although the former was found to overwhelm the latter. In nanocylinders with $D = 13.0$ nm, the *b* axis of PCL crystals oriented parallel to the nanocylinder axis, suggesting a one-dimensional crystal growth along the nanocylinder axis. The degree of orientation was slightly better in PCL homopolymers than in PCL block chains, indicating that the chain confinement interrupted the crystal growth along the nanocylinder axis. However, the *b* axis of PCL crystals in nanocylinders with $D = 17.9$ nm tilted against the nanocylinder axis, suggesting that PCL crystals grew not only along the *b* axis but also along the *a* axis, from which a two-dimensional crystal growth could be speculated. This would increase the lateral size of PCL crystals and hence enhance the overall crystallinity. Chain confinement had almost no effects on the crystal orientation in nanocylinders with $D = 17.9$ nm. The crystal orientation in nanocylinders with $D = 14.9$ nm was ambiguous. One possibility is that (110) plane normals slightly tilted against the nanocylinder axis, meaning that the growth along the *a* axis was partially permitted. The other possibility is that the one-dimensionally grown crystals and two-dimensionally grown ones coexisted in one sample.

References

1. He, W.-N.; Xu, J.-T. *Progress in Polymer Science* **2012**, *37*, 1350–1400.
2. Lin, M.-C.; Nandan, B.; Chen, H.-L. *Soft Matter* **2012**, *8*, 7306–7322.
3. Carr, J. M.; Langhe, D. S.; Ponting, M. T.; Hiltner, A.; Baer, E. *Journal of Materials Research* **2012**, *27*, 1326–1350.
4. Michell, R. M.; Blaszczyk-Lezak, I.; Mijangos, C.; Müller, A. J. *Journal of Polymer Science Part B: Polymer Physics* **2014**, *52*, 1179–1194.
5. Steinhart, M.; Senz, S.; Wehrspohn, R. B.; Go, U.; Wendorff, J. H. *Macromolecules* **2003**, *36*, 3646–3651.
6. Steinhart, M.; Goering, P.; Dernaika, H.; Prabhukaran, M.; Goesele, U.; Hempel, E.; Thurn-Albrecht, T. *Physical Review Letters* **2006**, *97*, 027801.
7. Shin, K.; Woo, E.; Jeong, Y. G.; Kim, C.; Huh, J.; Kim, K.-W. *Macromolecules* **2007**, *40*, 6617–6623.
8. Wu, H.; Wang, W.; Yang, H.; Su, Z. *Macromolecules* **2007**, *40*, 4244–4249.
9. Wu, H.; Wang, W.; Huang, Y.; Su, Z. *Macromolecular Rapid Communications* **2009**, *30*, 194–198.
10. Guan, Y.; Liu, G.; Gao, P.; Li, L.; Ding, G.; Wang, D. *ACS Macro Letters* **2013**, *2*, 181–184.
11. Guan, Y.; Liu, G.; Ding, G.; Yang, T.; Müller, A. J.; Wang, D. *Macromolecules* **2015**, *48*, 2526–2533.
12. Quiram, D. J.; Register, R. A.; Marchand, G. R.; Adamson, D. H. *Macromolecules* **1998**, *31*, 4891–8.
13. Huang, P.; Guo, Y.; Quirk, R. P.; Ruan, J.; Lotz, B.; Thomas, E. L.; Hsiao, B. S.; Avila-Orta, C. A.; Sics, I.; Cheng, S. Z. D. *Polymer* **2006**, *47*, 5457–5466.
14. Chung, T.-M.; Wang, T.-C.; Ho, R.-M.; Sun, Y.-S.; Ko, B.-T. *Macromolecules* **2010**, *43*, 6237–6240.

15. Nojima, S.; Ohguma, Y.; Kadena, K.-i.; Ishizone, T.; Iwasaki, Y.; Yamaguchi, K. *Macromolecules* **2010**, *43*, 3916–3923.

16. Nakagawa, S.; Kadena, K.-i.; Ishizone, T.; Nojima, S.; Shimizu, T.; Yamaguchi, K.; Nakahama, S. *Macromolecules* **2012**, *45*, 1892–1900.

17. Hamley, I. W.; Fairclough, J. P. A.; Ryan, A. J.; Bates, F. S.; Towns-Andrews, E. *Polymer* **1996**, *37*, 4425–4429.

18. Zhu, L.; Cheng, S. Z. D.; Calhoun, B. H.; Ge, Q.; Quirk, R. P.; Thomas, E. L.; Hsiao, B. S.; Yeh, F.; Lotz, B. *Journal of the American Chemical Society* **2000**, *122*, 5957–5967.

19. Huang, P.; Zhu, L.; Cheng, S. Z. D.; Ge, Q.; Quirk, R. P.; Thomas, E. L.; Lotz, B.; Hsiao, B. S.; Liu, L.; Yeh, F. *Macromolecules* **2001**, *34*, 6649–6657.

20. Huang, P.; Zhu, L.; Guo, Y.; Ge, Q.; Jing, A. J.; Chen, W. Y.; Quirk, R. P.; Cheng, S. Z. D.; Thomas, E. L.; Lotz, B.; Hsiao, B. S.; Avila-Orta, C. A.; Sics, I. *Macromolecules* **2004**, *37*, 3689–3698.

21. Sun, Y.-S.; Chung, T.-M.; Li, Y.-J.; Ho, R.-M.; Ko, B.-T.; Jeng, U.-S.; Lotz, B. *Macromolecules* **2006**, *39*, 5782–5788.

22. Sun, Y.-S.; Chung, T.-M.; Li, Y.-J.; Ho, R.-M.; Ko, B.-T.; Jeng, U.-S. *Macromolecules* **2007**, *40*, 6778–6781.

23. Myers, S. B.; Register, R. A. *Macromolecules* **2010**, *43*, 393–401.

24. Lin, M.-C.; Wang, Y.-C.; Chen, H.-L.; Müller, A. J.; Su, C.-J.; Jeng, U.-S. *Journal of Physical Chemistry B* **2011**, *115*, 2494–2502.

25. Liu, C.-L.; Lin, M.-C.; Chen, H.-L.; Müller, A. J. *Macromolecules* **2015**, *48*, 4451–4460.

26. Beckingham, B. S.; Register, R. A. *Macromolecules* **2013**, *46*, 3486–3496.

27. Ho, R.-M.; Lin, F.-H.; Tsai, C.-C.; Lin, C.-C.; Ko, B.-T.; Hsiao, B. S.; Sics, I. *Macromolecules* **2004**, *37*, 5985–5994.

28. Li, M.-C.; Chang, G.-W.; Lin, T.; Ho, R.-M.; Chuang, W.-T.; Kooi, S. *Langmuir* **2010**, *26*, 17640–8.

29. Chatani, Y.; Yasuo, O.; Tadokoro, H.; Yamashita, Y. *Polymer Journal* **1970**, *1*, 555–562.

30. Nojima, S.; Ohguma, Y.; Namiki, S.; Ishizone, T.; Yamaguchi, K. *Macromolecules* **2008**, *41*, 1915–1918.

31. Beekmans, L. G. M.; Vancso, G. J. *Polymer* **2000**, *41*, 8975–8981.

Chapter 4

Crystallization of Homopolymer/Block Chain Blends Confined in Nanocylinders

4.1 Introduction

Blending chemically different polymers is a convenient method to create polymeric materials having desirable properties. Particularly, binary blends of A-B diblock copolymers and A homopolymers are interesting because the resulting morphology can be controlled by the molecular weight ratio of A homopolymers and A block chains as well as blend composition. The phase behavior of A-B diblock copolymer/A homopolymer blends has been extensively studied both experimentally[1–14] and theoretically[15–17]. It is now well known that A homopolymers significantly shorter than A block chains are incorporated in nanodomains of A block chains to form a miscible homopolymer/block chain blend. Inclusion of A homopolymers into nanodomains also takes place when the molecular weight of A homopolymers and A block chains is comparable, though A homopolymers do not thoroughly mix with A block chains, resulting in the aggregation of A homopolymers near the center of the nanodomain. Crystallization of homopolymer/block chain blends confined in nanodomains is interesting because two kinds of polymer chains with different mobilities can interactively crystallize in the same nanodomain. This means that the effects of fixing chain-ends onto nanodomain interfaces (*chain confinement*) can possibly be regulated. Although the crystallization of binary blends of crystalline-amorphous block copolymers and crystalline homopolymers has been extensively studied[18–31], reports on the crystallization of homopolymer/block chain blends completely confined in microphase-separated structure are somewhat limited[20,26,28,29,31]. For example, Yu and coworkers[31] studied the crystallization of binary blends of PVCH-*b*-PE-*b*-PVCH triblock copolymers and PE homopolymers, where PE block chains tethered at both ends and PE homopolymers were confined in cylindrical nanodomains (nanocylinders). They argued that PE homopolymers and PE block chains crystallized separately, and found that the melting temperature of PE block chains increased with increasing the amount of PE homopolymers, while that of PE homopolymers was constant irrespective of the blend composition.

However, blending diblock copolymers with homopolymers inevitably leads to expansion of nanodomains, which makes it difficult to distinguish the effects of chain confinement from those by spatial restriction imposed by nanodomains (*space confinement*). In other words, the composition dependence of the crystallization behavior of homopolymer/block chain blends can only be observed when the blends are confined in an identical nanodomain. In Chapters 2 and 3, the author investigated the crystallization behavior and crystal orientation of PCL homopolymers and PCL block chains confined in an identical nanocylinder and found that the effects of chain confinement drastically varied with the nanocylinder diameter D. It is expected that the application of the same method to the study of homopolymer/block chain blends allows for decoupling of the effects of two parameters, namely the nanodomain size and blend composition, and leads to a better understanding of the effects of chain confinement and space confinement on crystallization. In this Chapter, the author investigates the crystallization behavior of PCL homopolymer/PCL block chain blends confined in an identical nanocylinder as a function of both the blend composition and nanocylinder diameter in order to gain insights on the combined effects of chain confinement and space confinement on polymer crystallization.

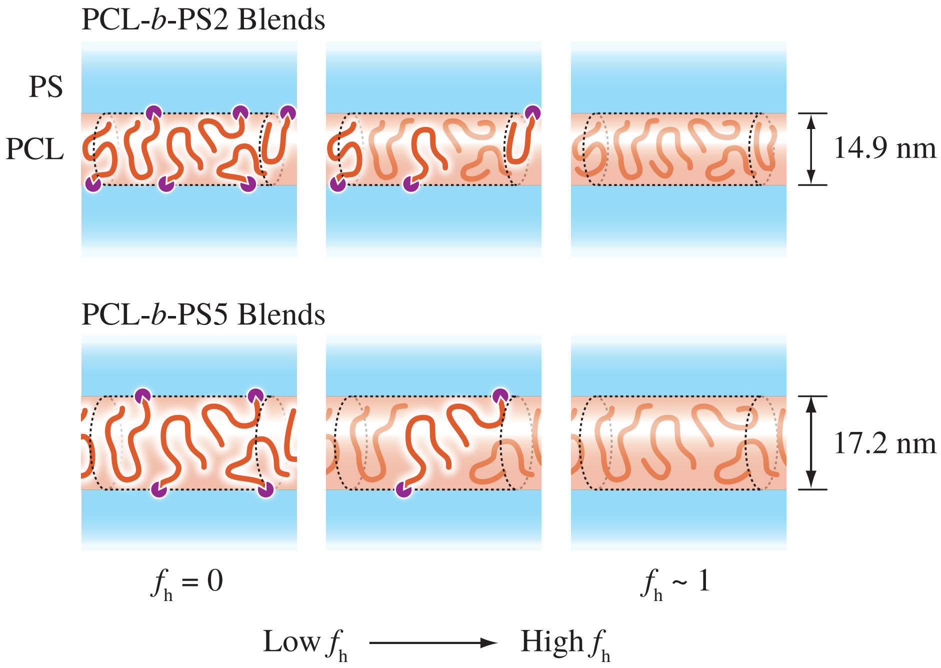

Figure 4.1. Schematic illustration showing the PCL homopolymer/PCL block chain blends confined in nanocylinders with $D = 14.9$ (upper) and 17.2 nm (lower).

4.2 Experimental

4.2.1 Model Systems

Figure 4.1 schematically illustrates the model systems used in this study. PCL homopolymer/PCL block chain blends are confined in nanocylinders formed by microphase separation of PCL-*b*-PS diblock copolymers. The blend composition is parametrized by the mole fraction of PCL homopolymers f_h in all PCL chains in the system (i.e., PCL homopolymers and PCL block chains), where low f_h means the abundance of PCL block chains (**Figure 4.1**, left) and high f_h the abundance of PCL homopolymers (right). PCL-*b*-PS diblock copolymers having a photocleavable ONB at the block junction first microphase separate to form nanocylinders containing PCL block chains ($f_\mathrm{h} = 0$). Then ONB at the block junction is cleaved by UV irradiation to turn PCL block chains into PCL homopolymers. It is possible to prepare the blend with an arbitrary f_h by controlling

Table 4.1. Characterization of the samples used in this study.

Code	M_n / g mol^{-1}			M_w/M_n[b]	ϕ_{PCL}[d]	D[e] / nm	Highest f_h[f]
	PCL[a]	PS[b]	Total[c]				
PCL-*b*-PS2 [g]	9400	27900	37300	1.03	0.25	14.9	0.87
PCL-*b*-PS5	12000	36300	48300	1.03	0.20 [h]	17.2	0.97

[a] Determined by ^{1}H-NMR.
[b] Determined by GPC.
[c] Sum of M_ns of the PCL and PS blocks.
[d] Volume fraction of PCL chains calculated from M_ns and specific volumes of PCL and PS at 100 °C.
[e] Nanocylinder diameter calculated from the primary peak position in SAXS curves and volume fraction of PCL blocks.
[f] Highest mole fraction of PCL homopolymers in the system calculated from GPC chromatograms.
[g] Identical to PCL-*b*-PS2 used in Chapter 2.
[h] Volume fraction of PCL chains in a blend of PCL-*b*-PS and a small amount of PS homopolymers.

the time and intensity of UV irradiation. Moreover, using a PCL-*b*-PS diblock copolymer with a similar block composition but higher molecular weight allows for confining the blends in nanocylinders with a larger diameter D (**Figure 4.1**, lower).

4.2.2 Samples and Sample Preparation

Two PCL-*b*-PS diblock copolymers having ONB between PCL and PS blocks, PCL-*b*-PS2 and PCL-*b*-PS5, were used in this study, where the former was the same sample employed in Chapters 2 and 3 and the latter was newly synthesized according to the method described in Appendix A. The molecular characterization of PCL-*b*-PS5 is presented in **Table 4.1** along with that of PCL-*b*-PS2, which is reproduced from **Table 2.1** in Chapter 2 for clarity. The volume fraction of PCL chains ϕ_{PCL} is 0.25 for PCL-*b*-PS2 and 0.20 for PCL-*b*-PS5, from which the formation of cylindrical microphase-separated structures is expected. Unfortunately, PCL-*b*-PS5 was actually a blend of the PCL-*b*-PS diblock copolymer described in the table and a small amount of PS homopolymers with the same molecular weight as the PS block, since it was difficult to completely remove the PS homopolymer having a relatively high molecular weight from the crude product of PCL-

b-PS diblock copolymer. Therefore, ϕ_{PCL} corrected for the amount of PS homopolymers is presented in **Table 4.1** for PCL-*b*-PS5.

PCL homopolymer/PCL block chain blends were prepared by exposing solution-cast PCL-*b*-PS sample films to UV light with the intensity of 1.0 $\mathrm{W\,cm^{-2}}$ for a prescribed time. Five blends were prepared from each of PCL-*b*-PS2 and PCL-*b*-PS5 and denoted PCL-*b*-PS2 blends and PCL-*b*-PS5 blends, respectively. The values of f_{h} determined by GPC measurements were as follows: $f_{\mathrm{h}} = 0, 0.19, 0.38, 0.61, 0.87$ for PCL-*b*-PS2 blends and $f_{\mathrm{h}} = 0, 0.15, 0.42, 0.70, 0.97$ for PCL-*b*-PS5 blends. Detailed experimental methods of film preparation and UV irradiation were the same as those described in Section 2.2 of Chapter 2.

4.2.3 Measurements

The progress of photocleavage was monitored by gel permeation chromatography (GPC). The microphase-separated structures of the samples were investigated using small-angle X-ray scattering (SAXS). Differential scanning calorimetry (DSC) was employed to pursue the melting and crystallization behavior of the blend systems. The equipment and set-up for the measurements in this study were the same as those in Chapter 2, so details on GPC, SAXS, and DSC measurements can be found in Section 2.2.

4.3 Results and Discussion

4.3.1 Photocleavage Behavior

Figure 4.2 shows the GPC chromatograms of PCL-*b*-PS2 obtained after controlled UV irradiation with the intensity of 1.0 $\mathrm{W\,cm^{-2}}$ for 0 (i.e., before irradiation), 2.5, 6.7, and 80 min. It is clearly seen that peak intensity arising from PCL-*b*-PS diblock copolymers gradually decreases and two new peaks grow with increasing irradiation time. Judging from the molecular weight at the peak top, these two peaks correspond

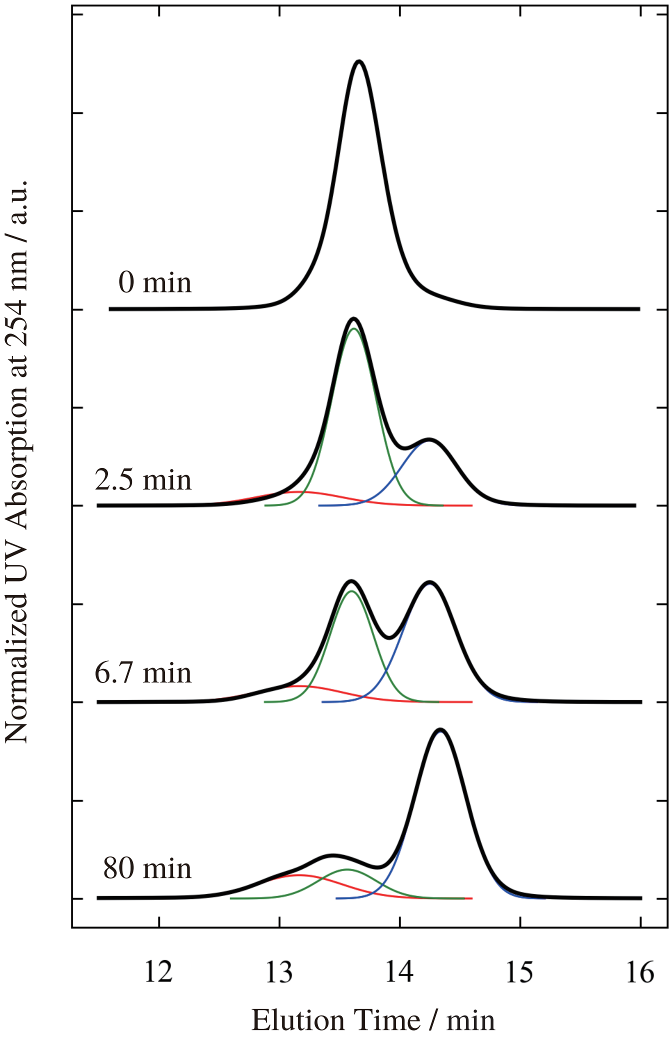

Figure 4.2. GPC chromatograms of PCL-*b*-PS2 after UV irradiation for 0, 2.5, 6.7, and 80 min with the intensity of 1.0 $\mathrm{W\,cm^{-2}}$ (black curves). Red, green, and blue curves indicate the results of peak deconvolution, each corresponding to dimerized PS homopolymers, unreacted PCL-*b*-PS, and PS homopolymers, respectively. The data at 0 and 80 min are reproduced from **Figure 2.3**.

to PS homopolymers (longer elution time) and dimerized PS homopolymers (shorter elution time), respectively. As was mentioned in Section 2.3.1 of Chapter 2, nitroso groups produced by photocleavage of ONB are known to dimerize[32], which should be responsible for the appearance of dimerized PS homopolymers in the chromatograms.

The mole fraction of PCL homopolymers f_h in all PCL chains (i.e., PCL homopolymers and PCL block chains) was calculated from the result of peak deconvolution, which is shown in **Figure 4.2** with colored curves, following the method described in

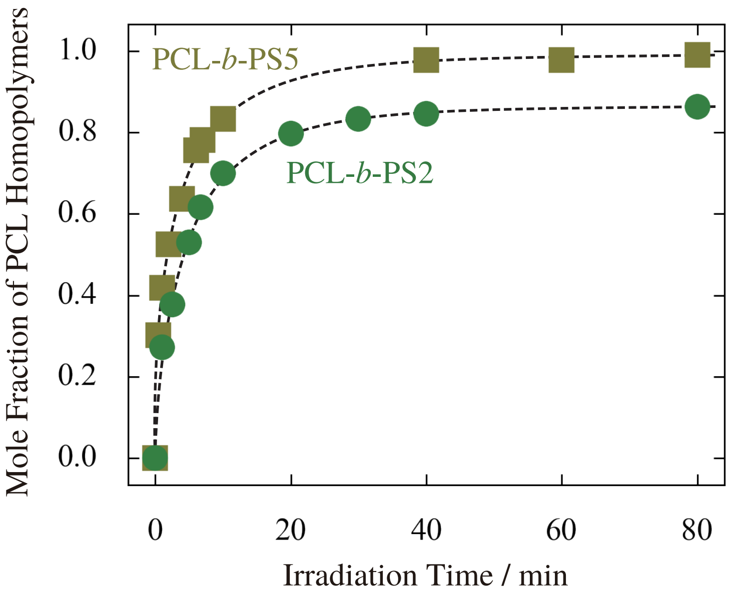

Figure 4.3. The mole fraction of PCL homopolymers f_{h} during UV irradiation with the intensity of 1.0 $\mathrm{W\,cm^{-2}}$ plotted against UV irradiation time for PCL-*b*-PS2 (circles) and PCL-*b*-PS5 (squares). Dahsed curves are just a guide for the eye.

Section C.2 of Appendix C. **Figure 4.3** shows f_{h} of PCL-*b*-PS2 and PCL-*b*-PS5 plotted against the UV irradiation time. For both PCL-*b*-PS2 (circles) and PCL-*b*-PS5 (squares), f_{h} changes continuously with the irradiation time, ensuring that PCL homopolymer/PCL block chain blends with arbitrary f_{h} can be prepared by adjusting the irradiation time. f_{h} rises rapidly at the beginning of UV irradiation and later asymptotically increases to reach a final value, suggesting the first-order nature of the reaction kinetics. Although the rate of photocleavage reaction is almost the same, the final f_{h} in PCL-*b*-PS2 is moderately lower than that in PCL-*b*-PS5. This is probably due to a slightly incomplete introduction of ONB in the course of synthesis of PCL-*b*-PS2. The UV irradiation time for preparation of PCL-*b*-PS2 blends and PCL-*b*-PS5 blends was determined on the basis of the data in **Figure 4.3**.

4.3.2 Microphase-separated Structure

SAXS curves of PCL-*b*-PS2 and PCL-*b*-PS5 are shown in **Figure 4.4**a and b, respectively, in the crystallized (solid blue curves) and amorphous state (dashed curves). The

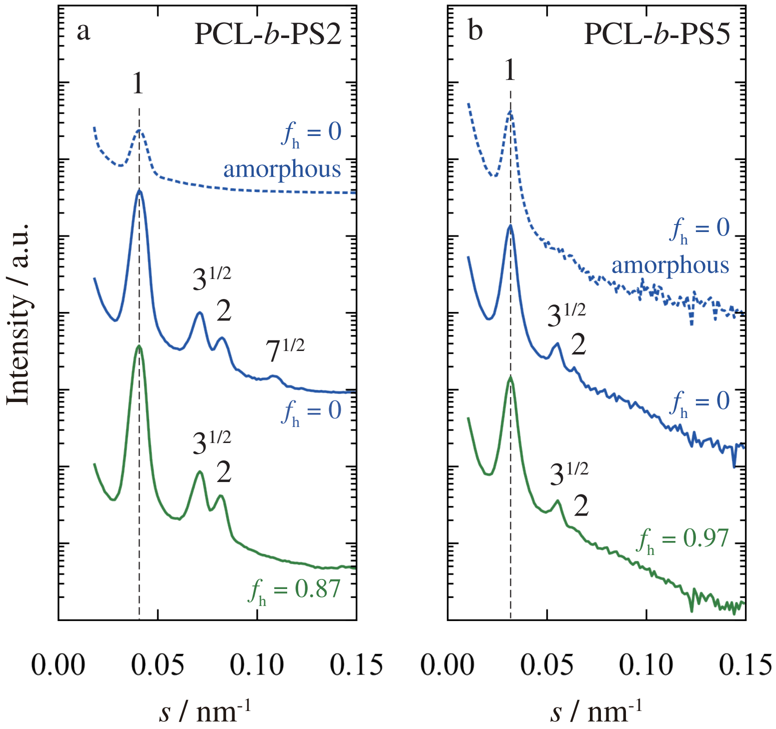

Figure 4.4. SAXS curves of crystallized PCL-*b*-PS2 (a) and PCL-*b*-PS5 (b) before (blue solid curves) and after UV irradiation for a sufficiently long time (green solid curves). The data with amorphous PCL chains are also shown in dashed curves. The curves in panel a are reproduced from **Figure 2.4**b. Vertical dashed lines indicate the primary peak positions.

data for PCL-*b*-PS2 were already presented in **Figure 2.4**b, but are reproduced here just for consistency. SAXS curves of both PCL-*b*-PS2 and PCL-*b*-PS5 in the crystallized state have a sharp primary peak and multiple higher order peaks at the positions exactly corresponding to a ratio of $1 : \sqrt{3} : 2(: \sqrt{7})$, indicating the formation of a hexagonally-packed cylindrical microphase-separated structure (nanocylinder). It can be judged from ϕ_{PCL} of the samples that PCL chains are confined in nanocylinders surrounded by a matrix of PS chains. Moreover, the primary peak positions in the crystallized state do not move from those in the amorphous state for both PCL-*b*-PS2 and PCL-*b*-PS5. This fact strongly suggests that the crystallization and melting of PCL chains in these samples take place without destroying the nanocylinder structure. A lack of higher order peaks in the amorphous state can be attributed to the change in electron density difference between PCL and PS domains upon the melting of PCL crystals, as was discussed in

Section 2.3.2 (Chapter 2). The SAXS curves of PCL-*b*-PS2 and PCL-*b*-PS5 after UV irradiation (i.e., $f_\mathrm{h} \sim 1$) and subsequent crystallization are almost identical to those before UV irradiation, indicating that the nanocylinders are completely preserved even after the photocleavage of block junctions. The results of SAXS measurements are sufficient to confirm that PCL homopolymer/PCL block chain blends prepared from the same PCL-*b*-PS diblock copolymer are all confined in an identical nanocylinder, which is stable against the crystallization and melting of PCL chains.

The diameter of nanocylinders D can be calculated from the spacing of primary peak L and volume fraction of PCL chains ϕ_PCL by the following equation (see discussion in Section 2.3.2 of Chapter 2):

$$D = 2\left(\frac{2\phi_\mathrm{PCL}}{3^{1/2}\pi}\right)^{1/2} L \tag{2.1}$$

The value of D is evaluated to be 14.9 nm for PCL-*b*-PS2 and 17.2 nm for PCL-*b*-PS5, therefore, PCL chains in PCL-*b*-PS2 blends are all confined in nanocylinders with $D = 14.9$ nm, and those in PCL-*b*-PS5 blends in nanocylinders with $D = 17.2$ nm.

4.3.3 Melting Behavior of the Blends

The final melting temperature T_m and crystallinity X_c of the blends after isothermal crystallization at a prescribed temperature T_c were determined using DSC. **Figure 4.5** shows T_m (a) and X_c (b) at $T_\mathrm{c} = -40$ °C as a function of f_h for PCL-*b*-PS2 blends (circles) and PCL-*b*-PS5 blends (squares). It should be noted that DSC heating scans on the melting of PCL crystals (not shown) contain only a single peak for all the blends, suggesting that the PCL homopolymers and PCL block chains in the blends do not crystallize separately but rather co-crystallize without discriminating each other. This is also supported by the smooth change of T_m and X_c with f_h. Since T_m is generally related to the crystal thickness through the Gibbs-Thomson equation, information on the crystal thickness can be obtained from T_m data. It is clear from **Figure 4.5**a that

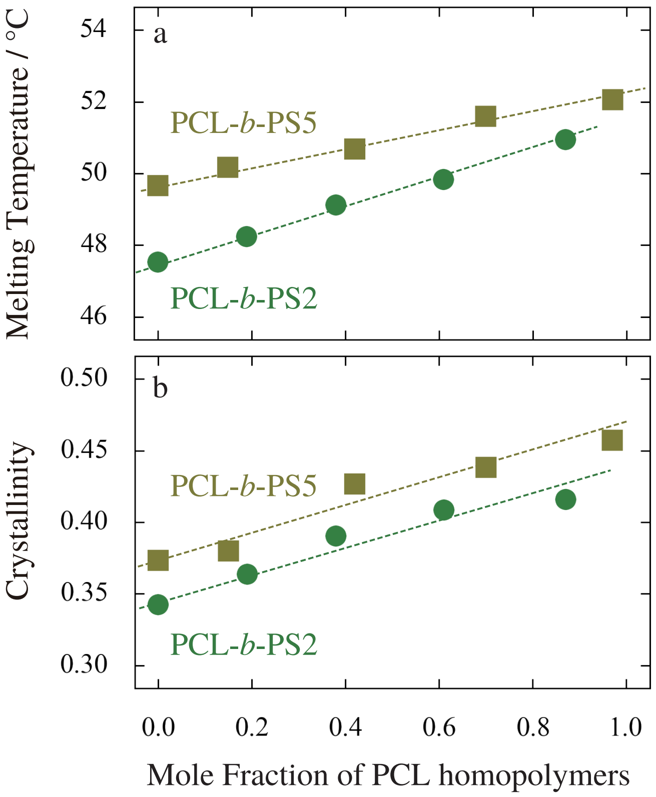

Figure 4.5. Final melting temperature T_m (a) and crystallinity X_c (b) of PCL crystals after isothermal crystallization at −40 °C plotted against the mole fraction of PCL homopolymers f_h for PCL-*b*-PS2 (circles) and PCL-*b*-PS5 (squares). Dashed lines are just a guide for the eye.

T_m of PCL-*b*-PS5 blends is always higher than that of PCL-*b*-PS2 blends, suggesting that the radial dimension of nanocylinders limits the thickening of PCL crystallites. T_m increases with increasing f_h, meaning that the crystal thickness increases with decreasing the amount of block chains. The change of X_c with D and f_h is qualitatively similar to that of T_m: PCL-*b*-PS5 blends show higher X_c than PCL-*b*-PS2 blends at every f_h, and X_c increases monotonously with increasing f_h in PCL-*b*-PS2 blends and PCL-*b*-PS5 blends.

The results presented above can be interpreted with the aid of the conclusions obtained in Chapters 2 and 3. Increasing D makes more free spaces available for both thickening and lateral growth of PCL crystals, and hence increases T_m and X_c. The reduction of T_m and X_c with decreasing f_h indicates that chain confinement hinders the thickening and lateral growth of PCL crystals, probably because PCL chains cannot take a favorable

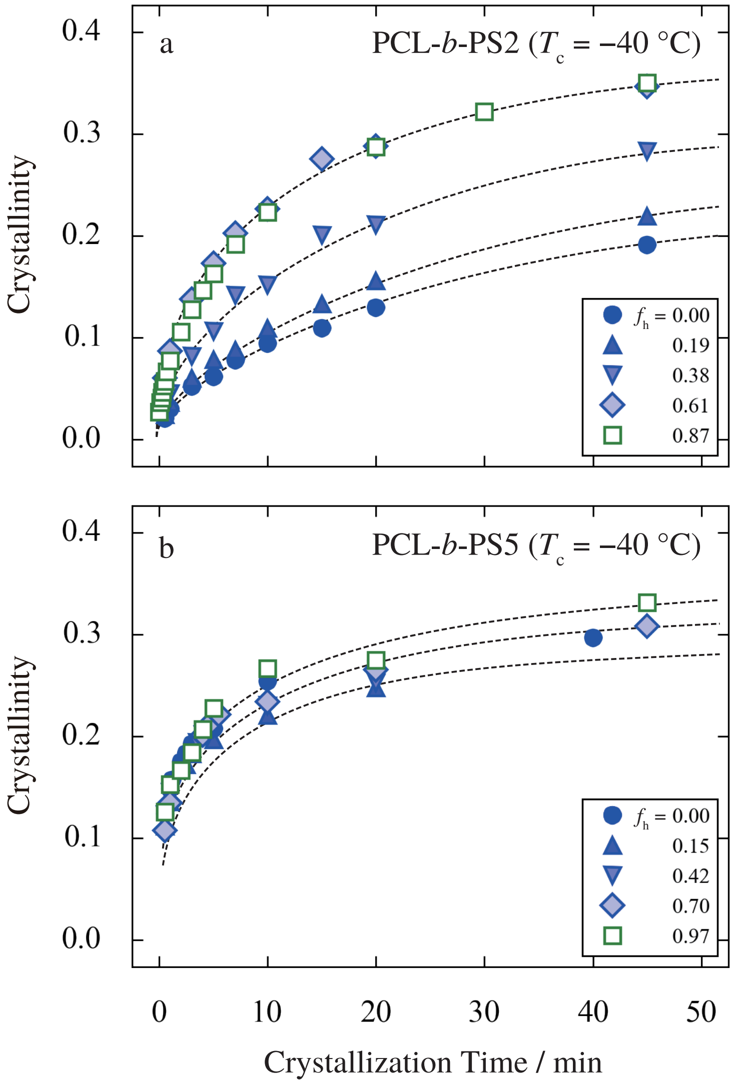

Figure 4.6. Time evolution of the crystallinity X_c of PCL chains in PCL-*b*-PS2 blends (a) and PCL-*b*-PS5 blends (b) during isothermal crystallization at −40 °C. Dashed curves are just a guide for the eye.

chain conformation to attain the optimal crystal thickness and size due to the reduced mobility by chain confinement.

4.3.4 Crystallization Kinetics of PCL-*b*-PS2 and PCL-*b*-PS5 Blends

Figure 4.6 shows the time development of the crystallinity X_c of PCL chains in PCL-*b*-PS2 blends (a) and PCL-*b*-PS5 blends (b) during isothermal crystallization at −40 °C. In all the blends, X_c starts to increase abruptly from time zero and then asymptotically reaches a final value, from which the crystallization kinetics is speculated to be controlled by homogeneous nucleation. It is clear that PCL block chains (i.e., $f_\mathrm{h} = 0$) in PCL-*b*-PS5 (**Figure 4.6**b, circles) crystallize faster than those in PCL-*b*-PS2 (a, circles), suggesting that the the chain mobility is significantly reduced in small nanocylinders. The influence of f_h on the crystallization behavior is different between PCL-*b*-PS2 blends and PCL-*b*-PS5 blends. For PCL-*b*-PS2 blends, the crystallization appears to be accelerated with increasing f_h, whereas the effect of f_h is less significant in the PCL-*b*-PS5 blends. This difference in the f_h-dependence between PCL-*b*-PS2 blends and PCL-*b*-PS5 blends means that the effects of chain confinement change with D, which is consistent with the conclusion of Chapter 2.

Crystallization kinetics of the blends was further examined using the Avrami equation[33,34]

$$\log(-\ln(1-\tilde{X}_\mathrm{c}(t))) = n\log t + \log K \tag{4.1}$$

where $\tilde{X}_\mathrm{c}$ is the normalized crystallinity calculated by dividing X_c by its final value, n the Avrami exponent, and K the rate constant. **Figure 4.7** shows a plot of $\log(-\ln(1-\tilde{X}_\mathrm{c}(t)))$ against $\log t$ (Avrami plot) for PCL-*b*-PS2 blends (a) and PCL-*b*-PS5 blends (b) with selected values of f_h. Good linearity is seen in all the samples, and the Avrami exponent n, which is equal to the slope of linear fitting, is less than unity for all the blends ($n \sim 0.6$ for PCL-*b*-PS2 blends and $n \sim 0.3$ for PCL-*b*-PS5 blends). The observed near-unity Avrami exponent strongly suggests that the crystallization of PCL-*b*-PS2 blends and PCL-*b*-PS5 blends obeys first-order-like kinetics where homogeneous nucleation is the only rate-determining step, though the origin of n values close to 1/2 is not clear.

The crystallization rate was quantitatively evaluated by the crystallization half time $t_{1/2}$, which is defined as the crystallization time required to attain half of the final X_c and calculated from the results of linear fitting in **Figure 4.7**. **Figure 4.8** shows a semi-log plot of $t_{1/2}$ at $T_\mathrm{c} = -40$ °C as a function of f_h for PCL-*b*-PS2 blends (circles) and

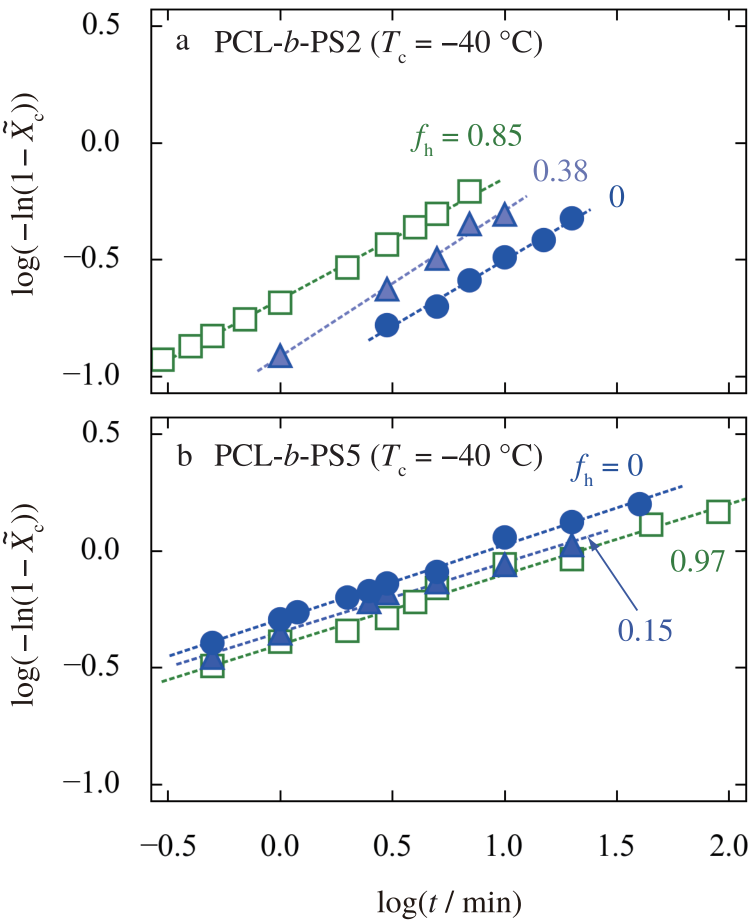

Figure 4.7. Avrami plots for the isothermal crystallization of PCL-*b*-PS2 blends (a) and PCL-*b*-PS5 blends (b) at −40 °C. Only the data for representative values of f_h are shown. Dashed lines indicate the results of linear fitting.

PCL-*b*-PS5 blends (squares). $t_{1/2}$ of PCL-*b*-PS2 blends monotonously decreases with increasing f_h, meaning that the nucleation is more frequent with less PCL block chains. On the other hand, $t_{1/2}$ of PCL-*b*-PS5 blends increases with increasing f_h at $f_\mathrm{h} \leq 0.42$ and becomes constant at higher f_h, indicating that reducing the amount of PCL block chains decelerates the nucleation. Interestingly, $t_{1/2}$ in PCL-*b*-PS2 blends and PCL-*b*-PS5 blends converges into a common value at $f_\mathrm{h} = 1$, where nucleation is affected only by space confinement. This suggests that the effects of space confinement on homogeneous nucleation are almost constant in nanocylinders with 14.9 nm $\leq D \leq$ 17.2 nm. The data in **Figure 4.8** clearly indicate that the f_h-dependence of $t_{1/2}$ in PCL-*b*-PS2 blends is completely reverse to that in PCL-*b*-PS5 blends, from which a coupling between the

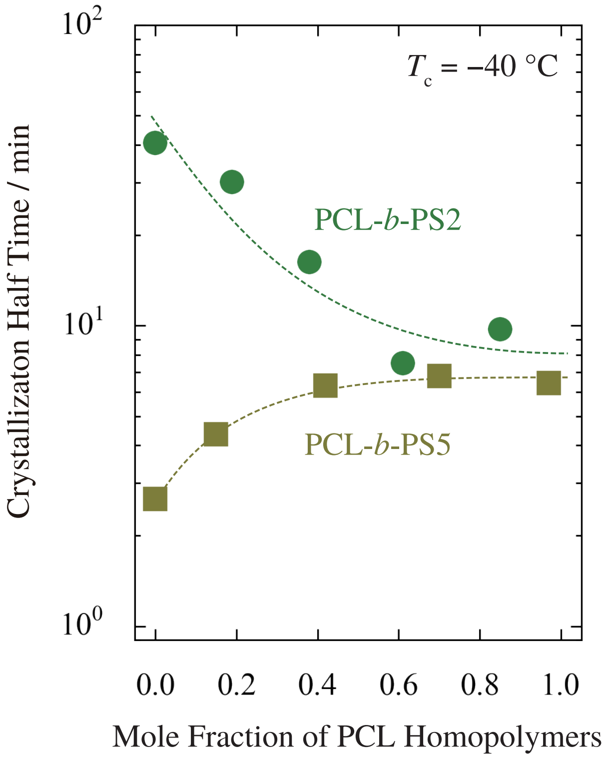

Figure 4.8. Crystallization half time of PCL-*b*-PS2 blends (circles) and PCL-*b*-PS5 blends (squares) plotted as a function of f_h. Dashed curves are just a guide for the eye.

effects of chain confinement and those of space confinement is speculated. Therefore, the next section discusses the combined effects of both confinement.

4.3.5 Coupled Effects of Chain Confinement and Space Confinement

As was revealed in the previous section, homogeneous nucleation is the only rate-determining step in the crystallization of PCL-*b*-PS2 blends and PCL-*b*-PS5 blends, therefore $t_{1/2}$ should be inversely proportional to the nucleation rate I^*. According to the pioneering theory of primary nucleation in polymer crystallization[35], the T_c-dependence of I^* is written as

$$I^* \propto \exp\left(-\frac{\Delta G^*}{kT_\mathrm{c}}\right)\exp\left(-\frac{\Delta G_\eta}{kT_\mathrm{c}}\right) \tag{4.2}$$

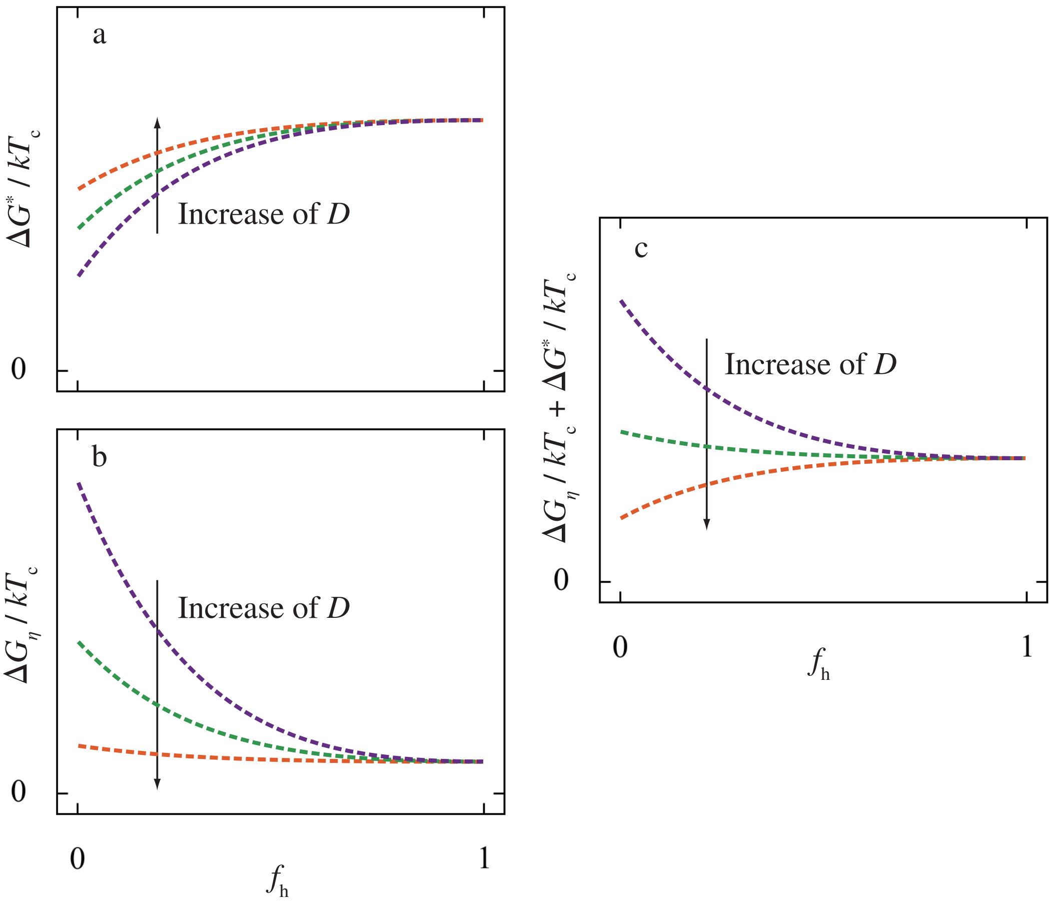

Figure 4.9. Schematic illustration showing a possible f_h-dependence of $\Delta G^*/kT_\mathrm{c}$ (a), $\Delta G_\eta/kT_\mathrm{c}$ (b), and $\Delta G^*/kT_\mathrm{c} + \Delta G_\eta/kT_\mathrm{c}$ (c) proposed for PCL homopolymer/PCL block chain blends confined in nanocylinders with varying D.

Here, ΔG^* is the free energy barrier for the formation of critical nuclei and varies as $\Delta G^* \propto 1/\Delta T^2$, where ΔT is the supercooling defined as the difference between T_c and the equilibrium melting temperature T_m°. ΔG_η is the free energy barrier associated with the diffusion of uncrystallized repeating units across the liquid-solid phase boundary, which is usually assumed to be $\Delta G_\eta \propto 1/(T_\mathrm{c} - T_0)$, where T_0 is the temperature at which the molecular diffusion completely ceases and is taken as several tens of degrees below the glass transition temperature.

Figure 4.9 is a schematic illustration of possible f_h-dependence of $\Delta G^*/kT_\mathrm{c}$ and $\Delta G_\eta/kT_\mathrm{c}$ for PCL chains confined in nanocylinders with varying D. In the case of bulk homopolymers, it is well known that the decrease of T_c leads to the reduction of chain mobility and hence lowers the free energy barrier for nucleation. Chain confinement is also supposed to reduce the chain mobility, therefore the free energy barrier $\Delta G^*/kT_\mathrm{c}$ would decrease monotonously with increasing the amount of PCL block chains, i.e., decreasing f_h (**Figure 4.9**a). This effect would be less significant in larger D because the number of tethered chain-ends per unit volume of PCL chains is smaller in larger nanocylinders. On the other hand, $\Delta G_\eta/kT_\mathrm{c}$ is expected to decrease drastically with increasing the amount of PCL block chains, i.e., decreasing f_h (**Figure 4.9**b), because the diffusion of PCL chains across the phase boundary would be severely hindered if chain-ends are fixed onto nanodomain interfaces. This effect would be dramatically diminished in nanocylinders with larger D, since the diffusion of uncrystallized repeating units would be much easier as the distance from fixed chain-ends becomes longer. Note that it is assumed in **Figure 4.9** that the free energy barriers do not depend on D at $f_\mathrm{h} = 1$ on the basis of the fact that $t_{1/2}$ at $f_\mathrm{h} \sim 1$ is almost the same in nanocylinders with $D = 14.9$ nm and 17.2 nm.

Since the crystallization half time $t_{1/2}$ is inversely proportional to I^*, $\ln t_{1/2}$ should be expressed as the sum of $\Delta G^*/kT_\mathrm{c}$, $\Delta G_\eta/kT_\mathrm{c}$, and a constant value. The $t_{1/2}$ data in **Figure 4.8** can be interpreted in terms of two free energy barriers in the following way. In nanocylinders with $D = 14.9$ nm (PCL-*b*-PS2 blends), the significant decrease of $\Delta G_\eta/kT_\mathrm{c}$ with increasing f_h (**Figure 4.9**b, purple curve) would overwhelm the increase of $\Delta G^*/kT_\mathrm{c}$ (a, purple curve), resulting in the decrease of the nucleation barrier with increasing f_h (c, purple curve). However, in larger nanocylinders with $D = 17.2$ nm, the f_h dependence of $\Delta G_\eta/kT_\mathrm{c}$ (b, orange curve) would be so trivial that the variation of $\Delta G^*/kT_\mathrm{c}$ (a, orange curve) would be dominant. This may result in the increase of the free energy of nucleation with increasing f_h (c, orange curve).

4.4 Conclusions

The crystallization behavior of PCL homopolymer/PCL block chain blends confined in an identical nanocylinder was investigated as a function of the mole fraction of PCL homopolymers f_h and nanocylinder diameter D. The blends were successfully prepared by the controlled UV irradiation on photocleavable PCL-*b*-PS diblock copolymers. It was confirmed by SAXS measurements that cylindrical microphase-separated structures (nanocylinders) were formed in two PCL-*b*-PS diblock copolymers used in this study (PCL-*b*-PS2 and PCL-*b*-PS5) and these nanocylinders were stable against crystallization and melting of PCL chains and also photocleavage of block junctions.

The results and discussion on the melting and crystallization of PCL homopolymer/PCL block chain blends can be summarized as follows:

1. Only a single endothermic peak was observed on the melting of all the blends, indicating the co-crystallization of PCL homopolymers and PCL block chains.

2. The lower melting temperature and crystallinity were observed in the blends with smaller f_h and D, suggesting that the thickening and lateral growth of PCL crystals were restricted by both space confinement and chain confinement.

3. Crystallization of the blends obeyed first-order-like kinetics, strongly indicating that homogeneous nucleation was the dominating process of the crystallization.

4. The nucleation rate of PCL homopolymer/PCL block chain blends in nanocylinders with $D = 14.9$ nm increased with increasing f_h, whereas it decreased with increasing f_h in nanocylinders with $D = 17.2$ nm. This result could be qualitatively explained using the pioneering theory of nucleation which described the nucleation rate in terms of free energy barriers for the formation of critical nuclei and molecular diffusion across the phase boundary. The latter factor would be dominant in smaller nanocylinders, but overtaken by the former factor in larger

nanocylinders.

References

1. Hashimoto, H.; Fujimura, M.; Hashimoto, T.; Kawai, H. *Macromolecules* **1981**, *10*, 377–384.
2. Tanaka, H.; Hasegawa, H.; Hashimoto, T. *Macromolecules* **1991**, *24*, 240–251.
3. Koizumi, S.; Hasegawa, H.; Hashimoto, T. *Macromolecules* **1994**, *27*, 6532–6540.
4. Koizumi, S.; Hasegawa, H.; Hashimoto, T. *Macromolecules* **1994**, *27*, 7893–7906.
5. Hashimoto, T.; Koizumi, S.; Hasegewa, H. *Physica B* **1995**, *214*, 676–681.
6. Winey, K. I.; Thomas, E. L.; Fetters, L. J. *Macromolecules* **1991**, *24*, 6182–6188.
7. Mayes, A. M.; Russell, T. P.; Satija, S. K.; Majkrzak, C. F. *Macromolecules* **1992**, *25*, 6523–6531.
8. Jeon, K.-J.; Roe, R.-J. *Macromolecules* **1994**, *27*, 2439–2447.
9. Kimishima, K.; Hashimoto, T.; Han, C. D. *Macromolecules* **1995**, *28*, 3842–3853.
10. Zhao, J.; Majumdar, B.; Schulz, M. F.; Bates, F. S.; Almdal, K.; Mortensen, K.; Hajduk, D. A.; Gruner, S. M. *Macromolecules* **1996**, *29*, 1204–1215.
11. Floudas, G. A.; Hadjichristidis, N.; Stamm, M.; Likhtman, A. E.; Semenov, A. N. *The Journal of Chemical Physics* **1997**, *106*, 3318–3328.
12. Vaidya, N. Y.; Han, C. D. *Polymer* **2002**, *43*, 3047–3059.
13. Jeong, U.; Ryu, D. Y.; Kho, D. H.; Lee, D. H.; Kim, J. K.; Russell, T. P. *Macromolecules* **2003**, *36*, 3626–3634.
14. Mykhaylyk, T. A.; Mykhaylyk, O. O.; Collins, S.; Hamley, I. W. *Macromolecules* **2004**, *37*, 3369–3377.
15. De La Cruz, M. O.; Sanchez, I. C. *Macromolecules* **1979**, *47*, 877–882.
16. Whitmore, M. D.; Noolandi, J. *Macromolecules* **1985**, *18*, 2486–2497.
17. Matsen, M. W. *Macromolecules* **1995**, *28*, 5765–5773.
18. Veith, C. A.; Cohen, R. E.; Argon, A. S. *Polymer* **1991**, *32*, 1545–1554.
19. Liu, L.; Li, H.; Jiang, B.; Zhou, E. *Polymer* **1994**, *35*, 5511–5517.
20. Liu, L.; Jiang, B.; Zhou, E. *Polymer* **1996**, *37*, 3937–3943.
21. Liu, L.-Z.; Yeh, F.; Chu, B. *Macromolecules* **1996**, *29*, 5336–5345.
22. Rangarajan, P.; Haisch, C. F.; Register, R. A.; Adamson, D. H.; Fetters, L. J. *Macromolecules* **1997**, *30*, 494–502.
23. Nojima, S.; Kuroda, M.; Sasaki, S. *Polymer Journal* **1997**, *29*, 642–648.
24. Liu, L.-Z.; Xu, W.; Li, H.; Su, F.; Zhou, E. *Macromolecules* **1997**, *30*, 1363–1374.
25. Akaba, M.; Nojima, S. *Polymer Journal* **2005**, *37*, 464–470.
26. Gao, Y.; Liu, H. *Journal of Applied Polymer Science* **2007**, *106*, 2718–2723.

27. Akaba, M.; Nojima, S. *Polymer Journal* **2006**, *38*, 559–566.
28. Takeshita, H.; Gao, Y.-J.; Natsui, T.; Rodriguez, E.; Miya, M.; Takenaka, K.; Shiomi, T. *Polymer* **2007**, *48*, 7660–7671.
29. Luo, C.; Han, X.; Gao, Y.; Liu, H.; Hu, Y. *Journal of Applied Polymer Science* **2009**, *113*, 907–915.
30. Shiomi, T.; Takeshita, H.; Gao, Y. J.; Takata, Y.; Takenaka, K.; Wu, C. F. *Polymer* **2010**, *51*, 799–806.
31. Yu, P.-Q.; Yan, L.-T.; Chen, N.; Xie, X.-M. *Polymer* **2012**, *53*, 4727–4736.
32. Guillier, F.; Orain, D.; Bradley, M. *Chemical Reviews* **2000**, *100*, 2091–158.
33. Avrami, M. *The Journal of Chemical Physics* **1939**, *7*, 1103–1112.
34. Avrami, M. *The Journal of Chemical Physics* **1940**, *8*, 212–224.
35. Wunderlich, B., *Macromolecular Physics Vol. 2*; Academic Press: New York: 1976.

Chapter 5

Crystallization of Homopolymers and Block Chains Confined in Nanolamellae

5.1 Introduction

Crystallization of homopolymers under spatial restriction has been studied using various confining geometries such as spherical or sphere-like droplets (nanospheres)[1–8], cylindrical nanopores (nanocylinders) of AAO templates,[9–16] or nanolamellae in co-extruded films[17,18]. Generally speaking, homopolymers confined in nanospheres[1–8] as well as nanocylinders with relatively small diameters[9–15] show crystallization dominated by homogeneous nucleation, while those in larger nanocylinders[11,15] and nanolamellae[17,18] crystallize by the conventional heterogeneous nucleation and growth mechanism. However, it is difficult to evaluate the effects of different nanodomain shapes by comparing the results from different methods, because the effects of nanodomain interfaces cannot be eliminated[6,16]. The use of crystalline-amorphous (C-A) diblock copolymers[19–46] allows for a direct comparison of the crystallization of block chains confined in nanodomains with various shapes including nanospheres, nanocylinders, gyroid structures, and nanolamellae. For example, Lee and coworkers[27] investigated the crystallization behavior of PEO block chains confined in nanospheres, nanocylinders, and nanolamellae formed by microphase separation of PEO-*b*-PB diblock copolymer/PB homopolymer blends, where rubbery PB matrices were crosslinked to prevent the destruction of microphase-separated structures by the crystallization of PEO block chains. PEO block chains confined in nanocylinders and nanospheres crystallized only at a supercooling as large as $\sim$ 100 °C via first-order kinetics, indicating that the crystallization was controlled by homogeneous nucleation. Meanwhile, PEO block chains in nanolamellae crystallized at a relatively small supercooling and showed the time development of the crystallinity similar to that of bulk homopolymers, strongly suggesting the conventional heterogeneous nucleation and growth mechanism. The result demonstrates that the crystallization behavior is strongly affected by the spatial restriction provided by nanodomains (*space confinement*).

In Chapters 2 through 4 of this thesis, the author examined the crystallization behavior and crystal orientation of homopolymers and block chains confined in an identical nanocylinder, and clarified the influences of constraints imposed by chain-ends fixed onto nanodomain interfaces (*chain confinement*). However, the kinetics of crystal growth could not be observed because crystal growth in nanocylinders was instantaneous and hence the overall crystallization rate was controlled only by homogeneous nucleation. By applying the approach of the previous chapters to the crystallization in nanolamellae, more fundamental understanding of the effects of chain confinement on crystal growth is expected. In this study, the crystallization behavior of PCL homopolymers and PCL block chains both confined in an identical nanolamella is investigated in order to clarify the effects of chain confinement on crystal growth.

5.2 Experimental

5.2.1 Model Systems

The overview and method of preparation of the model systems used in this study are schematically depicted in **Figure 5.1**. A PCL-*b*-PS diblock copolymer having ONB between PCL and PS blocks is used, which has a nearly symmetrical composition so that it forms a lamellar microphase-separated structure (nanolamella) consisting of alternating PCL and PS layers. Nanolamellae at this point contain PCL block chains with their one

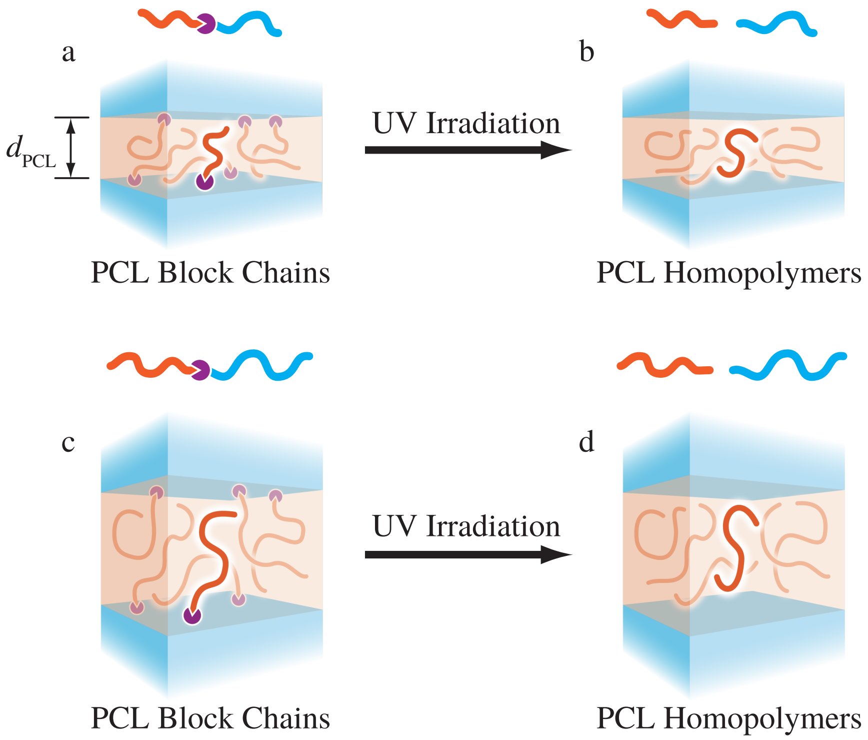

Figure 5.1. Schematic illustration describing the model systems and their preparation method used in this study. A PCL-*b*-PS diblock copolymer with ONB at the block junction is first microphase-separated to form nanolamellae confining PCL block chains tethered at one end (a), which are then converted into PCL homopolymers by photocleavage of ONB (b). The effects of chain confinement can be examined in a larger nanolamella (c and d) by using another PCL-*b*-PS diblock copolymer having a larger total molecular weight but similar block composition.

end tethered onto nanolamella interfaces (**Figure 5.1**a). Subsequent photocleavage of ONB at the block junction turns PCL block chains into PCL homopolymers (b). It is expected that the vitrification of PS layers prevents nanolamellae from collapsing, as long as the temperature is kept well below the glass transition temperature of PS chains. Moreover, a system with larger nanolamellae can be prepared by using PCL-*b*-PS diblock copolymers with the larger total molecular weight and near-symmetrical block composition (c and d).

Table 5.1. Characterization of the samples used in this study.

Code	M_n / g mol^{-1}			$M_\mathrm{w}/M_\mathrm{n}$[b]	ϕ_PCL[d]	d_PCL[e] / nm	f_h[f]
	PCL[a]	PS[b]	Total[c]				
PCL-*b*-PS6	10300	13400	23700	1.04	0.43	8.7	0
PCL/PS6	10300	13400	-	-	0.43	8.7	0.93
PCL-*b*-PS7	25400	29000	54400	1.05	0.47	15.8	0
PCL/PS7	25400	29000	-	-	0.47	15.8	0.90

[a] Determined by ^{1}H-NMR.

[b] Determined by GPC.

[c] Sum of M_ns of the PCL and PS blocks.

[d] Volume fraction of PCL chains calculated from M_ns and specific volumes of PCL and PS at 100 °C.

[e] Thickness of PCL layers calculated from the primary peak position in SAXS curves and volume fraction of PCL chains.

[f] Mole fraction of PCL homopolymers in the system calculated from GPC chromatograms.

5.2.2 Samples and Sample Preparation

PCL-*b*-PS diblock copolymers used in this study were synthesized according to the method described in Appendix A. **Table 5.1** summarizes the molecular characterization of the samples used. PCL-*b*-PS6 and PCL-*b*-PS7 denote diblock copolymer samples with lower and higher total molecular weight, respectively. The samples after UV irradiation are denoted as PCL/PS6 and PCL/PS7. Both PCL-*b*-PS diblock copolymers has nearly symmetrical composition, from which the formation of a lamellar microphase-separated structure is expected.

PCL-*b*-PS diblock copolymers were processed to films by solution casting before all experiments. PCL/PS6 and PCL/PS7 were prepared from precursor PCL-*b*-PS diblock copolymer films by UV irradiation with the intensity of 4.0 W cm^{-2} for 2 h. The condition for UV irradiation was determined based on the results of GPC measurements of UV-irradiated samples as a function of the total irradiation energy E_t, which are presented in Section 5.3.1. The film preparation and UV irradiation were carried out following the methods described in Section 2.2.2 of Chapter 2.

5.2.3 Gel Permeation Chromatography (GPC)

The progress of the photocleavage reaction in PCL-*b*-PS samples was examined by gel permeation chromatography (GPC) as a function of the total UV energy E_t defined as the product of UV intensity and irradiation time. The equipment and conditions of GPC measurements can be found in Section 2.2.3 of Chapter 2.

5.2.4 Small-angle X-ray Scattering (SAXS)

The microphase-separated structure formed in the samples was examined using static small-angle X-ray scattering (SAXS). Time-resolved SAXS measurements were also conducted to probe possible morphological changes during annealing above the melting temperature of PCL chains, as well as to pursue the progress of isothermal crystallization at selected temperatures. The experiments were performed using the small-angle X-ray equipment for solution (SAXES) at beam-line BL-10C of Photon Factory in High Energy Accelerator Research Organization, Tsukuba, Japan, with synchrotron X-ray having the wavelength λ of 0.1488 nm. The detector used was a two-dimensional pixel-array detector (PILATUS3 300K-W, Dectris Ltd., Switzerland) having 1475×195 pixels with 172×172 $\mu\mathrm{m}^2$ in each size, placed at the point where the distance from the sample is ca. 2 m. Typical exposure time was 1-5 min for static measurements. In time-resolved measurements, a 10 sec exposure was repeated with a 5 sec interval. The obtained images were then circularly averaged into one-dimensional scattering curves and corrected for background scattering and absorption, and finally plotted against the magnitude of scattering vector $s = 2\sin\theta/\lambda$ calculated from the 6th order scattering peak of a chicken tendon collagen having a long period of 65.3 nm.

5.2.5 Differential Scanning Calorimetry (DSC)

Differential scanning calorimetry (DSC) was used to investigate the crystallization behavior of PCL chains using a calorimeter (Diamond DSC, Perkin Elmer, USA) connected with a liquid nitrogen supply system. All measurements were carried out on sample films (ca. 5 - 10 mg) sealed in an aluminum pan. A sample was first annealed at temperature $T_\mathrm{a} = 60$ °C (for PCL-*b*-PS6 and PCL/PS6) or 62 °C (for PCL-*b*-PS7 and PCL/PS7) prior to each measurement run to erase previous thermal histories.

The crystallizable temperature was estimated by the non-isothermal program, where a sample was cooled from T_a to -90 °C at -10 °C min^{-1}, and then heated back to T_a at 10 °C min^{-1}. The melting temperature T_m and crystallinity X_c after isothermal crystallization were measured by the following temperature program. A sample was quenched from T_a to a selected crystallization temperature T_c at -500 °C min^{-1}, kept for a prescribed time t, and heated back to T_a at 10 °C min^{-1} to collect endothermic peak due to the melting of PCL crystals. T_m and X_c were calculated from the endothermic peak following the method described in Section 2.2.5 of Chapter 2. The time development of X_c was also pursued by repeating the above isothermal crystallization program with varying t.

5.3 Results and Discussion

5.3.1 Photocleavage Behavior

Figure 5.2 shows the results of GPC measurements of PCL-*b*-PS7 before (dashed curve) and after (solid green curve) UV irradiation. A sharp and unimodal chromatogram of PCL-*b*-PS7 decomposes on UV irradiation, yielding a complex chromatogram consisting of several peaks. The presence of a shoulder at the elution time of ca. 12.5 min is puzzling, since the PS-equivalent molecular weight of the shoulder is larger than that of PCL-*b*-PS7. This result can only be explained by assuming the trimerization of PS homopolymers. In Section 2.3.1 of Chapter 2, it was found that some PS homopolymers generated by the photocleavage reaction undergo dimerization, possibly due to active nitroso moieties at the chain ends[47]. Although this kind of side reaction involving nitroso

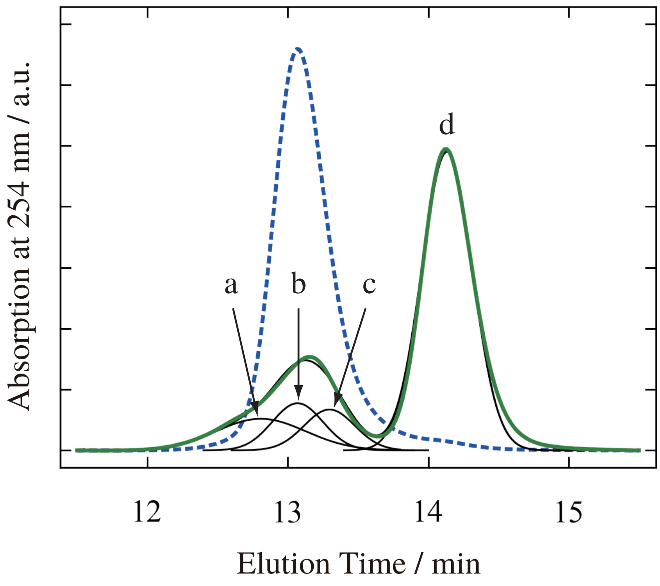

Figure 5.2. GPC chromatograms of PCL-*b*-PS7 before (dashed curve) and after (solid green curve) UV irradiation with the intensity of 1.5 $\mathrm{W\,cm^{-2}}$ for 4 h. The results of peak deconvolution are shown in black curves, where peaks a, b, c, and d correspond to trimerized PS homopolymers, PCL-*b*-PS diblock copolymers, dimerized PS homopolymers, and PS homopolymers, respectively.

groups needs to be studied in much more detail, it is true that the chromatogram is successfully fitted only when both the trimerization and dimerization of PS homopolymers are assumed.

The chromatogram after UV irradiation was fitted by the sum of four Gaussian functions with fixed positions, each corresponding to trimerized PS homopolymers (peak a in **Figure 5.2**), unreacted PCL-*b*-PS diblock copolymers (b), dimerized PS homopolymers (c), and PS homopolymers (d), respectively. The progress of photocleavage was quantified by the mole fraction of PCL homopolymers f_h in all PCL chains in the system (i.e., PCL homopolymers and PCL block chains), following the method described in Appendix C. **Figure 5.3** shows f_h for PCL-*b*-PS6 (circles) and PCL-*b*-PS7 (squares) as a function of the total UV energy E_t, which is calculated as the product of UV intensity and irradiation time. The increase of f_h with E_t is extremely steep at low E_t and asymptotic at high E_t for both PCL-*b*-PS6 and PCL-*b*-PS7. This first-order-like behavior is qualitatively the same as that observed in the cylinder-forming PCL-*b*-PS diblock copolymers presented

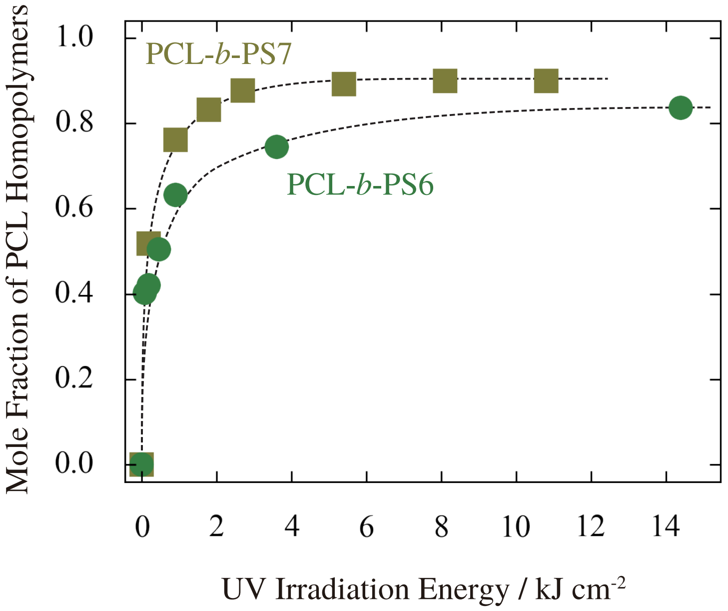

Figure 5.3. The mole fraction of PCL homopolymers f_h for PCL-*b*-PS6 (circles) and PCL-*b*-PS7 (squares) plotted against the total UV energy E_t. Dashed curves are just a guide for the eye.

in Section 4.3.1 of Chapter 4, despite the complex side reactions observed in PCL-*b*-PS6 and PCL-*b*-PS7. The condition for preparing PCL/PS samples was determined on the basis of **Figure 5.3** to be 4.0 W cm^{-2} in intensity and 2 h in time (i.e., $E_\mathrm{t} = 28.8\ \mathrm{kJ\,cm^{-2}}$).

5.3.2 Microphase-separated Structure

Figure 5.4 shows the SAXS curves of PCL-*b*-PS6 and PCL/PS6 (a) and PCL-*b*-PS7 and PCL/PS7 (b) in the crystallized state. Both PCL-*b*-PS6 and PCL-*b*-PS7 display several sharp scattering peaks whose positions exactly correspond to a ratio of $1:2:3(:4)$, indicating the formation of a lamellar microphase-separated structure (nanolamella) consisting of alternating layers of PCL and PS chains. The SAXS curves of PCL-*b*-PS6 and PCL-*b*-PS7 in the amorphous state (dashed curves in each panel) exhibit primary peaks at the same position as in the crystallized state, suggesting the complete preservation of nanolamellae on the crystallization and melting of PCL chains. The higher order peaks are weaker in the amorphous state than in the crystallized state, which can be explained by

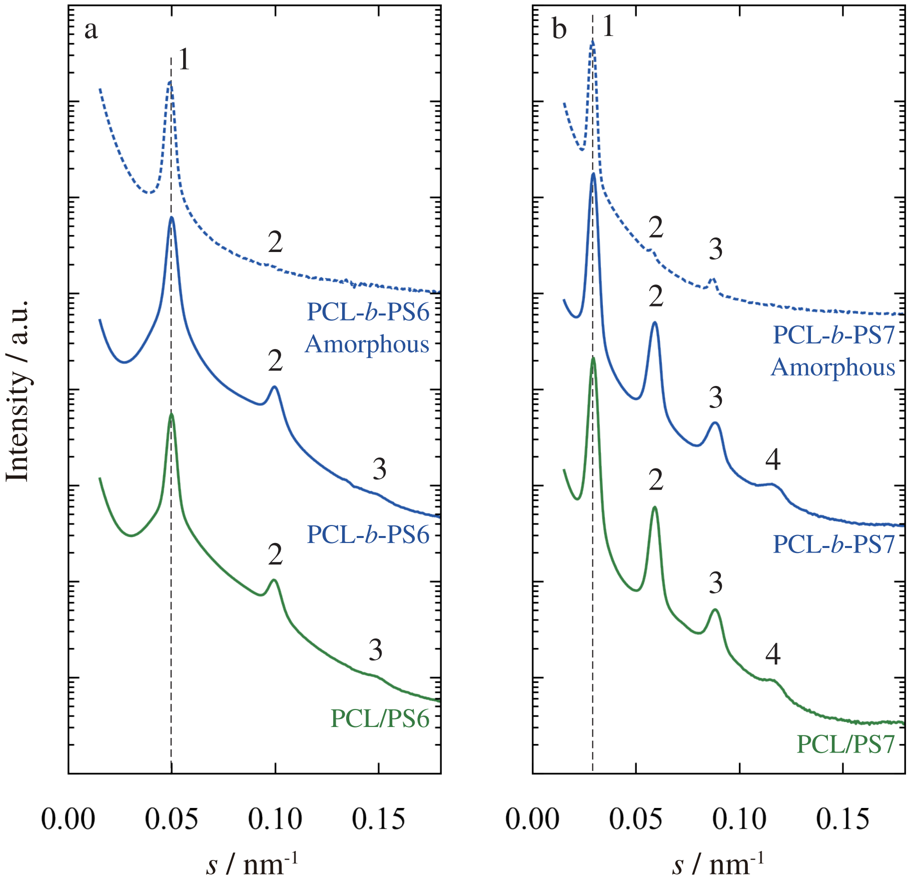

Figure 5.4. SAXS curves of PCL-*b*-PS6 (a) and PCL-*b*-PS7 (b) obtained when PCL chains are crystallized (solid blue curves) and amorphous (dashed blue curves). SAXS curves of the samples after UV irradiation and subsequent crystallization are shown in green solid curves in each panel. Vertical dashed lines indicate primary peak positions.

a significant reduction of the electron density contrast between PCL and PS layers on the melting of PCL crystals (see discussion in Section 2.3.2). It is also clear that the primary peak positions and scattering patterns from UV-irradiated samples are almost identical to those before UV irradiation, implying that the photocleavage of block junctions does not lead to the destruction of nanolamellae, despite the fact that PCL/PS samples are in effect a polymer blend mainly composed of PCL and PS homopolymers. The thickness of nanolamellae d_{PCL} in which PCL chains are confined can be calculated simply by multiplying the long spacing of the primary peak by ϕ_{PCL} (**Table 5.1**) to be 8.7 nm for PCL-*b*-PS6 and 15.8 nm for PCL-*b*-PS7.

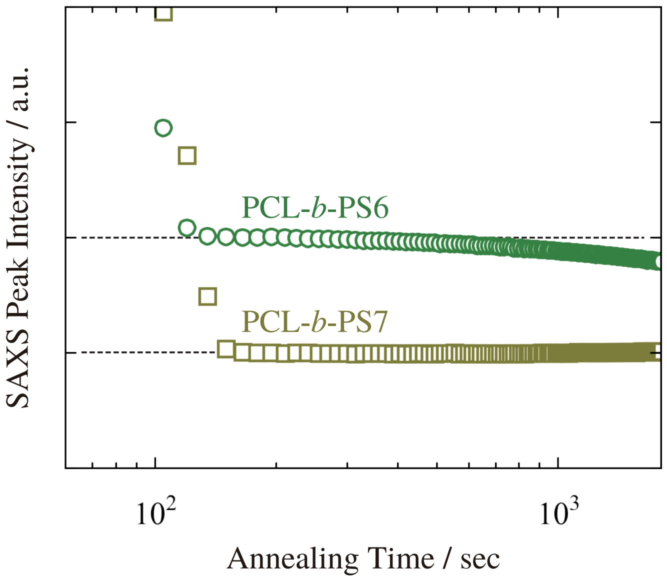

Figure 5.5. Variation of the SAXS primary peak intensity from PCL/PS6 (circles) and PCL/PS7 (squares) during annealing at 60 °C (for PCL/PS6) or 62 °C (for PCL/PS7). The data of PCL/PS6 is shifted upward for legibility. Horizontal dashed lines are just a guide for the eye.

To examine the thermal stability of nanolamellae in PCL/PS6 and PCL/PS7 more closely, time-resolved SAXS measurements were carried out during heating from room temperature to the temperature just above T_m of PCL chains (60 °C for PCL/PS6 and 62 °C for PCL/PS7) and subsequent isothermal annealing. **Figure 5.5** shows the variation of primary peak intensity plotted against the time elapsed from the beginning of heating from room temperature. In both samples, the intensity first quickly decreases due to the reduction of the electron density difference between PCL and PS layers on the melting of PCL crystals. Subsequently, the primary peak intensity of PCL/PS7 remains constant for more than 20 min, whereas that of PCL/PS6 starts to decrease gradually from ca. 300 s. This result suggests that nanolamellae in PCL/PS6 may be partially destroyed or distorted when kept above T_m of PCL chains for more than 300 s. Since PCL/PS7, which has PCL and PS chains with larger molecular weights compared to PCL/PS6, does not show any reduction in the primary peak intensity, the thermal stability of nanolamellae probably depends on the molecular weight and hence the mobility of PCL and/or PS chains. Based on the above observation, all measurements on PCL/PS6 were always

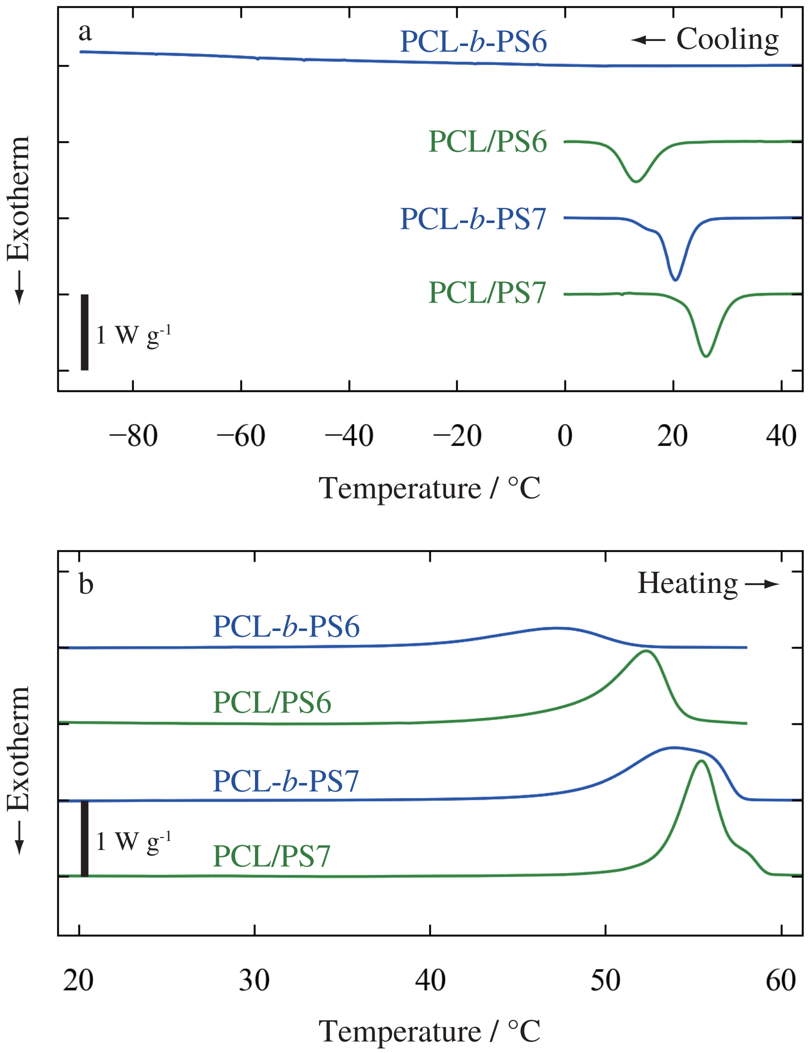

Figure 5.6. DSC thermograms on cooling (a) and heating (b) of the samples indicated. Samples were first annealed just above the melting temperature of PCL chains and cooled to 0 °C (or −90 °C for PCL-*b*-PS6) at -10 °C min^{-1} and then heated at 10 °C min^{-1}.

performed on freshly prepared films.

5.3.3 Melting Behavior of PCL Chains

Non-isothermal DSC measurements were carried out to estimate the crystallizable temperature and melting temperature of PCL chains. **Figure 5.6** shows the DSC thermograms on cooling to 0 °C (or −90 °C for PCL-*b*-PS6) at -10 °C min^{-1} (a) and subsequent heating at 10 °C min^{-1} (b). PCL/PS6, PCL-*b*-PS7, and PCL/PS7 exhibit an exothermic peak due to the crystallization of PCL chains, whereas no peak is detected for PCL-*b*-PS6 even by cooling down to -90 °C. However, all the samples including PCL-*b*-PS6 clearly display an endothermic peak on subsequent heating arising from the melting of PCL crystals. PCL chains in PCL-*b*-PS6 may crystallize only slowly at low temperatures, which would considerably broadens the exothermic peak to an undetectable level. Moreover, the endothermic peak of PCL-*b*-PS6 is particularly broad and located at a relatively low temperature, indicating that PCL block chains in PCL-*b*-PS6 can only form thin and immature crystals with a broad distribution of their thickness. The qualitative difference in crystallization and melting behaviors between PCL-*b*-PS6 and the other samples is attributed to the difference in the crystallization mechanism, as will be discussed later.

The melting behavior of PCL chains was further quantitatively analyzed under isothermal crystallization conditions using DSC. **Figure 5.7** shows the melting temperature T_m (a) and crystallinity X_c (b) of the samples observed after isothermal crystallization as a function of crystallization temperature T_c. T_m and X_c of bulk PCL homopolymers ($M_\mathrm{n} = 27400$ g mol^{-1}, $M_\mathrm{w}/M_\mathrm{n} = 1.06$) are also shown for comparison. Note that T_c applied for PCL-*b*-PS6 is much lower than other samples because PCL-*b*-PS6 does not show any crystallinity at T_c around room temperature within an experimental time scale. T_m and X_c of PCL block chains in PCL-*b*-PS6 are constant independent of T_c and lower than those in other samples, indicating that the thickening of PCL crystals is significantly frustrated in PCL-*b*-PS6. On the other hand, T_m and X_c of PCL/PS6, PCL-*b*-PS7, and PCL/PS7 increase with increasing T_c. It is known that T_m of bulk homopolymers obeys the Gibbs-Thomson equation, where inverse of T_m depends linearly on the thickness of lamellar crystals. Therefore, this behavior can be attributed to the thickening mechanism of PCL crystals at higher temperatures to minimize the surface free energy, as is commonly observed in crystallization of bulk homopolymers. Surprisingly, T_m of PCL block chains in PCL-*b*-PS7, PCL homopolymers in PCL/PS6 and PCL/PS7, and bulk PCL homopolymers seems to fall on a common straight line. This observation indicates that the crystal thickness in PCL/PS6, PCL-*b*-PS7, and PCL/PS7 is determined solely by

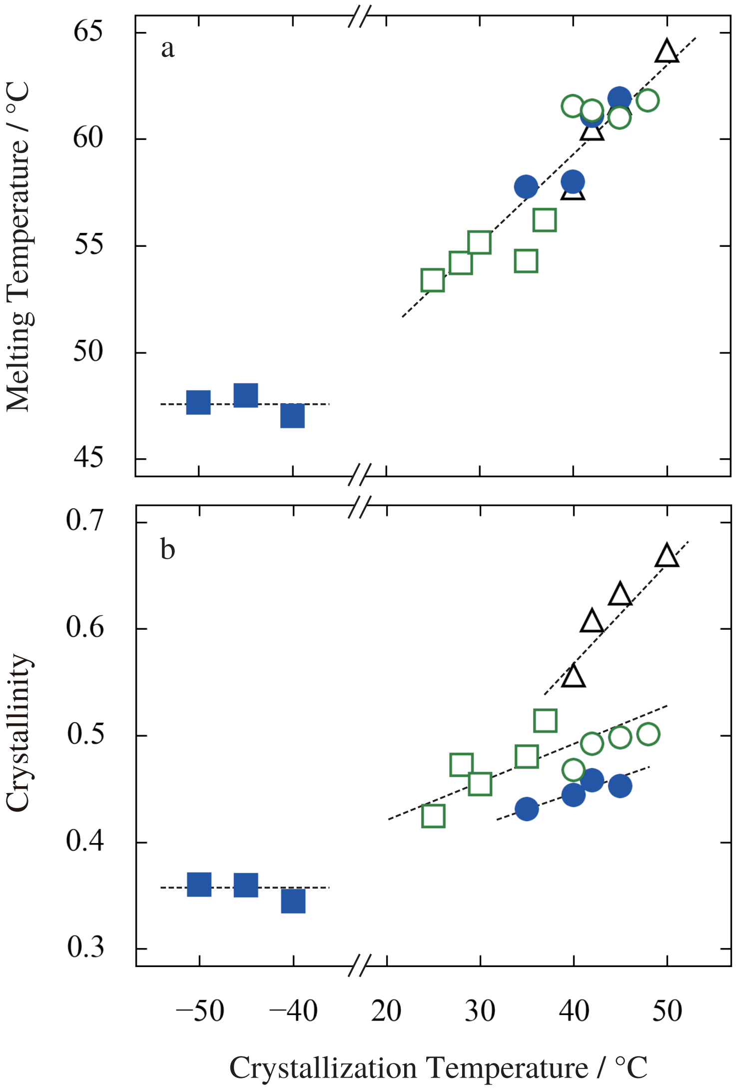

Figure 5.7. Melting temperature T_m (a) and crystallinity X_c (b) of PCL chains plotted against the crystallization temperature T_c for PCL-*b*-PS6 (closed squares), PCL/PS6 (open squares), PCL-*b*-PS7 (closed circles), and PCL/PS7 (open circles). The data for bulk PCL homopolymers are also shown in open triangles for comparison. Dashed lines are just a guide for the eye.

thermodynamic requirements and is scarcely affected by chain confinement and space confinement in the T_c range investigated. X_c of PCL/PS6, PCL-*b*-PS7, and PCL/PS7 also increases with increasing T_c, reflecting the thickening and/or lateral growth of PCL crystals at higher T_c. X_c of PCL homopolymers in PCL/PS6 and PCL/PS7 is lower than that of bulk PCL homopolymers. PCL-*b*-PS7 shows even lower X_c than PCL/PS6 and PCL/PS7. These observations suggest that both space confinement and chain confinement moderately hamper the lateral growth of PCL crystals.

It is revealed that there is a substantial difference in the non-isothermal crystallization and melting behavior, as well as the melting behavior after isothermal crystallization, between PCL-*b*-PS6 and other samples. This fact may reflect the difference in the crystallization mechanism, which will be clarified later by analyzing crystallization kinetics.

5.3.4 Crystallization Behavior of PCL Chains

Figure 5.8 shows the time evolution of X_c during isothermal crystallization of PCL-*b*-PS6 at −50 °C and PCL/PS6 at 25 °C (a) and PCL-*b*-PS7 and PCL/PS7 at 45 °C (b) pursued by DSC measurements. A marked difference is observed between PCL block chains in PCL-*b*-PS6 and PCL homopolymers in PCL/PS6. In PCL-*b*-PS6, X_c rises abruptly from time zero and later asymptotically increases to attain a final value. This behavior is similar to those observed for the crystallization of PCL chains confined in nanocylinders (see Chapters 2 and 4), and implies that the crystallization of PCL block chains in PCL-*b*-PS6 may be dominated by homogeneous nucleation. However, X_c of PCL homopolymers in PCL/PS6 starts to increase after a short but finite induction time, which is a behavior commonly observed for the crystallization of bulk homopolymers, implying the crystallization via the heterogeneous nucleation and growth mechanism. The time development of X_c in PCL-*b*-PS7 and PCL/PS7 is qualitatively similar to that of PCL/PS6, that is, both have a finite induction time before a sharp increase of X_c and subsequent asymptotic increase to a final value.

The progress of crystallization of PCL/PS6 and PCL/PS7 was also pursued using time-resolved SAXS, which is advantageous over the DSC measurements in that it can non-destructively follow the progress of crystallization in a single measurement run, though it is not suitable for determining the absolute crystallinity X_c of PCL chains. Therefore, time-resolved SAXS measurements are especially useful to track crystallization dynamics of samples like PCL/PS6 whose morphology is potentially unstable against

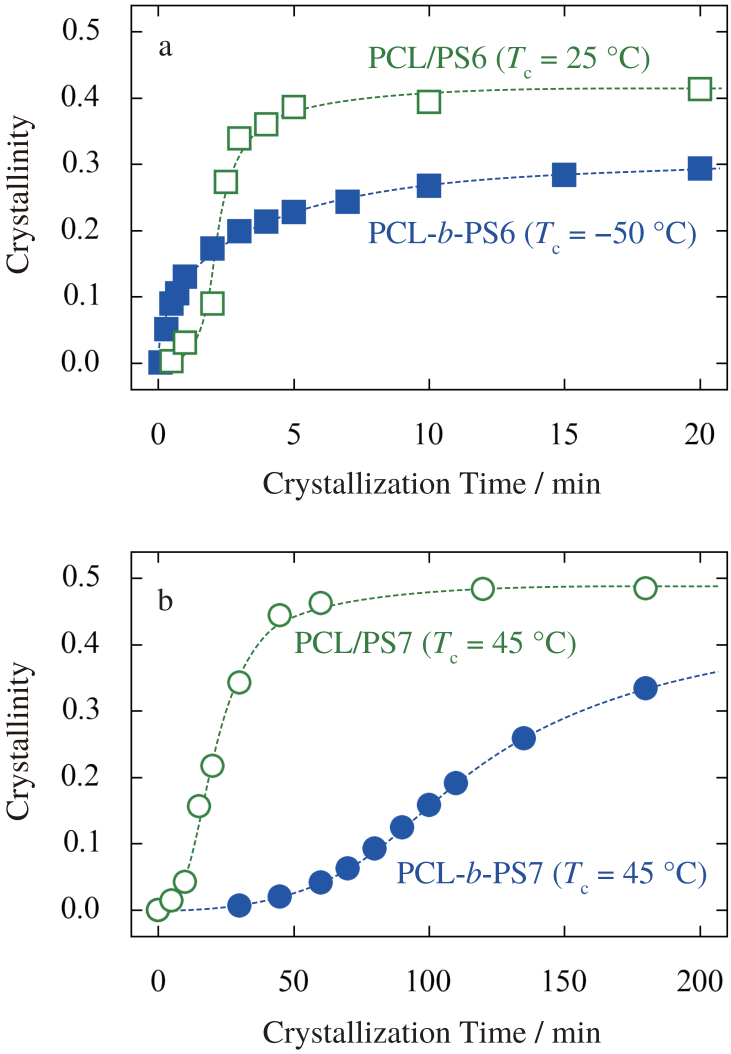

Figure 5.8. Time evolution of crystallinity in PCL-*b*-PS6 and PCL/PS6 (a) and PCL-*b*-PS7 and PCL/PS7 (b) during isothermal crystallization at indicated temperatures. Dashed curves are just a guide for the eye.

repeated melting and crystallization. **Figure 5.9**a shows the time-resolved SAXS curves of PCL/PS7 during isothermal crystallization at $T_c = 40$ °C. The position and shape of the primary peak arising from alternating layers of PCL and PS chains are completely preserved throughout the crystallization process, confirming that the crystallization of PCL chains is effectively confined in nanolamellae. On the other hand, the primary peak intensity evolves with time due to the enhanced electron density contrast between PCL and PS layers on the crystallization of PCL chains. Therefore, the time evolution of

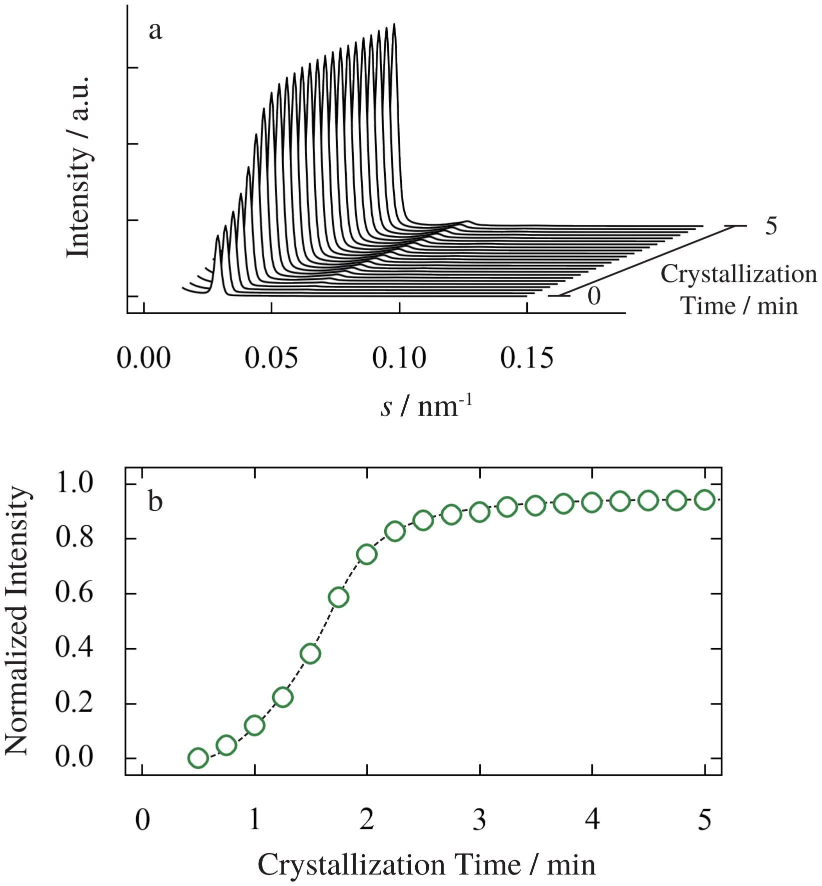

Figure 5.9. Time development of SAXS curves (a) and normalized primary peak intensity (b) for PCL/PS7 during isothermal crystallization at $T_c = 40$ °C. A dashed curve is just a guide for the eye.

primary peak intensity should directly reflect the progress of crystallization. **Figure 5.9**b plots the time evolution of the primary peak intensity after subtracting the initial intensity in the amorphous state and normalizing by the final value. The shape of the curve is qualitatively similar to that of the time-X_c curve obtained using DSC (open circles in **Figure 5.8**b), indicating that the time-resolved SAXS measurement can satisfactorily track the progress of crystallization of PCL chains confined in nanolamellae.

5.3.5 Analyses on Crystallization Kinetics of PCL Chains

The data in **Figure 5.8** clearly indicate that the crystallization mechanism of PCL-*b*-PS6 is substantially different from that in PCL/PS6, PCL-*b*-PS7, and PCL/PS7. In

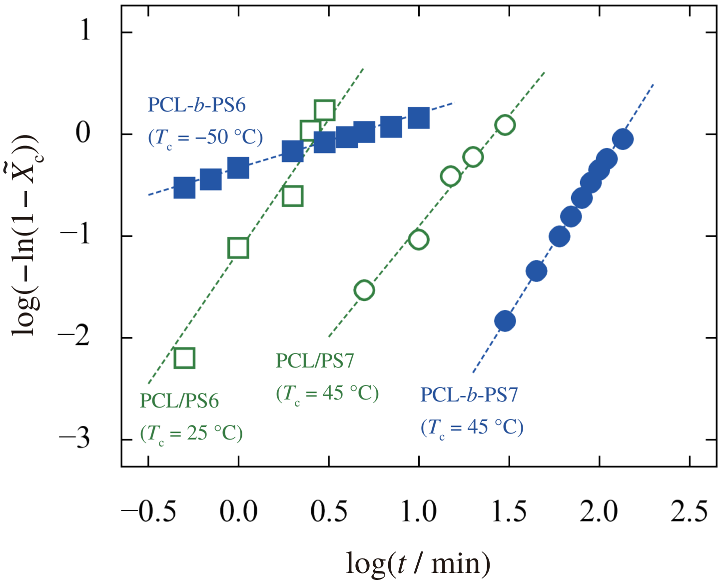

Figure 5.10. Avrami plots of the isothermal crystallization of PCL-*b*-PS6 (closed squares), PCL/PS6 (open squares), PCL-*b*-PS7 (closed circles), and PCL/PS7 (open circles) at indicated temperatures. The results of linear fitting are drawn with dashed lines.

order to analyse the crystallization mechanism in detail and to quantify the crystallization rate, the Avrami equation[48,49]

$$\log(-\ln(1-\tilde{X}_c)) = n\log t + K \tag{5.1}$$

was used, where $\tilde{X}_c$ is the normalized crystallinity calculated by dividing X_c by its final value, n the Avrami exponent, and K the rate constant. **Figure 5.10** shows the plot of $\log(-\ln(1-\tilde{X}_c))$ against $\log t$ (the Avrami plot) for the data in **Figure 5.8**. It is readily discernible that the slope of the plot, which is equal to the Avrami exponent n, is clearly different between PCL-*b*-PS6 and other samples. In fact, the Avrami exponent n is 0.6 for PCL-*b*-PS6, which is extremely small compared to 2.9 for PCL/PS6, 2.8 for PCL-*b*-PS7, and 2.2 for PCL/PS7. The near-unity n value of PCL-*b*-PS6 indicates that the crystallization obeys the first-order-like kinetics, which was also observed for PCL chains confined in nanocylinders (see Chapters 2 and 4). This kinetics strongly suggests that the crystallization in PCL-*b*-PS6 is controlled only by homogeneous nucleation. In other words, homogeneous nucleation is the only rate-determining step in the crystallization of PCL block chains in PCL-*b*-PS6. In contrast, the n values ranging from 2 to 4 are commonly observed in bulk homopolymers as well as homopolymers[17,18] and block chains[28,33,34] confined in nanolamellae and imply that the conventional heterogeneous nucleation and growth mechanism is dominant. Hence, it is sufficient to state that the crystallization of PCL chains in PCL/PS6, PCL-*b*-PS7, and PCL/PS7 is controlled by heterogeneous nucleation and growth.

It was reported that the crystallization mechanism of block chains confined in nanolamellae depended on the nanolamella thickness. Sun and coworkers[33,34] examined the crystallization of PCL block chains confined in nanolamellae formed in PCL-*b*-P4VP as a function of the PCL layer thickness d_{PCL}, and found that the heterogeneous nucleation observed in nanolamellae with $d_{\mathrm{PCL}} \geq 8.8$ nm was replaced by homogeneous nucleation in nanolamellae with $d_{\mathrm{PCL}} = 6.6$ nm. But, as far as the author knows, the present study is the first to show that such a drastic change in crystallization mechanism can be invoked merely by tethering one chain-end on a nanolamella interface. It should be noted that the change of the crystallization mechanism is not observed in PCL-*b*-PS7 and PCL/PS7 ($d_{\mathrm{PCL}} = 15.8$ nm), which have larger nanolamellae than PCL-*b*-PS6 and PCL/PS6 ($d_{\mathrm{PCL}} = 8.7$ nm), indicating that the combined effects of space confinement and chain confinement is responsible for the change of the crystallization mechanism in PCL-*b*-PS6 and PCL/PS6.

As a quantitative measure of the crystallization rate, crystallization half time $t_{1/2}$, defined as the crystallization time at $\tilde{X}_{\mathrm{c}} = 0.5$, was calculated by $t_{1/2} = (\ln 2/K)^{1/n}$. The values of n and K were determined from the Avrami plot of time-X_{c} data obtained by DSC measurements as well as time-intensity data obtained by time-resolved SAXS measurements. **Figure 5.11** plots $t_{1/2}$ against the crystallization temperature T_{c}. It is clear that the temperature range in which PCL chains can crystallize in an experimentally accessible time is extremely lower in PCL-*b*-PS6 than in PCL/PS6. As was stated earlier, this is due to the difference in the crystallization mechanism caused by chain confinement.

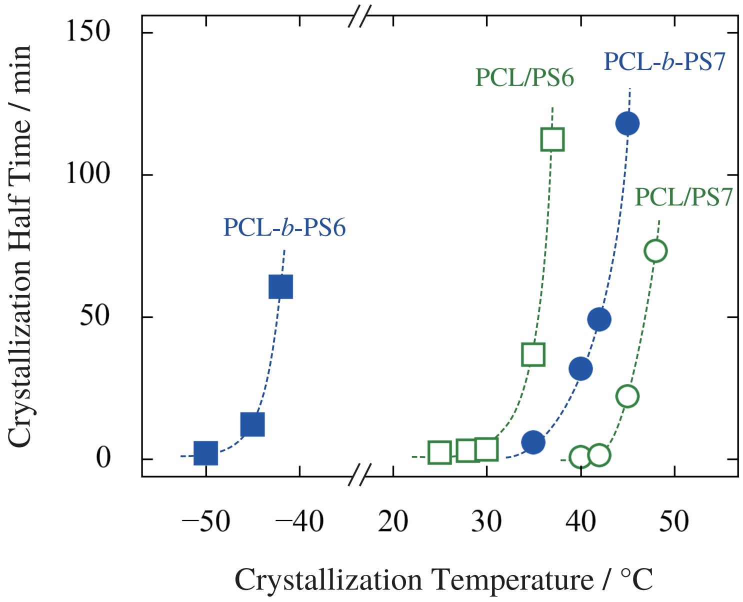

Figure 5.11. Crystallization half time $t_{1/2}$ plotted against crystallization temperature T_c for PCL-*b*-PS6 (closed squares), PCL/PS6 (open squares), PCL-*b*-PS7 (closed circles), and PCL/PS7 (open circles), with eye-guides drawn in dashed curves.

PCL block chains in PCL-*b*-PS6 can crystallize only by homogeneous nucleation, which has a much higher free energy barrier and hence requires a larger supercooling, whereas heterogeneous nucleation in PCL/PS6 takes place at a smaller supercooling owing to the lower free energy barrier of nucleation. PCL block chains in PCL-*b*-PS7 show longer $t_{1/2}$, i.e., slower crystallization than PCL homopolymers in PCL/PS7 when compared at the same T_c. Assuming that the number of heterogeneous nuclei per unit volume of PCL chains is constant, this observation indicates that chain confinement decelerates the growth of PCL crystals. However, the difference in crystallization rates between PCL-*b*-PS7 and PCL/PS7 is much less significant than that between PCL-*b*-PS6 and PCL/PS6. Therefore, as was mentioned earlier, chain confinement has more profound effects on crystallization in nanolamellae with smaller d_{PCL}. The conclusion is consistent with that of Chapters 2 and 4, where it was revealed that the effects of chain confinement on the nucleation rate of PCL chains were stronger in smaller nanocylinders.

Comparison of the crystallization rate of PCL homopolymers in nanolamellae with different d_{PCL} provides information about the influences of space confinement alone.

Clearly, PCL/PS6 ($d_{\mathrm{PCL}} = 8.7$ nm) crystallizes much slower than PCL/PS7 ($d_{\mathrm{PCL}} = 15.8$ nm). There are two possible explanations for this observation. One is that the crystal growth would be moderately limited in small spaces sandwiched by hard walls of vitrified PS chains. The other is that the number of heterogeneous nuclei *per nanolamella* would become smaller as the number of nanolamellae per unit volume increases with decreasing d_{PCL}, assuming that the number of nuclei *per unit volume* of PCL chains is constant. It is, however, difficult to specify which factor is dominant, since it is impossible to evaluate the nucleation rate and crystal growth rate separately.

5.3.6 Effects of Chain Confinement on Crystallization Mechanism

The crystallization behavior of PCL-*b*-PS6 is qualitatively different from that of PCL/PS6, PCL-*b*-PS7, and PCL/PS7, because of the combined effects of space confinement and chain confinement. In order to understand the crystallization mechanism of PCL-*b*-PS6 in more detail, the time development of X_{c} during the special thermal history shown in **Figure 5.12**a was measured using DSC. PCL-*b*-PS6 is first annealed at 60 °C to erase previous thermal histories and quenched to -50 °C, where it is annealed for short time t_1 to form some PCL crystals by homogeneous nucleation. The sample is then heated to 25 °C and annealed for time t_2 for additional crystal growth, followed by heating to 60 °C at 10 $^{\circ}\mathrm{C\,min^{-1}}$ to determine X_{c}. **Figure 5.12**b shows the time evolution of X_{c} in PCL-*b*-PS6 with $t_1 = 0.5$ min and 2.0 min. Additional crystallization is observed at 25 °C after the partial crystallization at -50 °C. This result is interesting because isothermal crystallization of PCL-*b*-PS6 at 25 °C does not yield any crystallinity within the experimental time scale. It is speculated that homogeneous nucleation at -50 °C generated many tiny crystallites randomly distributed within nanolamellae, which act as nuclei for further crystal growth at 25 °C. If the number of crystallites formed at -50 °C is large enough, the evolution of the overall crystallinity can be observed even if crystal growth from the individual nucleus is extremely slow. Therefore, it is possible that the crystallization via the heterogeneous nucleation and growth mechanism is prohibited for

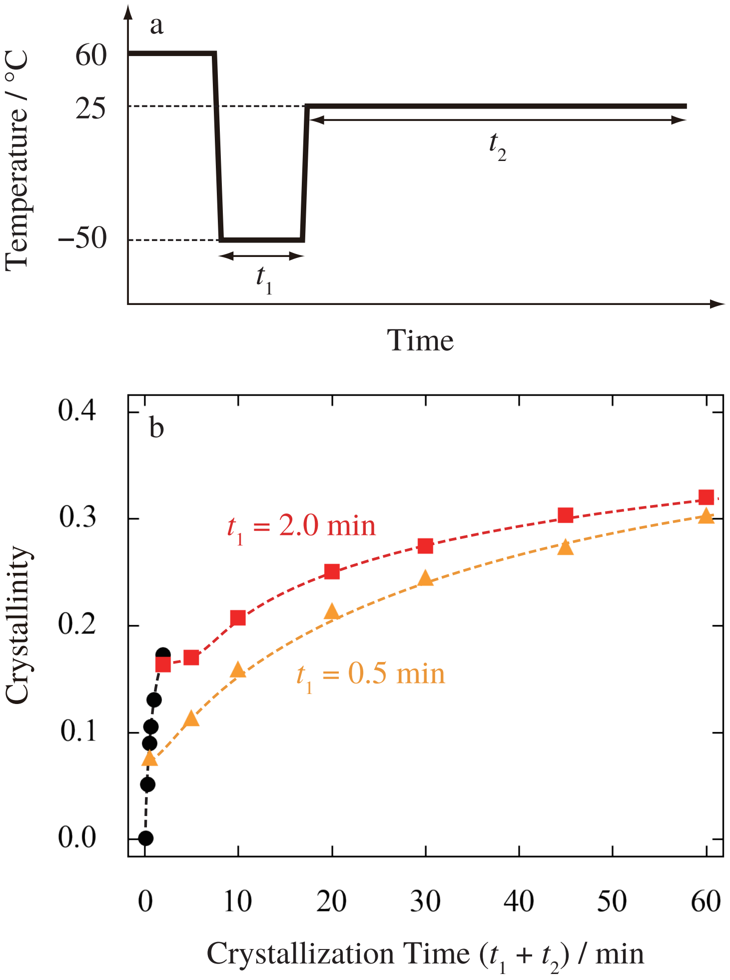

Figure 5.12. Temperature program (a) and time evolution of crystallinity (b) during the temperature jump experiments for PCL-*b*-PS6. PCL-*b*-PS6 was first crystallized at −50 °C for time t_1 and then instantaneously heated to 25 °C, followed by isothermal annealing for time t_2. The time evolution of crystallinity in PCL-*b*-PS6 with $t_1 = 0.5$ min (triangles) and $t_1 = 2.0$ min (squares) is plotted against crystallization time $t = t_1 + t_2$.

PCL block chains in PCL-*b*-PS6 because the crystal growth is extraordinarily slow due to the reduced mobility of PCL chains by chain confinement.

Figure 5.13 illustrates the effects of chain confinement and space confinement revealed in the above discussion. PCL homopolymers confined in nanolamellae with $d_{\mathrm{PCL}} = 8.7$ nm (top right) crystallize via the heterogeneous nucleation and growth mechanism, while PCL block chains in an identical nanolamella (top left) can crystallize only by homogeneous nucleation because chain confinement significantly retards the crystal

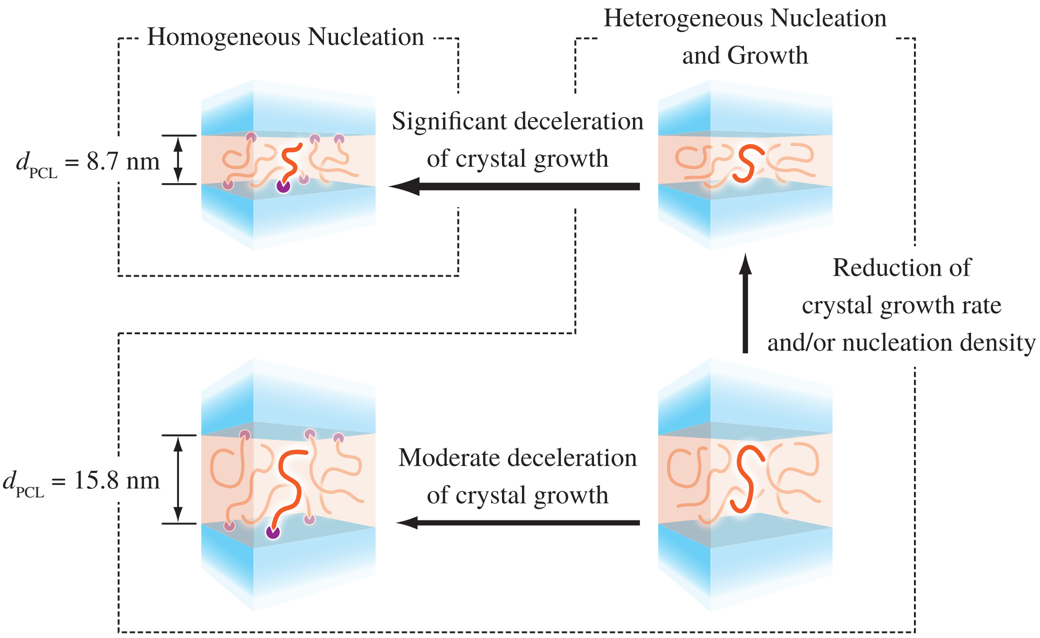

Figure 5.13. Schematic illustration of the conclusions as to the effects of space confinement and chain confinement on the crystallization of PCL chains confined in nanolamellae.

growth. In larger nanolamellae with $d_{\mathrm{PCL}} = 15.8$ nm (bottom left and bottom right), chain confinement moderately hinders the crystal growth but does not change the crystallization mechanism. The crystallization is also decelerated by confining PCL homopolymers in smaller nanolamellae (bottom right → top right), which would be caused by the decrease of the crystal growth rate and/or number of nuclei in one nanolamella.

5.4 Conclusions

The crystallization behavior of PCL homopolymers and PCL block chains confined in an identical nanolamella was examined to clarify the effects of chain confinement and space confinement on the crystallization mechanism. Two PCL-*b*-PS diblock copolymers were used, each forming lamellar microphase-separated structures (nanolamellae) with the PCL layer thickness d_{PCL} of 8.7 or 15.8 nm. PCL block chains in PCL-*b*-PS diblock copolymers were successfully converted into PCL homopolymers by photocleavage of ONB inserted at the block junction. SAXS measurements revealed that the nanolamellae were not destroyed on the crystallization and melting of PCL chains as well as photocleavage of block junctions, although time-resolved SAXS measurements showed that nanolamellae in the samples after photocleavage might be partially perturbed by annealing above the melting temperature T_{m} of PCL chains for a long time.

The melting and crystallization behavior were investigated using DSC measurements and time-resolved SAXS measurements, the results of which provided the following conclusions:

1. The melting temperature T_{m} and crystallinity X_{c} of PCL block chains in nanolamellae with $d_{\mathrm{PCL}} = 8.7$ nm were constant regardless of T_{c}, while the increase of T_{m} and X_{c} with increasing T_{c} was observed for PCL homopolymers in the same nanolamella as well as for PCL homopolymers and PCL block chains in nanolamellae with $d_{\mathrm{PCL}} = 15.8$ nm. This difference was attributed to the difference in the crystallization mechanism.

2. In nanolamellae with $d_{\mathrm{PCL}} = 8.7$ nm, PCL block chains and homopolymers showed qualitatively different crystallization behaviors. The time evolution of X_{c} in PCL block chains obeyed first-order-like kinetics, whereas that in PCL homopolymers was similar to that commonly observed in crystallization of bulk homopolymers. The results suggested that the crystallization mechanism was changed by chain confinement from the conventional heterogeneous nucleation and growth mechanism to the homogeneous nucleation-controlled mechanism, presumably because the chain confinement reduced the mobility of PCL chains which led to the extremely slow crystal growth.

3. In nanolamellae with $d_{\mathrm{PCL}} = 15.8$ nm, both PCL homopolymers and PCL block chains crystallized via the heterogeneous nucleation and growth mechanism and chain confinement moderately hindered the crystal growth. This fact indicates that the effects of chain confinement is less significant in larger nanolamellae.

4. Crystallization of PCL homopolymers was slower in smaller nanolamellae, possibly because the crystal growth rate was slower and/or the number of heterogeneous nuclei in a single nanolamella was lower.

References

1. Taden, A.; Landfester, K. *Macromolecules* **2003**, *36*, 4037–4041.
2. Massa, M. V.; Dalnoki-Veress, K. *Physical Review Letters* **2004**, *92*, 1–4.
3. Massa, M. V.; Lee, M. S. M.; Dalnoki-Veress, K. *Journal of Polymer Science Part B: Polymer Physics* **2005**, *43*, 3438–3443.
4. Massa, M. V.; Carvalho, J. L.; Dalnoki-Veress, K. *Physical Review Letters* **2006**, *97*, 1–4.
5. Kailas, L.; Vasilev, C.; Audinot, J.-N.; Migeon, H.-N.; Hobbs, J. K. *Macromolecules* **2007**, *40*, 7223–7230.
6. Carvalho, J. L.; Dalnoki-Veress, K. *Physical Review Letters* **2010**, *105*, 237801–1.
7. Carvalho, J. L.; Dalnoki-Veress, K. *The European Physical Journal E* **2011**, *34*, 1–6.
8. Michell, R. M.; Blaszczyk-Lezak, I.; Mijangos, C.; Müller, A. J. *Polymer* **2013**, *54*, 4059–4077.
9. Shin, K.; Woo, E.; Jeong, Y. G.; Kim, C.; Huh, J.; Kim, K.-W. *Macromolecules* **2007**, *40*, 6617–6623.
10. Woo, E.; Huh, J.; Jeong, Y. G.; Shin, K. *Physical Review Letters* **2007**, *98*, 136103.
11. Duran, H.; Steinhart, M.; Butt, H.-J.; Floudas, G. *Nano letters* **2011**, *11*, 1671–1675.
12. Michell, R. M.; Lorenzo, A. T.; Müller, A. J.; Lin, M.-C.; Chen, H.-L.; Blaszczyk-Lezak, I.; Martín, J.; Mijangos, C. *Macromolecules* **2012**, *45*, 1517–1528.
13. Maiz, J.; Martin, J.; Mijangos, C. *Langmuir* **2012**, *28*, 12296–303.
14. Guan, Y.; Liu, G.; Gao, P.; Li, L.; Ding, G.; Wang, D. *ACS Macro Letters* **2013**, *2*, 181–184.
15. Suzuki, Y.; Duran, H.; Akram, W.; Steinhart, M.; Floudas, G.; Butt, H.-J. *Soft Matter* **2013**, *9*, 9189.
16. Guan, Y.; Liu, G.; Ding, G.; Yang, T.; Müller, A. J.; Wang, D. *Macromolecules* **2015**, *48*, 2526–2533.
17. Wang, H.; Keum, J. K.; Hiltner, A.; Baer, E. *Macromolecules* **2010**, *43*, 3359–3364.
18. Ponting, M.; Lin, Y.; Keum, J. K.; Hiltner, A.; Baer, E. *Macromolecules* **2010**, *43*, 8619–8627.

19. Zhu, L.; Cheng, S. Z. D.; Calhoun, B. H.; Ge, Q.; Quirk, R. P.; Thomas, E. L.; Hsiao, B. S.; Yeh, F.; Lotz, B. *Journal of the American Chemical Society* **2000**, *122*, 5957–5967.

20. Loo, Y.-L.; Register, R. A.; Ryan, A. J. *Physical Review Letters* **2000**, *84*, 4120–4123.

21. Loo, Y.-L.; Register, R. A.; Ryan, A. J.; Dee, G. T. *Macromolecules* **2001**, *34*, 8968–8977.

22. Zhu, L.; Mimnaugh, B. R.; Ge, Q.; Quirk, R. P.; Cheng, S. Z. D.; Thomas, E. L.; Lotz, B.; Hsiao, B. S.; Yeh, F.; Liu, L. *Polymer* **2001**, *42*, 9121–9131.

23. Huang, P.; Zhu, L.; Cheng, S. Z. D.; Ge, Q.; Quirk, R. P.; Thomas, E. L.; Lotz, B.; Hsiao, B. S.; Liu, L.; Yeh, F. *Macromolecules* **2001**, *34*, 6649–6657.

24. Shiomi, T.; Tsukada, H.; Takeshita, H.; Takenaka, K.; Tezuka, Y. *Polymer* **2001**, *42*, 4997–5004.

25. Nojima, S.; Toei, M.; Hara, S.; Tanimoto, S.; Sasaki, S. *Polymer* **2002**, *43*, 4087–4090.

26. Chen, H.-L.; Li, H.-C.; Huang, Y.-Y.; Chiu, F.-C. *Macromolecules* **2002**, *35*, 2417–2422.

27. Lee, W.; Chen, H.-L.; Lin, T.-L. *Journal of Polymer Science Part B: Polymer Physics* **2002**, *40*, 519–529.

28. Ho, R.-M.; Lin, F.-H.; Tsai, C.-C.; Lin, C.-C.; Ko, B.-T.; Hsiao, B. S.; Sics, I. *Macromolecules* **2004**, *37*, 5985–5994.

29. Huang, P.; Zhu, L.; Guo, Y.; Ge, Q.; Jing, A. J.; Chen, W. Y.; Quirk, R. P.; Cheng, S. Z. D.; Thomas, E. L.; Lotz, B.; Hsiao, B. S.; Avila-Orta, C. A.; Sics, I. *Macromolecules* **2004**, *37*, 3689–3698.

30. Takeshita, H.; Ishii, N.; Araki, C.; Miya, M.; Takenaka, K.; Shiomi, T. *Journal of Polymer Science Part B: Polymer Physics* **2004**, *42*, 4199–4206.

31. Huang, P.; Guo, Y.; Quirk, R. P.; Ruan, J.; Lotz, B.; Thomas, E. L.; Hsiao, B. S.; Avila-Orta, C. A.; Sics, I.; Cheng, S. Z. D. *Polymer* **2006**, *47*, 5457–5466.

32. Lorenzo, A. T.; Arnal, M. L.; Müller, A. J.; Boschetti-de-Fierro, A.; Abetz, V. *European Polymer Journal* **2006**, *42*, 516–533.

33. Sun, Y.-S.; Chung, T.-M.; Li, Y.-J.; Ho, R.-M.; Ko, B.-T.; Jeng, U.-S.; Lotz, B. *Macromolecules* **2006**, *39*, 5782–5788.

34. Sun, Y.-S.; Chung, T.-M.; Li, Y.-J.; Ho, R.-M.; Ko, B.-T.; Jeng, U.-S. *Macromolecules* **2007**, *40*, 6778–6781.

35. Boschetti-de-Fierro, A.; Lorenzo, A. T.; Müller, A. J.; Schmalz, H.; Abetz, V. *Macromolecular Chemistry and Physics* **2008**, *209*, 476–487.

36. Nojima, S.; Inokawa, D.; Kawamura, T.; Nitta, K.-h. *Polymer Journal* **2008**, *40*, 986–991.

37. Cai, T.; Qian, Y.; Ma, Y.; Ren, Y.; Hu, W. *Macromolecules* **2009**, *42*, 3381–3385.

38. Myers, S. B.; Register, R. A. *Macromolecules* **2010**, *43*, 393–401.

39. Gitsas, A.; Floudas, G.; Butt, H. J.; Pakula, T.; Matyjaszewski, K. *Macromolecules* **2010**, *43*, 2453–2462.

40. Chung, T.-M.; Wang, T.-C.; Ho, R.-M.; Sun, Y.-S.; Ko, B.-T. *Macromolecules* **2010**, *43*, 6237–6240.

41. Lin, M.-C.; Wang, Y.-C.; Chen, H.-L.; Müller, A. J.; Su, C.-J.; Jeng, U.-S. *Journal of Physical Chemistry B* **2011**, *115*, 2494–2502.

42. Lin, M.-C.; Nandan, B.; Chen, H.-L. *Soft Matter* **2012**, *8*, 7306–7322.

43. Kim, Y. Y.; Ahn, B.; Sa, S.; Jeon, M.; Roth, S. V.; Kim, S. Y.; Ree, M. *Macrmolecules* **2013**, *46*, 8235–8244.

44. Malek, A.; Dingenouts, N.; Beskers, T. F.; Fehrenbacher, U.; Barner, L.; Wilhelm, M. *European Polymer Journal* **2013**, *49*, 2704–2720.

45. Huang, C.-L.; Jiao, L.; Zeng, J.-B.; Zhang, J.-J.; Yang, K.-K.; Wang, Y.-Z. *The Journal of Physical Chemistry B* **2013**, *117*, 10665–10676.

46. Chen, L.; Jiang, J.; Wei, L.; Wang, X.; Xue, G.; Zhou, D. *Macromolecules* **2015**, *48*, 1804–1812.

47. Guillier, F.; Orain, D.; Bradley, M. *Chemical Reviews* **2000**, *100*, 2091–158.

48. Avrami, M. *The Journal of Chemical Physics* **1939**, *7*, 1103–1112.

49. Avrami, M. *The Journal of Chemical Physics* **1940**, *8*, 212–224.

Chapter 6

Crystallization of Ends-Tethered Polymer Chains Confined in Nanolamellae

6.1 Introduction

Crystallization of homopolymers confined in nanodomains has been extensively studied using a variety of systems including droplets[1–5], nanopores of AAO templates[6–10], and nanolayered films[11–15]. Block copolymers have also been exploited to explore the confined crystallization of polymer chains[16–20], though the effects of fixed ends of block chains (*chain confinement*) should also be considered in addition to the effects of spatial restriction by nanodomains (*space confinement*). Preceding chapters of this thesis aimed to clarify the effects of both *chain confinement* and *space confinement* on polymer crystallization. It was revealed that chain confinement significantly affected the crystallization behavior and crystal orientation of PCL chains confined in nanodomains, and the effects drastically depended on the shape and size of nanodomains, indicating that chain confinement and space confinement cooperatively worked on the dynamics of PCL chains. One of the most striking result was obtained in Chapter 5, where it was found that PCL homopolymers and PCL block chains confined in an identical nanolamella crystallized by completely different crystallization mechanisms.

Until now, chain confinement has been considered only in diblock copolymers, in which one end of the crystallizable chain was fixed on the nanodomain interface. Considering the significant effects of chain confinement found in the preceding chapters, it

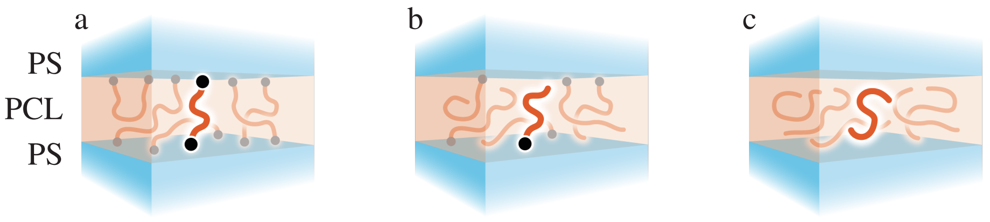

PCL chains tethered at both ends "T2-PCL"

PCL chains tethered at one end "T1-PCL"

PCL chains tethered at no end "T0-PCL"

Figure 6.1. Schematic illustration of PCL chains tethered at both ends (a), one end (b), and no end (c) all confined in an identical nanolamella sandwiched with vitrified PS layers.

is interesting to explore the effects of chain tethering at *both ends* on polymer crystallization. Various systems including triblock, multiblock, and cyclic block copolymers contain polymer chains tethered at both ends, among which ABA triblock copolymers are the simplest and hence best understood. It is known both theoretically[21–23] and experimentally[24,25] that microphase-separated structures formed in symmetric ABA triblock copolymers are nearly identical to those formed in AB diblock copolymers with the same block composition but half the molecular weight of the ABA triblock copolymers. Although crystallization of middle block chains in amorphous-crystalline-amorphous triblock copolymers has been studied by several authors[26–31], none of these researches successfully evaluated the impacts of chain confinement, because it is experimentally difficult to distinguish the effects of chain confinement from those of space confinement.

In this study, the author investigates the crystallization behavior of PCL chains tethered at both ends, one end, and no end, all confined in an identical nanolamella, which are hereafter designated as T2-PCL, T1-PCL, and T0-PCL, respectively (**Figure 6.1**). The aim of this study is to capture the entire picture of the roles of chain confinement in polymer crystallization. To confine T2-PCL, T1-PCL, and T0-PCL in an identical nanolamella, the author developed a set of model systems constructed from two photocleavable PS-*b*-PCL-*b*-PS triblock copolymers bearing ONB at either or both of block junctions.

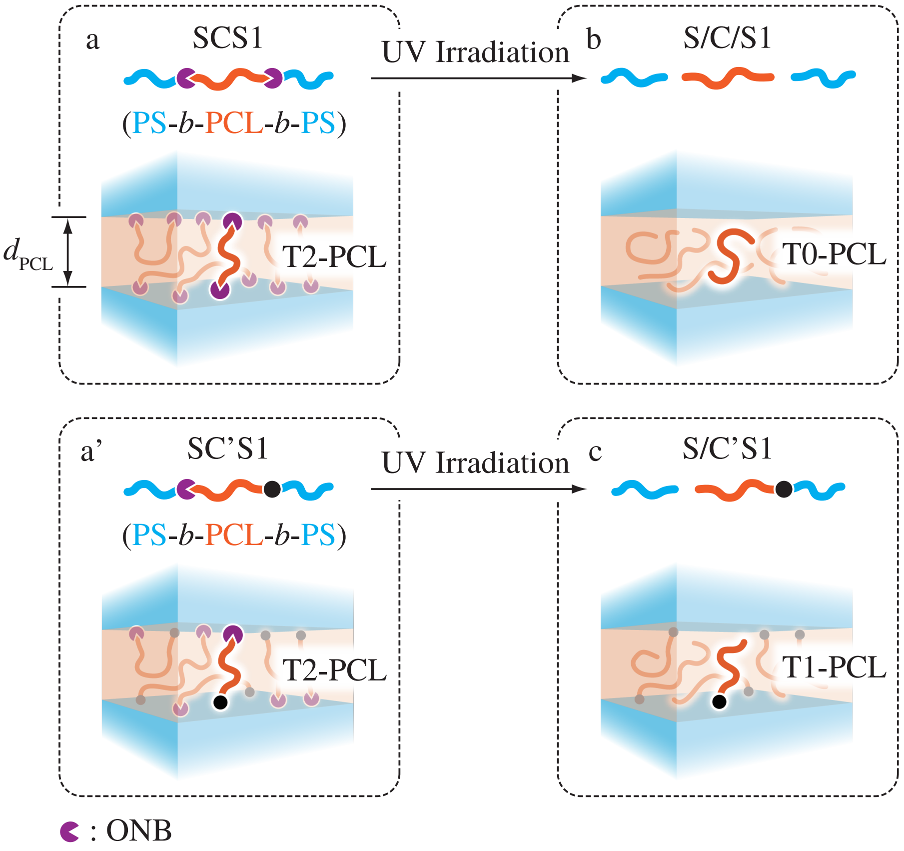

Figure 6.2. Schematic illustration showing the construction of model systems for the current study. Two PS-*b*-PCL-*b*-PS triblock copolymers (a and a’) forming an identical lamellar microphase-separated structure are subjected to UV irradiation, by which T2-PCL is converted to T0-PCL (b) or T1-PCL (c).

6.2 Experimental Section

6.2.1 Model Systems

Figure 6.2 illustrates the sample preparation strategy of this study. First, two lamella-forming symmetric PS-*b*-PCL-*b*-PS triblock copolymers with the same total molecular weight and block composition are synthesized. The only difference between two triblock copolymers is that one has photocleavable *o*-nitrobenzyl groups (ONB) in both of two block junctions, whereas the other has only one ONB in either of two block junctions. The former triblock copolymer is hereafter called SCS1 and the latter SC’S1.

Table 6.1. Characterization of the samples used in this study.

Code	M_n / g mol^{-1}			M_w/M_n [b]	ϕ_{PCL} [d]	d_{PCL} [e]/ nm	x_0 [f]	x_1 [g]
	PCL [a]	PS [b]	Total [c]					
SCS1	27400	13500×2	54400	1.04	0.50	10.9	0	0
S/C/S1	27400	13500×2	-	-	0.50	10.9	0.79	0.16
SC'S1	27400	13500×2	54400	1.05	0.50	11.0	0	0
S/C'S1	27400	13500×2	-	-	0.50	11.0	0	0.95

[a] Determined by ^{1}H-NMR.
[b] Determined by GPC.
[c] Sum of M_ns of the PCL and PS blocks.
[d] Volume fraction of PCL chains calculated from M_ns and specific volumes of PCL and PS at 100 °C.
[e] The thickness of nanolamellae in which PCL chains are confined, calculated from the primary peak position in SAXS curves and volume fraction of PCL chains.
[f] Mole fraction of T0-PCL in the system determined by GPC.
[g] Mole fraction of T1-PCL in the system determined by GPC.

Microphase-separated SCS1 (**Figure 6.2**a) and SC'S1 (a') both contain T2-PCL confined in nanolamellae sandwiched between PS layers. ONB at the block junctions of SCS1 and SC'S1 is then cleaved by UV irradiation to yield T0-PCL (b) and T1-PCL (c), respectively. SCS1 and SC'S1 after UV irradiation are designated as S/C/S1 and S/C'S1, respectively. Although the lamellar microphase-separated structure formed in SCS1 and SC'S1 is no longer the equilibrium morphology after the photocleavage, vitrified PS layers will prevent the nanolamellae from collapsing, as long as the temperature is kept well below the glass transition temperature T_g of PS homopolymers ($\sim$ 100 °C).

6.2.2 Samples and Sample Preparation

The method of synthesis and chemical structure of the PS-*b*-PCL-*b*-PS triblock copolymers are illustrated in Appendix B, and the molecular characterization of each sample is summerized in **Table 6.1**. SCS1 and SC'S1 were synthesized from the same PCL and PS homopolymers, therefore the molecular weights of PCL blocks and PS blocks are common in these samples. The volume fraction of PCL chains ϕ_{PCL} in SCS1 and SC'S1 is equal to 1/2, from which the formation of a lamellar microphase-separated structure is expected.

All the experiments were carried out on solution-cast films of SCS1 and SC'S1. S/C/S1 and S/C'S1 were prepared by UV irradiation to the films of SCS1 and SC'S1 with the intensity of 4.0 $\mathrm{W\,cm^{-2}}$ for 40 min. The methods of film preparation and UV irradiation were already described in Section 2.2.2 of Chapter 2.

6.2.3 Gel Permeation Chromatography (GPC)

Gel permeation chromatography (GPC) was used to investigate the progress of the photocleavage reaction in SCS1 and SC'S1. Details of the equipment and setup were the same as those described in Section 2.2.3, except for that chloroform was used as an eluent in this study.

6.2.4 Small-angle X-ray Scattering (SAXS)

The microphase-separated structure formed in SCS1 and SC'S1 was examined by small-angle X-ray scattering (SAXS) using small-angle X-ray scattering equipment for solution (SAXES) installed at beam-line BL-10C of Photon Factory in High Energy Accelerator Research Organization, Tsukuba, Japan. The X-ray wavelength λ was 0.1488 nm and the sample-to-detector distance was ca. 2.6 m. A pixel-array detector (PILATUS3 2M, Dectris Ltd., Switzerland) having 1475×1679 pixels with each size of $172 \times 172\ \mu\mathrm{m}^2$ was used to collect 2-d scattering images, which were then circularly averaged to obtain 1-d profiles and corrected for background scattering and absorption. SAXS intensity was plotted against the magnitude of scattering vector $s = 2\sin\theta/\lambda$ (2θ: scattering angle) calibrated by silver behenate[32].

6.2.5 Differential Scanning Calorimetry (DSC)

The melting temperature T_m and crystallinity X_c of PCL chains were measured using differential scanning calorimetry (DSC). Details of equipment can be found in

Section 2.2.5 of Chapter 2. The temperature program applied is as follows. First, previous thermal histories of PCL chains were erased by annealing at 60 °C for 3 min. After that, the sample was quenched at 500 $^\circ\mathrm{C\,min^{-1}}$ to a selected crystallization temperature T_c and crystallized there for time t, and heated back to 60 °C at 10 $^\circ\mathrm{C\,min^{-1}}$ while collecting endothermic heat flow arising from the melting of PCL chains. T_m and X_c were determined from the endothermic peak by the method described in Section 2.2.5 of Chapter 2. The development of X_c during isothermal crystallization of T2-PCL in SCS1 and SC'S1, which could crystallize only below room temperature, was measured by repeating the above temperature program for varying t. Since PCL chains in S/C/S1 and S/C'S1 could crystallize above room temperature, the progress of the crystallization could be pursued using time-resolved IR measurements described in the next section. Therefore, DSC was used only to determine the final values of X_c and T_m for S/C/S1 and S/C'S1.

6.2.6 Infrared Spectroscopy (IR)

The development of the normalized crystallinity $\tilde{X}_c$, defined as X_c at time t divided by its final value, was observed by time-resolved infrared spectroscopy (IR) using a Fourier-transform IR spectrometer (FT-IR 6200, JASCO, Japan) in transmission mode. Measurements were carried out on a sample film with the thickness of ca. 20 μm placed on a silicon substrate, which was set in a hand-made temperature-controlled sample holder. The sample was first annealed at 60 °C for 3 min to erase previous thermal histories, quenched to a prescribed crystallization temperature T_c, and isothermally annealed until the crystallization of PCL chains completed. IR spectra with the resolution of 4 $\mathrm{cm^{-1}}$ and the integration number of 16 were iteratively recorded during isothermal annealing. **Figure 6.3** shows the IR spectra collected during isothermal crystallization of S/C/S1 at $T_c = 32.5$ °C. Several absorption bands increase with time, which can be assigned to the crystalline bands of PCL[33]. $\tilde{X}_c$ is calculated by normalizing the area of the band at 1295 $\mathrm{cm^{-1}}$ (evaluated by fitting with a Gaussian function) by its final value. Unfortunately, this

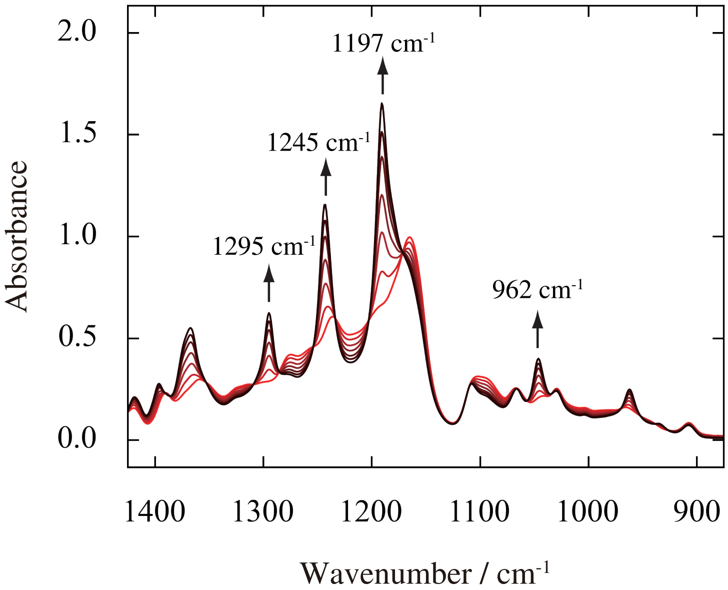

Figure 6.3. IR spectra collected during the isothermal crystallization of S/C/S1 at $T_c = 32.5$ °C. Curve colors change from red to black with the progress of crystallization. Several crystalline bands are marked with upward arrows according to the literature[33].

measurement was unavailable below room temperature due to instrumental limitations, so the time evolution of crystallinity in SCS1 and SC'S1, which could not crystallize in an experimental time scale at room temperature, was tracked by DSC measurements.

6.3 Results and Discussion

6.3.1 Photocleavage Behavior

Figure 6.4 shows the GPC chromatograms of SCS1 (a) and SC'S1 (b) after UV irradiation with changing total UV irradiation energy E_t, which is defined as the product of UV intensity and irradiation time. With increasing E_t, the unimodal peak observed for SCS1 and SC'S1 at $E_t = 0$ (before UV irradiation) turns into multiple overlapped peaks. The results of curve fitting shown in colored curves indicate that the chromatograms are actually a superposition of four different peaks, each corresponding to unreacted PS-*b*-PCL-*b*-PS triblock copolymers, PCL-*b*-PS diblock copolymers, dimerized PS homopolymers, and PS homopolymers, in the increasing order of elution time. The

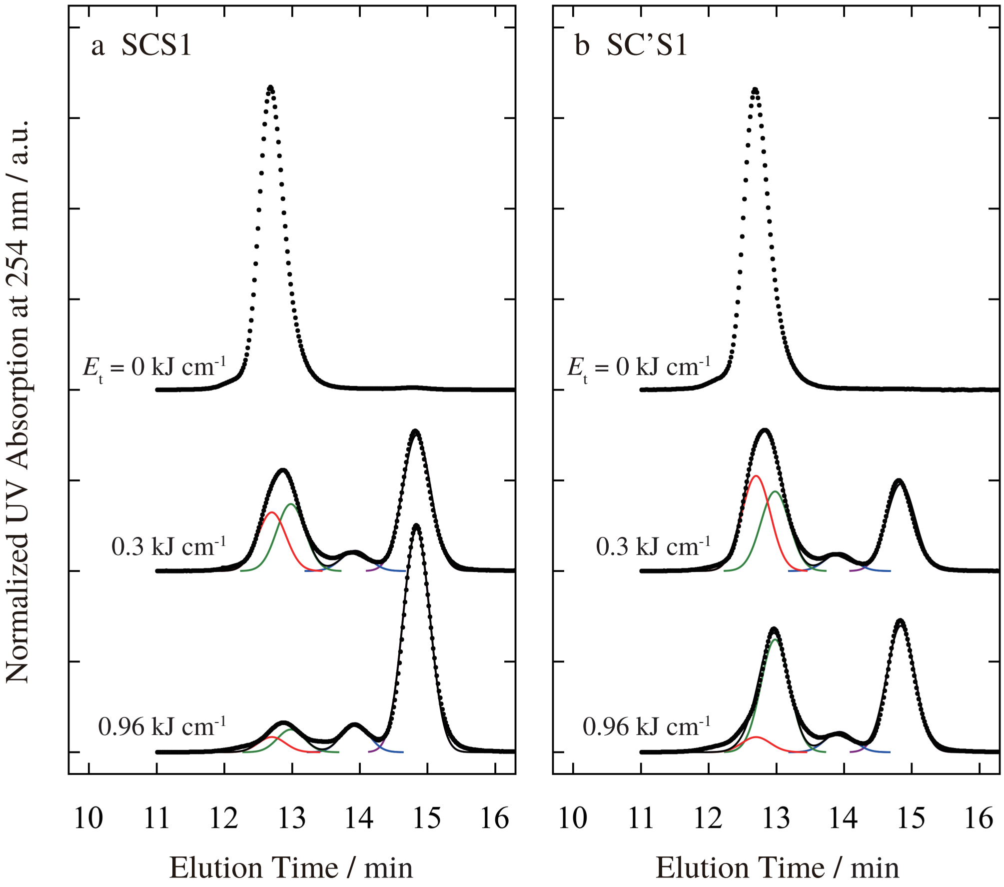

Figure 6.4. GPC chromatograms of SCS1 (a) and SC'S1 (b) after UV irradiation with indicated total irradiation energy E_t. Black dots represent experimental data. The results of curve fitting are shown in black curves, and individual Gaussian functions corresponding to PS-*b*-PCL-*b*-PS, PCL-*b*-PS, dimerized PS homopolymers, and PS homopolymers are drawn with red, green, blue, and purple curves, respectively.

dimerization of PS homopolymers was presumably caused by a coupling reaction between nitroso groups^{34} generated at the end of PS homopolymer by the photocleavage of ONB groups, as was mentioned in the previous chapters (see Sections 2.3.1 and 5.3.1). Note that PCL homopolymers that should appear by photocleavage of SCS1 are not detected because PCL chains are transparent to the wavelength used for the measurements.

As a quantitative measure of the progress of photocleavage, the mole fractions of T0-PCL, T1-PCL, and T2-PCL were defined as x_0,x_1, and x_2, respectively. These quantities can be calculated from the area ratio of four GPC peaks assigned above, according to the method described in Sections C.3 (for SCS1) and C.4 (for SC'S1) of Appendix

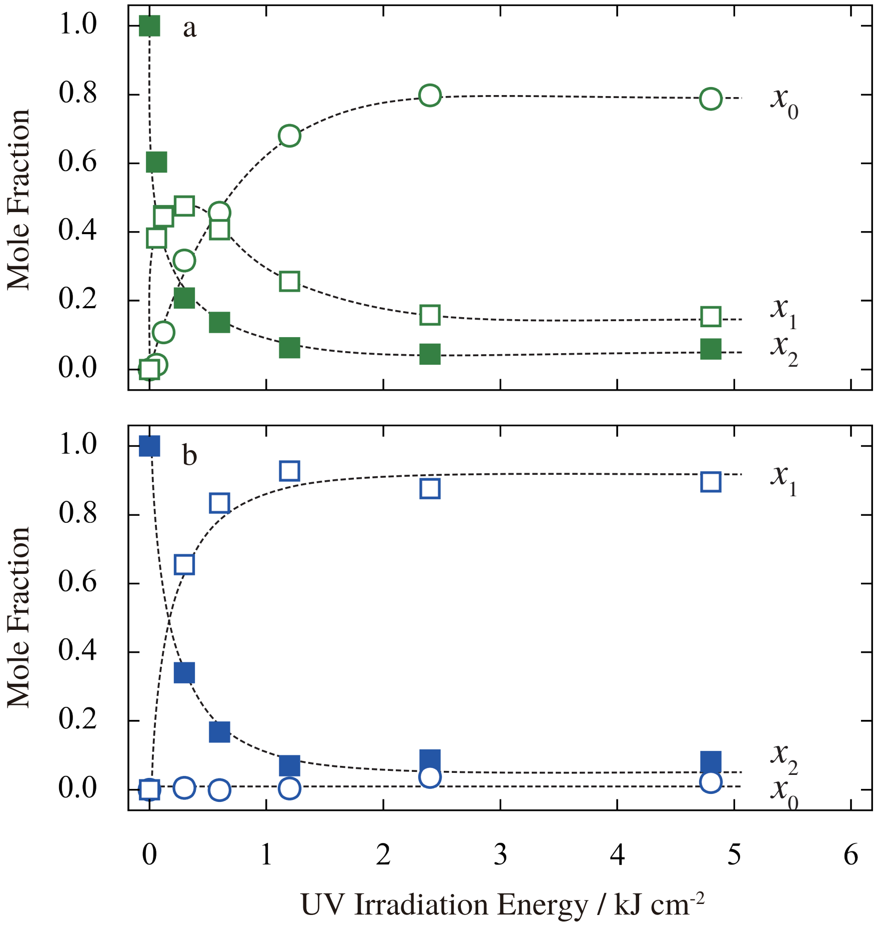

Figure 6.5. Mole fractions of T2-PCL (x_2, solid squares), T1-PCL (x_1, open squares), and T0-PCL (x_0, open circles) in SCS1 (a) and SC'S1 (b) plotted against total UV energy irradiated, with eye-guides drawn in dashed curves.

C. **Figure 6.5** shows x_0, x_1, and x_2 as a function of E_t for SCS1 (a) and SC'S1 (b). x_2 in both SCS1 and SC'S1 monotonically decreases with increasing E_t, while the behaviors of x_1 and x_0 are completely different between the two samples. In SCS1, x_0 increases monotonically with increasing E_t, whereas x_1 increases to reach a maximum at $E_t \sim 0.3\,\mathrm{kJ\,cm^{-2}}$ and then asymptotically decreases to ~ 0.16. This behavior should result from a simple two-step reaction, in which two PS block chains are sequentially detached from a PS-*b*-PCL-*b*-PS triblock copolymer. On the other hand, x_1 of SC'S1 increased monotonically with increasing E_t, while x_0 remained almost zero regardless of E_t, indicating that either of two block junctions in SC'S1 is selectively cleaved by UV

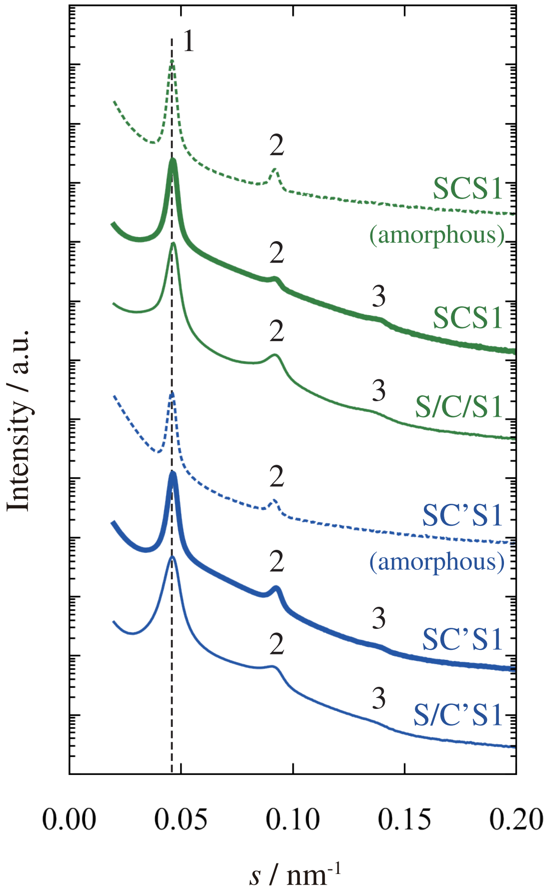

Figure 6.6. SAXS curves of SCS1 (thick green curve), S/C/S1 (thin green curve), S/C'S1 (thick blue curve), and S/C'S1 (thin blue curve) in the crystallized state. The data in the amorphous state (at 60 °C) are plotted with dashed green and blue curves for SCS1 and SC'S1, respectively. The vertical dashed line indicates primary peak positions.

irradiation. The data in **Figure 6.5** generally indicate that the photocleavage behavior of SCS1 and SC'S1 is completely consistent with the molecular design.

6.3.2 Microphase-separated Structure

Figure 6.6 shows the SAXS curves of SCS1 (green curves) and SC'S1 (blue curves), where thick solid curves and dashed curves represent the data in the crystallized state and amorphous state (measured at 60 °C), respectively. The curves for SCS1 and SC'S1 in the crystallized state display a sharp primary peak and two higher order peaks, the relative positions of which precisely correspond to a ratio of 1 : 2 : 3, clearly indicating the formation of a lamellar microphase-separated structure (nanolamella). Primary peak positions of SCS1 and SC'S1 nearly coincide with each other, suggesting that nanolamellae in the two samples are almost identical. Moreover, the primary peak position in the amorphous state is completely identical to that in the crystallized state for both SCS1 and SC'S1, indicating that PCL chains are effectively confined in nanolamellae during the crystallization and melting process. However, the third order peak observed in the crystallized state is absent in the amorphous state for both samples. Similar phenomena were observed for cylinder-forming and lamella-forming PCL-*b*-PS diblock copolymers (Chapters 2, 4, and 5), and can be explained by a change in the electron density contrast: the difference of electron density between PS chains and amorphous PCL chains is much smaller than that between PS chains and crystallized PCL chains (see Section 2.3.2). **Figure 6.6** also shows the SAXS curves of crystallized S/C/S1 (thin green curve) and S/C'S1 (thin blue curve), the samples after UV irradiation. The shape and primary peak position of SCS1 and SC'S1 are essentially preserved after UV irradiation, suggesting that the nanolamellae formed in these samples are not perturbed even by the photocleavage of block junctions.

The stability of nanolamellae in S/C/S1 and S/C'S1 should be examined carefully because they are actually blend systems mainly consisting of PCL homopolymers and PS homopolymers (for S/C/S1) or PCL-*b*-PS diblock copolymers and PS homopolymers (for S/C'S1). To evaluate the stability of nanolamellae against melting and crystallization of PCL chains, S/C/S1 and S/C'S1 were subjected to repeated cycles of crystallization and melting. One cycle consisted of the crystallization at 5 °C for 10 min and subsequent melting at 60 °C, and each melt morphology was measured using SAXS. **Figure 6.7** shows the intensity (circles) and long period (squares) of SAXS primary peak measured at the end of each cycle plotted against the number of cycles for S/C/S1 (green) and S/C'S1 (blue). The long period is completely unchanged by crystallization/melting cycles in both samples. However, the primary peak intensity for S/C/S1 gradually decreases with increasing the number of cycles, whereas it remains almost constant for S/C'S1. The

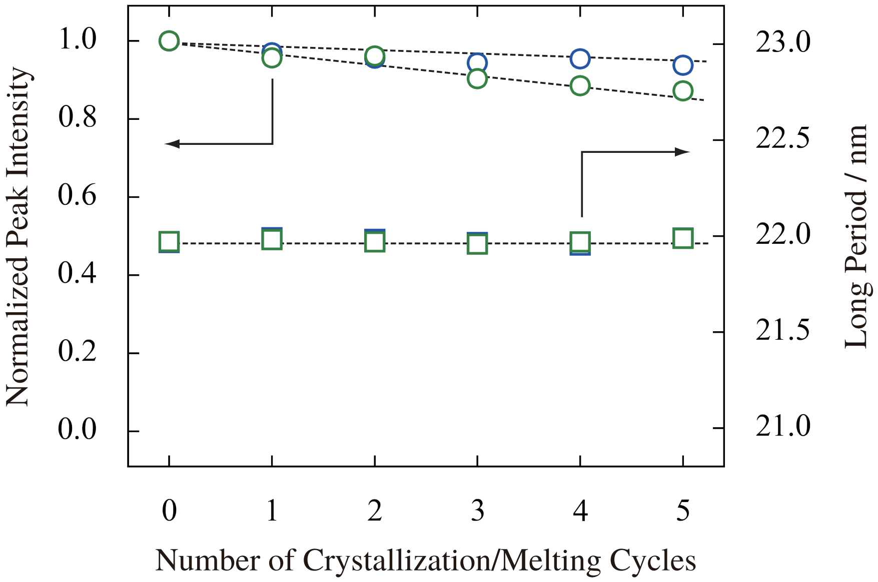

Figure 6.7. Variation of SAXS primary peak intensity (circles) and long period (squares) of S/C/S1 (green) and S/C'S1 (blue) plotted against the number of crystallization/melting cycles. In each cycle, PCL chains in the samples were first crystallized at 5 °C and then melted at 60 °C before the SAXS measurement. Peak intensity is normalized by the initial value. Dashed lines are just a guide for the eye.

results suggest that nanolamellae in both samples are not destroyed by the crystallization and melting of PCL chains, but those in S/C/S1 may be slightly distorted either by the crystallization and/or melting of PCL chains. This hypothesis is also supported by the fact that the crystallinity of PCL chains in S/C/S1 measured by DSC gradually increased when the same crystallization condition was repeatedly applied to one sample, probably due to a deformation of nanolamellae to accommodate larger PCL crystals. On the other hand, the crystallinity of PCL chains in S/C'S1 showed a good reproducibility. The difference in the stability of nanolamellae between S/C/S1 and S/C'S1 may be attributed to the fact that T0-PCL in S/C/S1 can move freely while the long-range diffusion of T1-PCL in S/C'S1 is strictly prohibited by a chain-end fixed onto a nanolamella interface. Based on the above consideration, freshly prepared S/C/S films were always used for all isothermal crystallization experiments by DSC and IR.

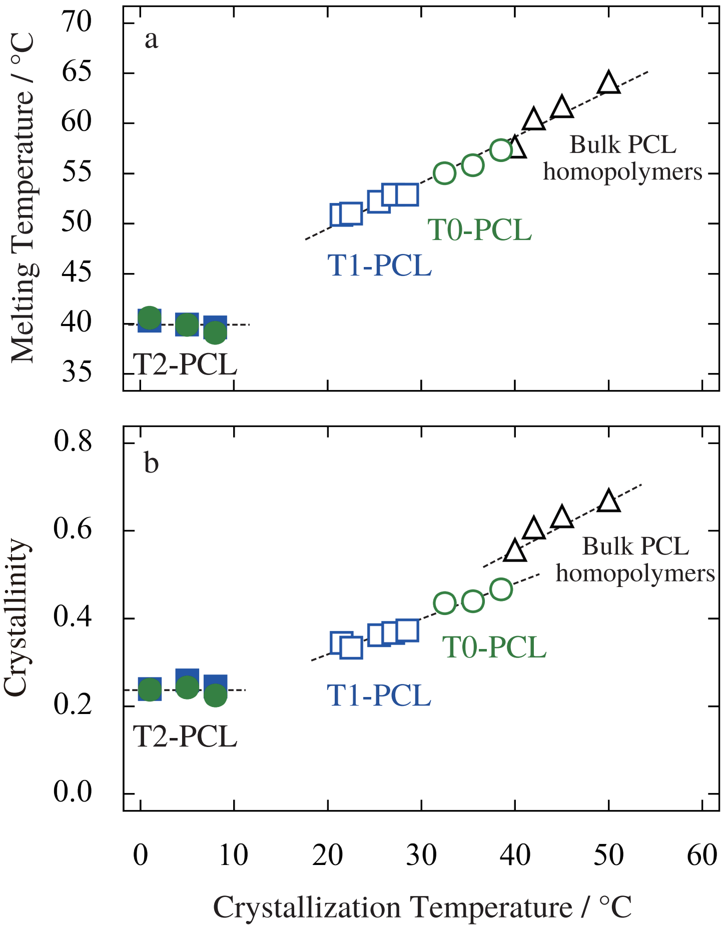

Figure 6.8. Melting temperature T_m (a) and crystallinity X_c (b) plotted as a function of crystallization temperature T_c for PCL chains in SCS1 (closed circles), SC'S1 (closed squares), S/C'S1 (open squares), and S/C/S1 (open circles). The data for bulk PCL homopolymers (open trialgles) with the molecular weight identical to that of PCL block chains in SCS1 and SC'S1 are also shown. Dashed lines are just a guide for the eye.

6.3.3 Melting Behavior of PCL Chains

The final melting temperature T_m and crystallinity X_c of PCL chains in SCS1, SC'S1, S/C/S1, and S/C'S1 are plotted in **Figure 6.8** against the crystallization temperature T_c. The data for bulk PCL homopolymers, which have the same molecular weight as PCL block chains in SCS1 and SC'S1, are also plotted for comparison. T_m of T0-PCL in S/C/S1 and T1-PCL in S/C'S1 increases with increasing T_c. Since T_m is generally related to the crystal thickness d_c by the Gibbs-Thomson equation, this result indicates that d_c of T0-PCL and T1-PCL is larger at higher T_c, as is usually observed for the crystallization of bulk homopolymers. In fact, **Figure 6.8**a shows that T_m of bulk PCL homopolymers also increases with increasing T_c. Interestingly, T_m of T0-PCL, T1-PCL, and bulk PCL homopolymers appears to fall on a common straight line, strongly suggesting that d_c of T0-PCL and T1-PCL is affected by neither chain confinement nor space confinement, at least in the T_c range investigated. X_c for T0-PCL and T1-PCL also shows a similar temperature dependence, though it is inherently lower than that of bulk PCL homopolymers. Since d_c of T0-PCL and T1-PCL is scarcely influenced by chain confinement and space confinement, lower X_c may indicate that the lateral dimension of crystals decreases by confining PCL chains in nanolamellae.

On the other hand, T_m and X_c of T2-PCL in SCS1 an SC'S1 are constant regardless of T_c and significantly lower than those of T0-PCL and T1-PCL, suggesting that the thickness and probably the lateral size of PCL crystals are restricted by chain tethering at both ends. Note that the data for SCS1 and SC'S1 perfectly coincide with each other, indicating that T2-PCL in both samples crystallizes in similar environment. There are several factors that potentially limit the crystal thickening of T2-PCL. It is plausible that d_c cannot exceed d_{PCL}, if the crystal stems orient random or perpendicular with respect to nanolamella interfaces. d_c would also be limited in the case where the crystal stems lie parallel to nanolamella interfaces, since nanolamellae are not infinitely straight. Therefore, d_c of PCL chains confined in nanolamellae should have an upper limit mainly determined by d_{PCL}. Moreover, the PCL repeating units near the tethered chain-ends would not be able to participate in the crystallization, which would further reduce the upper limit of d_c. This limit of d_c should be responsible for constant values of T_m independent of T_c for T2-PCL. The upper limit of d_c should also exist for T1-PCL and T0-PCL, but it will require a high T_c and a long crystallization time to actually confirm the limiting behavior.

On the basis of the above speculation, it is interesting to compare d_c with d_{PCL}. d_c

can be estimated roughly from T_m using the Gibbs-Thomson equation

$$T_\mathrm{m}^\circ - T_\mathrm{m} \propto \frac{1}{d_\mathrm{c}} \tag{6.1}$$

where T_m° is the equilibrium melting temperature. However, one should bear in mind that the conformational entropy of melted PCL chains confined in nanolamellae may be different from that of bulk PCL homopolymers, leading to the modification of T_m. Therefore, calculated d_c should be regarded as a rough estimation. T_m° and the proportional factor in equation (6.1) were obtained from experimentally determined T_m and d_c of bulk PCL homopolymers with the same molecular weight as PCL block chains in SCS1 and SC'S1. The PCL homopolymer was first crystallized at selected T_c ranging between 40 and 50 °C. T_m and X_c were then determined by the DSC measurement (**Figure 5.7**), and d_c was determined using SAXS by multiplying the long spacing of the primary peak by volume crystallinity. Plotting $1/d_\mathrm{c}$ against T_m gave a linear relation

$$86.6 - (T_\mathrm{m}/^\circ\mathrm{C}) = \frac{219}{(d_\mathrm{c}/\mathrm{nm})} \tag{6.2}$$

The value of $T_\mathrm{m}^\circ = 86.6$ °C thus determined is in the range of reported values for bulk PCL homopolymers (between 65 and 99 °C[35–38]). It is now possible to estimate d_c for PCL crystals from T_m using equation (6.2). For example, d_c for T0-PCL in S/C/S1 crystallized at $T_\mathrm{c} = 38.5$°C (the highest T_c applied for S/C/S1) is estimated to be 7.5 nm, possibly suggesting that T0-PCL in nanolamellae with $d_\mathrm{PCL} = 11.0$ nm can grow thicker until d_c reaches d_PCL. On the other hand, $T_\mathrm{m} \sim 40$ °C observed for T2-PCL in SCS1 and SC'S1 corresponds to $d_\mathrm{c} \sim 4.7$ nm, indicating that the crystal thickening for T2-PCL is greatly impeded by chain tethering at both ends.

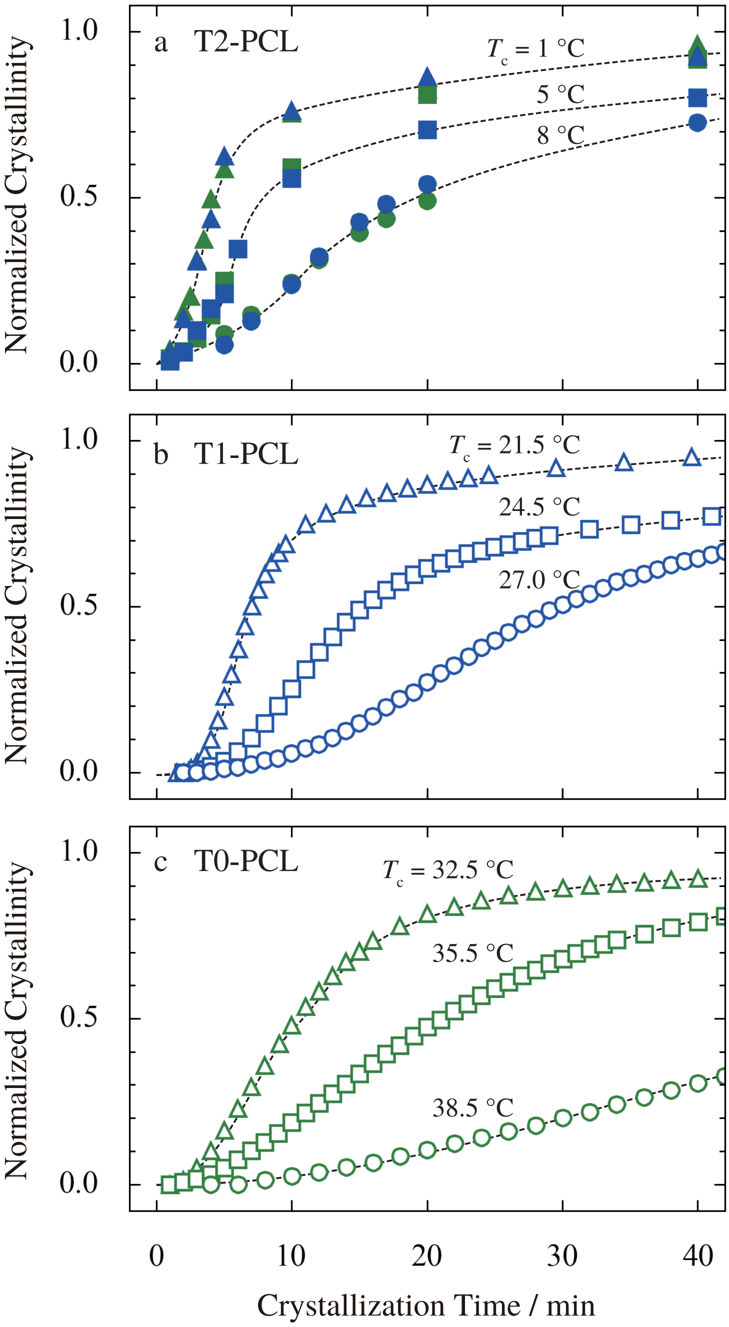

Figure 6.9. Time evolution of normalized crystallinity $\tilde{X}_c$ during isothermal crystallization of SCS1 (green symbols in a), SC'S1 (blue symbols in a), S/C'S1 (b), S/C/S1 (c) at the crystallization temperatures T_c indicated. Data in panel a were obtained by DSC measurements, while those in panels b and c were obtained by time-resolved IR measurements. Dashed curves are just a guide for the eye.

6.3.4 Crystallization Behavior of PCL Chains

Figure 6.9 shows the time evolution of the normalized crystallinity $\tilde{X}_c$ for SCS1 and SC'S1 (a), S/C'S1 (b), and S/C/S1 (c) during isothermal crystallization at the indicated crystallization temperature T_c. $\tilde{X}_c$ was measured by either DSC for $T_c < 10$ °C or time-resolved IR for $T_c > 20$ °C. It is readily recognizable that all the samples exhibit S-shaped curves having a finite induction time, which are commonly observed in crystallization of bulk homopolymers and indicative of the conventional heterogeneous nucleation and growth mechanism. This result is in contrast with that obtained in Chapter 5, where the PCL block chains (T1-PCL) confined in nanolamellae with $d_{\mathrm{PCL}} = 8.7$ nm were found to crystallize only by the homogeneous nucleation-controlled mechanism. The effects of chain confinement in nanolamellae with $d_{\mathrm{PCL}} = 11.0$ nm would be weaker than those in nanolamellae with $d_{\mathrm{PCL}} = 8.7$ nm and not strong enough to induce such a drastic change of the crystallization mechanism. Also evident from **Figure 6.9**a is that the $\tilde{X}_c$ curves of SCS1 and SC'S1 completely coincide with each other, indicating that T2-PCL in both samples crystallizes under the same condition.

The crystallization kinetics of PCL chains was further analysed in detail by fitting the data in **Figure 6.9** to the Avrami equation[39,40]

$$\log(-\ln(1-\tilde{X}_c)) = n\log t + K \tag{6.3}$$

where n is the index called the Avrami exponent and K the rate constant. **Figure 6.10** shows the left hand side of equation (6.3) plotted against $\log t$ (the Avrami plot) for T2-PCL in SCS1 and SC'S1 (a), T1-PCL in S/C'S1 (b), and T0-PCL in S/C/S1 (c), in which the data exhibit excellent linearity. The values of n (equal to the slope of the Avrami plot) approximately range between 2 and 4 for all the samples, which are usually observed for the crystallization of bulk homopolymers proceeding via the heterogeneous nucleation and growth mechanism. Therefore, it is sufficient to state that T0-PCL, T1-PCL, and

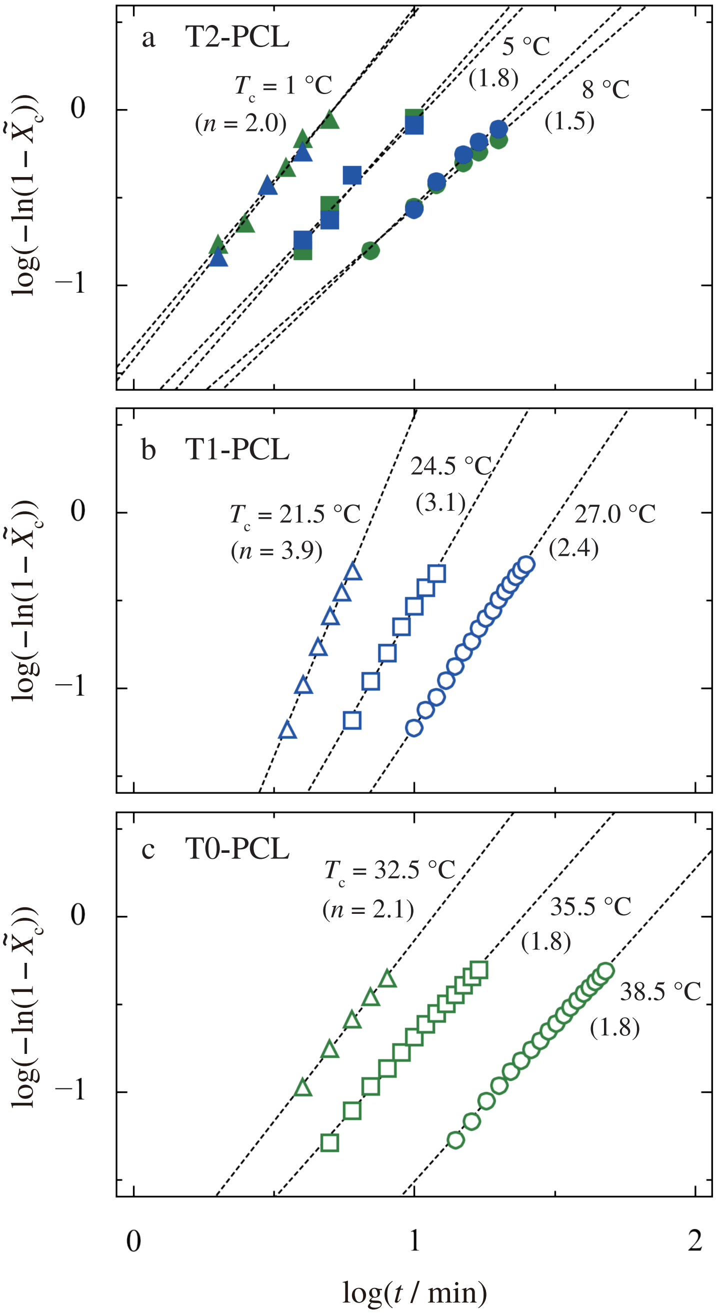

Figure 6.10. Avrami plots for isothermal crystallization of SCS1 (green symbols in a), SC'S1 (blue symbols in a), S/C'S1 (b), and S/C/S1 (c) at temperatures indicated. Dashed lines represent results of the linear fitting, whose slope *n* is presented in parentheses.

T2-PCL in nanolamellae with $d_{\mathrm{PCL}} = 11.0$ nm also crystallize via the conventional heterogeneous nucleation and growth mechanism. Interestingly, *n* for T1-PCL varies from 4 to 2 with increasing T_c from 21.5 °C to 27.0 °C, while that for T0-PCL and

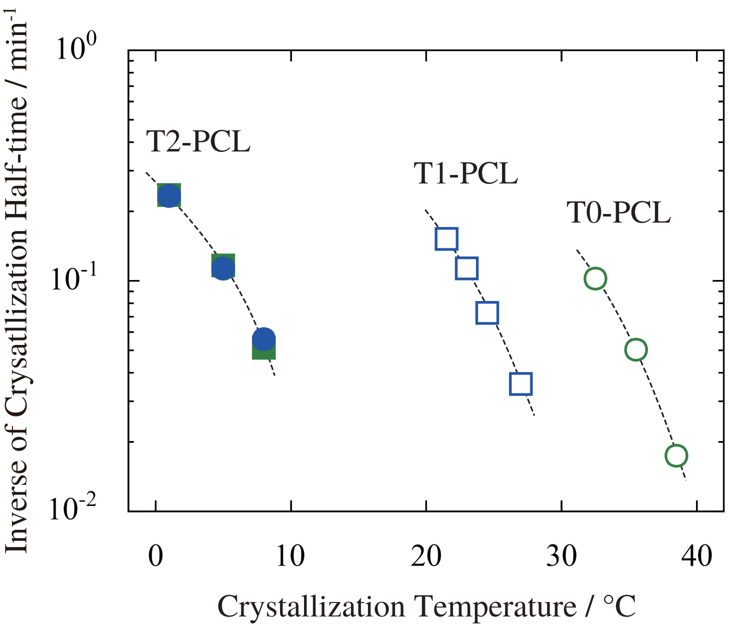

Figure 6.11. Inverse of the crystallization half time ${t_{1/2}}^{-1}$ plotted against the crystallization temperature T_c for T2-PCL in SCS1 (solid circles) and SC'S1 (solid square), T1-PCL in S/C'S1 (open squares), and T0-PCL in S/C/S1 (open circles). Dashed curves are just a guide for the eye.

T2-PCL is almost constant at ~ 2. The variation of n may reflect the change of the crystal growth mode. An additional study on the crystal orientation of T2-PCL, T1-PCL, and T0-PCL will provide further explanation for this result.

6.3.5 Analyses on Crystallization Rate of PCL Chains

For a quantitative comparison of the crystallization rate, the crystallization half time $t_{1/2}$ was defined as the crystallization time at $\tilde{X}_c = 1/2$, and calculated from fitting parameters of the Avrami plot. **Figure 6.11** shows the inverse of $t_{1/2}$ plotted as a function of T_c. If the crystallization rate is compared at the same T_c, T1-PCL crystallizes moderately slower than T0-PCL, whereas T2-PCL crystallizes extremely slow compared to T0-PCL, indicating that chain tethering at both ends retards the crystallization more effectively than chain tethering at one end. However, it is difficult to extrapolate the ${t_{1/2}}^{-1}$ data to quantitatively compare the crystallization rate at the same T_c. Therefore, a new quantity T_{10} is defined here as the crystallization temperature at $t_{1/2} = 10$ min,

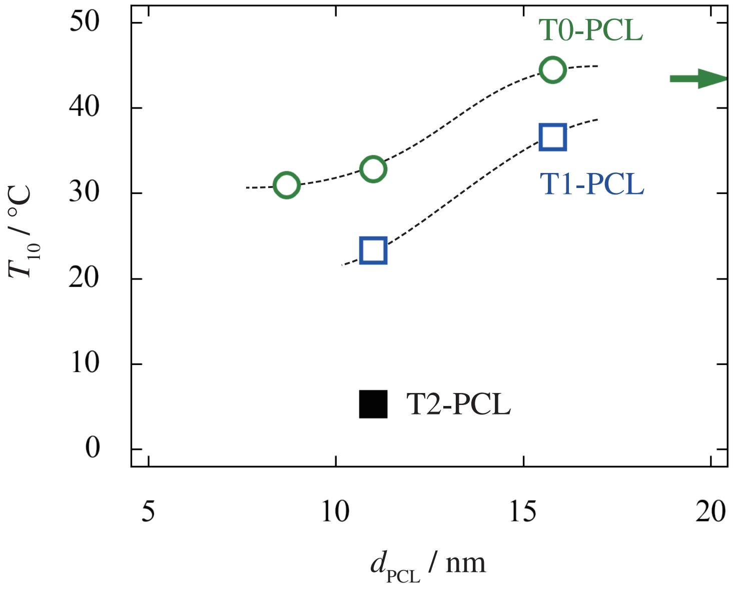

Figure 6.12. T_{10}, the temperature at which the crystallization half-time is equal to 10 min, plotted against nanolamella thickness d_{PCL} for T2-PCL (solid circle), T1-PCL (open squares), and T0-PCL (open circles). An arrow at the right edge indicates T_{10} of bulk PCL homopolymers with the same molecular weight as PCL block chains in SCS1 and SC'S1. The values of T_{10} at $d_{\mathrm{PCL}} = 8.7$ and 15.8 nm are calculated from the data in **Figure 5.11** of Chapter 5.

which can be estimated by interpolating the data in **Figure 6.11**, assuming that $t_{1/2}$ obeys an Arrhenius-type temperature dependence: $\ln t_{1/2} = A + B/T_{\mathrm{c}}$, where A and B are constants[41]. **Figure 6.12** shows T_{10} as a function of d_{PCL}. The values at $d_{\mathrm{PCL}} = 8.7$ and 15.8 nm are estimated from the data in **Figure 5.11** of Chapter 5, and the value for bulk PCL homopolymers, which have the molecular weight identical to that of PCL block chains in SCS1 and SC'S1, is indicated by a right arrow. In nanolamellae with 11.0 nm $\leq d_{\mathrm{PCL}} \leq$ 15.8 nm, T_{10} of T1-PCL is lower than that of T0-PCL by 8 - 10 °C, while confining T0-PCL (PCL homopolymers) in nanolamellae with $d_{\mathrm{PCL}} = 11.0$ nm reduces T_{10} by $\sim$ 11 °C. These results indicate that, for 11.0 nm $\leq d_{\mathrm{PCL}} \leq$ 15.8 nm, the effects of chain tethering at one end on the crystallization rate is comparable to those of space confinement. However, T_{10} of T2-PCL is lower than that of T0-PCL by 27 °C in nanolamellae with $d_{\mathrm{PCL}} = 11.0$ nm, indicating that the impact of chain tethering at both ends on the crystallization rate overwhelms that of chain tethering at one end, as well as

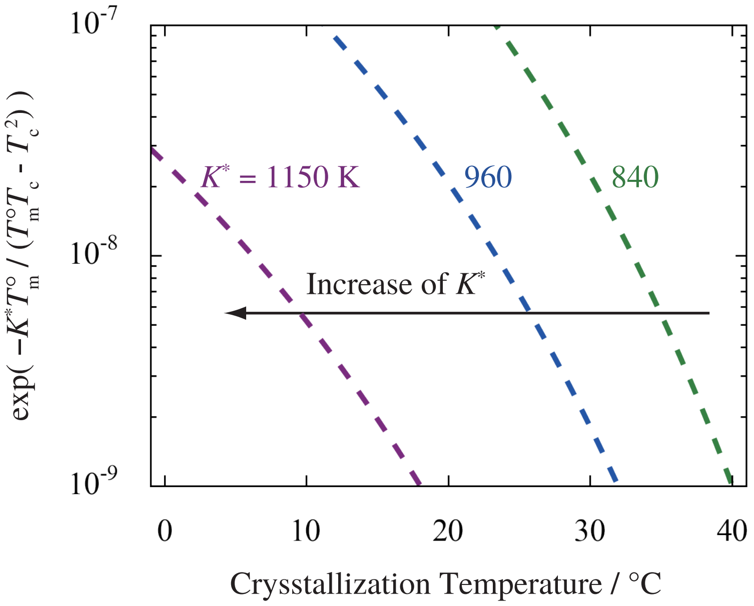

Figure 6.13. Plot of $\exp(-K^*T^\circ_{\mathrm{m}}/(T^\circ_{\mathrm{m}}T_{\mathrm{c}}-T_{\mathrm{c}}^2))$ against crystallization temperature T_{c} for $K^* = 730$, 870, and 1060 K and $T^\circ_{\mathrm{m}} = 86.6$ °C.

that of space confinement by nanolamellae with $d_{\mathrm{PCL}} = 11.0$ nm or 8.7 nm.

The inverse of the crystallization half time $t_{1/2}{}^{-1}$ in **Figure 6.11** can be regarded as proportional to the spherulitic growth rate G if it is assumed that the number of heterogeneous nuclei does not vary among T0-PCL, T1-PCL, and T2-PCL in an identical nanolamella. The T_{c} dependence of G for bulk homopolymers is often explained by the Hoffman-Lauritzen theory

$$G \propto \exp\left(\frac{-U^*}{T_{\mathrm{c}} - T_\infty}\right)\exp\left(\frac{-K^*T^\circ_{\mathrm{m}}}{T^\circ_{\mathrm{m}}T_{\mathrm{c}} - T_{\mathrm{c}}^2}\right) \tag{6.4}$$

where U^* is the constant representing the energy barrier to a diffusion of crystallizing chains across the liquid-solid phase boundary, T_∞ the temperature below which the diffusion completely ceases (usually taken as ~ 30 °C below the glass transition temperature T_{g}), and K^* the constant reflecting the energy barrier to the secondary nucleation process. Since T_{c} of interest is sufficiently higher than T_{g} of bulk PCL homopolymers (~ -68 °C[42]), the contribution of the first exponential in equation (6.4) will be insignificant compared to that of the second one. Therefore, the variation of K^* will be responsible for the difference in ${t_{1/2}}^{-1}$ among T0-PCL, T1-PCL, and T2-PCL. **Figure 6.13** shows the term $\exp\left(-K^{*}T_{\mathrm{m}}^{\circ}/(T_{\mathrm{m}}^{\circ}T_{\mathrm{c}}-T_{\mathrm{c}}^{2})\right)$ in equation (6.4) as a function of T_{c} for $K^{*}=840$, 960, and 1150 K and $T_{\mathrm{m}}^{\circ}=86.6$ °C. The values of K^{*} and the range of the vertical axis were arbitrarily adjusted so that the horizontal positions of calculated curves roughly match with the ${t_{1/2}}^{-1}$ curves in **Figure 6.11**. The value of T_{m}° determined in Section 6.3.3 was used. Increasing K^{*} lowers the crystallization rate and hence the crystallizable temperature, which is consistent with the result in **Figure 6.11**. It is speculated that secondary nucleation is difficult (i.e., K^{*} increases) when PCL chains are tethered at either or both of chain-ends, because chain confinement reduces the mobility of PCL chains.

6.4 Conclusions

The crystallization behavior of PCL chains tethered at both ends (T2-PCL), one end (T1-PCL), and no end (T0-PCL) all confined in an identical nanolamella was investigated using novel model systems constructed from two PS-*b*-PCL-*b*-PS triblock copolymers having ONB at either or both of block junctions. It was confirmed by GPC measurements that T2-PCL in PS-*b*-PCL-*b*-PS triblock copolymers turned into T1-PCL or T0-PCL, as was expected from the molecular design of the triblock copolymers. SAXS measurements revealed that T2-PCL, T1-PCL, and T0-PCL were confined in an identical nanolamella with the thickness d_{PCL} of 11.0 nm.

The following conclusions were reached as to the melting and crystallization behavior of T2-PCL, T1-PCL, and T0-PCL.

1. The melting temperature T_{m} and crystallinity X_{c} of isothermally crystallized T1-PCL and T0-PCL increased with increasing crystallization temperature T_{c} as is often observed for the crystallization of bulk homopolymers, indicating that space confinement and chain tethering at one end had almost no effect on the thickness of PCL crystals. On the other hand, T_{m} and X_{c} of T2-PCL were constant irrespective

of T_c and lower than those of T1-PCL and T0-PCL, suggesting that chain tethering at both ends significantly restricted the thickening of PCL crystals.

2. The time evolution of the normalized crystallinity $\tilde{X}_c$ during the isothermal crystallization of T2-PCL, T1-PCL, and T0-PCL was characterized by a S-shaped curve with an initial induction time, strongly suggesting that the crystallization proceeded via the conventional heterogeneous nucleation and growth mechanism.

3. T2-PCL crystallized much slower than T0-PCL, whereas crystallization of T1-PCL was moderately slower than T0-PCL, indicating that chain confinement retarded the crystallization of PCL chains and the effects of chain tethering at both ends were more significant than those of chain tethering at one end. The deceleration of the crystallization might be attributed to the reduced mobility of PCL chains by chain confinement which would increase the energy barrier to the secondary nucleation process.

References

1. Taden, A.; Landfester, K. *Macromolecules* **2003**, *36*, 4037–4041.
2. Massa, M. V.; Carvalho, J. L.; Dalnoki-Veress, K. *Physical Review Letters* **2006**, *97*, 1–4.
3. Kailas, L.; Vasilev, C.; Audinot, J.-N.; Migeon, H.-N.; Hobbs, J. K. *Macromolecules* **2007**, *40*, 7223–7230.
4. Carvalho, J. L.; Dalnoki-Veress, K. *The European Physical Journal E* **2011**, *34*, 1–6.
5. Michell, R. M.; Blaszczyk-Lezak, I.; Mijangos, C.; Müller, A. J. *Polymer* **2013**, *54*, 4059–4077.
6. Woo, E.; Huh, J.; Jeong, Y. G.; Shin, K. *Physical Review Letters* **2007**, *98*, 136103.
7. Duran, H.; Steinhart, M.; Butt, H.-J.; Floudas, G. *Nano letters* **2011**, *11*, 1671–1675.
8. Michell, R. M.; Lorenzo, A. T.; Müller, A. J.; Lin, M.-C.; Chen, H.-L.; Blaszczyk-Lezak, I.; Martín, J.; Mijangos, C. *Macromolecules* **2012**, *45*, 1517–1528.
9. Maiz, J.; Martin, J.; Mijangos, C. *Langmuir* **2012**, *28*, 12296–303.
10. Suzuki, Y.; Duran, H.; Akram, W.; Steinhart, M.; Floudas, G.; Butt, H.-J. *Soft Matter* **2013**, *9*, 9189.

11. Wang, H.; Keum, J. K.; Hiltner, A.; Baer, E.; Freeman, B.; Rozanski, A.; Galeski, A. *Science* **2009**, *323*, 757–760.

12. Wang, H.; Keum, J. K.; Hiltner, A.; Baer, E. *Macromolecules* **2010**, *43*, 3359–3364.

13. Lai, C.; Ayyer, R.; Hiltner, A.; Baer, E. *Polymer* **2010**, *51*, 1820–1829.

14. Ponting, M.; Lin, Y.; Keum, J. K.; Hiltner, A.; Baer, E. *Macromolecules* **2010**, *43*, 8619–8627.

15. Zhang, G.; Lee, P. C.; Jenkins, S.; Dooley, J.; Baer, E. *Polymer* **2014**, *55*, 663–672.

16. Sun, Y.-S.; Chung, T.-M.; Li, Y.-J.; Ho, R.-M.; Ko, B.-T.; Jeng, U.-S.; Lotz, B. *Macromolecules* **2006**, *39*, 5782–5788.

17. Cai, T.; Qian, Y.; Ma, Y.; Ren, Y.; Hu, W. *Macromolecules* **2009**, *42*, 3381–3385.

18. Chung, T.-M.; Wang, T.-C.; Ho, R.-M.; Sun, Y.-S.; Ko, B.-T. *Macromolecules* **2010**, *43*, 6237–6240.

19. Myers, S. B.; Register, R. A. *Macromolecules* **2010**, *43*, 393–401.

20. Chen, L.; Jiang, J.; Wei, L.; Wang, X.; Xue, G.; Zhou, D. *Macromolecules* **2015**, *48*, 1804–1812.

21. Helfand, E.; Wasserman, Z. *Macromolecules* **1976**, *9*, 879–888.

22. Matsen, M. W.; Schick, M. *Macromolecules* **1994**, *27*, 187–192.

23. Matsen, M. W.; Thompson, R. B. *The Journal of Chemical Physics* **1999**, *111*, 7139–7146.

24. Hadziioannou, G.; Skoulios, A. *Macromolecules* **1982**, *262*, 258–262.

25. Matsushita, Y.; Nomura, M.; Watanabe, J.; Mogi, Y.; Noda, I.; Imai, M. *Macromolecules* **1995**, *28*, 6007–6013.

26. Weimann, P. A.; Hajduk, D. A.; Chu, C.; Chaffin, K. A.; Brodil, J. C.; Bates, F. S. *Journal of Polymer Science Part B: Polymer Physics* **1999**, *37*, 2053–2068.

27. Xu, J.-T.; Yuan, J.-J.; Cheng, S.-Y. *European Polymer Journal* **2003**, *39*, 2091–2098.

28. Takeshita, H.; Ishii, N.; Araki, C.; Miya, M.; Takenaka, K.; Shiomi, T. *Journal of Polymer Science Part B: Polymer Physics* **2004**, *42*, 4199–4206.

29. Luo, C.; Han, X.; Gao, Y.; Liu, H.; Hu, Y. *Journal of Applied Polymer Science* **2009**, *113*, 907–915.

30. Zhou, Y.; Ahn, S.-k.; Lakhman, R. K.; Gopinadhan, M.; Osuji, C. O.; Kasi, R. M. *Macromolecules* **2011**, *44*, 3924–3934.

31. Yu, P.-Q.; Yan, L.-T.; Chen, N.; Xie, X.-M. *Polymer* **2012**, *53*, 4727–4736.

32. Huang, T. C.; Toraya, H.; Blanton, T. N.; Wu, Y. *Journal of Applied Crystallography* **1993**, *26*, 180–184.

33. Duan, Y.; Zhang, J.; Chang, H.; Yan, S.; Yang, C.; Takahashi, I.; Ozaki, Y. *Macromolecules* **2010**, *43*, 5315–5322.

34. Guillier, F.; Orain, D.; Bradley, M. *Chemical Reviews* **2000**, *100*, 2091–158.

35. Chen, H.-L.; Li, L.-J.; Ou-Yang, W.-C.; Hwang, J. C.; Wong, W.-Y. *Macromolecules* **1997**, *30*, 1718–1722.

36. Heck, B.; Hugel, T.; Iijima, M.; Sadiku, E.; Strobly, G. *New Journal of Physics* **1999**, *1*, 17.1–17.29.

37. Strobl, G. *Reviews of Modern Physics* **2009**, *81*, 1287–1300.

38. Cordova, M. E.; Lorenzo, A. T.; Müller, A. J.; Hoskins, J. N.; Grayson, S. M. *Macromolecules* **2011**, *44*, 1742–1746.

39. Avrami, M. *The Journal of Chemical Physics* **1939**, *7*, 1103–1112.

40. Avrami, M. *The Journal of Chemical Physics* **1940**, *8*, 212–224.

41. Shiomi, T.; Tsukada, H.; Takeshita, H.; Takenaka, K.; Tezuka, Y. *Polymer* **2001**, *42*, 4997–5004.

42. Aubin, M.; Prud'homme, R. E. *Macromolecules* **1988**, *21*, 2945–2949.

Chapter 7

General Conclusions

In this study, the crystallization of PCL homopolymers and block chains confined in nanocylinders or nanolamellae was investigated to reveal the effects of chain confinement and space confinement on polymer crystallization as well as mechanisms by which these confinement affect the crystallization. Here, the results of previous chapters are reviewed from the viewpoint of three processes characterizing the crystallization of polymers, namely the (primary) *nucleation*, *growth*, and *thickening*. For the sake of brevity, PCL chains tethered at both ends (= PCL block chains in PS-*b*-PCL-*b*-PS triblock copolymers), one end (= PCL block chains in PCL-*b*-PS diblock copolymers), and no end (= PCL homopolymers) are referred to as T2-PCL, T1-PCL, and T0-PCL, respectively.

7.1 Effects of Chain Confinement and Space Confinement on Crystal Nucleation

Bulk homopolymers generally start to crystallize via *heterogeneous* nucleation, which usually occurs from some heterogeneity such as impurities and interfaces naturally present in the system. In this case, the overall crystallization kinetics depends on both nucleation and subsequent crystal growth. On the other hand, nucleation can also take place homogeneously in the absence of such heterogeneous nuclei. Homogeneous nucleation involves a formation of crystal embryos by a spontaneous alignment of polymer chains into crystal-like order, rendering the energy barrier of nucleation much larger than that

Table 7.1. Nucleation mechanisms of PCL chains confined in nanocylinders or nanolamellae.

PCL Chains	Nanocylinders				Nanolamellae		
	D: 13.0	14.9	17.2	17.9 nm	d_{PCL}: 8.7	11.0	15.8 nm
T2-PCL	-	-	-	-	-	hetero	-
T1-PCL	homo	homo	homo	homo	homo	hetero	hetero
T0-PCL	homo	homo	homo	homo	hetero	hetero	hetero

homo : Homogeneous nucleation mechanism.

hetero : Heterogeneous nucleation and growth mechanism.

of heterogeneous nucleation. Therefore, homogeneous nucleation can be observed only at an extremely large supercooling. When polymer chains are confined in nanodomains and the number of nanodomains per unit volume is much larger than the number of heterogeneous nuclei per unit volume, polymer chains in most of the nanodomains cannot start crystallizing by heterogeneous nucleation and the crystallization by homogeneous nucleation prevails instead. In this case, crystallites growing from homogeneous nuclei instantaneously impinge on nanodomain walls or other growing crystallites and eventually cease growing. As a result, the lifetime of crystal growth is much shorter than the time necessary for homogeneous nucleation, leading to the first-order crystallization kinetics which is controlled solely by the nucleation rate.

Table 7.1 summarizes the nucleation modes judged from overall crystallization kinetics for T2-PCL, T1-PCL, and T0-PCL confined in nanocylinders or nanolamellae. In nanocylinders in the range of D investigated, both T1-PCL and T0-PCL crystallize via homogeneous nucleation, indicating that the two-dimensional spatial restriction prohibits the heterogeneous nucleation. In this case, it is possible to directly evaluate the effects of space confinement and chain confinement on the nucleation rate, since the crystallization is controlled exclusively by homogeneous nucleation. **Figure 7.1** shows the inverse of crystallization half time ${t_{1/2}}^{-1}$ (proportional to the crystallization rate and hence to the nucleation rate) of T1-PCL and T0-PCL as a function of D. It is

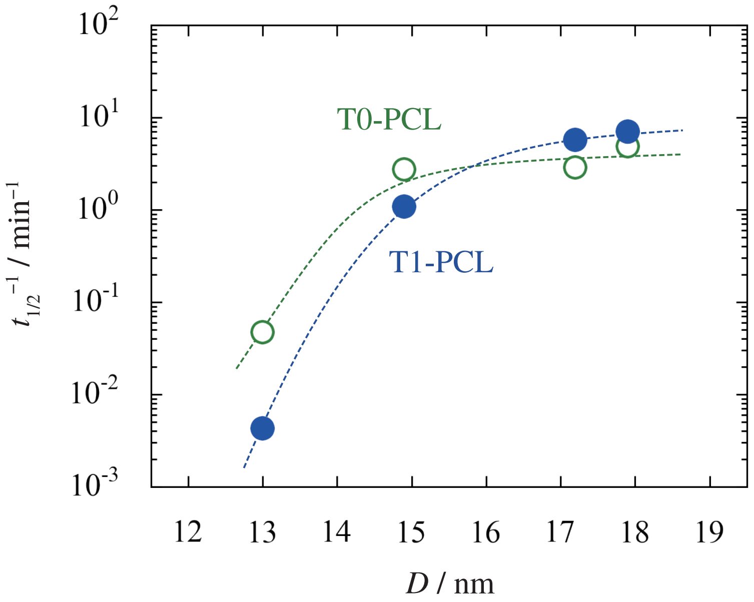

Figure 7.1. Inverse of crystallization half time $t_{1/2}{}^{-1}$ at crystallization temperature $T_c = -48$ °C plotted against nanocylinder diameter D for T1-PCL (solid circles) and T0-PCL (open circles) confined in nanocylinders. Data were taken from Chapters 2 and 4. Dashed curves are just a guide for the eye.

clear that T1-PCL displays an extremely lower nucleation rate than T0-PCL at small D, whereas the relation is completely reversed at $D \geq 17.2$ nm, indicating that chain confinement decelerates the nucleation at small D but accelerates the nucleation at large D. The study on PCL homopolymer/PCL block chain blends confined in nanocylinders suggests that this complex behavior can be explained by two terms constituting the energy barrier for homogeneous nucleation: the energy barrier for the formation of critical nuclei and that for the diffusion of crystallizing repeating units across the phase boundary. In nanocylinders with 13.0 nm $\leq D \leq$ 14.9 nm, chain confinement would substantially increase the energy barrier for the molecular diffusion and hence impede the nucleation, whereas at 17.2 nm $\leq D \leq$ 17.9 nm the contribution of the diffusion would be negligible and the energy barrier to form critical nuclei would be moderately lowered by chain confinement, leading to a higher nucleation rate.

On the other hand, for PCL chains confined in nanolamellae, only T1-PCL at $d_{\text{PCL}} =$ 8.7 nm crystallizes by homogeneous nucleation, and all the other PCL chains in the range of d_{PCL} investigated crystallize via heterogeneous nucleation and growth mechanism (**Table 7.1**). The difference in the nucleation mode between PCL chains confined in nanocylinders and nanolamellae is explained by the fact that PCL chains are much more finely partitioned in nanocylinders than in nanolamellae. It is astonishing that T1-PCL at $d_{\mathrm{PCL}} = 8.7$ nm can crystallize only by homogeneous nucleation at an extremely large supercooling, in contrast to T0-PCL in the same nanolamella which can crystallize via the heterogeneous nucleation and growth mechanism at a small supercooling. This result indicates that the crystal growth of T1-PCL is extremely slow compared to that of T0-PCL, presumably because chain confinement significantly reduces the mobility of PCL chains. In larger nanolamellae with 11.0 nm $\leq d_{\mathrm{PCL}} \leq$ 15.8 nm, the crystallization mechanism is not modified by chain confinement, suggesting that the effects of chain confinement are less significant in larger nanolamellae.

7.2 Effects of Chain Confinement and Space Confinement on Crystal Growth

In this study, the crystal growth was examined in two different ways. For PCL chains confined in nanolamellae, crystallization occurs via the heterogeneous nucleation and growth mechanism, which automatically means that the overall crystallization rate reflects the crystal growth rate. However, crystal growth for PCL chains confined in nanocylinders is instantaneous and hence does not contribute to the overall crystallization rate. In this case, the orientation of PCL crystals with respect to the nanocylinder axis offers information on the growth mode of PCL crystals.

Figure 7.2 shows the schematic illustration of the preferential orientation of PCL crystals in nanocylinders with $D = 13.0$ and 17.9 nm. For T0-PCL (a) and T1-PCL (a') at $D = 13.0$ nm, the *b* axis of PCL crystals orients parallel to the nanocylinder axis, indicating that PCL crystals grow one-dimensionally along the nanocylinder axis, pointing the *b* axis in the growth direction. The degree of orientation is slightly higher

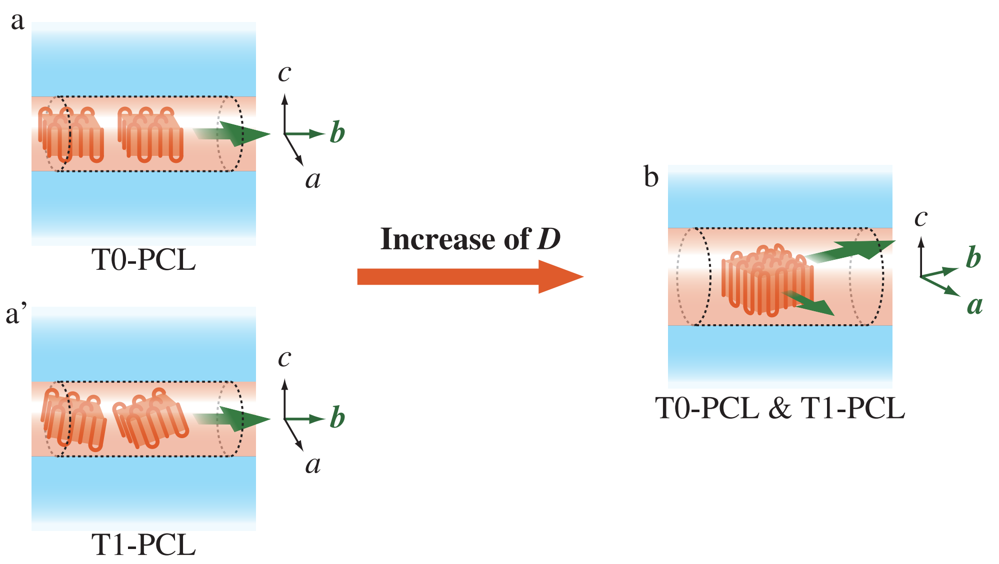

Figure 7.2. The orientation of PCL crystals in nanocylinders observed for T0-PCL (a) and T1-PCL (a') confined in nanocylinders with $D = 13.0$ nm and T0-PCL and T1-PCL confined in nanocylinders with $D = 17.9$ nm (b).

for T0-PCL than for T1-PCL, indicating that chain confinement moderately impedes the favorable crystal growth. However, PCL crystals at $D = 17.9$ nm orient in a way that (110) plane normals are parallel to the nanocylinder axis (b), suggesting that PCL crystals can grow along the a axis as well as the b axis (two-dimensional growth). This change of the crystal growth mode may be induced by a larger space available in nanocylinders with $D = 17.9$ nm, and is consistent with the fact that the crystallinity of PCL chains increases with increasing D. The crystal orientation is quantitatively the same for both T0-PCL and T1-PCL, indicating that the effects of chain confinement on crystal growth diminishes with increasing D.

Although the overall crystallization rate in the heterogeneous nucleation and growth mechanism is affected by both the nucleation rate and growth rate, the effects of chain confinement and space confinement on the crystal growth kinetics can be estimated from the overall crystallization rate data for PCL chains confined in nanolamellae. For a quantitative measure for ease of crystal growth, the author defines T_{10}, the temperature at which the crystallization half time is 10 min. Higher T_{10} implies that the energy

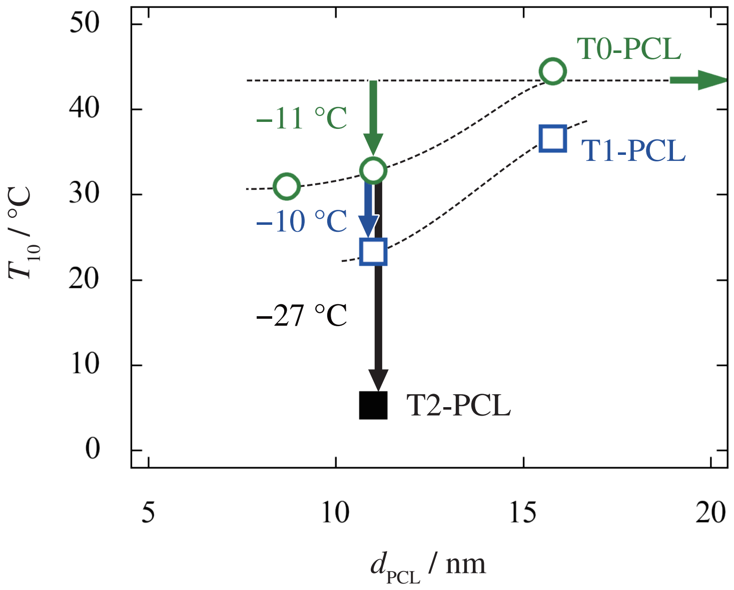

Figure 7.3. T_{10} plotted against d_{PCL} for T2-PCL (closed square), T1-PCL (open squares), and T0-PCL (open circles). Right arrow at the edge represents T_{10} for bulk PCL homopolymers. Downward arrows and attached values at $d_{\mathrm{PCL}} = 11.0$ nm indicate the reduction of T_{10} by space confinement or chain confinement. Data were reproduced from **Figure 6.12**.

barrier for secondary nucleation is lower and hence the crystals can grow at higher T_c. **Figure 7.3** shows T_{10} for T2-PCL, T1-PCL, and T0-PCL as a function of d_{PCL}. It is interesting that T_{10} does not decrease by confining PCL homopolymers in nanolamellae with $d_{\mathrm{PCL}} = 15.8$ nm, indicating that space confinement has no effect on crystal growth in large nanolamellae. T_{10} decreases by 11 °C when confined in nanolamellae with $d_{\mathrm{PCL}} =$ 11.0 nm, suggesting that crystal growth is moderately impeded by chain confinement in relatively small nanolamellae. The effects of chain confinement can be more prominent than those of space confinement. It was already stated in the previous section that the crystallization mechanism of PCL chains in nanolamellae with $d_{\mathrm{PCL}} = 8.7$ nm was changed when tethered at one end, due to the significant deceleration of the crystal growth by chain confinement. In nanolamellae with $d_{\mathrm{PCL}} = 11.0$ nm, however, the effects of chain tethering at one end is less significant, resulting in a moderate reduction of T_{10} by 10 °C. The reduction of T_{10} by chain tethering at both ends at $d_{\mathrm{PCL}} = 11.0$ nm is 27 °C, clearly indicating that chain tethering at both ends hampers the crystal growth

Table 7.2. T_c-dependence of T_m for PCL chains confined in nanocylinders and nanolamellae.

PCL Chains	Nanocylinders				Nanolamellae		
	D: 13.0	14.9	17.2	17.9 nm	d_{PCL}: 8.7	11.0	15.8 nm
T2-PCL	-	-	-	-	-	→	-
T1-PCL	→	→	→	→	→	↗	↗
T0-PCL	→	→	→	→	↗	↗	↗

→ : T_m is constant independent of T_c ↗ : T_m increases with increasing T_c

more effectively than chain tethering at one end.

7.3 Effects of Chain Confinement and Space Confinement on Crystal Thickening

Generally, lamellar crystals of polymers are known to grow thicker at higher crystallization temperature T_c in order to minimize the surface free energy. Since the melting temperature T_m is positively related to the crystal thickness by the Gibbs-Thomson equation, the thickening of PCL crystals can be evaluated from the T_c-dependence of T_m.

In this study, the observed T_c-dependence of T_m can be classified in two patterns: *constant* T_m independent of T_c or *increasing* T_m with increasing T_c. **Table 7.2** shows the classification based on the above criterion for PCL chains confined in nanocylinders and nanolamellae. It is clear that PCL homopolymers in nanocylinders always show constant T_m against T_c, while those in nanolamellae show increasing T_m with increasing T_c, indicating that the crystal thickness is severely limited by the two-dimensional restriction imposed by nanocylinders. The effects of chain confinement change with the size and shape of nanodomains. In nanocylinders, T_m is reduced by chain confinement (see **Figure 2.6**a in Chapter 2). In nanolamellae, PCL chains tend to display constant T_m against T_c when tethered at either or both of chain-ends and confined in nanolamellae with relatively small d_{PCL}. There are two possible mechanisms by which chain confinement impedes the thickening. One is that PCL repeating units near the tethered chain ends may not participate in crystallization. The other is that the conformation of PCL chains may be constrained by chain confinement, which reduces the chance to attain an ideal conformation necessary to maximize the crystal thickness. Interestingly, T_m of PCL chains that increases with T_c depends only on T_c irrespective of d_PCL and whether PCL chains are T0-PCL or T1-PCL (see **Figure 5.7**a in Chapter 5 and **Figure 6.8**a in Chapter 6), indicating that the crystal thickness is determined solely by thermodynamic requirements and free of any influences from space confinement and chain confinement.

7.4 Perspectives

In this thesis, the effects of chain confinement and space confinement on polymer crystallization were revealed. The approach utilized in this study which involves photo-cleavable block copolymers will also be applied for other crystalline polymers including polyethylene, polypropylene, poly(ethylene oxide), and many other polyesters. It is also interesting to study the effects of chain confinement on other physical properties of polymer chains such as the glass transition temperature, mechanical strength, and conductivity. The author hopes that the knowledge acquired in this study will be an aid for the development and application of nanostructured polymeric materials and the nature of chain confinement will be examined from more various points of view.

Appendix A

Synthesis of Photocleavable PCL-*b*-PS Diblock Copolymers

A.1 Overview of the Synthetic Method

Figure A.1 shows the synthetic scheme of PCL-*b*-PS diblock copolymers having a photocleavable *o*-nitrobenzyl group (ONB) at the block junction.

First, the PCL homopolymer having carboxylic acid and hydroxy terminals **1** (HOOC-PCL-OH) was synthesized by ring-opening polymerization of ε-caprolactone (CL), followed by the methylation of the carboxylic acid terminal to obtain the PCL homopolymer with a hydroxy terminal **2** (MeOOC-PCL-OH). The hydroxy terminal was then capped with succinic anhydride to give a PCL homopolymer with a carboxylic acid end **3** (MeOC-PCL-COOH).

A PS homopolymer having a phenolic hydroxy terminal protected by a *tert*-butyldimethylsilyl (TBS) group **7** (PS-OTBS) was synthesized by means of living anionic polymerization of styrene and end-capping with a diphenylethylene derivative **6** (DPE-OTBS). It was then deprotected and coupled with an *o*-nitrobenzyl alcohol derivative having 3-bromopropyl group **9** (Br-ONB-OH) to obtain a PS homopolymer with an ONB terminal **10** (PS-ONB-OH). Br-ONB-OH **9** was kindly provided by Prof. Kazuo Yamaguchi at Kanagawa University.

The synthesized PCL and PS homopolymers **3**, **10** were then coupled by the esterification reaction using carbodiimide.

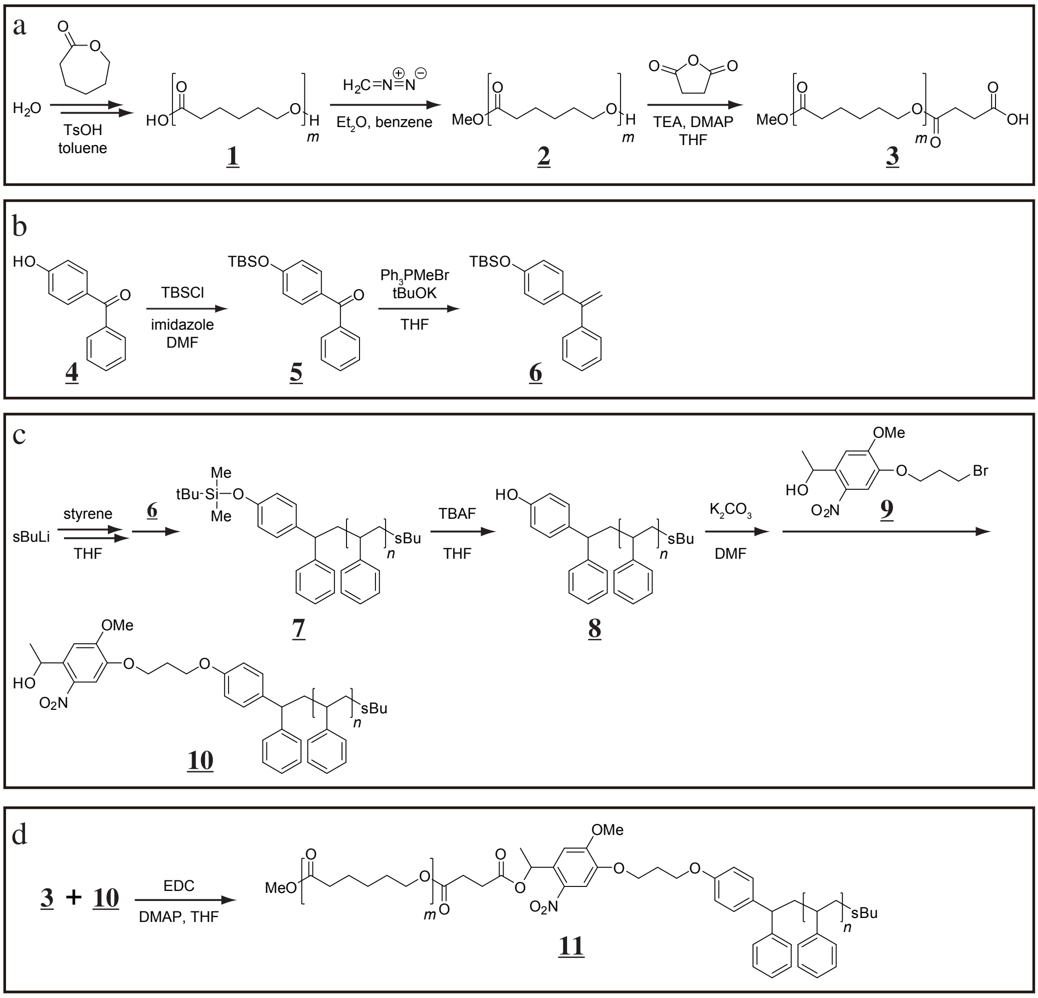

Figure A.1. Synthetic scheme for PCL-*b*-PS diblock copolymers having ONB group between two blocks.

General procedures and results are described in the following sections taking PCL-*b*-PS7 as an example. All other PCL-*b*-PS samples were synthesized by the same methods.

A.2 Experimental

A.2.1 Purification Methods

Reagents were purified according to the following methods.

ε-Caprolactone (CL) CL was dried over calcium hydride overnight and distilled under reduced pressure before use.

Dimethylformamide (DMF) DMF was dried over calcium hydride for a night, distilled under reduced pressure, and stored in a Schlenk tube with molecular sieves.

Heptane Heptane was first dried over calcium hydride and distilled to a round-bottom flask charged with *n*-butyllithium and DPE using a trap-to-trap technique. The solution was left for a night to complete the reaction between *n*-butyllithium and DPE. It was further distilled on a vacuum line by a trap-to-trap technique at the point of use.

Styrene Styrene was washed first with aqueous sodium hydroxide twice and then with water until the aqueous layer became neutral. It was dried over magnesium sulfate then over calcium hydride for a night and distilled under reduced pressure. It was again dried over calcium hydride overnight, distilled by a trap-to-trap technique, and diluted with dry toluene or THF.

Tetrahydrofuran (THF) Stabilizer-free THF was dried over sodium chips and naphthalene after degassing by freeze-pump-thaw cycles. It was stirred until the deep green color appeared before using it by distilling via a trap-to-trap technique.

Toluene Toluene used for polymerization of CL was dried by refluxing over sodium and benzophenone at 120-130 °C for an hour and distilled under nitrogen atmosphere. For living anionic polymertization of styrene, it was dried over sodium and benzophenone for two days with occasional degassing on a vacuum line and distilled via a trap-to-trap technique.

Triethylamine (TEA) TEA was dried over calcium hydride, distilled under nitrogen flow, and stored under argon atmosphere when used in condensation reactions.

Other reagents were used as received.

A.2.2 Synthesis of HOOC-PCL-OH 1 (TT19)

Before the polymerization, an initiator and acid catalyst solutions were prepared by following procedures. The initiator solution (water/toluene) was prepared by mixing distilled water and toluene and distilling the organic layer by a trap-to-trap technique. The acid catalyst solution was prepared by drying *p*-toluenesulfonic acid (TsOH) monohydrate *in vacuo* at 100 °C for 3 h and diluting with dry-toluene.

The polymerization reaction was performed in the following method. CL 17.0 mL (17.51 g, 153 mmol) and water/toluene mixture 12.0 mL were taken in a flame-dried two-neck 200 mL round-bottom flask and cooled to 0 °C under nitrogen flow. TsOH/toluene solution 35.0 mL (containing TsOH 0.709 g, 4.12 mmol) was then poured at once with vigorous stirring. The reaction mixture was kept at 0 °C under argon atmosphere with occasional stirring. A small aliquot was sampled from the reaction mixture and quenched with TEA to monitor the progress of polymerization by ^{1}H-NMR and GPC. After leaving it for 25 h, the reaction was quenched by neutralization of TsOH by TEA and the product was recovered by precipitating in excess methanol, which gave a white solid (17.16 g, 98.0%). Since undesired fractions having higher and lower molecular weight than the main fraction were detected by GPC, the crude product was purified by repeated fractional precipitation in a THF/methanol system. Freeze-drying the purified product with benzene gave a white solid (5.26g, 32%, $M_\mathrm{n} = 25400\ \mathrm{g\,mol^{-1}}$ by ^{1}H-NMR, $M_\mathrm{w}/M_\mathrm{n} = 1.06$ by GPC).

A.2.3 Synthesis of MeOC-PCL-OH 2 (TT21)

Diazomethane is an excellent *O*-methylating reagent with high reactivity and selectivity on carboxylic acids. However, it is notorious for its highly toxic, carcinogenic, and explosive nature. Therefore it has to be prepared at the time of use using a dedicated apparatus having no conical joints, which is illustrated in **Figure A.2**.

Vessel A in **Figure A.2** was charged with *N*-methyl-*N*-nitroso-*p*-toluenesulfonamide

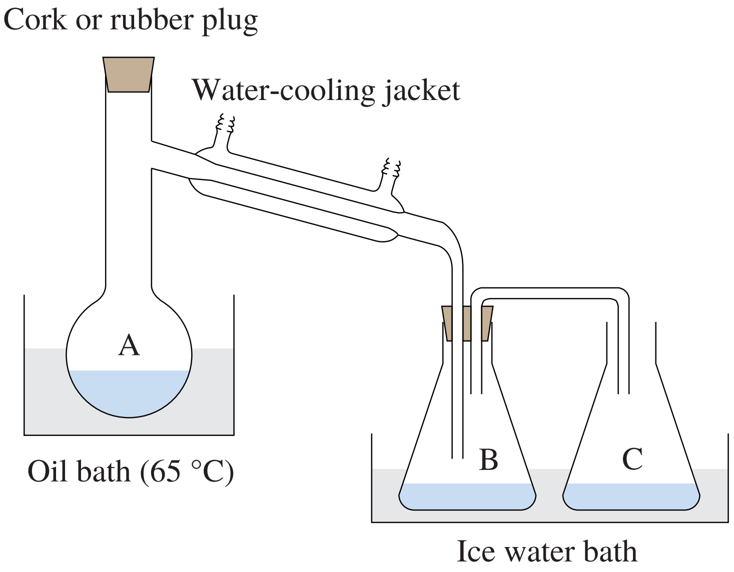

Figure A.2. Illustration of the apparatus for diazomethane synthesis.

2.14 g (10.0 mmol), diethyl ether 30 mL, and solution of potassium hydroxide 0.40 g in water/ethanol 1 mL/9 mL, and heated to 65 °C. Yellow diazomethane gas emerged was trapped in ice-cold diethyl ether 20 mL in flask B and C. Solution in flask B was mixed with benzene solution of HOOC-PCL-OH **1** 5.06 g (0.199 mmol) and left overnight. Remaining diazomethane was quenched by excess acetic acid, which was confirmed by the disappearance of the yellow color. The product was recovered by precipitating in excess methanol twice and freeze-drying with benzene (white solid, 4.45 g, 88%).

A.2.4 Synthesis of MeOC-PCL-COOH **3** (TT26)

MeOC-PCL-OH **2** 1.15 g (0.0447 mmol, 1 eq.), dry-THF 4.5 mL, *N*,*N*-dimethyl-4-aminopyridine (DMAP) 36.28 mg (0.297 mmol, 6.6 eq.), and dry-TEA 0.20 mL (1.43 mmol, 32 eq.) were taken in a flame-dried two-neck 50 mL round-bottom flask under nitrogen atmosphere. Succinic anhydride 0.126 g (1.26 mmol, 28 eq.) was then added at 0 °C and stirred for 15 min, followed by stirring at room temperature for 33 h. Then distilled water 1.0 mL was added and stirred overnight. Finally the product was recovered from the reaction mixture by precipitating in excess methanol twice and freeze-drying with benzene, which yielded a white solid (0.94 g, 82%).

A.2.5 Synthesis of 4-(*tert*-butyldimethylsilyloxy)benzophenone 5 (SN1)

4-Hydroxybenzophenone 10.02 g (50.6 mmol, 1 eq.) and imidazole 3.78 g (55.6 mmol, 1.10 eq.) were taken in a two-neck round-bottom flask, dried *in vacuo*, and purged with nitrogen. Then DMF 20 mL was added to dissolve the solids and cooled to 0 °C, which gave a deep brown solution. DMF solution of *tert*-butyldimethylsilyl chloride (TBSCl) 8.67 g (57.8 mmol, 1.14 eq.) 20 mL was added dropwise to the reaction mixture followed by stirring at room temperature for 18 h. After quenching the reaction with a small amount of water, residual solvent was evaporated under reduced pressure. The crude product was then dissolved in diethyl ether 100 mL, washed with aqueous $NaHCO_3$ and brine, and dried over magnesium sulfate. Removing solvents by evaporation under reduced pressure and drying under high vacuum at 40 °C gave brown viscous liquid (13.7 g, 87%).

A.2.6 Synthesis of DPE-OTBS 6 (SN2)

Methyltriphenylphosphonium bromide 18.85 g (52.8 mmol, 1.20 eq.) and potassium *tert*-butoxide 7.62 g (68.0 mmol, 1.55 eq.) were taken in a two-neck round-bottom flask, purged with nitrogen, and dissolved in dry-THF 60 mL at 0 °C. THF solution of 4-(*tert*-butyldimethylsilyloxy)benzophenone **5** 13.7 g (44.0 mmol, 1 eq.) 30 mL was then added dropwise, followed by stirring for 1 hour at 0 °C and 16 h at room temperature. After quenching the reaction by adding water 100 mL, the aqueous layer was extracted by diethyl ether 100 mL twice. All the organic layers were combined, dried over magnesium sulfate, and the solvent was evaporated under reduced pressure. The residue was again dissolved in THF, poured into hexane 600 mL, and the precipitated yellow-white solid was removed by filtration under reduced pressure. The filtrate was concentrated and poured again into hexane 200 mL, filtered through a layer of silica gel treated with TEA/hexane 5v/v% solution. Removing the solvents from the filtrate by evaporation under reduced pressure followed by drying under high vacuum gave the crude product (10.6 g, 77.9%).

The crude product was then purified by silica gel column chromatography using silica gels treated with TEA/hexane 5v/v% solution as a stationary phase and hexane as an eluent, to obtain colorless viscous liquid (8.40 g, 27.1 mmol, 61.8%). Before using for end-functionalization in living anionic polymerization, it was mixed with ca. 5 mol% *n*-butyllithium, distilled on a high vacuum line by a trap-to-trap technique, and diluted with dry-heptane.

A.2.7 Synthesis of PS-OTBS **7** (TT20)

The sythesis and end-functionalization of PS homopolymers were conducted using a break-seal technique under high vacuum.

The reaction vessel was flame-dried, evacuated on a high vacuum line and sealed off. Inner walls of the vessel was washed with red 1,1-diphenylhexyllithium/heptane solution. After removing the wash solution, 0.0630 M heptane solution of *sec*-butyllithium 4.60 mL (0.290 mmol, 1 eq.) was introduced and cooled to −78 °C. Styrene/toluene 3.64 M 19.03 mL (69.27 mmol, 239 eq.) was then added at once with vigorous stirring and left for 1 h in water bath (at room temperature), which lead to orange viscous solution. The reaction mixture was diluted with THF 20.4 mL at −78 °C. It required 4 h of stirring at −78 °C to obtain homogeneous orange solution. Then, DPE-OTBS **6**/heptane 0.0482 M 3.68 mL and 0.0982 M 2.99 mL (total 0.451 mmol, 1.56 eq.) was introduced with vigorous stirring, which lead to a change in color from orange to deep red. The solution was left for 1 h at −78 °C before quenching the living anion by adding methanol/THF 1.05 M 2.35 mL (2.47 mmol, 8.5 eq.). The product was recovered by precipitating in excess methanol twice and freeze-drying with benzene, which gave a white solid (7.18 g, 99%).

A.2.8 Synthesis of PS-ONB-OH **10** (TT28)

The PS homopolymer **7** 2.80 g (0.0996 mmol, 1 eq.) was dissolved in THF 15 mL and mixed with tetrabutylammonium fluoride (TBAF)/THF 1.0 M 4.5 mL (4.5 mmol, 47 eq.), followed by stirring for 20 h at room temperature. The product was recovered by precipitating into excess methanol and hexane and freeze-drying with benzene, yielding a white solid of PS-OH **8** (2.59 g, 93%).

Next, **8** 1.19 g (0.0410 g, 1 eq.) was mixed with ground powders of potassium carbonate 0.116 g (0.839 mmol, 21 eq.) and dry-DMF 3 mL in a flame-dried two-neck round-bottom flask and stirred for 8 h at room temperature under argon atmosphere. Then the *o*-nitrobenzyl alcohol derivative **9** was added and stirred at 60 °C for 66 h. The resulting reaction mixture was diluted with THF and poured in excess methanol to obtain the product, which was further freeze-dried with benzene to be a yellow-white solid (1.08 g, 91%).

A.2.9 Synthesis of PCL-ONB-PS **11** (TT29)

The PCL homopolymer (MeOC-PCL-COOH) **3** 0.86 g (0.0335 mmol, 1 eq) and PS homopolymer (PS-ONB-OH) **10** 0.99 g (0.0341, 1.0 eq.), and DMAP 1.27 g (10.4 mmol, 310 eq.) were dissolved in dry-THF 6.0 mL in a flame-dried two-neck round-bottom flask under nitrogen flow. To this solution 1-(3-dimethylaminopropyl)-3-ethylcarbodiimide hydrochloride (EDC) 0.317 g (1.65 mmol, 48 eq.) was added at 0 °C, stirred for 15 min at 0 °C, and then 71 h at room temperature. Polymers were recovered by precipitating in excess methanol and freeze-drying with benzene. The crude product was further purified by fractional precipitation in cyclohexane/hexane and benzene/methanol systems to remove unreacted substrates. Precipitation in methanol and freeze-drying with benzene gave white solid (0.99 g, 54%).

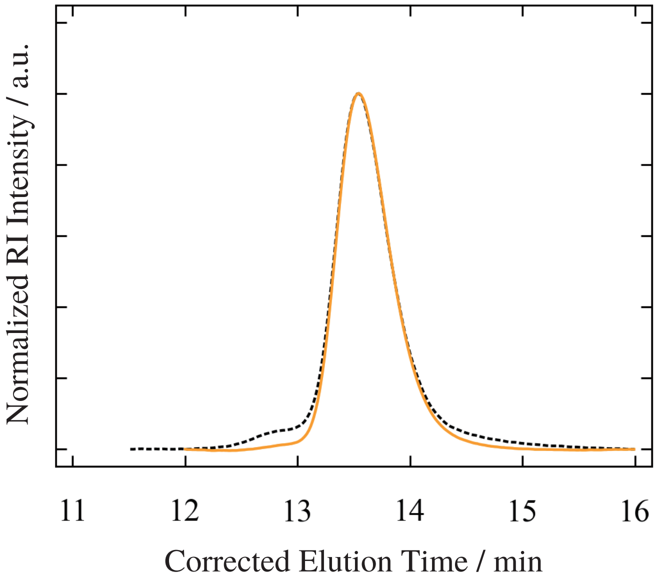

Figure A.3. GPC chromatograms of the PCL homopolymer before (dotted curve) and after (solid curve) fractional precipitation.

A.3 Results

A.3.1 Synthesis of PCL Homopolymers

PCL homopolymers were synthesized by ring-opening polymerization of CL. Once activated by a strong acid such as hydrochloric acid[1] and diphenyl phosphate[2], CL undergoes a nucleophilic attack by relatively weak nucleophiles including aliphatic alcohols and water. Therefore, end-functionalized PCL homopolymers can be synthesized by using alcohols bearing functional groups such as terminal alkyne and azide[2]. However, the presence of water in the system inevitably gives PCL homopolymers lacking the desired end-functionality. To avoid this problem, the author synthesized PCL homopolymers using water as an initiator, which gave a carboxylic acid at the α-terminal and hydroxy group at the ω-terminal. It is necessary to keep the reaction mixture at 0 °C for a controlled polymerization, otherwise the reaction proceeds too fast and results in a broad molecular weight distribution.

Figure A.3 shows the GPC chromatogram of the as-polymerized PCL homopolymer

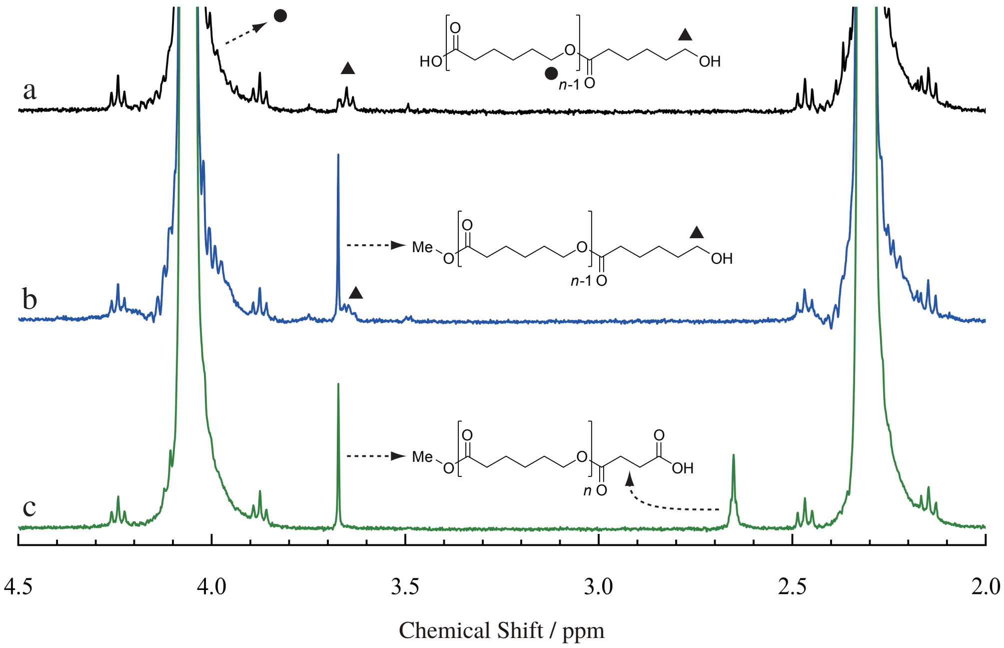

Figure A.4. ^{1}H-NMR spectra of the PCL homopolymers having carboxylic acid and hydroxy terminals (a), after methyl esterification (b), and after condensation with succinic anhydride (c).

(dotted curve), in which a shoulder on the higher molecular side of the main fraction is detected. The molecular weight of this by-product is twice that of the main product, but its origin is still unknown. **Figure A.3** also shows the GPC chromatogram after removing this by-product by a repeated fractional precipitation in a THF/methanol system (solid curve), from which the successful removal of the high molecular weight shoulder was confirmed.

M_n of the PCL homopolymer was calculated from the ^{1}H-NMR spectrum, which is presented in **Figure A.4**a. The integral ratio of the triplet marked by a circle against the one marked by a triangle is equal to the number of repeating units excluding the terminal one, which directly gives the number-averaged degree of polymerization.

End-capping of the PCL homopolymer involved two steps: methyl esterification of the carboxylic acid terminal and conversion of the hydroxy terminal to a carboxylic acid terminal. **Figure A.4** shows the comparison of ^{1}H-NMR spectra after each procedure. The appearance of a singlet at $\delta = 3.67$ ppm after the reaction with diazomethane (b) indicates that the carboxylic acid terminal of the substrate is quantitatively capped by methyl esterification. The completion of the second step could be confirmed by the disappearance of the triplet at $\delta = 3.65$ ppm and the appearance of the peak at $\delta = 2.65$ ppm arising from the succinic acid substructure (c). The results of GPC measurements at each step (not shown) indicate that the molecular weight and its distribution of the PCL homopolymer was preserved throughout the end-capping reactions.

A.3.2 Synthesis of PS Homopolymers

PS homopolymers were synthesized by living anionic polymerization of styrene and subsequent end-functionalization by a DPE derivative. Anionic polymerization is often carried out in aprotic polar solvents such as THF, taking an advantage of the extremely fast propagation reaction. However, removal of the reaction heat is difficult in a large-scale synthesis. Therefore, styrene was polymerized in non-polar solvent (toluene). The reaction between living styryl anion and DPE derivatives, however, requires the solvent to be polar, therefore THF was added before adding DPE-OTBS. It should also be noted that the living anions should be completely terminated before breaking the vacuum of the reaction vessel, otherwise a considerable amount of PS homopolymers are homocoupled, presumably by some side reaction involving oxygen.

The GPC chromatogram of the synthesized PS homopolymer (not shown) contained a narrow and unimodal peak, indicating that the polymerization was completely under control. $M_{\mathrm{w}}/M_{\mathrm{n}}$ was around 1.05 for all PS homopolymers synthesized in this study.

The ^{1}H-NMR spectrum of the as-polymerized PS homopolymer is shown in **Figure A.5**a. The presence of *tert*-butyldimethylsilyl (TBS) terminal is confirmed by two peaks from a TBS group at $\delta = 0.14 \sim 0.19$ and $0.95 \sim 1.00$ ppm. These peaks vanish after the deprotection of TBS ether (b). The appearance of the signals at $\delta = 3.93$, 4.07, and 4.24 ppm in **Figure A.5**c indicates that the ONB linker is quantitatively introduced at the chain end. However, ONB was incompletely introduced when PS-OH $\underline{\mathbf{8}}$ was left for few days after the deprotection, presumably due to an oxidation of the phenolic OH. Therefore, the introduction of the ONB linker should be conducted as soon as possible

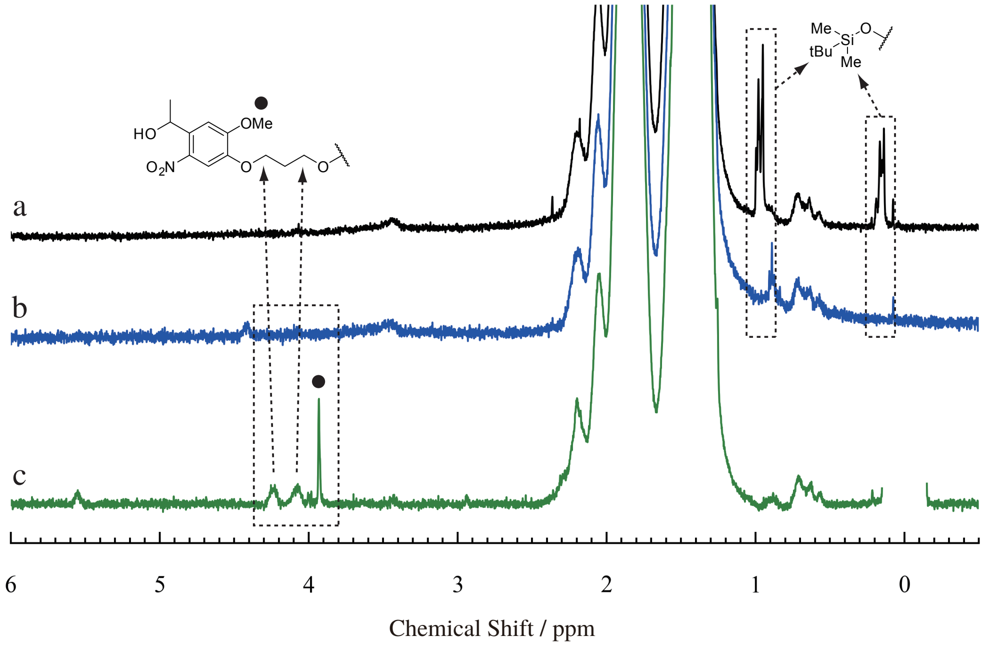

Figure A.5. ^{1}H-NMR spectra of PS homopolymers having a TBS-protected hydroxy group (PS-OTBS 7) (a), unprotected hydroxy group (PS-OH **8**) (b), and ONB linker (PS-ONB-OH **10**) (c) at the terminal. The chemical shift was calibrated using chloroform for curves a and b and TMS for curve c. The signal from TMS is omitted for brevity. The intensity is normalized by the integrated intensity of the broad signal at $\delta = 7.5 \sim 6.5$ ppm.

after the deprotection of the hydroxy terminal.

A.3.3 Synthesis of PCL-*b*-PS diblock copolymers

PCL-*b*-PS diblock copolymers were synthesized by a condensation between the carboxylic acid terminal of MeOC-PCL-COOH 3 and hydroxy terminal of PS-ONB-OH **10**. **Figure A.6**a shows the GPC chromatograms of the crude product right after the reaction (black curve), as well as the substrate PCL (orange curve) and PS (blue curves) homopolymers. The main peak position of the product is clearly shifted from that of the PCL and PS homopolymer, to the high molecular weight side, strongly suggesting the formation of a PCL-*b*-PS diblock copolymer. GPC chromatograms before and after the repeated fractional precipitation in a benzene/methanol and cyclohexane/hexane system (b) indicate that unreacted PCL homopolymers and PS homopolymers are successfully

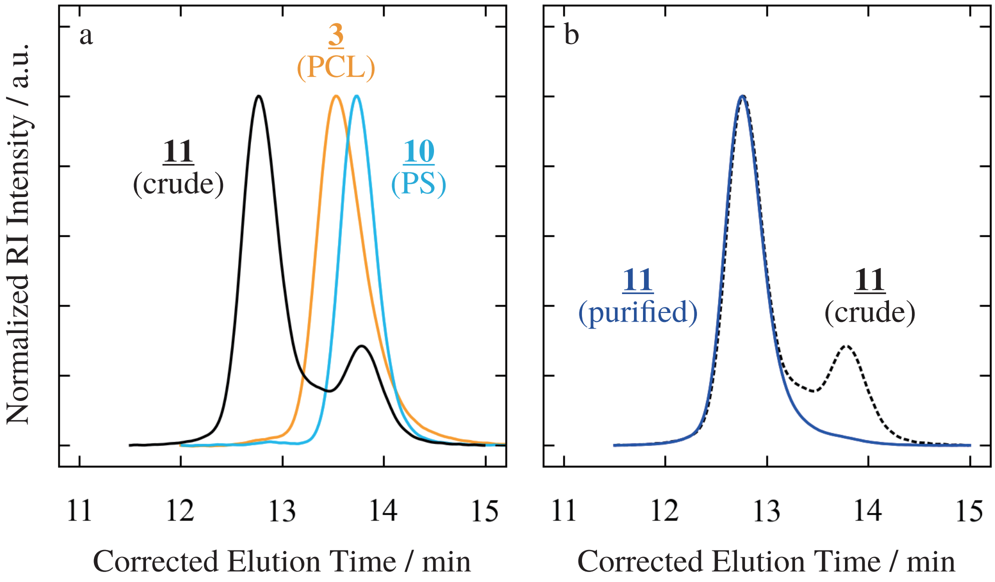

Figure A.6. GPC chromatograms of the crude PCL-*b*-PS diblock copolymer **11** (black curve in panel a), precursor PCL homopolymer **3** (orange curve in panel a), and PS homopolymer **10** (blue curve in panel a). Panel b shows the chromatograms of the product before (dotted curve) and after (solid curve) the purification by fractional precipitation.

removed.

References

1. Shibasaki, Y.; Sanada, H.; Yokoi, M.; Sanda, F.; Endo, T. *Macromolecules* **2000**, *33*, 4316–4320.
2. Makiguchi, K.; Satoh, T.; Kakuchi, T. *Macromolecules* **2011**, *44*, 1999–2005.

A.4 Spectrum Charts

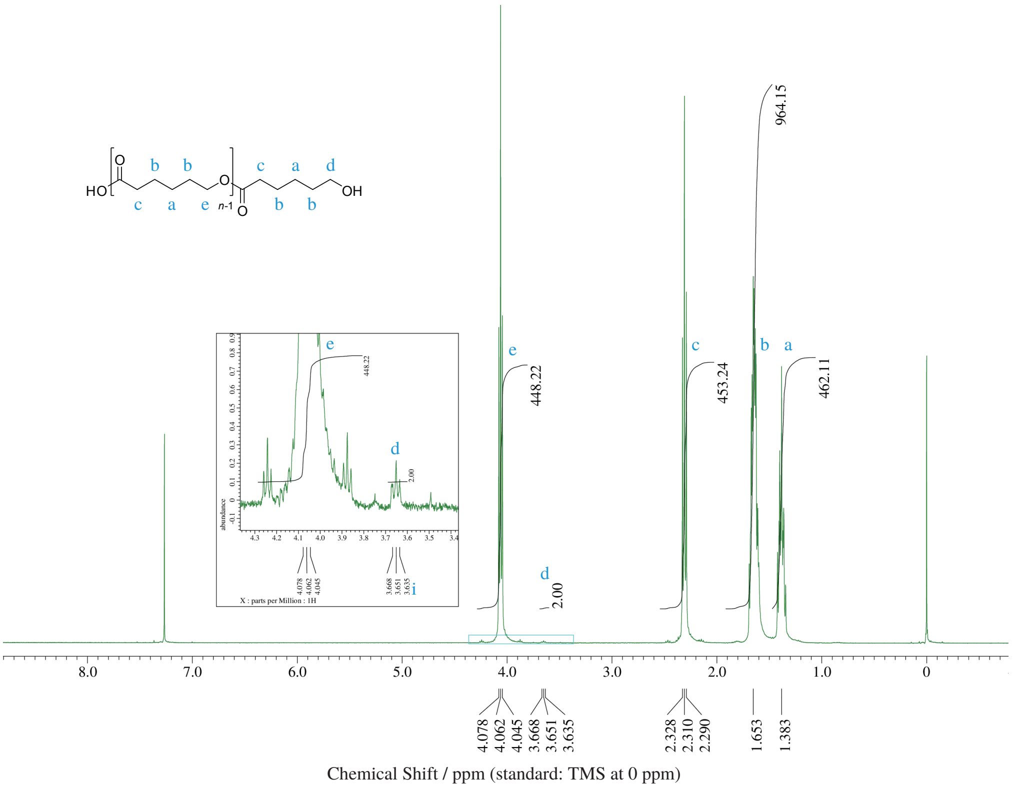

Figure A.7. ^{1}H-NMR spectrum of HOOC-PCL-OH **1**.

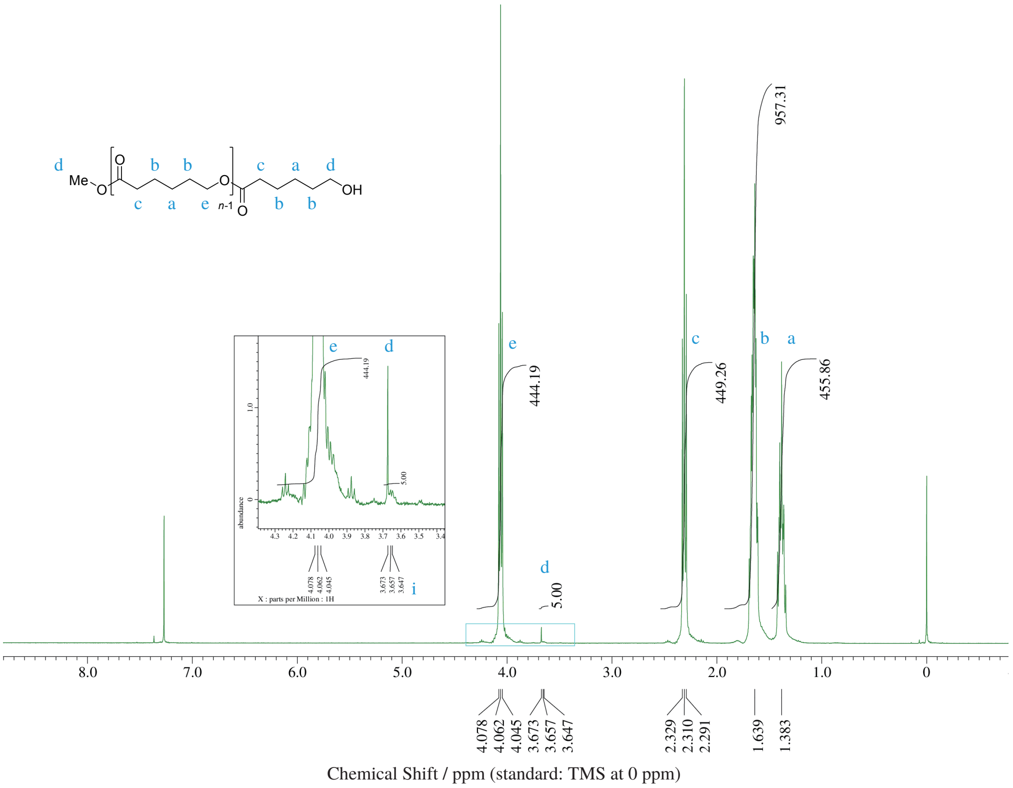

Figure A.8. ^{1}H-NMR spectrum of MeOC-PCL-OH <u>2</u>.

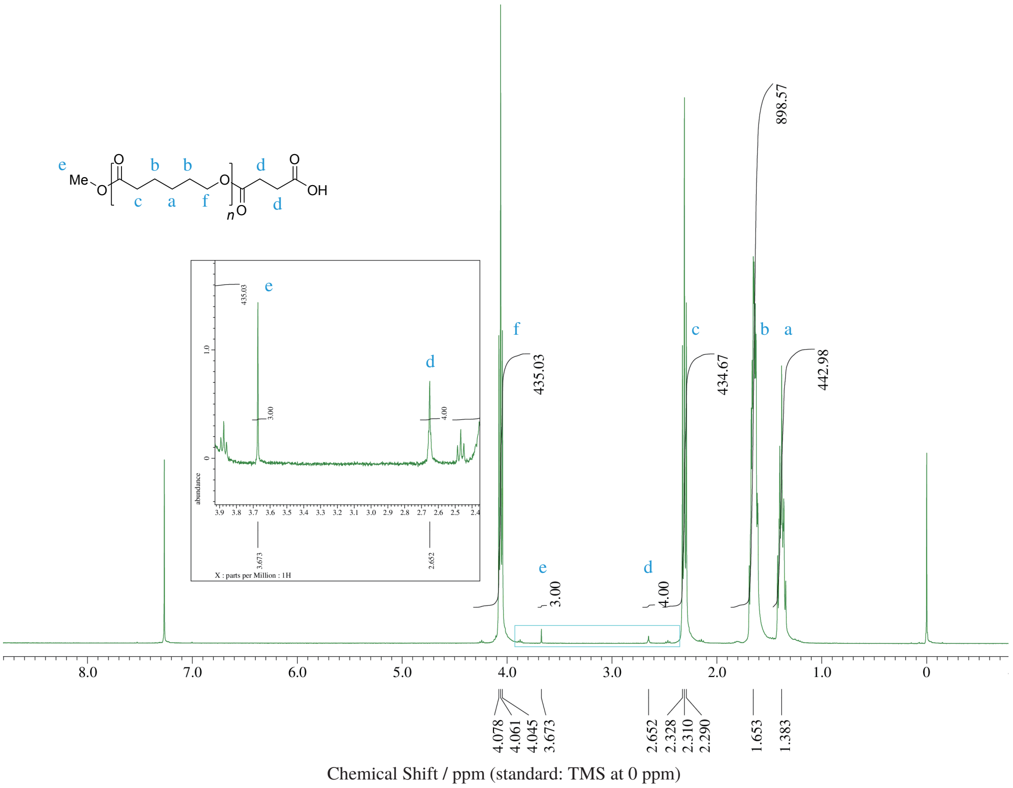

Figure A.9. ^{1}H-NMR spectrum of MeOC-PCL-COOH <u>3</u>.

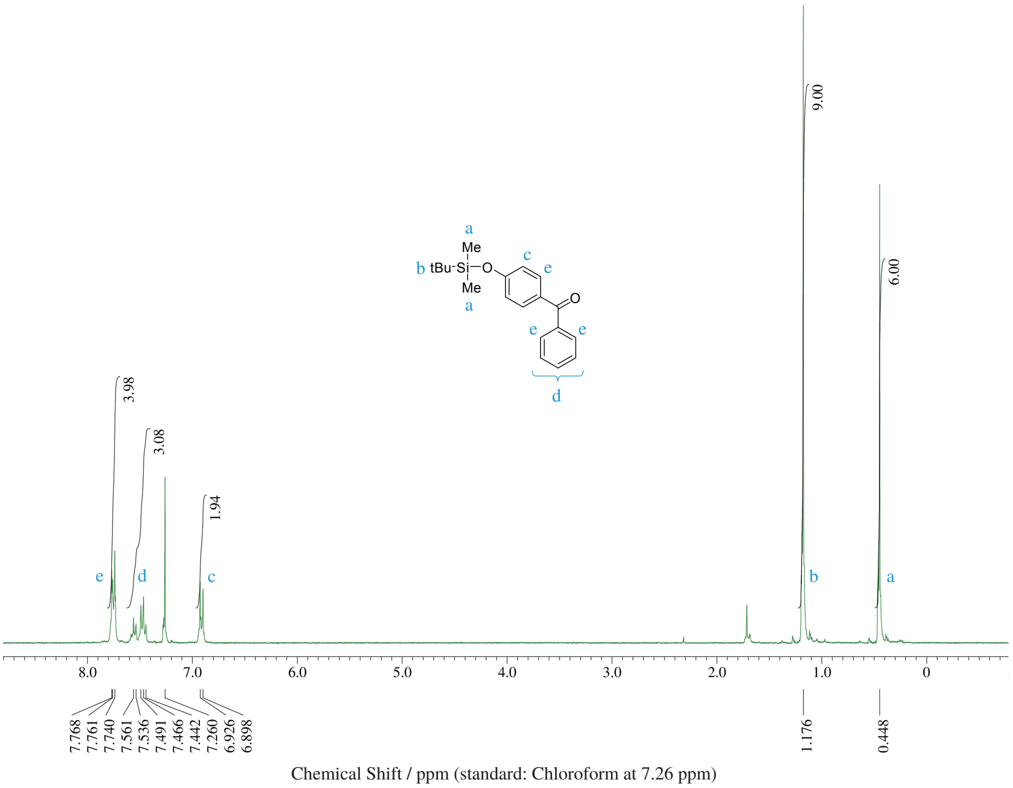

Figure A.10. ^{1}H-NMR spectrum of the compound **5**.

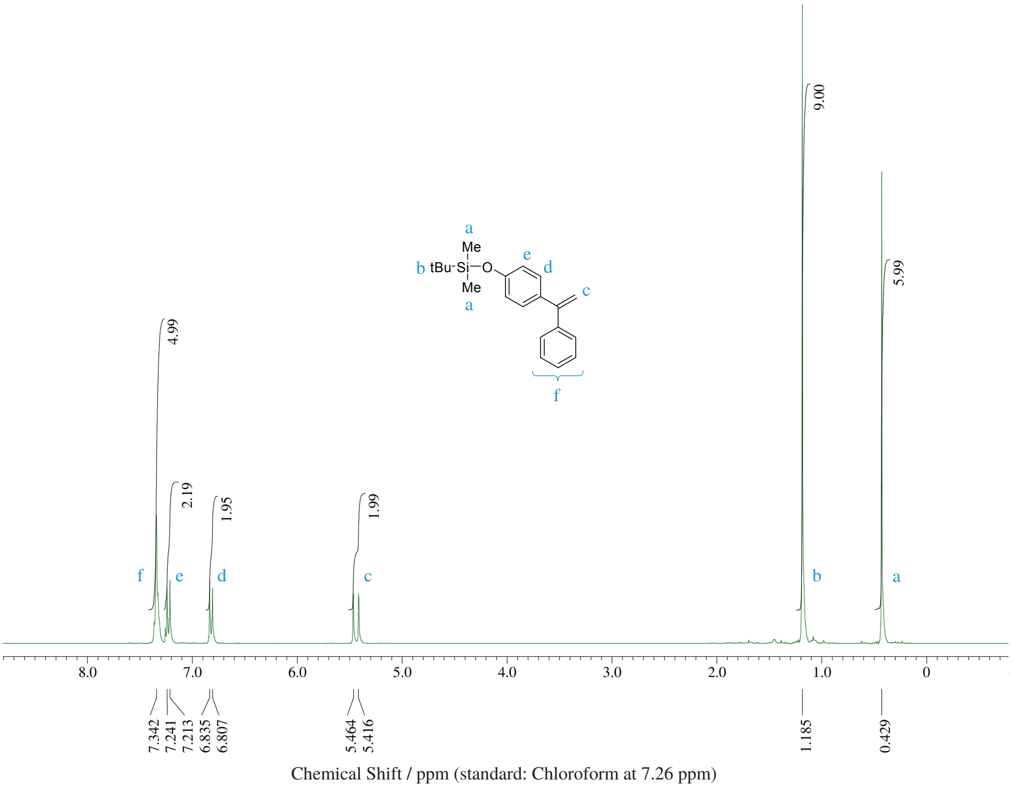

Figure A.11. ^{1}H-NMR spectrum of DPE-OTBS **6**.

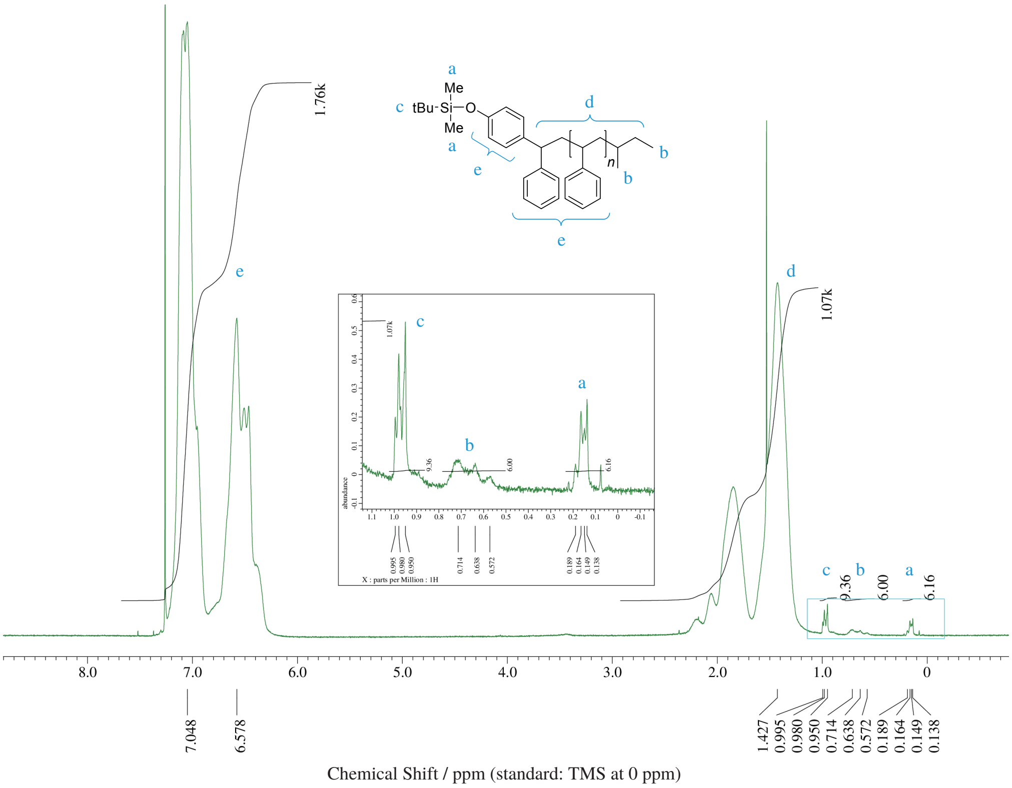

Figure A.12. ^{1}H-NMR spectrum of PS-OTBS **7**.

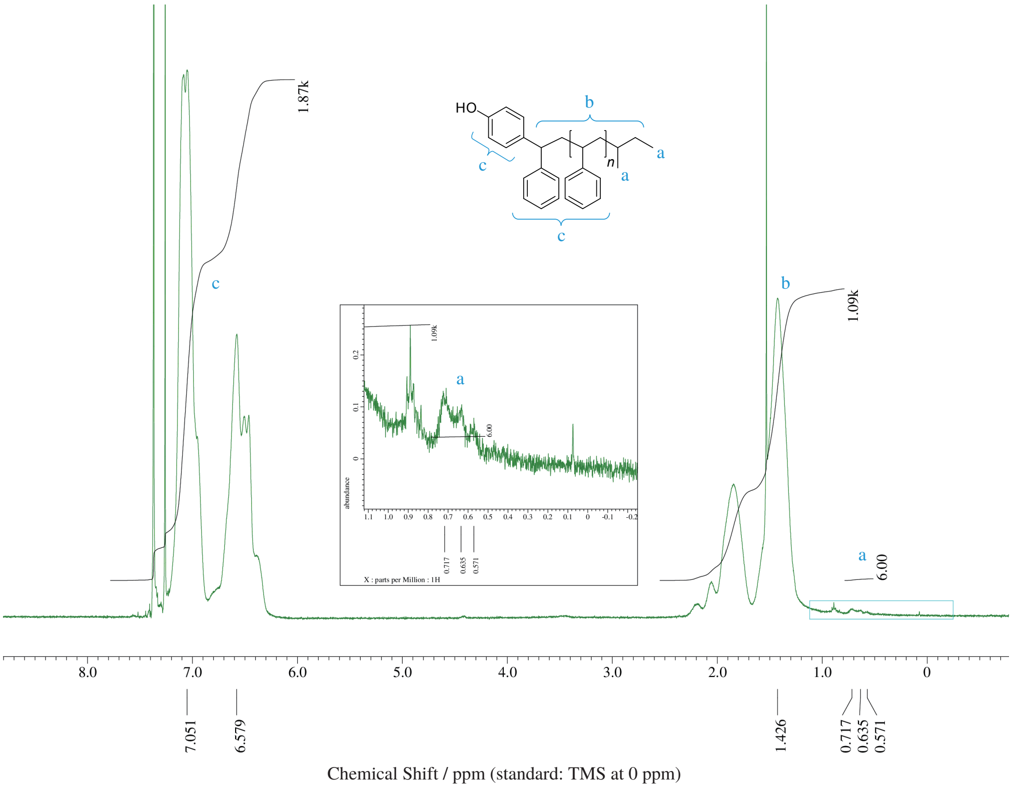

Figure A.13. ^{1}H-NMR spectrum of PS-OH **8**.

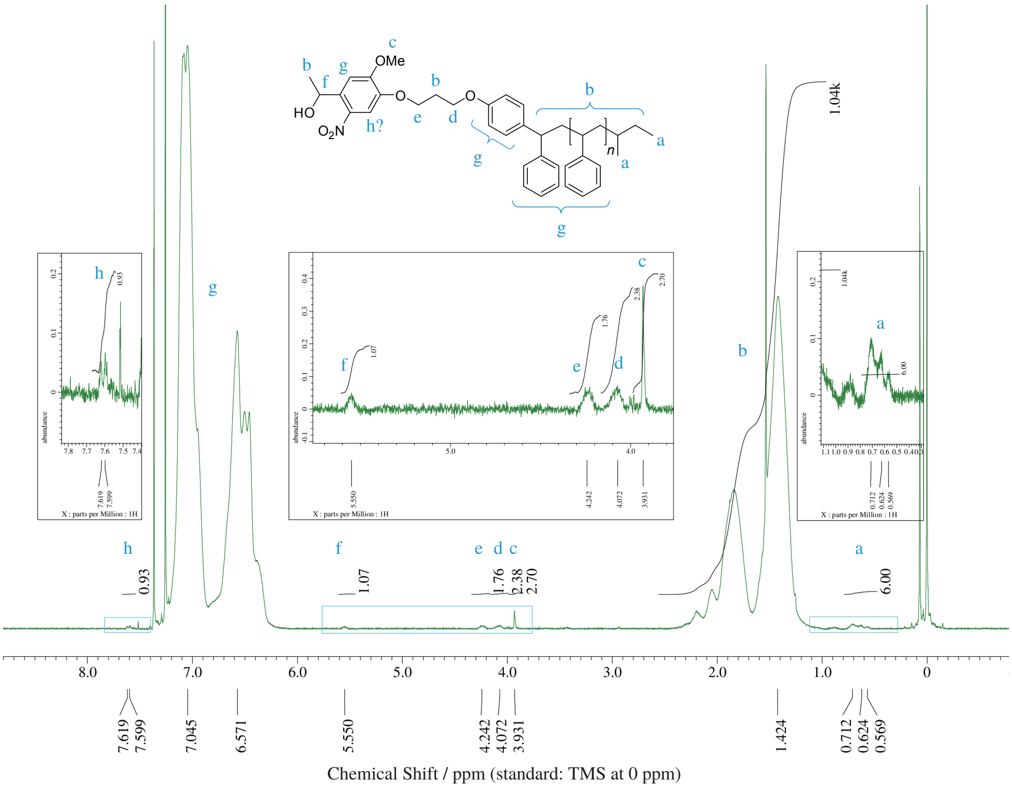

Figure A.14. ^{1}H-NMR spectrum of PS-ONB-OH **10**.

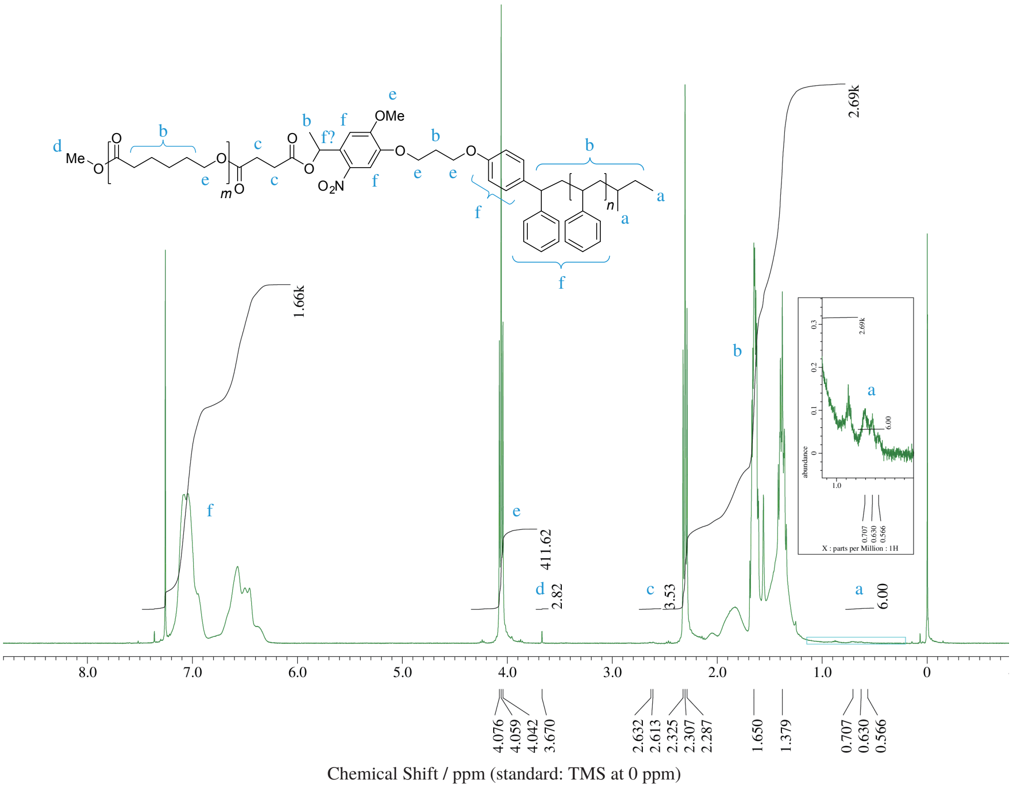

Figure A.15. ^{1}H-NMR spectrum of PCL-ONB-PS **11**.

Appendix B

Synthesis of Photocleavable PS-*b*-PCL-*b*-PS Triblock Copolymers

B.1 Overview of the Synthetic Method

The synthetic scheme of PS-*b*-PCL-*b*-PS triblock copolymers having ONB groups in either or both of two block junctions is shown in **Figure B.1**.

The PCL homopolymer **1** was synthesized by ring-opening polymerization of CL initiated from water and catalyzed by TsOH. First, the hydroxy end of the PCL homopolymer **1** was protected with a TBS group (**12**). Then the remaining carboxylic acid terminal was capped with an *o*-nitrobenzyl alcohol derivative **13** having a terminal alkyne moiety, followed by the deprotection of the TBS ether, which gave the PCL homopolymer having hydroxy and ONB terminal **15**. The PCL homopolymer was further reacted with an *o*-nitrobenzyl ester derivative **16** to yield compound **17**. **15** was also coupled with another linker **16'**, which has the structure similar to **16** but is photoinert. The photocleavable linkers (**13** and **16**) and photoinert linker (**16'**) were kindly provided by Prof. Kazuo Yamaguchi at Kanagawa University.

A bromoalkyl-terminated PS homopolymer **18** was synthesized via living anionic polymerization of styrene followed by sequential end-capping with 1,1-diphenylethylene and 1,3-bromopropane. The terminal bromine was then substituted with azide group to give an azide-terminated PS homopolymer **19**.

PCL (**17** or **17'**) and PS homopolymers **19** thus synthesized were coupled via cop-

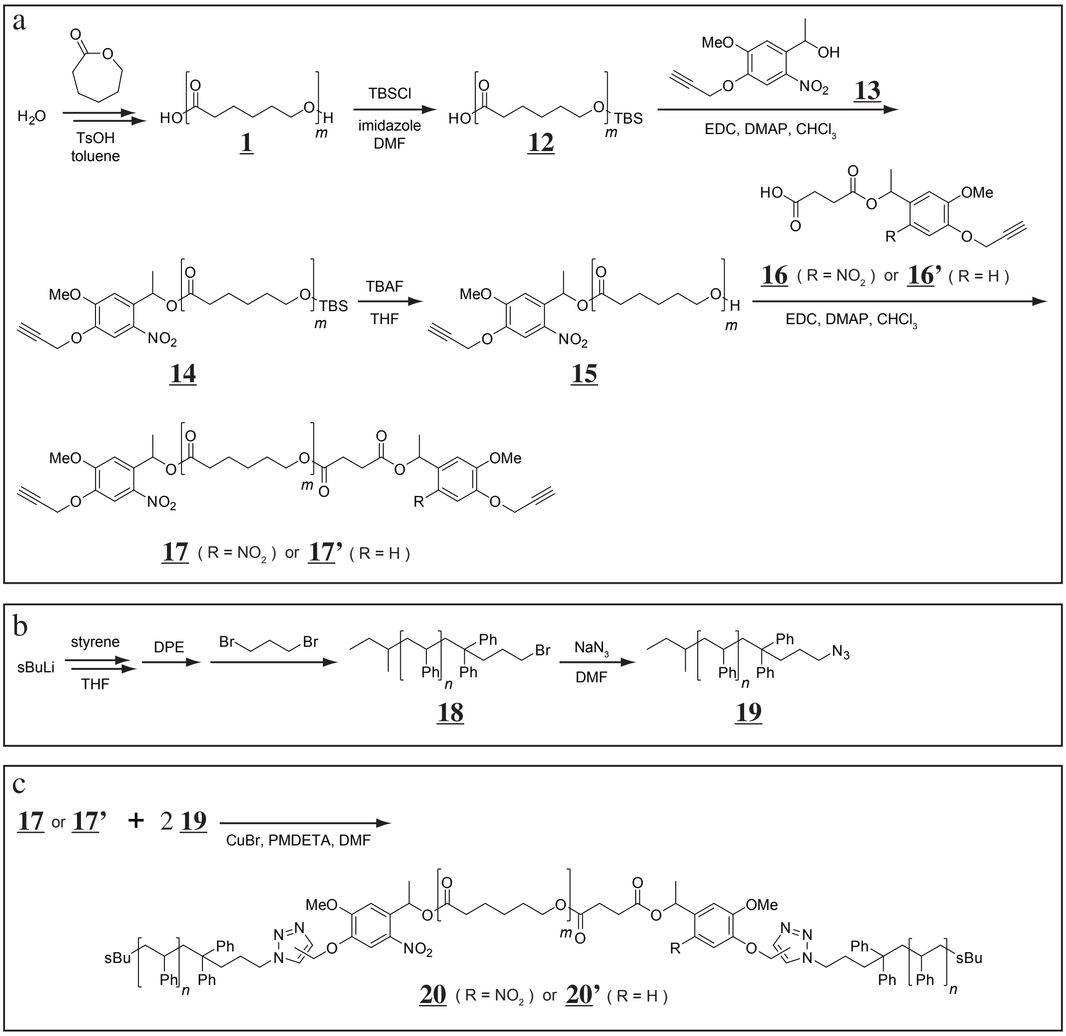

Figure B.1. Synthetic scheme for PS-*b*-PCL-*b*-PS triblock copolymers having ONB groups in either or both of two block junctions.

per(I)-catalyzed azide-alkyne cycloaddition (CuAAC), which gives the final product **20** or **20'**.

Detailed experimental procedures and results for SCS1 and SC'S1 are given in the following sections.

B.2 Experimental

B.2.1 Purification methods

Reagents were purified according to the following methods.

Chloroform Chloroform was washed with distilled water three times, dried over magnesium sulfate and calcium hydride, and distilled under nitrogen atmosphere before using it for synthesis.

1,3-Dibromopropane 1,3-Dibromopropane was dried over calcium hydride overnight, distilled by a trap-to-trap technique, and diluted with THF.

1,1-Diphenylethylene (DPE) DPE was distilled in the presence of 1,1-diphenylhexyllithium by a trap-to-trap technique and diluted with THF.

Copper(I) bromide (CuBr) CuBr ca. 1.0 g was washed with acetic acid 2 mL by stirring overnight, followed by a removal of the blue liquid layer by decantation to obtain gray powder. It was further washed with ethanol and diethyl ether three times, dried *in vacuo* for 1.5 h and stored in argon atmosphere.

Others PMDETA (Wako) and sodium azide (Wako) were used as received. DMF, chloroform, THF, and styrene were purified by the methods described in Section A.2.1.

B.2.2 Synthesis of HOOC-PCL-OH 1 (SN76)

TsOH monohydrate 0.481 g (2.53 mmol) was taken in a 500 mL three-neck round-bottom flask and azeotropically dried with toluene 50 mL at 130 °C for 4 h under nitrogen flow using a Dean-Stark apparatus to obtain partially dehydrated TsOH/toluene solution (ca. 30 mL). After cooling the solution to room temperature, CL 36.0 mL (37.1 g, 325 mmol) was added through a septum rubber. The reaction mixture was stirred at room temperature for 10 min then at 0 °C for 49.5 h. Small aliquots of the reaction mixture were sampled through the septum rubber to monitor the monomer conversion by ^{1}H-NMR. After quenching the reaction by adding excess TEA, the polymer was recovered by precipitating into ice-cold hexane and filtering. Since the crude product contained a low molecular weight fraction as revealed by GPC, it was further purified by fractional precipitation in a THF/methanol system. The fractionated polymer was dissolved in toluene and precipitated in hexane, filtered, and freeze-dried with benzene to give a white solid (20.4 g, 55%, $M_\mathrm{n} = 27400\ \mathrm{g\,mol^{-1}}$ by ^{1}H-NMR, $M_\mathrm{w}/M_\mathrm{n} = 1.06$ by GPC).

B.2.3 Synthesis of HOOC-PCL-OTBS 12 (SN115)

HOOC-PCL-OH 1 6.71 g ($M_\mathrm{n} = 27400\ \mathrm{g\,mol^{-1}}$, 0.245 mmol) and imidazole 0.693 g (10.2 mmol) were dissolved in DMF 12.0 mL in a flame-dried and nitrogen-purged 100 mL two-neck round-bottom flask. TBSCl 1.16 g (7.68 mmol) was then added and the reaction mixture was stirred for 24 h under argon atmosphere. DMF 20 mL and distilled water 2.0 mL were then added, followed by stirring for another 16 h. The polymer was recovered by precipitation in ice-cold methanol and subsequent filtering. It was then dissolved in chloroform, precipitated in ice-cold methanol, filtered, and freeze-dried with benzene which gave a white solid (6.68 g, 99%).

B.2.4 Synthesis of Alkyne-ONB-PCL-OH 15 (SN117)

HOOC-PCL-OTBS 12 6.51 g ($M_\mathrm{n} = 27500\ \mathrm{g\,mol^{-1}}$, 0.237 mmol, 1 eq.), DMAP 0.881 g (7.22 mmol, 30 eq.), and Alkyne-ONB-OH 13 0.403 g (1.61 mmol, 6.8 eq.) were dissolved in dry-chloroform 5.0 mL in a flame-dried and nitrogen-purged 100 mL two-neck round-bottom flask. Then EDC 1.11 g (5.78 mmol, 24 eq.) was added, followed by stirring for 22 h in dark. The polymer was recovered by precipitation in ice-cold methanol and subsequent filtering. It was then dissolved in chloroform, precipitated in ice-cold methanol, filtered, and freeze-dried with benzene, yielding a slightly brown white solid (6.47 g, 99%).

Alkyne-ONB-PCL-OTBS **<u>14</u>** 6.47 g ($M_\mathrm{n} = 27800\,\mathrm{g\,mol^{-1}}$, 0.233 mmol, 1 eq.), THF 10 mL, and acetic acid 0.7 mL (0.74 g, 12 mmol, 52 eq.) were taken in a 500 mL recovery flask and stirred for complete dissolution. Then 1.0 M TBAF/THF 8.0 mL (8.0 mmol, 34 eq.) was added and the reaction mixture was stirred for 29 h. The polymer was then recovered by precipitation in ice-cold methanol twice and freeze dried with benzene, which gave a slightly brown white solid (6.67 g, $\sim$ 100%).

B.2.5 Synthesis of Alkyne-ONB-PCL-ONB-Alkyne <u>17</u> (SN118)

Alkyne-ONB-PCL-OH **<u>15</u>** 3.20 g ($M_\mathrm{n} = 27700\,\mathrm{g\,mol^{-1}}$, 0.116 mmol, 1 eq.), DMAP 510 mg (4.18 mmol, 36 eq.), and Alkyne-ONB-COOH **<u>16</u>** 241 mg (0.687 mmol, 5.9 eq.) were dissolved in dry-chloroform 6.0 mL in a flame-dried and nitrogen-purged 100 mL two-neck round-bottom flask. Next, EDC 596 mg (3.10 mmol, 27 eq.) was added to the reaction mixture, which was stirred for 24 h in the dark. The polymer was then recovered by precipitation in ice-cold methanol twice and freeze dried with benzene, which gave a slightly brown white solid (3.16 g, 97%).

B.2.6 Synthesis of Alkyne-ONB-PCL-B-Alkyne <u>17</u>’ (SN119)

The condensation reaction of Alkyne-ONB-PCL-OH and Alkyne-B-COOH was carried out in the same manner as Alkyne-ONB-PCL-ONB-Alkyne **<u>17</u>** (previous section). Alkyne-ONB-PCL-OH 3.15 g ($M_\mathrm{n} = 27700\,\mathrm{g\,mol^{-1}}$, 0.114 mmol, 1 eq.) with Alkyne-B-COOH 210 mg (0.686 mmol, 6.0 eq.) gave a slightly brownish white solid (3.16 g, 99%).

B.2.7 Synthesis of PS-Br **18** (SN121)

The living anionic polymerization of styrene and subsequent end-functionalization were carried out by a break-seal technique under high vacuum condition. A reaction vessel was evacuated, flame-dried, sealed off from the vacuum line, and washed with red 1,1-diphenylhexyllithium/heptane solution. After removing the washing solution, 0.0930 M *sec*-butyllithium/heptane 2.67 mL (0.248 mmol) was introduced in the vessel cooled to −78 °C, and 1.08 M styrene/THF 28.6 mL (30.9 mmol), carefully cooled to −78 °C, was introduced to the vessel through a break-seal followed by vigorous stirring for several minutes. After holding it for 20 min, 0.164 M DPE/THF 1.92 mL (0.315 mmol), cooled to −78 °C, was added to the reaction mixture and stirred until the mixture becomes homogeneous. After leaving it for 20 min, 0.261 M 1,3-dibromopropane/THF 6.23 mL (1.63 mmol), cooled to −78 °C, was poured into the reaction mixture, vigorously stirred until the red color of the living anion was disappeared, and held for 1 h. The reaction mixture was poured into methanol and the precipitate was recovered by filtering. The recovered polymer was dissolved in toluene, precipitated in methanol, filtered, and freeze-dried with benzene which gave a white solid (3.09 g, 96 %).

B.2.8 Synthesis of PS-N_3 **19** (SN122)

PS-Br **18** 3.10 g ($M_\mathrm{n} = 13500\,\mathrm{g\,mol^{-1}}$, 0.230 mmol, 1 eq.) was dissolved in DMF 20 mL in an Erlenmeyer flask, and sodium azide 0.234 g (3.60 mmol, 16 eq.) was added subsequently. After stirring for 23 h, the reaction mixture was poured in methanol to recover the precipitated polymer by filtering. The polymer was again dissolved in toluene, precipitated in methanol, filtered, and freeze-dried with benzene which gave a white solid (3.05 g, 98%).

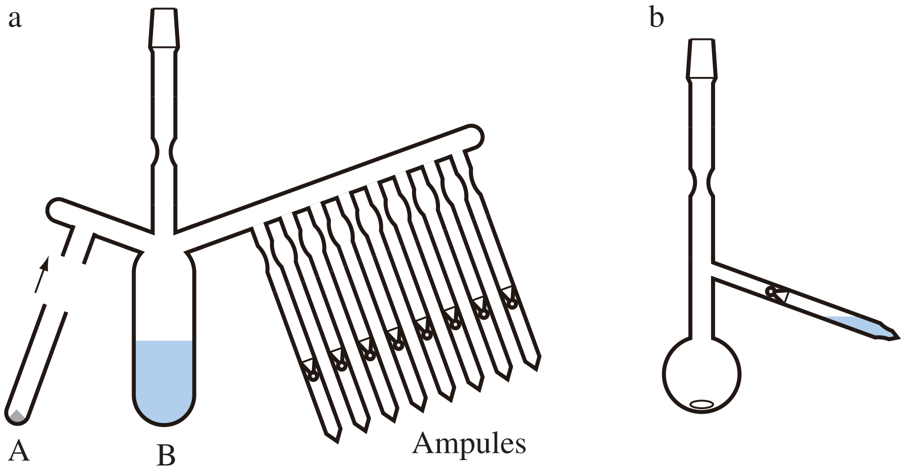

Figure B.2. Illustration of the apparatus used to prepare the ampules of catalyst solution for CuAAC (a) and that for the CuAAC reaction itself (b).

B.2.9 Synthesis of PS-ONB-PCL-ONB-PS <u>20</u> (SN124)

CuAAC reaction of PCL and PS homopolymers was carried out by a standard break-seal technique to prevent the oxidation of the copper catalyst and oxidative coupling between terminal alkyne moieties. Hence it is required to prepare catalyst solution containing CuBr and PMDETA sealed in an evacuated ampule beforehand. The apparatus used to prepare the ampules is described in **Figure B.2**a. Tube A containing CuBr 20.5 mg (0.143 mmol) was first joined to the apparatus, and then DMF 28 mL and PMDETA 58 μL (0.28 mmol) were taken in the tube B, followed by evacuation and degassing by freeze-pump-thaw cycles. After sealing the apparatus from a vacuum line, CuBr in tube A was mixed with the liquid in tube B which gave a slightly blue solution. The solution was partitioned into 8 ampules to obtain 3-4 mL DMF solution containing CuBr 14-20 µmol and PMDETA 28-38 µmol.

The PCL homopolymer <u>**17**</u> 328 mg ($M_\mathrm{n} = 28000\ \mathrm{g\,mol^{-1}}$, 11.7 µmol, 1 eq.) and PS homopolymer <u>**19**</u> 475 mg ($M_\mathrm{n} = 13500\ \mathrm{g\,mol^{-1}}$, 35.2 µmol, 3.0 eq.) were taken in a reaction vessel (**Figure B.2**b) fitted with an ampule of CuBr/PMDETA/DMF solution 3.82 mL (CuBr 18.6 µmol, 1.6 eq.; PMDETA 36 µmol, 3.1 eq.), evacuated, and sealed off from a vacuum line. The CuBr/PMEDETA/DMF solution was then introduced to the vessel and dissolved the PCL and PS homopolymers. After stirring for 17.5 h in the dark, the crude product was recovered by precipitating in excess methanol/water 2/1 v/v and freeze-drying with benzene (slightly brown white solid, 807 mg, 100%). It was further purified by fractional precipitation in cyclohexane/hexane and toluene/methanol systems to remove unreacted substrates and PCL-*b*-PS diblock copolymers.

B.2.10 Synthesis of PS-ONB-PCL-B-PS <u>20’</u> (SN126)

The method of synthesis for PS-ONB-PCL-B-PS **<u>20’</u>** was the same as that of PS-ONB-PCL-ONB-PS **<u>20</u>** (previous section). The PCL homopolymer **<u>21</u>** 256 mg (M_n = 28000 $\mathrm{g\,mol^{-1}}$, 9.14 µmol, 1 eq.) and PS homopolymer **<u>19</u>** 363 mg (M_n = 13500 $\mathrm{g\,mol^{-1}}$, 26.9 µmol, 2.9 eq.) were dissolved in CuBr/PMDETA/DMF solution 3.83 mL (CuBr 18.7 µmol, 2.0 eq.; PMDETA 36 µmol, 3.9 eq.) and stirred *in vacuo* for 5.5 h in the dark. The crude product was recovered by precipitating in excess methanol/water 2/1 v/v and freeze-drying with benzene (slightly brown white solid, 629 mg, $\sim$ 100%). The remaining substrates and PCL-*b*-PS diblock copolymers were removed by fractional precipitation in a cyclohexane/hexane and toluene/methanol systems.

B.3 Results

B.3.1 Synthesis of PCL Homopolymers

The result of the polymerization of CL is similar to that described in Section A.3.1, therefore it is not repeated here again. **Figure B.3** shows the ^{1}H-NMR spectra of PCL homopolymers at each synthetic step. The protection and deprotection of the hydroxy terminal (**<u>1</u>**→**<u>12</u>** and **<u>14</u>**→**<u>15</u>**) can be verified by the presence of singlets at $\delta = 0.03$ and 0.88 ppm (a) arising from a TBS group and by shifting of a triplet at $\delta = 3.65$ ppm (b) to the higher field side. It should be noted that TBSCl also reacts with the carboxylic acid terminal to form a TBS ester, which was actually confirmed by the presence of

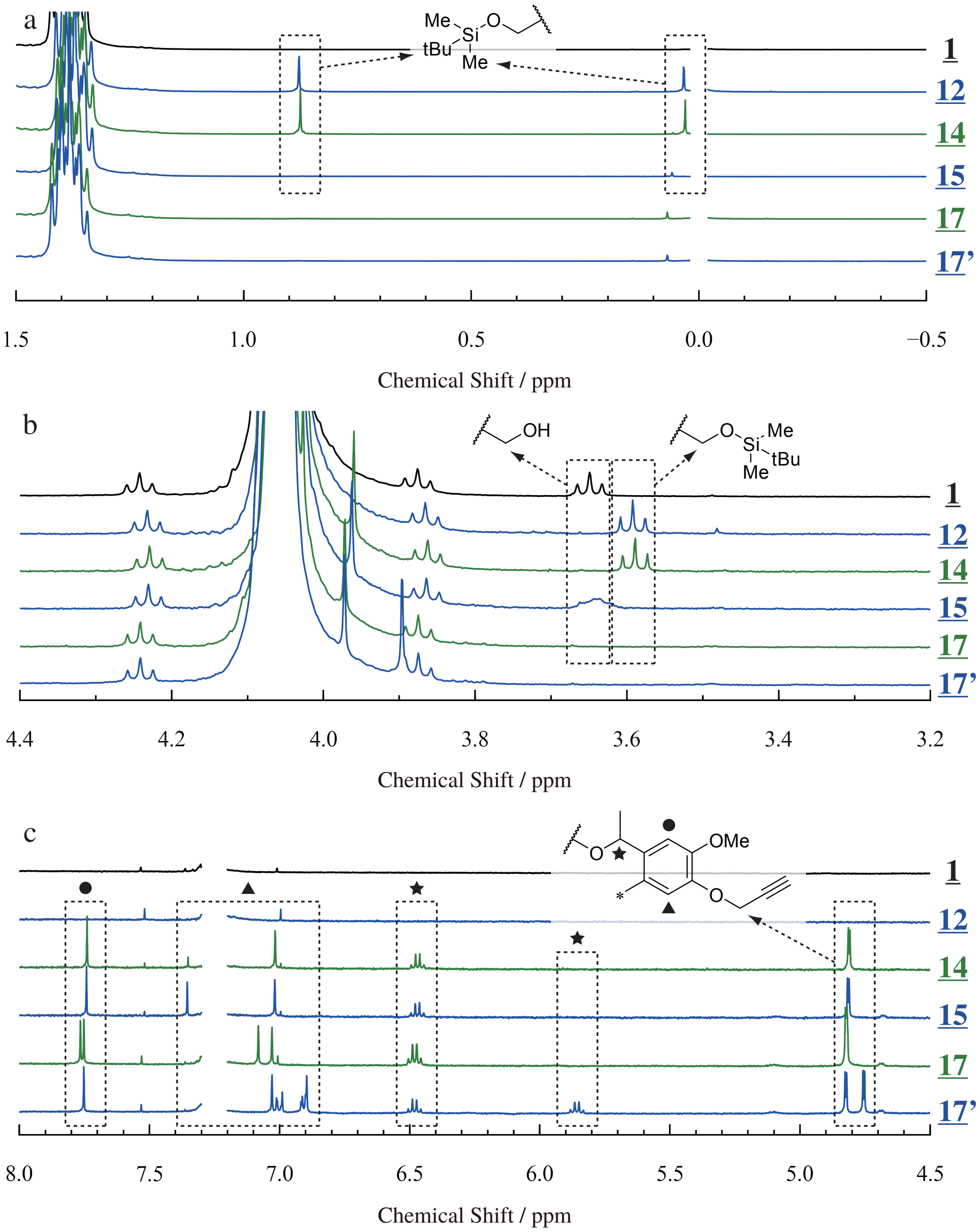

Figure B.3. ^{1}H-NMR spectra of HOOC-PCL-OH 1, HOOC-PCL-OTBS 12, Alkyne-ONB-PCL-OTBS 14, Alkyne-ONB-PCL-OH 15, Alkyne-ONB-PCL-ONB-Alkyne 17, and Alkyne-ONB-PCL-B-Alkyne 17’ in different spectral regions (panels a, b, and c). The chemical shift was calibrated by chloroform for curves 2 to 4 and TMS for others. Intensity is normalized by the integrated intensity of the triplet at $\delta = 4.05$ ppm. Signals from chloroform and TMS are omitted for clarity.

extra singlets at $\delta = 0.23$ and 0.90 ppm. TBS esters were easily hydrolyzed by the presence of water. Signals from aromatic protons, benzyl protons, and methylene protons

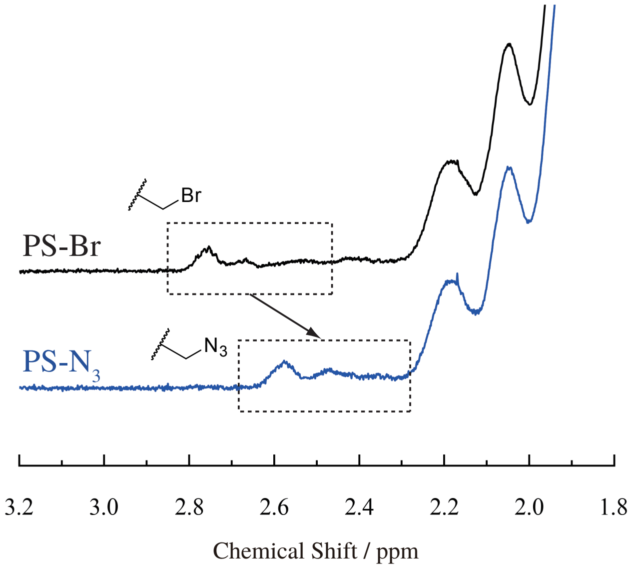

Figure B.4. ^{1}H-NMR spectra of PS-Br and PS-N$_3$.

next to an alkyne unit are quantitatively observed in **Figure B.3**c, indicating that the photocleavable and photoinert linkers are successfully introduced at the terminals of the PCL homopolymer.

The results of GPC measurements (not shown) ensured that the molecular weight and its distribution did not changed throughout the series of reactions. However, the deprotection of TBS-capped hydroxy terminal using TBAF alone resulted in significant broadening of the GPC peak, presumably due to a degradation caused by basic TBAF. This could be avoided by adding acetic acid.

B.3.2 Synthesis of PS Homopolymers

The PS homopolymer bearing a bromoalkyl group at the terminal (PS-Br, **18**) was synthesized by living anionic polymerization followed by end-functionalization with 1,3-dibromopropane[1]. The GPC chromatogram of the product (not shown) showed a unimodal and narrow peak, which ensures that coupling between PS homopolymers did not occur. **Figure B.4** shows the ^{1}H-NMR spectrum of PS-Br, in which the presence of a signal due to methylene protons next to the terminal bromine suggests the successful end-

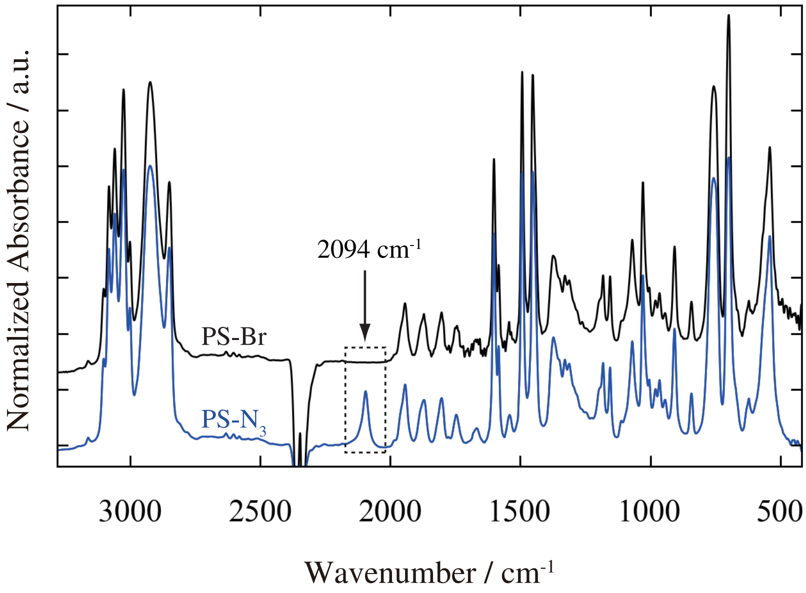

Figure B.5. IR spectra of the compound **18** (PS-Br) and **19** (PS-N$_3$). The measurements were performed on a solution-cast film having thickness of ca. 50 µm. The data were normalized and vertically shifted for legibility.

functionalization, though the signal is extremely broad and weak. This signal shifted to the high field side after the reaction with sodium azide, indicating that bromine is substituted by azide. The introduction of the terminal azide was also confirmed qualitatively by infrared spectroscopy (IR). IR spectra of PS homopolymers before (PS-Br, **18**) and after (PS-N$_3$, **19**) the reaction with sodium azide is shown in **Figure B.5**. An absorption at 2094 cm^{-1} in the spectrum of PS-N$_3$, which can be assigned to N≡N asymmetric stretching of the aliphatic azide[2], clearly indicates the presence of azide groups after the reaction.

B.3.3 Synthesis of PS-*b*-PCL-*b*-PS Triblock Copolymers

Photocleavable PS-*b*-PCL-*b*-PS triblock copolymers were synthesized by coupling the PCL homopolymer **17** or **17’** and the PS homopolymer **19** via CuAAC, well known as one of the “click” reactions[3]. The GPC chromatograms of **17**, **19**, and the crude product of the coupling reaction between these two are shown in **Figure B.6**. The main peak position clearly shifted to the high molecular weight side after the coupling

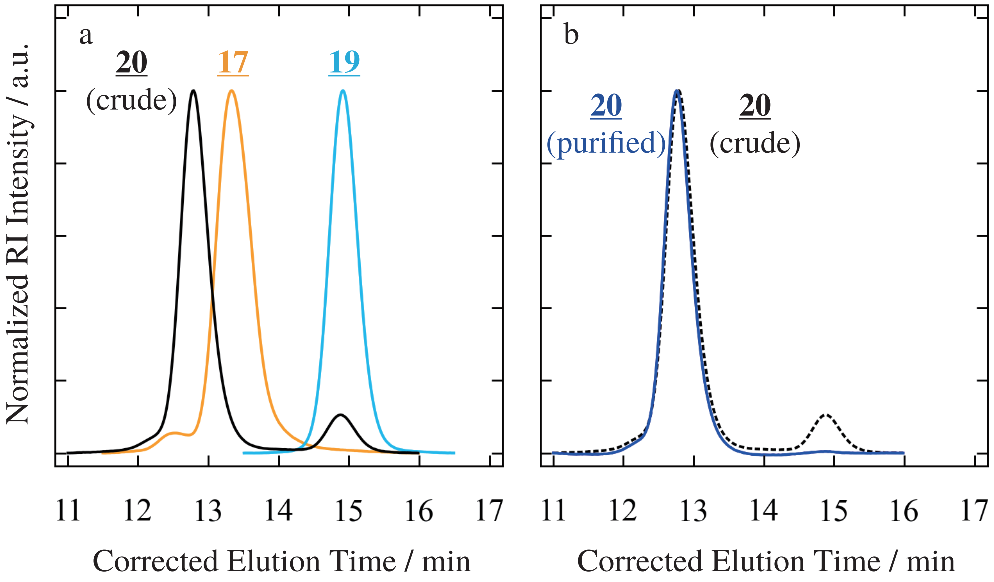

Figure B.6. GPC chromatograms of the PCL homopolymer **17** (orange curve in a), PS-N_3 **19** (blue curve in b), and the crude product of the PS-*b*-PCL-*b*-PS triblock copolymer **20** (black curve in a). Panel b shows the chromatograms of the PS-*b*-PCL-*b*-PS triblock copolymer before (dashed curve) and after (solid curve) the fractional precipitation. All chromatograms were detected by refractive index (RI) detector and normalized by peak heights. Chloroform was used as an eluent, and the elution time was calibrated using PS standards.

reaction. M_n of the product was almost equal to the sum of $M_n$of two PS homopolymers and one PCL homopolymer, indicating that the PS-*b*-PCL-*b*-PS triblock copolymer was successfully obtained. Moreover, it is clear that the product contained only the PS-*b*-PCL-*b*-PS triblock copolymer and PS homopolymer, which suggests that the PCL homopolymer was completely consumed. The excess PS homopolymer remained, as well as a small amount of PCL-*b*-PS diblock copolymers formed by incomplete reaction, could be removed quite easily by the fractional precipitation using a cyclohexane/hexane and toluene/methanol system.

References

1. Hirao, A.; Tohoyama, M.; Nakahama, S. *Macromolecules* **1997**, *30*, 3484–3489.
2. Lieber, E.; Rao, C. N. R.; Chao, T. S.; Hoffman, C. W. W. *Analytical Chemistry* **1957**, *29*, 916–918.
3. Espeel, P.; Du Prez, F. E. *Macromolecules* **2015**, *48*, 2–14.

B.4 Spectrum Charts

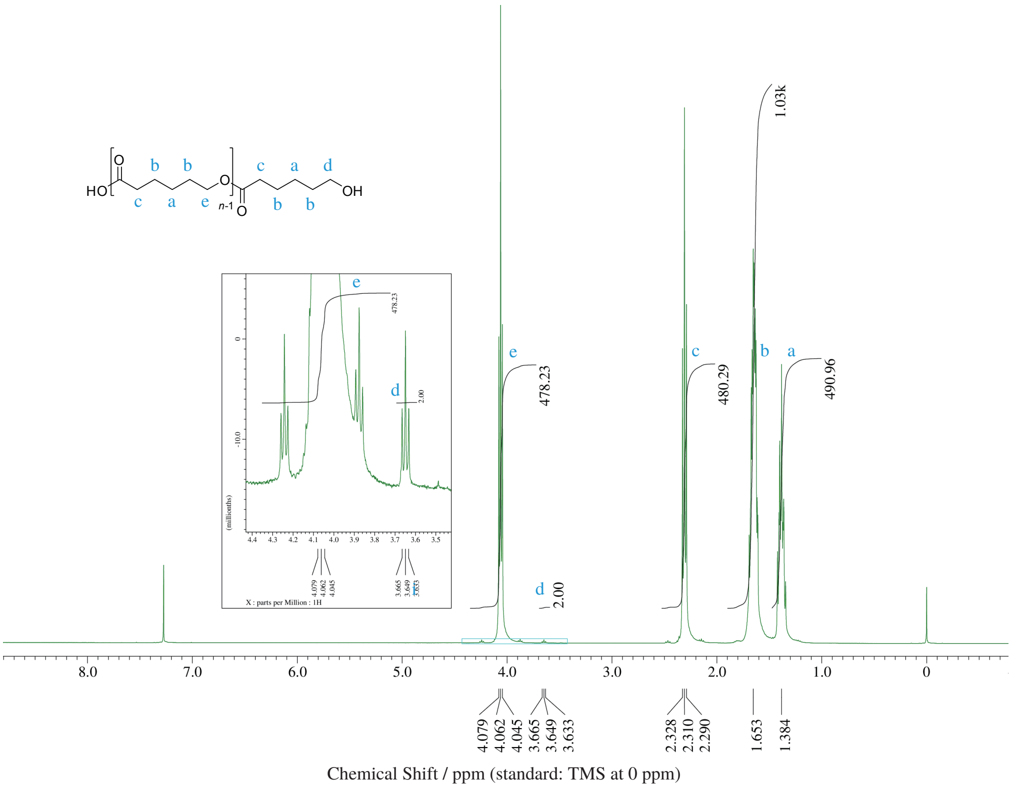

Figure B.7. ^{1}H-NMR spectrum of HOOC-PCL-OH **1**.

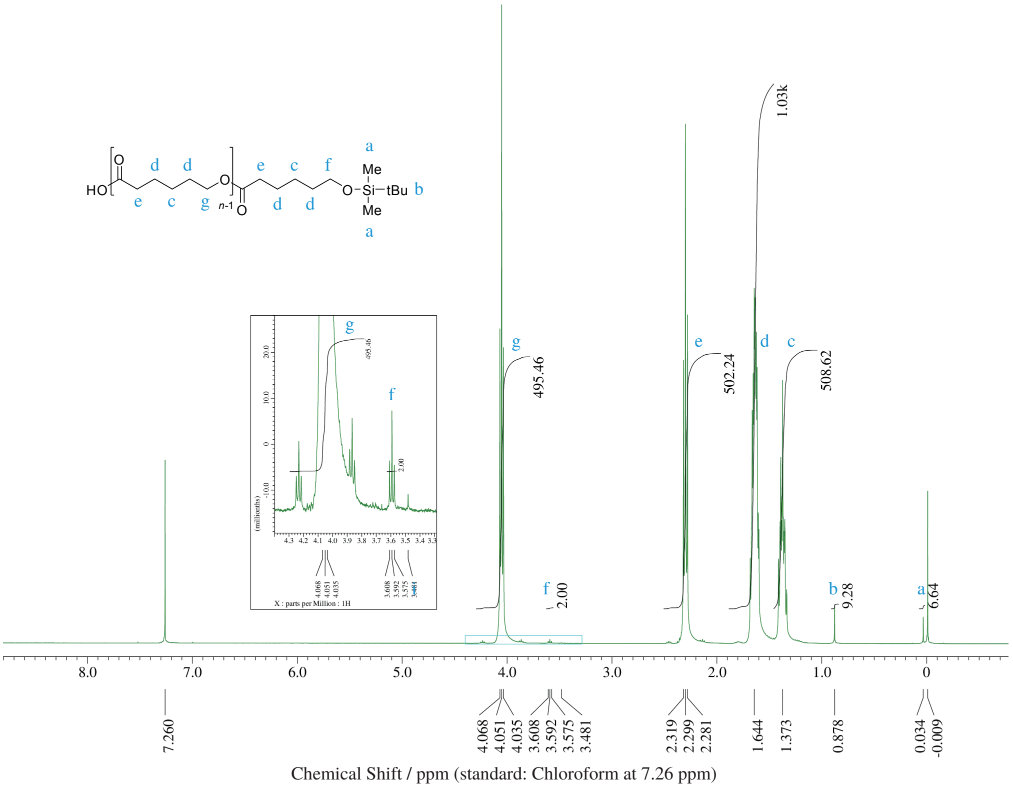

Figure B.8. ^{1}H-NMR spectrum of HOOC-PCL-OTBS **<u>12</u>**.

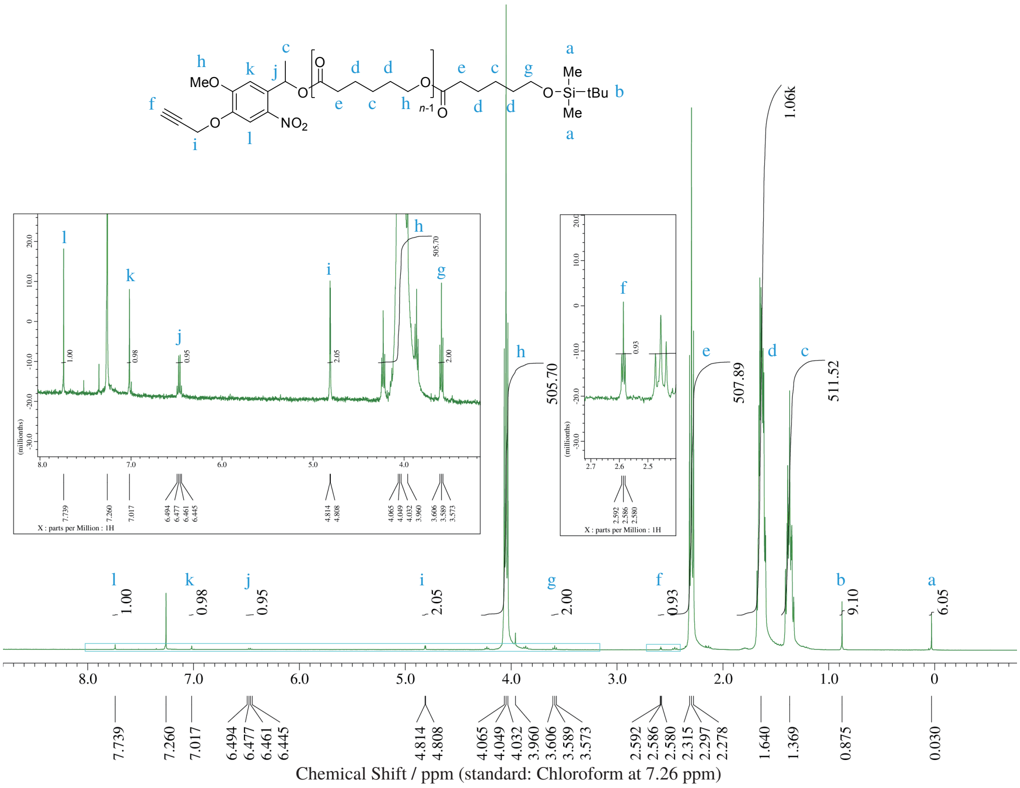

Figure B.9. ^{1}H-NMR spectrum of Alkyne-ONB-PCL-PCL-OTBS **<u>14</u>**.

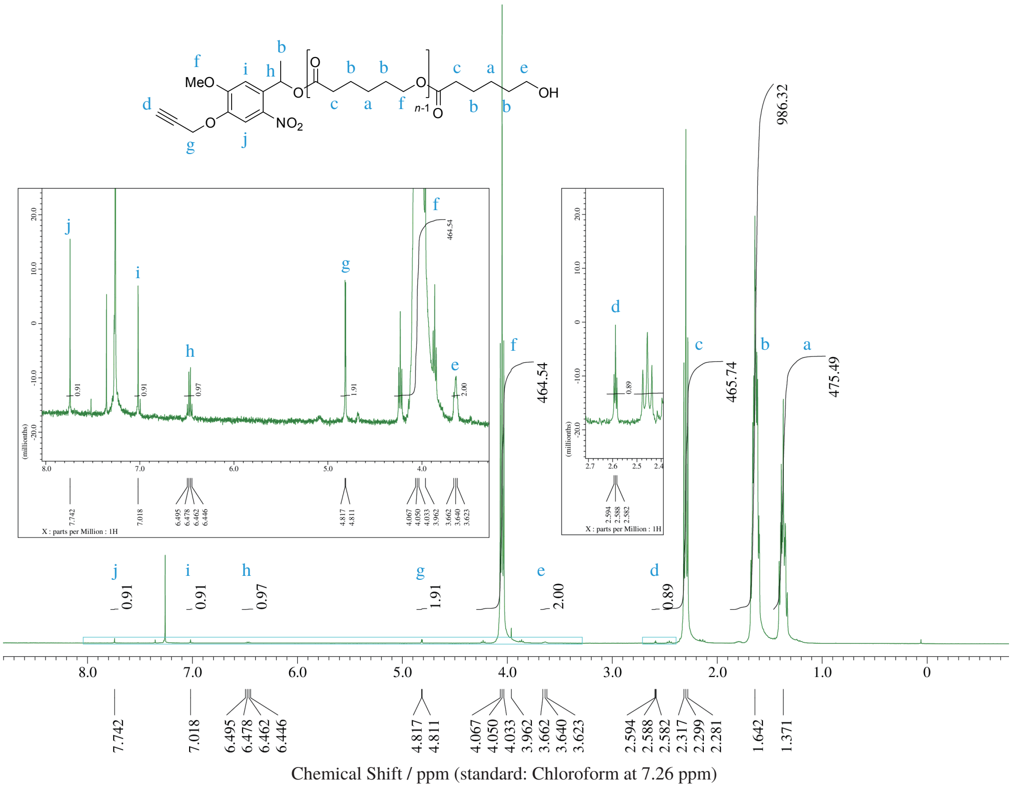

Figure B.10. ^{1}H-NMR spectrum of Alkyne-ONB-PCL-OH <u>**15**</u>.

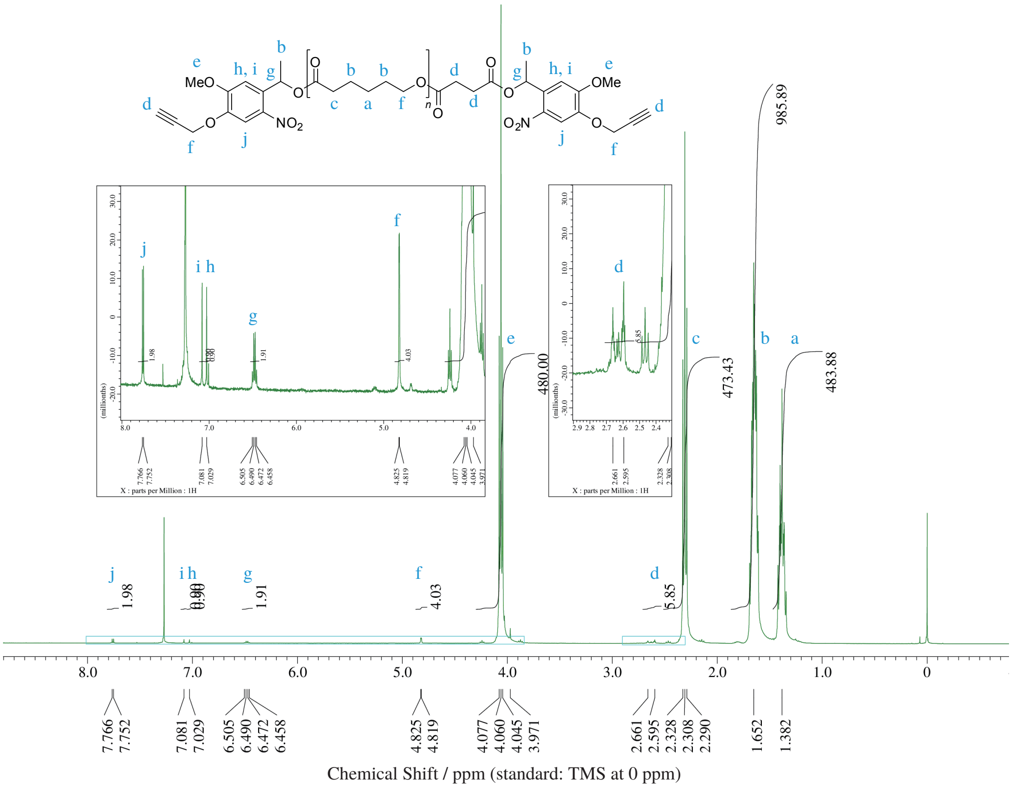

Figure B.11. ^{1}H-NMR spectrum of Alkyne-ONB-PCL-ONB-Alkyne <u>**17**</u>.

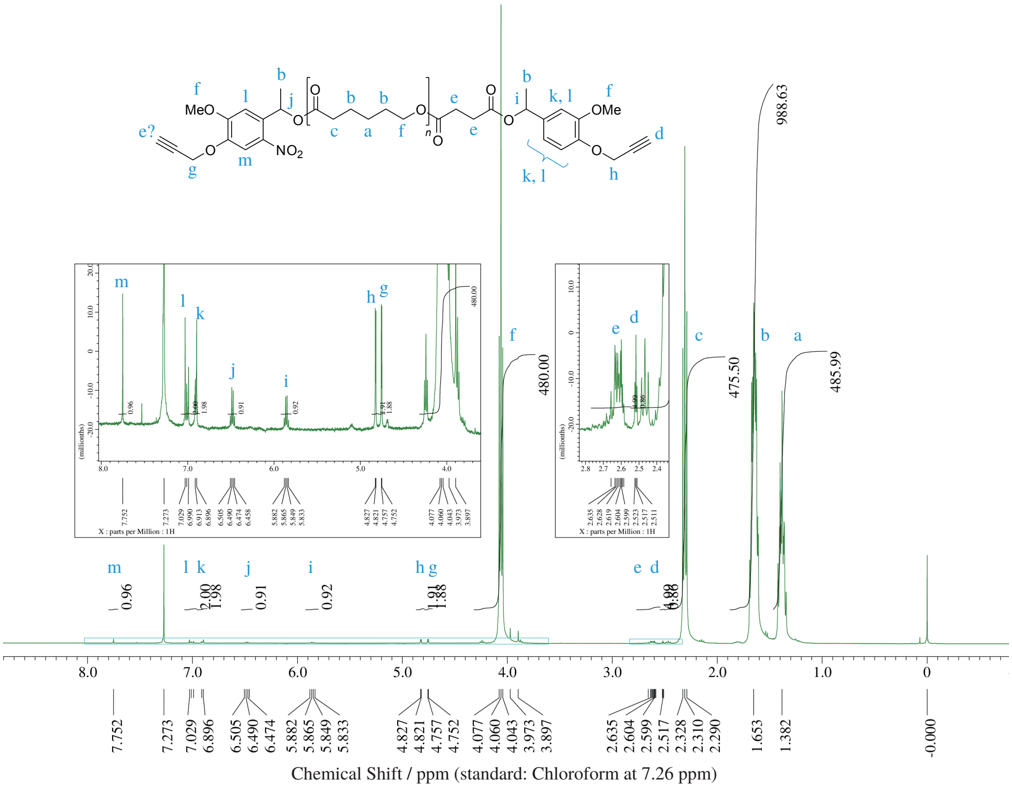

Figure B.12. ^{1}H-NMR spectrum of Alkyne-ONB-PCL-B-Alkyne **17’**.

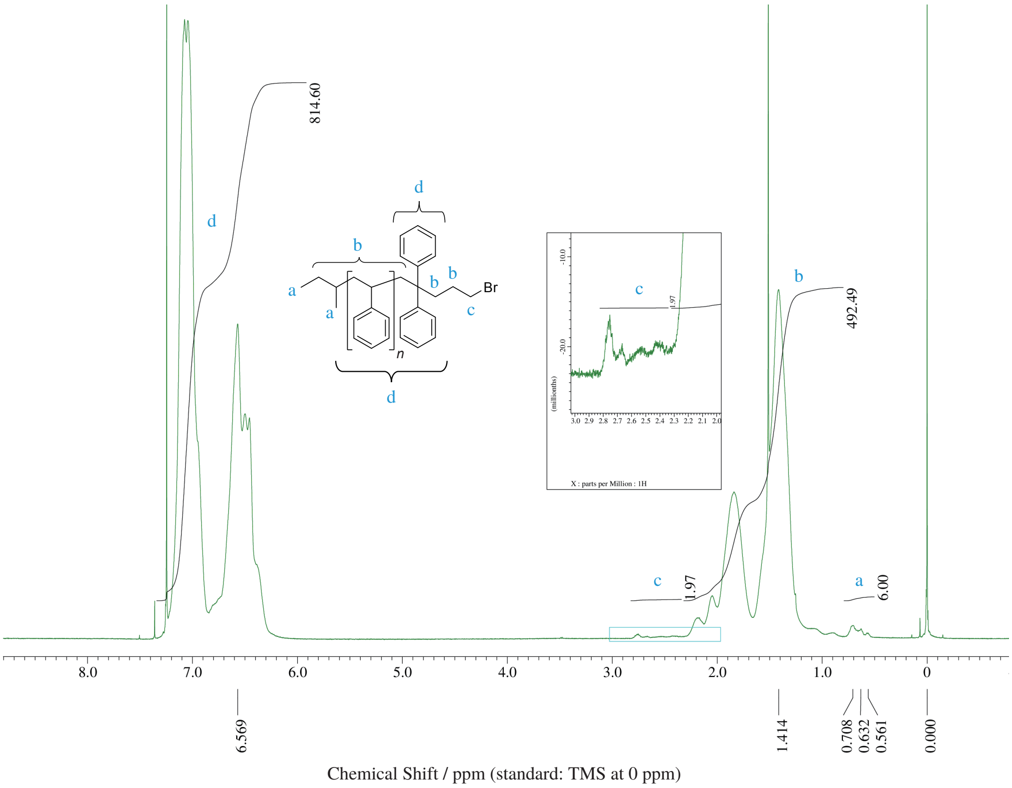

Figure B.13. ^{1}H-NMR spectrum of PS-Br **18**.

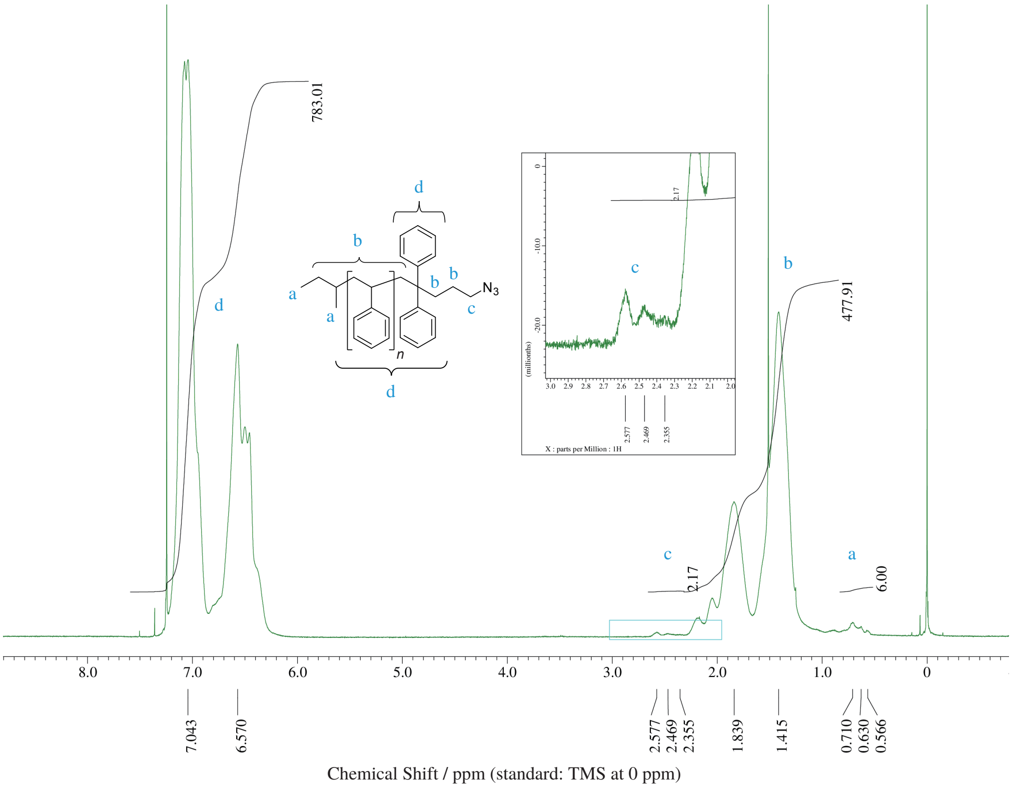

Figure B.14. ^{1}H-NMR spectrum of PS-N_3 **19**.

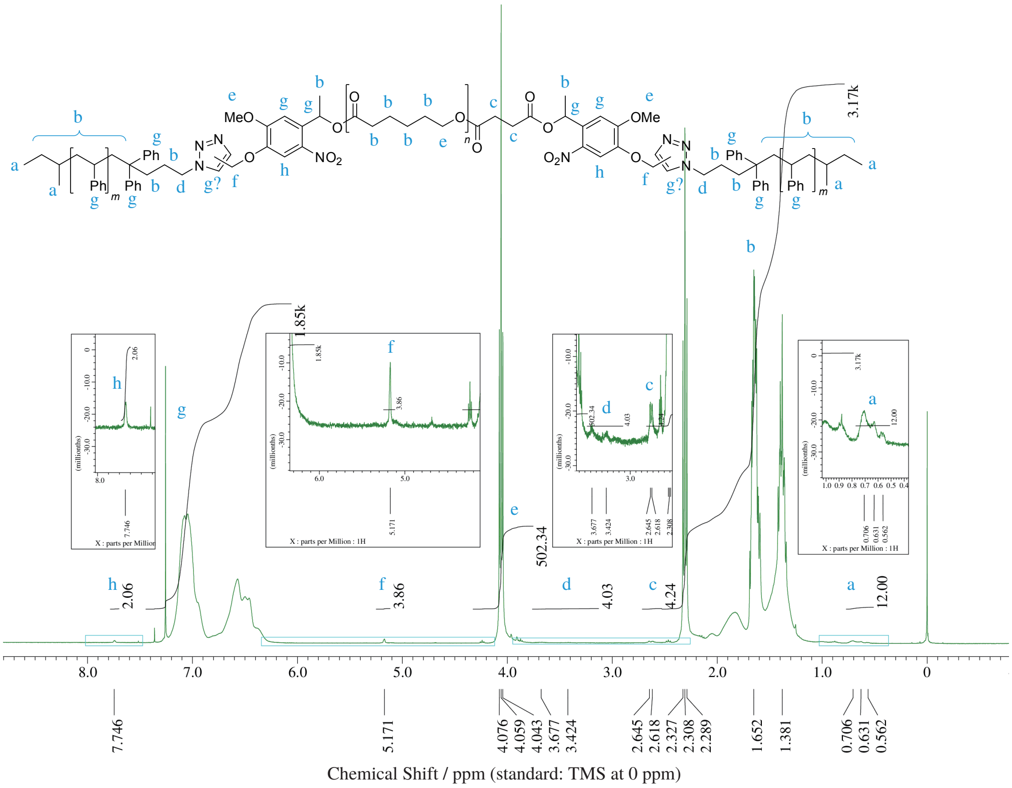

Figure B.15. ^{1}H-NMR spectrum of PS-ONB-PCL-ONB-PS **20**.

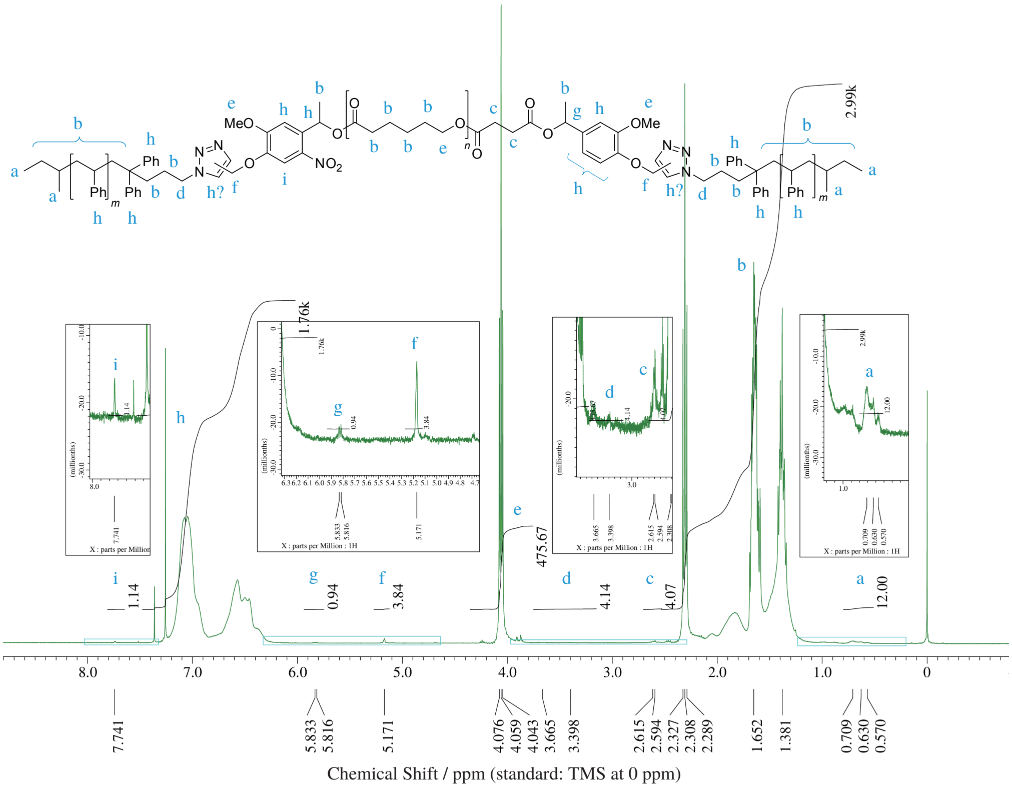

Figure B.16. ^{1}H-NMR spectrum of PS-ONB-PCL-B-PS **20’**.

Appendix C

Calculation of Photocleavage Yield

C.1 General Assumptions and Definitions

In this study, the photocleavage reaction of PCL-*b*-PS diblock and PS-*b*-PCL-*b*-PS triblock copolymers is monitored by GPC measurements after UV irradiation. However, what GPC observes is not the reaction itself but the fractions of polymeric species generated by the reaction. Therefore following assumptions have to be made to estimate the actual photocleavage yield from the area ratio of deconvoluted GPC peaks:

Assumption (1): The peak area in GPC chromatograms recorded by a UV detector is proportional to the absorbance of the corresponding component.

Assumption (2): The absorbance at $\lambda = 254$ nm arises from absorption by PS repeating units and ONB in either PS-*b*-PCL-*b*-PS, PCL-*b*-PS, or PS homopolymers and contributions from the other structures are negligible.

Assumption (3): The absorbance of ONB at $\lambda = 254$ nm does not change by photocleavage.

Following symbols are used in this Appendix:

- a_S and a_N represent the molar absorption coefficient of a PS repeating unit and ONB at $\lambda = 254$ nm, respectively.
- f is the ratio $a_\mathrm{N}/a_\mathrm{S}$.

- m_S is the number-averaged degree of polymerization of PS block chains in the block copolymer sample.
- x_0, x_1, and x_2 are the mole fractions of PCL chains tethered at no end (T0-PCL), one end (T1-PCL), and both ends (T2-PCL), respectively. In the case of PCL-*b*-PS, $x_2 = 0$ and $x_0 + x_1 = 1$ hold, while in the case of PS-*b*-PCL-*b*-PS $x_0 + x_1 + x_2 = 1$.
- A_T, A_D, and A_{PS} represent the area fractions of GPC peaks corresponding to PS-*b*-PCL-*b*-PS, PCL-*b*-PS , and PS homopolymers, respectively. In the case of PCL-*b*-PS $A_T = 0$ and $A_D + A_{PS} = 1$, while in the case of PS-*b*-PCL-*b*-PS $A_T + A_D + A_{PS} = 1$.

C.2 PCL-*b*-PS Diblock Copolymers

In the case of PCL-*b*-PS diblock copolymers having one ONB between two blocks, the absorbance of PCL-*b*-PS and PS homopolymer is proportional to x_1 and x_0, respectively, which simply leads to

$$A_D = K(m_S a_S + a_N)x_1, \tag{C.1}$$

$$A_{PS} = K(m_S a_S + a_N)x_0, \tag{C.2}$$

where K is a normalization factor to set $A_D + A_{PS} = 1$. Therefore,

$$x_1 = A_D, \tag{C.3}$$

$$x_0 = A_{PS}. \tag{C.4}$$

C.3 PS-*b*-PCL-*b*-PS Triblock Copolymers Having ONB in Both of Block Junctions

In the case of PS-*b*-PCL-*b*-PS triblock copolymers having ONB at both of two block junctions, the presence of one T2-PCL is equivalent to the presence of one PS-*b*-PCL-*b*-PS (having $2m_\mathrm{S}$ PS repeating units and two ONB). Likewise, the generation of one T1-PCL is equivalent to the generation of one PCL-*b*-PS (having m_S PS repeating units and one ONB) and one PS homopolymer (having m_S PS repeating units and one ONB). Furthermore, when one T0-PCL is generated, two PS homopolymers are liberated. Formulating these conditions give

$$A_\mathrm{T} = K' \cdot 2(m_\mathrm{S} a_\mathrm{S} + a_\mathrm{N}) x_2, \tag{C.5}$$

$$A_\mathrm{D} = K'(m_\mathrm{S} a_\mathrm{S} + a_\mathrm{N}) x_1, \tag{C.6}$$

$$A_\mathrm{PS} = K'((2m_\mathrm{S} a_\mathrm{S} + 2a_\mathrm{N}) x_0 + (m_\mathrm{S} a_\mathrm{S} + a_\mathrm{N}) x_1), \tag{C.7}$$

where K' is a normalization factor to set $A_\mathrm{T} + A_\mathrm{D} + A_\mathrm{PS} = 1$. The solution of the equation set is independent of m_S, a_S, and a_N:

$$x_2 = A_\mathrm{T}, \tag{C.8}$$

$$x_1 = 2A_\mathrm{D}, \tag{C.9}$$

$$x_0 = A_\mathrm{PS} - A_\mathrm{D}. \tag{C.10}$$

C.4 PS-*b*-PCL-*b*-PS Triblock Copolymers Having ONB in Either of Block Junctions

Since SC'S has two PS chains and one ONB, the right hand side of equation (C.5) and the first term in the right hand side of equation (C.7) should be replaced by $2m_\mathrm{S} a_\mathrm{S} + a_\mathrm{N}$, which leads to

$$A_{\mathrm{T}} = K'(2m_{\mathrm{S}}a_{\mathrm{S}} + a_{\mathrm{N}})x_2, \tag{C.5'}$$

$$A_{\mathrm{D}} = K'm_{\mathrm{S}}a_{\mathrm{S}}x_1, \tag{C.6'}$$

$$A_{\mathrm{PS}} = K'((2m_{\mathrm{S}}a_{\mathrm{S}} + a_{\mathrm{N}})x_0 + (m_{\mathrm{S}}a_{\mathrm{S}} + a_{\mathrm{N}})x_1), \tag{C.7'}$$

where K'' is another normalization factor. These equations can be solved to give

$$x_2 = A_{\mathrm{T}}, \tag{C.8'}$$

$$x_1 = (2 + f/m_{\mathrm{S}})A_{\mathrm{D}}, \tag{C.9'}$$

$$x_0 = A_{\mathrm{PS}} - (1 + f/m_{\mathrm{S}})A_{\mathrm{D}}, \tag{C.10'}$$

where $f = a_{\mathrm{N}}/a_{\mathrm{S}}$. f was estimated to be 39.5 from the GPC chromatograms of SC'S1 and PCL homopolymers having an ONB group in one chain-end.

List of Publications

Peer-Reviewed Papers

1. Nakagawa, S.; Kadena, K.; Ishizone, T.; Nojima, S.; Shimizu, T.; Yamaguchi, K.; Nakahama, S.; "Crystallization Behavior and Crystal Orientation of Poly(ε-caprolactone) Homopolymers Confined in Nanocylinders: Effects of Nanocylinder Dimension", *Macromolecules*, **45**, 1892-1900 (2012).
2. Nakagawa, S.; Tanaka, T.; Ishizone, T.; Nojima, S.; Kakiuchi, Y.; Yamaguchi, K.; Nakahama, S.; "Crystallization Behavior of Poly(ε-caprolactone) Chains Confined in Nanocylinders: Effects of Block Chains Tethered to Nanocylinder Interfaces", *Macromolecules*, **46**, 2199-2205 (2013).
3. Nakagawa, S.; Tanaka, T.; Ishizone, T.; Nojima, S.; Kamimura, K.; Yamaguchi, K.; Nakahama, S.; "Crystallization behavior of poly(ε-caprolactone) chains confined in lamellar nanodomains", *Polymer*, **55**, 4394-4400 (2014).
4. Nakagawa, S.; Marubayashi, H.; Nojima, S.; "Crystallization of Polymer Chains Confined in Nanodomains", *European Polymer Journal*, **70**, 262-275 (2015).
5. Nakagawa, S.; Ishizone, T.; Nojima, S.; Kamimura, K.; Yamaguchi, K.; Nakahama, S.; "Effects of Chain-Ends Tethering on the Crystallization Behavior of Poly(ε-caprolactone) Confined in Lamellar Nanodomains", *Macromolecules*, **48**, 7138-7145 (2015).

6. Nakagawa, S.; Yoneguchi, Y.; Ishizone, T.; Nojima, S.; Kamimura, K.; Yamaguchi, K.; Nakahama, S.; “Crystallization Behavior and Crystal Orientation of Spatially Confined Polymer Chains Tethered at Either or Both of Chain-Ends”, *In Preparation*.

Non Peer-Reviewed Papers

1. Nakagawa, S.; Tanaka, T.; Nojima, S.; “Crystallization Behavior of Homopolymer/-Block Chain Blends Confined in Nanocylinders with Different Diameters”, *Photon Factory Activity Report*, **29**, 172 (2012).

2. Nakagawa, S.; Tanaka, T.; Nojima, S.; “Crystallization of Poly(ε-caprolactone) Chains Confined in Lamellar Nanodomains”, *Photon Factory Activity Report*, **31**, 217 (2014).

3. Nakagawa, S.; Kawazu, K.; Nojima, S.; “Crystallization of Both-ends-tethered, One-end-tethered, and Untethered Polymer Chains Confined in Lamellar Nanodomains”, *Photon Factory Activity Report*, **32**, 69 (2014).

Non Peer-Reviewed Presentations

The presenter is marked by a circle.

1. ○Nakagawa, S.; Kadena, K.; Nojima, S.; Ishizone, T.; Shimizu, T.; Yamaguchi, K.; Nakahama, S.; “Crystallization of Homopolymers Confined in Cylindrical Nanodomains with Various Sizes”, *60th SPSJ Annual Meeting*, 1E12 (Oral), Osaka, Japan (2011).

2. ○Nakagawa, S.; Kadena, K.; Nojima, S.; Ishizone, T.; Shimizu, T.; Yamaguchi, K.; Nakahama, S.; “Crystallization Behavior of Homopolymer/Block Chain Blends

Confined in Cylindrical Nanodomains", *60th SPSJ Annual Meeting*, 3Pd036 (Poster), Osaka, Japan (2011).

3. Kadena, K.; ○Nakagawa, S.; Nojima, S.; "Crystallization of Homopolymers Confined in Cylindrical Nanodomains with Various Dimensions", *28th PF Symposium*, UG02-06 (Poster), Tsukuba, Japan (2011).

4. ○Nakagawa, S.; Nojima, S.; Ishizone, T.; Shimizu, T.; Kakiuchi, Y.; Yamaguchi, K.; Nakahama, S.; "Crystallization of Homopolymer/Block Chain Blends Confined in Nanocylinders", *60th Symposium on Macromolecules*, 1I11 (Oral), Okayama, Japan (2011).

5. Tanaka, Takumi; ○Nakagawa, S.; Nojima, S.; "Crystallization Behavior of Block Chain/Homopolymer Blends Confined in Nanocylinders: Effects of Cylinder Size", *28th PF Symposium*, UG02-06 (Poster), Tsukuba, Japan (2012).

6. ○Tanaka, Takumi; Nakagawa, S.; Nojima, S.; Ishizone, T.; Kakiuchi, Y.; Yamaguchi, K.; Nakahama, S.; "Crystallization of Homopolymer/Block Chain Blends Confined in Nanocylinders with Different Dimensions", *61st SPSJ Annual Meeting*, 2Pc029 (Poster), Yokohama, Japan (2012).

7. ○Nakagawa, S.; Tanaka, Takumi; Nojima, S.; Ishizone, T.; Kakiuchi, Y.; Yamaguchi, K.; Nakahama, S.; "Effects of Chain-end Tethering on Crystallization of Polymer Chains Confined in Nanodomains", *61st Symposium on Macromolecules*, 1J13 (Oral), Nagoya, Japan (2011).

8. ○Nakagawa, S.; Tanaka, Takumi; Nojima, S.; Ishizone, T.; Kakiuchi, Y.; Yamaguchi, K.; Nakahama, S.; "Effects of Chain End Tethering on Crystallization Behavior of Polymer Chains within Isolated Nanodomains", *62nd SPSJ Annual Meeting*, 2D16 (Oral), Kyoto, Japan (2013).

9. ○Nakagawa, S.; Tanaka, Takumi; Nojima, S.; Ishizone, T.; Yamaguchi, K.; Nakahama, S.; “Effects of Chain-end Tethering on Crystallization of Polymer Chains Confined in Nanodomains with Various Shapes and Dimensions”, *62nd Symposium on Macromolecules*, 2K09 (Oral), Kanazawa, Japan (2013).

10. ○Nakagawa, S.; Tanaka, Takumi; Nojima, S.; Ishizone, T.; Kamimura, K.; Yamaguchi, K.; Nakahama, S.; “Crystallization of Homopolymers Confined in Lamellar Nanodomains”, *63rd SPSJ Annual Meeting*, 1Pe017 (Poster), Nagoya, Japan (2014).

11. ○Nakagawa, S.; Tanaka, Takumi; Nojima, S.; Ishizone, T.; Kamimura, K.; Yamaguchi, K.; Nakahama, S.; “Effects of Chain End Tethering on Crystallization of Spatially-confined Polymer Chains”, *63rd Symposium on Macromolecules*, 2I04 (Oral), Nagasaki, Japan (2014).

12. ○Nakagawa, S.; Nojima, S.; Ishizone, T.; Kamimura, K.; Yamaguchi, K.; Nakahama, S.; “Effects of Chain-end Tethering on Crystallization of Polymer Chains within Nanodomains”, *64th SPSJ Annual Meeting*, 3D04 (Oral), Sapporo, Japan (2015).

13. ○Nakagawa, S.; Nojima, S.; Ishizone, T.; Kamimura, K.; Yamaguchi, K.; Nakahama, S.; “Controlling Crystallization of Polymer Chains Confined in Nanodomains by Chain-end Tethering”, *64th Symposium on Macromolecules*, 3H11 (Oral), Sendai, Japan (2015).

14. ○Kawazu, K; Nakagawa, S.; Nojima, S.; Ishizone, T.; Arai, D.; Yamaguchi, K.; Nakahama, S.; “Effects of Chain-ends on Crystallization of Polymer Chains Confined in Nanodomains”, *64th Symposium on Macromolecules*, 2Pe055 (Poster), Sendai, Japan (2015).

Acknowledgment

Foremost, the author wishes to express his sincere gratitude to his adviser Professor Shuichi Nojima at Tokyo Institute of Technology (Tokyo Tech) for invaluable advices and encouraging guidance. A sincere thank of the author also goes to Professor Takashi Ishizone at Tokyo Tech and Professor Kazuo Yamaguchi and Professor Seiichi Nakahama at Kanagawa University for their helpful advices in the course of collaborative researches. The author is grateful to Assistant Professor Hironori Marubayashi at Tokyo Tech for fruitful suggestions on both the research and career of the author.

The author also offers his gratitude to Lecturer Satoshi Uchida and Assistant Professor Raita Goseki at Tokyo Tech for their indispensable support and suggestion, and also special thanks to the members of Ishizone laboratory at Tokyo Tech and Yamaguchi laboratory at Kanagawa University for their kind cooperation. The author's gratitude also goes to his coworkers in Nojima laboratory at Tokyo Tech, especially to Mr. Yuki Yoneguchi, Mr. Koshun Kawazu, Mr. Takumi Tanaka, and Mr. Ken-ichi Kadena, for their kind help and support.

A part of this work was supported by JSPS Grant-in-Aid for Scientific Research (Grant No. 15J10502). The author gratefully acknowledges a JSPS Research Fellowship for Young Scientists.

Last but not least, the author wishes to express deep appreciation to his parents, Erika and Mikio, and his brother, Tetsuro, who gave the author selfless love and the courage that enabled him to finish this work.

Shintaro Nakagawa, February 2016